

# ISOLATED PHOTON PRODUCTION IN DEEP-INELASTIC SCATTERING AT HERA

---

**Dissertation**  
**zur**  
**Erlangung der naturwissenschaftlichen Doktorwürde**  
**(Dr. sc. nat.)**

**vorgelegt der**

**Mathematisch-naturwissenschaftlichen Fakultät**  
**der**  
**Universität Zürich**

**von**

**CARSTEN SCHMITZ**

**aus**  
**Deutschland**

**Promotionskomitee**

Prof. Dr. Ulrich Straumann (Vorsitz)  
Prof. Dr. Thomas Gehrman  
Dr. Katharina Müller

**Zürich, 2007**



# ABSTRACT

---

This thesis presents the measurement of isolated photon production in deep-inelastic  $ep$  scattering with the H1 detector at HERA. The measurement is performed in the kinematic range of the negative four-momentum transfer squared  $4 < Q^2 < 150 \text{ GeV}^2$  and mass of the hadronic system  $W_X > 50 \text{ GeV}$ . The analysis is based on data taken during the HERA I and HERA II data taking periods with a total integrated luminosity of  $227 \text{ pb}^{-1}$ . The production cross section of isolated photons with a transverse energy range  $3 < E_T^\gamma < 10 \text{ GeV}$  and pseudorapidity range  $-1.2 < \eta^\gamma < 1.8$  is measured as a function of  $E_T^\gamma$ ,  $\eta^\gamma$  and  $Q^2$ . Isolated photon cross sections are also measured for events with no further jet or at least one hadronic jet. The measurements are compared with predictions from Monte Carlo generators modelling the photon radiation from the quark and the electron lines, as well as with calculations at leading and next to leading order in the strong coupling. The predictions significantly underestimate the measured cross sections. In addition, less isolated photons in a close hadronic vicinity are measured and compared to the Monte Carlo predictions, which increasingly underestimate the measured cross sections for diminishing isolation of the photons.

# KURZFASSUNG

---

In dieser Arbeit wird die Messung der Produktion von isolierten Photonen in tiefinelastischer  $ep$  Streuung mit dem H1 Detektor bei HERA vorgestellt. Die Messung erstreckt sich über den kinematischen Bereich des negativen Viererimpulsübertragsquadrates von  $4 < Q^2 < 150 \text{ GeV}^2$  und den Bereich der Masse des hadronischen Systems von  $W_X > 50 \text{ GeV}$ . Die Analyse basiert auf Daten der HERA I und HERA II Datennahmeperioden entsprechend einer totalen integrierten Luminosität von  $227 \text{ pb}^{-1}$ . Der Wirkungsquerschnitt von isolierten Photonen mit einer transversalen Energie im Bereich  $3 < E_T^\gamma < 10 \text{ GeV}$  und einer Pseudorapidität im Bereich  $-1.2 < \eta^\gamma < 1.8$  werden als Funktion von  $E_T^\gamma$ ,  $\eta^\gamma$  und  $Q^2$  gemessen. Des Weiteren werden die Wirkungsquerschnitte isolierter Photonen gemessen für Ereignisse mit keinem weiteren Jet oder mindestens einem hadronischen Jet. Die Messungen werden verglichen mit den Vorhersagen von Monte Carlo Generatoren, die die Photonabstrahlung von den Quark- und Elektronenlinien modellieren, sowie mit Rechnungen in führender und nächst führender Ordnung in der starken Kopplung. Die Vorhersagen unterschätzen die gemessenen Wirkungsquerschnitte beträchtlich. Zudem wird eine Messung schwach isolierter Photonen in unmittelbarer hadronischer Umgebung vorgestellt und mit den Monte Carlo Vorhersagen verglichen. Die Monte Carlo Vorhersagen unterschätzen die gemessenen Wirkungsquerschnitte zunehmend bei abnehmender Isolation der Photonen.



# CONTENTS

---

<b>Introduction</b>	<b>1</b>
<b>1 Theoretical Framework</b>	<b>5</b>
1.1 Fundamentals of the Electron-Proton Scattering . . . . .	5
1.2 Deep-Inelastic Scattering . . . . .	7
1.2.1 Neutral Current DIS Cross Section at low $Q^2$ . . . . .	7
1.2.2 Quark Parton Model . . . . .	9
1.2.3 The Strong Interaction . . . . .	10
1.2.4 Factorisation and Parton Evolution . . . . .	11
1.3 Isolated Photon Production in DIS . . . . .	13
1.3.1 Fragmentation and Collinear Contribution . . . . .	16
1.4 Neutral Hadron Background . . . . .	18
1.5 Recent Isolated Photon Research . . . . .	19
1.5.1 Results at HERA . . . . .	19
1.5.2 Results in Hadronic Collisions . . . . .	22
1.5.3 Measurement of the Photon Fragmentation Function at LEP . . . . .	25
<b>2 Calculations</b>	<b>27</b>
2.1 Fixed Order QCD Calculations . . . . .	27
2.1.1 Inclusive LO Calculation . . . . .	27
2.1.2 Exclusive Photon plus Jet NLO Calculation . . . . .	28
2.2 Monte Carlo Simulations . . . . .	29
2.2.1 Event Generators . . . . .	30
2.2.2 Isolated Photon Simulations . . . . .	31
2.2.3 Neutral Hadron Background Simulation . . . . .	33
2.2.4 Single Particle Monte Carlo . . . . .	34
2.2.5 Photoproduction Background Monte Carlo . . . . .	36
<b>3 The H1 Experiment at HERA</b>	<b>39</b>
3.1 HERA Storage Ring . . . . .	39

3.1.1	Luminosity Upgrade Project for HERA . . . . .	40
3.2	H1 Detector . . . . .	41
3.2.1	Calorimetry . . . . .	42
3.2.2	Tracking . . . . .	50
3.2.3	Luminosity System . . . . .	53
3.2.4	Time-of-Flight System . . . . .	54
3.2.5	Trigger System and Data Acquisition . . . . .	54
3.2.6	Detector Simulation . . . . .	56
<b>4</b>	<b>Event Selection</b>	<b>57</b>
4.1	Data Taking Periods and Preselection . . . . .	57
4.2	Triggering . . . . .	58
4.2.1	Downscaled Subtriggers . . . . .	59
4.2.2	Trigger Efficiency . . . . .	61
4.3	Selection of DIS Events . . . . .	64
4.3.1	Electron Reconstruction . . . . .	64
4.3.2	Kinematic Selection . . . . .	65
4.3.3	Hadronic Final State . . . . .	67
4.3.4	Rejection of $\gamma p$ Events . . . . .	67
4.4	Selection of Photon Candidates . . . . .	68
4.5	Jet Algorithm and Isolation Requirement . . . . .	71
4.6	Selection Summary . . . . .	72
4.7	Energy Calibration . . . . .	79
4.7.1	Electron Energy Calibration . . . . .	79
4.7.2	Photon Energy Calibration . . . . .	81
<b>5</b>	<b>Photon Signal Extraction</b>	<b>85</b>
5.1	Shower Shape Variables . . . . .	86
5.1.1	Variables . . . . .	86
5.1.2	Correlations . . . . .	88
5.2	Classifiers . . . . .	92
5.2.1	Performance . . . . .	94
5.3	Signal Extraction . . . . .	97
5.3.1	Consistency Checks . . . . .	99
<b>6</b>	<b>Cross Section Measurement and Systematic Uncertainties</b>	<b>107</b>
6.1	Cross Section Measurement . . . . .	107
6.1.1	Acceptance Corrections . . . . .	107
6.1.2	Hadron Corrections . . . . .	109
6.2	Systematic Uncertainties . . . . .	110

---

<b>7</b>	<b>Results</b>	<b>117</b>
7.1	Inclusive Isolated Photon Production . . . . .	117
7.2	Isolated Photons at high $Q^2$ . . . . .	122
7.3	Photons plus Jet and Photons plus no-Jets . . . . .	123
7.4	Photons in Jet Vicinity . . . . .	126
7.4.1	Measurement at low $z$ . . . . .	126
7.4.2	Measurement at small $R_0$ . . . . .	133
<b>8</b>	<b>Conclusions and Outlook</b>	<b>137</b>
<b>A</b>	<b>Kinematics of the Neutral Pion Decay</b>	<b>141</b>
<b>B</b>	<b>Multivariate Classification Methods</b>	<b>147</b>
<b>C</b>	<b>DVCS and BH Event Samples</b>	<b>153</b>
<b>D</b>	<b>Track Quality Criteria</b>	<b>155</b>
<b>E</b>	<b>Analysis Bins</b>	<b>157</b>
<b>F</b>	<b>Cross Section Tables</b>	<b>159</b>
	<b>List of Figures</b>	<b>167</b>
	<b>List of Tables</b>	<b>170</b>
	<b>Bibliography</b>	<b>178</b>





# INTRODUCTION

---

The strong force as one of three fundamental interactions described in the Standard Model (SM) of particle physics is mediated between quarks, the constituents of hadrons, by the exchange of massless gauge bosons, the gluons. The strong interaction is exceptional, in that the strong coupling increases towards larger distances and accordingly lower energies, which gives rise to the concept of quark confinement. The concept explains why no free quarks have ever been observed.

At short distances the strong coupling constant is sufficiently small to allow perturbative calculations, where scattering amplitudes are expressed in power series of the coupling constant. Perturbative calculations have proven to be extremely successful when hard energy scales are involved. For larger distances and lower energy scales, however, the predictive power of perturbative Quantum Chromodynamics (QCD, the theory of the strong interaction) is weakened and requires further understanding. Likewise, the long distance process of hadronisation by which quarks, emerging from high energy collisions, fragment into *jets* of colour-neutral hadrons cannot be calculated within perturbation theory and leads to uncertainties in the reconstruction of the underlying event kinematics.

As opposed to jets of hadrons, isolated photons<sup>1</sup> originating from the hard interaction are largely insensitive to the effects of hadronisation and thus provide a sensitive probe for precision tests of perturbative QCD. They carry unaltered information of the hard scatter. Furthermore, a good understanding of the SM production mechanism of isolated photons is important for new physics searches at hadron colliders, where decay photons from new particles have to be separated from the background induced by isolated photon production. A famous example is the search for the Higgs boson in the di-photon channel for relatively small Higgs masses ( $M_H \lesssim 140$  GeV).

In this work a measurement of isolated photons in deep-inelastic scattering (DIS) is presented. The measurement provides a test of perturbative QCD in a kinematic range with two hard scales, the negative four-momentum transfer squared  $Q^2$  of the exchanged virtual photon, and the transverse energy of the emitted photon  $E_T^\gamma$ . The measurement range covered by this analysis significantly extends the kinematic range probed by the previous ZEUS measure-

---

<sup>1</sup>Photons coupling to the interacting partons are often called “prompt” in contrast to photons from hadron decays or photons emitted by leptons.

ment [1] with respect to  $Q^2$ , transverse energy and pseudorapidity of the photons. In DIS the final state photon may be emitted by a quark ( $QQ$ ) and by wide angle radiation from the lepton ( $LL$ ). In contrast to photoproduction the measurement of isolated photons in DIS has less uncertainties from contributions of resolved photon processes.

Beside the direct radiation of a photon from the quark, the  $QQ$  process also includes contributions from the quark-to-photon fragmentation function, corresponding to the fragmentation of the quark into a hadronic jet containing a photon which carries a large fraction of the jet energy. Whereas the direct radiation of a photon can be perturbatively calculated, the fragmentation contribution is based on a long distance process, which is not accessible within perturbation theory and needs to be determined from data. This fragmentation contribution cannot be eliminated but is suppressed by the isolation requirement for the photon.

Additionally, this is the first time at HERA that also less isolated photons in a close vicinity of jets are measured by variation of the isolation requirement. These measurements may allow the extraction of the quark-to-photon fragmentation function as was suggested by Gehrmann-De Ridder, Gehrmann and Poulsen [2].

The analysed data of electron<sup>2</sup>-proton collisions at a centre-of-mass energy of 319 GeV were collected during the HERA I and HERA II data taking periods using the H1 detector at the HERA collider with a total integrated luminosity of  $227 \text{ pb}^{-1}$ . The production of isolated photons is investigated inclusively and for the exclusive production of a photon accompanied by no or at least one hadronic jet in the acceptance of the detector. Photons are identified using a multivariate analysis of the shapes of the calorimeter energy deposits to separate the photons from neutral hadrons and their decay products.

The results of this work on the production of isolated photons are in the process of being published by the H1 collaboration [3].<sup>3</sup>

The outline of the thesis is as follows:

- The theoretical concepts necessary for the understanding of the presented measurement of isolated photons in DIS are introduced in chapter 1. In this chapter also a brief review on recent isolated photon research is given.
- The fixed order calculations and Monte Carlo (MC) predictions used for comparisons are described in chapter 2.
- Chapter 3 provides a brief overview of the H1 detector and its main components at the HERA collider.
- The main selection of isolated photon candidates in deep-inelastic scattering events is presented in chapter 4.

---

<sup>2</sup>The analysis uses data from periods when the beam lepton was either a positron or an electron. Unless otherwise stated, the term electron refers to both the electron and the positron.

<sup>3</sup>Throughout this work, figures marked H1 can also be found in the corresponding H1 publication.

- After the event selection the photon candidates still contain a sizeable fraction of background from neutral hadrons, which is subtracted by a dedicated shower shape analysis. This photon signal extraction is explained in chapter 5.
- The cross section measurement and corrections to the data are described in chapter 6 followed by a discussion of the systematic errors of the measurement.
- The final cross sections are presented and discussed in chapter 7.



# CHAPTER 1

## THEORETICAL FRAMEWORK

---

The chapter introduces the theoretical framework necessary for the understanding of isolated photon production in deep-inelastic scattering. It starts with fundamental concepts of electron-proton ( $ep$ ) collisions and gives a phenomenological introduction on deep-inelastic scattering extended by the theory of the strong interaction. In this context the production of isolated photons is discussed with close attention to the treatment of non-perturbative fragmentation contributions. Finally, a review on recent isolated photon research is given.

### 1.1 Fundamentals of the Electron-Proton Scattering

Within the theory of electroweak interactions the scattering of electrons and protons is described by the exchange of virtual gauge bosons ( $\gamma, Z^0, W^\pm$ ). *Neutral current* (NC) interactions are mediated by either a photon or the  $Z^0$  boson, while in *charged current* (CC) interactions a  $W^\pm$  boson is exchanged. As illustrated in figure 1.1, the final state in generic  $ep$  collisions consists of the hadronic system  $X$ <sup>1</sup> and the final state lepton, which is an electron in NC reactions ( $ep \rightarrow eX$ ) and a neutrino for CC reactions ( $ep \rightarrow \nu_e X$ ).

For a fixed centre-of-mass energy  $\sqrt{s}$  the kinematics of the reaction is fully determined by two Lorentz invariant variables defined by the four-momenta of the scattering particles. It is, however, convenient to define further invariants depending on the aspects of interest. Following the notation used in the figure,  $k$  and  $k'$  denote the four-momenta of the incoming and outgoing lepton,  $P$  corresponds to the incoming proton. When neglecting the electron and proton mass,  $\sqrt{s}$  is given by the electron and proton beam energies  $E_e$  and  $E_p$

$$s = (k + P)^2 \approx 4E_e E_p. \quad (1.1)$$

The four-momentum transfer at the electron vertex  $q = k - k'$  defines the invariant mass of the exchanged virtual boson  $\sqrt{q^2}$ . As  $q^2$  is a negative quantity, the notations usually use the

---

<sup>1</sup>X refers to any possible (hadronic) final state.

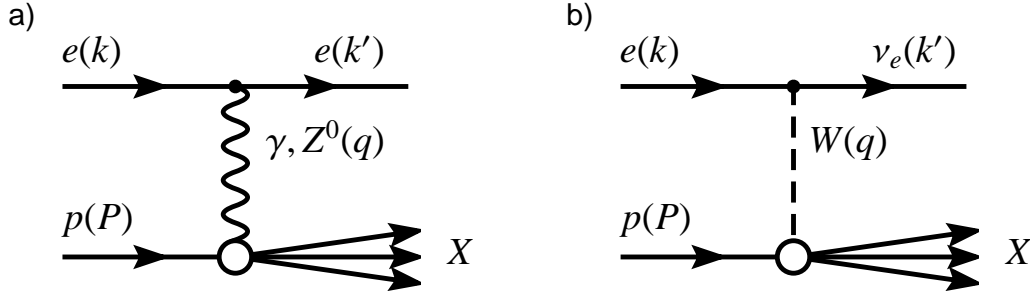


FIGURE 1.1: Lowest order Feynman graphs for the  $ep$  scattering process. a) Neutral current reaction (NC) with an exchange of a photon or  $Z^0$  boson. b) Charged current process (CC) with an exchange of a  $W^\pm$  boson.

negative four-momentum transfer squared

$$Q^2 = -q^2 = -(k - k')^2 > 0, \quad (1.2)$$

which is also referred to as the *virtuality* of the exchanged boson. When  $Q^2 \approx 0 \text{ GeV}^2$ , the exchanged photons are termed quasi-real or on mass-shell.

Furthermore, the inelasticity  $y$ , defined as

$$y = \frac{q \cdot P}{k \cdot P}, \quad (1.3)$$

describes the relative energy transfer of the electron in the proton rest frame. Besides  $Q^2$ ,  $s$  and  $y$ , also the Bjorken scaling variable  $x$  is used to describe the event kinematics:

$$x = \frac{Q^2}{2P \cdot q}. \quad (1.4)$$

When the interacting parton in the proton (see section 1.2.2) has negligible transverse momentum, the Bjorken scaling variable  $x$  resembles the fraction of the proton's momentum carried by the parton. Both variables,  $x$  and  $y$ , are dimensionless and limited to the range  $0 \leq x, y \leq 1$ . Neglecting the particle masses, the above defined Lorentz invariant variables can be related by

$$Q^2 \approx xys, \quad (1.5)$$

which indicates the redundancy in the chosen set of variables. In addition to these observables the invariant mass of the hadronic final state  $W_X$  is of importance in the present analysis, which is defined by<sup>2</sup>

$$W_X^2 = (q + P)^2. \quad (1.6)$$

<sup>2</sup>In presence of isolated photons in the final state, the definition needs to be specified more carefully (cf. section 1.3).

The total  $ep$  cross section contains contributions from the exchange of all three mentioned gauge bosons. With  $\sigma_{\text{int}}(\gamma Z^0)$  being the interference term the NC cross section can hence be written as the sum  $\sigma^{\text{NC}} = \sigma(Z^0) + \sigma_{\text{int}}(\gamma Z^0) + \sigma(\gamma)$ . The relative contributions can be estimated by

$$\frac{\sigma_{\text{int}}(\gamma Z^0)}{\sigma(\gamma)} \sim \frac{Q^2}{Q^2 + M_{Z^0}^2}, \quad \frac{\sigma(Z^0)}{\sigma(\gamma)} \sim \left( \frac{Q^2}{Q^2 + M_{Z^0}^2} \right)^2. \quad (1.7)$$

As the typical four-momentum transfer relevant to this analysis is small compared to the mass of the  $Z^0$  boson ( $Q^2 \ll M_{Z^0}^2 \approx 91^2 \text{ GeV}^2$ ), the exchange of the  $Z^0$  boson is henceforth neglected. Analogously the CC interaction is suppressed at comparatively low  $Q^2$  as can be seen in figure 1.2. The figure shows the neutral and charged current cross section measured by the H1 experiment as a function of  $Q^2$  and it also demonstrates a small difference in the NC cross section between  $e^+p$  and  $e^-p$  scattering at high  $Q^2$ , which is due to the increasing effect of the  $\gamma Z^0$  interference in the region  $Q^2 \geq M_{Z^0}^2$ .

## 1.2 Deep-Inelastic Scattering

In contrast to *photoproduction* ( $\gamma p$ ) events, in which a quasi-real photon is exchanged at  $Q^2 \approx 0 \text{ GeV}^2$ , events with higher virtualities of the exchanged photon  $Q^2 > 1 \text{ GeV}^2$  are referred to as *deep-inelastic scattering* (DIS).

### 1.2.1 Neutral Current DIS Cross Section at low $Q^2$

In Quantum Electro-Dynamics (QED) the neutral current DIS cross section can be derived from the tensor product

$$d\sigma \sim L_{\mu\nu} W^{\mu\nu}, \quad (1.8)$$

where the leptonic tensor  $L_{\mu\nu}$  describes the interaction between the point-like lepton and the exchanged gauge boson. The leptonic tensor is precisely predicted from electroweak theory, while the hadronic tensor  $W^{\mu\nu}$  cannot be calculated from first principles due to the unknown internal structure of the proton and is therefore expressed in terms of two unknown structure functions. Considering the pure photon exchange, the inclusive differential neutral current cross section at low  $Q^2$  is usually expressed by means of the two independent proton structure functions  $F_2$  and  $F_L$ :

$$\frac{d^2\sigma_{\text{NC}}}{dx dQ^2} = \frac{2\pi\alpha^2}{xQ^4} Y_+ \left( F_2(x, Q^2) - \frac{y^2}{Y_+} F_L(x, Q^2) \right), \quad (1.9)$$

where  $\alpha$  is the fine structure constant and  $Y_+ = 1 + (1 - y)^2$  the *helicity factor*. The cross section at low  $Q^2$  can be interpreted as the interaction of a flux of incoming virtual photons

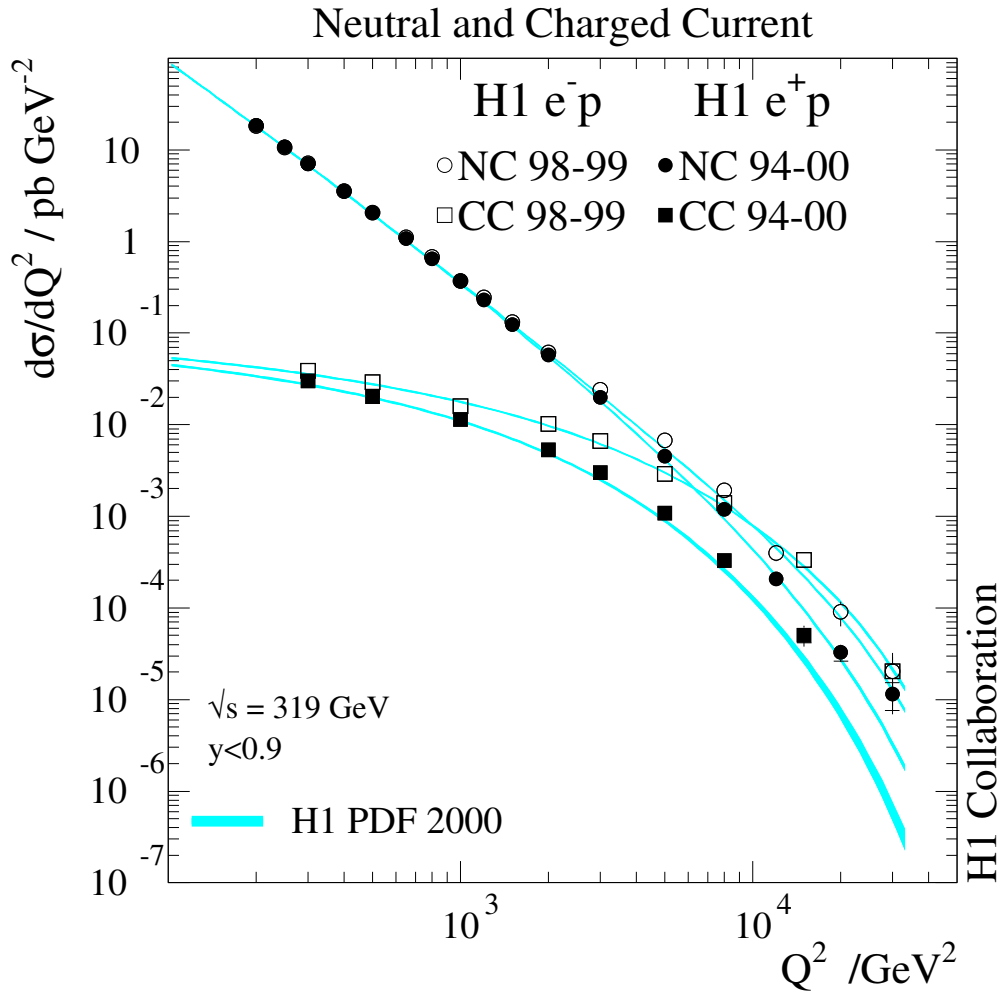


FIGURE 1.2: The  $Q^2$  dependence of the NC (circles) and CC (squares) cross sections  $d\sigma/dQ^2$  shown for  $e^+p$  (solid points) data and  $e^-p$  (open points) data measured by the H1 experiment together with the corresponding Standard Model expectation [4].



with the proton. Since the virtual photons can have transversal as well as longitudinal polarisation, the structure functions can be associated to the absorption cross sections  $\sigma_T$  and  $\sigma_L$  for transversally and longitudinally polarised virtual photons:

$$F_2(x, Q^2) = \frac{Q^2}{4\pi^2\alpha} (\sigma_T(x, Q^2) + \sigma_L(x, Q^2)), \quad (1.10)$$

$$F_L(x, Q^2) = \frac{Q^2}{4\pi^2\alpha} \sigma_L(x, Q^2). \quad (1.11)$$

Because of the direct relation to the cross section for longitudinally polarised photons,  $F_L$  is termed *longitudinal structure function*. Since cross sections are always positive, the following constraint can be derived from equations (1.10) and (1.11):

$$0 \leq F_L(x, Q^2) \leq F_2(x, Q^2). \quad (1.12)$$

Due to the factor  $y^2/Y_+$  in equation (1.9) the  $F_L$  contribution to the DIS cross section is only of significance at high values of inelasticity. For the major part of the phase space accessible at HERA the cross section is dominated by  $F_2$ . A simultaneous measurement of  $F_2$  and  $F_L$  is only possible if the inelasticity is varied for fixed values of  $x$  and  $Q^2$ . According to equation (1.5) this implies a variation of the centre-of-mass energy.<sup>3</sup>

## 1.2.2 Quark Parton Model

The naïve quark parton model (QPM) describes the proton as a state of point-like spin- $\frac{1}{2}$  particles (partons) that can be associated to three quarks, which are needed to reproduce the quantum numbers of the proton. When viewing the  $ep$  interaction in the *infinite momentum frame* ( $P^2 \gg m_p^2$ ), the transverse momenta of the quarks can be neglected and the proton is considered as a parallel stream of independent partons which carry a fraction  $\xi_i$  of the longitudinal proton momentum, such that  $\sum_i \xi_i = 1$ . Figure 1.3 shows the electron-proton scattering in the quark parton model. The DIS process is thus interpreted as an incoherent sum of elastic electron-quark scattering processes, of which the cross section is well predicted by QED:

$$\left( \frac{d^2\sigma}{dx dQ^2} \right)_{eq_i \rightarrow eq_i} = \frac{2\pi\alpha^2}{Q^4} e_i^2 Y_+ \delta(x - \xi), \quad (1.13)$$

where  $e_i$  is the quark charge. Furthermore, if the probability to find a quark  $i$  at a momentum fraction of the proton  $\xi$  is expressed in terms of *parton density functions*  $q_i(\xi)$ , the differential NC cross section can be written as a sum over all quark flavours

$$\frac{d^2\sigma}{dx dQ^2} = \sum_i \int_0^1 d\xi q_i(\xi) \left( \frac{d^2\sigma}{dx dQ^2} \right)_{eq_i \rightarrow eq_i}. \quad (1.14)$$

<sup>3</sup>The last months in the running of HERA are primarily dedicated to the measurement of the longitudinal proton structure function  $F_L$ . The centre-of-mass energy in the  $ep$  collisions was reduced from previously 319 GeV to 225 GeV.

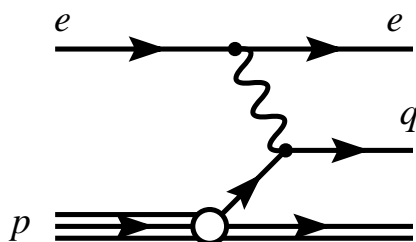


FIGURE 1.3: Deep-inelastic scattering in lowest order perturbation theory according to the quark parton model.

The  $\delta$ -function in equation (1.13) implies that the momentum fraction of the quark  $\xi$  is equivalent to the formerly introduced Bjorken scaling variable  $x$ . Inserting equation (1.13) in (1.14) and comparing the result to equation (1.9) yields

$$F_2(x, Q^2) = x \sum_i e_i^2 q_i(x) \quad \text{and} \quad (1.15)$$

$$F_L(x, Q^2) = 0. \quad (1.16)$$

It should be noted that in the QPM the proton structure function  $F_2$  is independent of the scale  $Q^2$ . This so-called *scaling* behaviour of  $F_2$  was indeed observed in the accessible  $x$  range of first DIS experiments [5, 6] supporting the QPM picture of the proton. Later, the observation of *scaling violations* at lower or higher  $x$  values gave rise to the assumption that also gluons and gluon splitting (see section 1.2.3) had to be considered for the successful description of the proton content. The scaling violations are clearly visible in the H1 measurement of  $F_2$  in dependence of  $Q^2$  shown in figure 1.6, which is further discussed in section 1.2.4.

Furthermore, the QPM predicts the longitudinal structure function  $F_L$  to vanish, which is a consequence of helicity and momentum conservation for massless spin- $\frac{1}{2}$  partons and known as the *Callan-Gross* relation [7].

### 1.2.3 The Strong Interaction

The QPM fails to explain why quarks are never observed in the final state of any particle reaction, although they appear to be quasi-free in deep-inelastic scattering experiments. The model also fails entirely in describing the mentioned scaling violations observed at lower and higher  $x$  values. These deficiencies were finally overcome by the theory of the strong interaction termed *Quantum Chromodynamics* (QCD).

QCD is a non-Abelian gauge theory obeying SU(3) symmetry, which provides the quarks with an additional quantum number, the *colour charge* red, green or blue. The mediating gauge bosons of QCD are eight massless gluons, which carry themselves a combination of colour and anti-colour allowing for gluon self-interactions as illustrated in figure 1.4.

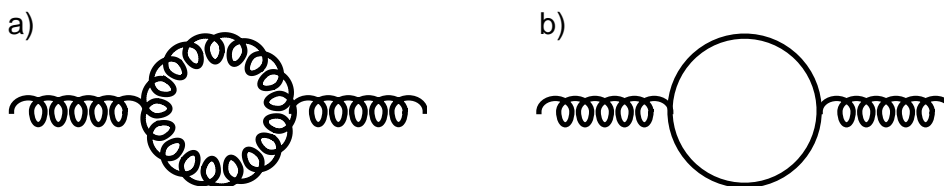


FIGURE 1.4: Higher order corrections in Quantum Chromodynamics: a) gluon loop, b) fermion loop.

The gluon-gluon interaction results in an *anti-screening* effect as opposed to the *screening* effect in the electroweak theory, where vacuum polarisation leads to an increase in the coupling constant  $\alpha$  with decreasing distance and correspondingly higher  $Q^2$ . In QCD the so-called *running coupling constant*  $\alpha_s$  decreases with increasing  $Q^2$  (short distances), which in the limit of  $Q^2 \rightarrow 0 \text{ GeV}^2$  is referred to as *asymptotic freedom*. This is the reason why partons confined in nucleons can be considered as quasi-free as previously hypothesised in the QPM. At the same time the coupling strength becomes very large at low momentum transfers (large distances) explaining why no free quarks have ever been observed. This effect is known as *quark confinement*.

In perturbative QCD (pQCD) cross sections are expressed in power series of  $\alpha_s$ . Beyond leading order (LO) quark and gluon loop diagrams as shown in figure 1.4 start to contribute and the integration over all particle momenta in the loops leads to (ultraviolet) divergencies at high particle energies, which can be absorbed by means of an arbitrary renormalisation scale  $\mu_r$ , above which the virtual loops in the force propagator are absorbed into the coupling. In first order QCD the strong coupling constant  $\alpha_s$  at the scale  $\mu_r > \Lambda_{\text{QCD}}$  can be written as

$$\alpha_s(\mu_r^2) = \frac{12\pi}{(33 - 2N_f) \cdot \ln(\mu_r^2/\Lambda_{\text{QCD}}^2)}, \quad (1.17)$$

where  $N_f$  is the number of quark flavours with  $m_q < \mu_r$ . The parameter  $\Lambda_{\text{QCD}}$  determines the scale at which  $\alpha_s$  becomes large, so that power series in  $\alpha_s$  no longer converge and perturbation theory is not applicable anymore. Since  $\Lambda_{\text{QCD}}$  also separates confined from quasi-free quarks, it is not surprising that its value of roughly 200 MeV resembles the inverse of the radius of a nucleon<sup>4</sup>. Equation (1.17) describes the evolution of  $\alpha_s$ . If  $\alpha_s$  is known at some value  $\mu_r$ , the effective coupling can be extracted at any scale.

## 1.2.4 Factorisation and Parton Evolution

At lowest order, QCD reproduces the same results for the  $ep$  cross sections as are obtained under the assumptions of the naïve QPM. However, at higher orders of the  $\alpha_s$  expansion, infinities arise from collinear or soft gluon radiation, which cannot be treated perturbatively. These infrared (low energy) divergencies need to be renormalised in a similar way as the ultraviolet divergencies mentioned above. According to the *factorisation theorem* a factorisation scale  $\mu_f$

<sup>4</sup>Units:  $197.33 \text{ MeV fm} = \hbar c = 1$ .

is introduced, separating the interaction into two independent contributions, a *short distance* part for which perturbation theory is applicable and a *long distance* part to be determined from experiment.

Processes in the *soft* region ( $Q^2 < \mu_f^2$ ) are absorbed in the renormalised parton density functions (pdfs)  $f(x, \mu_f^2)$ , which now also depend on the factorisation scale. Under these assumptions the proton structure function  $F_2$  can be expressed as a convolution of perturbatively calculable coefficient functions  $C^i$  and parton density functions  $f_{i/p}$  summed over all contributing partons  $i$  (quarks  $q$ , gluons  $g$ ):

$$F_2(x, Q^2) = \sum_{i=q,g} \int_x^1 dz C^i \left( \frac{x}{z}, \frac{Q^2}{\mu_r^2}, \frac{\mu_f^2}{\mu_r^2}, \alpha_s(\mu_r^2) \right) f_{i/p}(z, \mu_r^2, \mu_f^2). \quad (1.18)$$

If  $\mu_f \gg \Lambda_{\text{QCD}}$ , reliable perturbative calculations can be done. The separation between the coefficient functions and the parton density functions is arbitrary. In order to avoid this ambivalence a certain *factorisation scheme* needs to be applied. The most important schemes are the DIS scheme and the modified minimal subtraction scheme  $\overline{\text{MS}}$ . In case of the DIS scheme,  $F_2$  follows the QPM prediction, except that the parton densities now introduce a scale dependence. If the factorisation and renormalisation scale are chosen to equal  $Q^2$ , the proton structure function  $F_2$  in the DIS scheme is given by

$$F_2(x, Q^2) = \sum_{i=q} e_i^2 x f_{i/p}(x, Q^2). \quad (1.19)$$

The parton distribution  $f_{i/p}(x, Q^2)$  in equation (1.19) cannot be predicted, but the requirement that the cross sections should not depend on the factorisation or renormalisation scale leads to a prediction of the parton density *evolution*. If the parton density is measured at a certain scale, it can be predicted for any other scale provided that both scales are significantly greater than  $\Lambda_{\text{QCD}}$ . The evolution is reflected in the DGLAP equations [8, 9, 10] named after Dokshitzer, Gribov, Lipatov, Altarelli and Parisi:

$$\frac{dq_i(x, Q^2)}{d \ln Q^2} = \frac{\alpha_s(Q^2)}{2\pi} \int_x^1 \frac{dz}{z} \left[ \sum_j q_j(z, Q^2) P_{ij} \left( \frac{x}{z} \right) + g(z, Q^2) P_{ig} \left( \frac{x}{z} \right) \right] \quad (1.20)$$

$$\frac{dg(x, Q^2)}{d \ln Q^2} = \frac{\alpha_s(Q^2)}{2\pi} \int_x^1 \frac{dz}{z} \left[ \sum_j q_j(z, Q^2) P_{gj} \left( \frac{x}{z} \right) + g(z, Q^2) P_{gg} \left( \frac{x}{z} \right) \right], \quad (1.21)$$

where  $q_i(x, Q^2)$  and  $g(x, Q^2)$  denote the quark and gluon density functions, respectively. The functions  $P_{ij}$  and  $P_{gj}$ , known as *splitting functions*, are calculable within pQCD and illustrated in figure 1.5. When expanding the splitting functions into a power series in  $\alpha_s$ , the leading order splitting function  $P_{\alpha\beta}^{(0)}(x/z)$  can be interpreted as the probability that a parton  $\alpha$  carrying a fraction  $x$  of the proton's momentum originates from a parton  $\beta$  with a momentum fraction  $z$ .

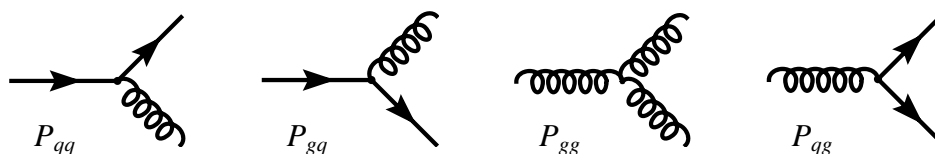


FIGURE 1.5: Feynman diagrams for the four splitting functions in the DGLAP evolution equations.

In order to determine parton density functions from experimental data, the functions are usually parametrised by smooth analytical functions at a low scale  $\mu_0^2$  with a given number of free parameters. After evolving the pdfs to the  $Q^2$  range of the measurement, the structure functions and cross sections are evaluated, still depending on the chosen parameter set, and the free parameters are constrained by a fit to the data.

Several pdf sets from different groups exist, which are based on global fits to the data of various experiments. Most relevant to the present analysis are the CTEQ [11] parton distribution functions. Further parametrisations are available from Glück, Reya and Vogt (GRV) [12] and from Martin, Roberts, Stirling and Thorne (MRST) [13, 14]. As shown in figure 1.6, also the H1 collaboration has performed a QCD fit based on  $ep$  collision data measured with the H1 detector in the years 1994 to 2000 [4]. In the figure the proton structure function  $F_2$  is shown as a function of  $Q^2$  for various values of  $x$ . At comparatively high or low  $x$  values, clear scaling violations can be observed, which can readily be explained within the framework of QCD. The radiation of a gluon reduces the original momentum fraction of the scattering quark and in addition gluons can split into quark-antiquark pairs with relatively small momentum fractions of the proton. At higher momentum transfers more such processes can be resolved and hence the quark densities are expected to rise with  $Q^2$  at low  $x$  and to decrease with  $Q^2$  at high  $x$ .

### 1.3 Isolated Photon Production in DIS

As discussed in section 1.2, the DIS cross section can in first order be described by an incoherent sum of elastic electron-quark scattering processes. Correspondingly, the production of final state photons is described in leading order,  $\mathcal{O}(\alpha^3)$ , by the  $2 \rightarrow 3$  parton level process

$$q(p_q) + e(k) \rightarrow \gamma(p_\gamma) + q(p'_q) + e(k'), \quad (1.22)$$

where the photon  $\gamma$  is either emitted by the electron  $e$  ( $LL$  contribution) or the quark or anti-quark  $q$  ( $QQ$  contribution) as illustrated in figure 1.7. In order to obtain the deep-inelastic scattering cross section for the production of final state photons, analogous to equation (1.14), the parton level cross section convoluted with the corresponding parton distribution function is summed over all contributing quark and anti-quark flavours.

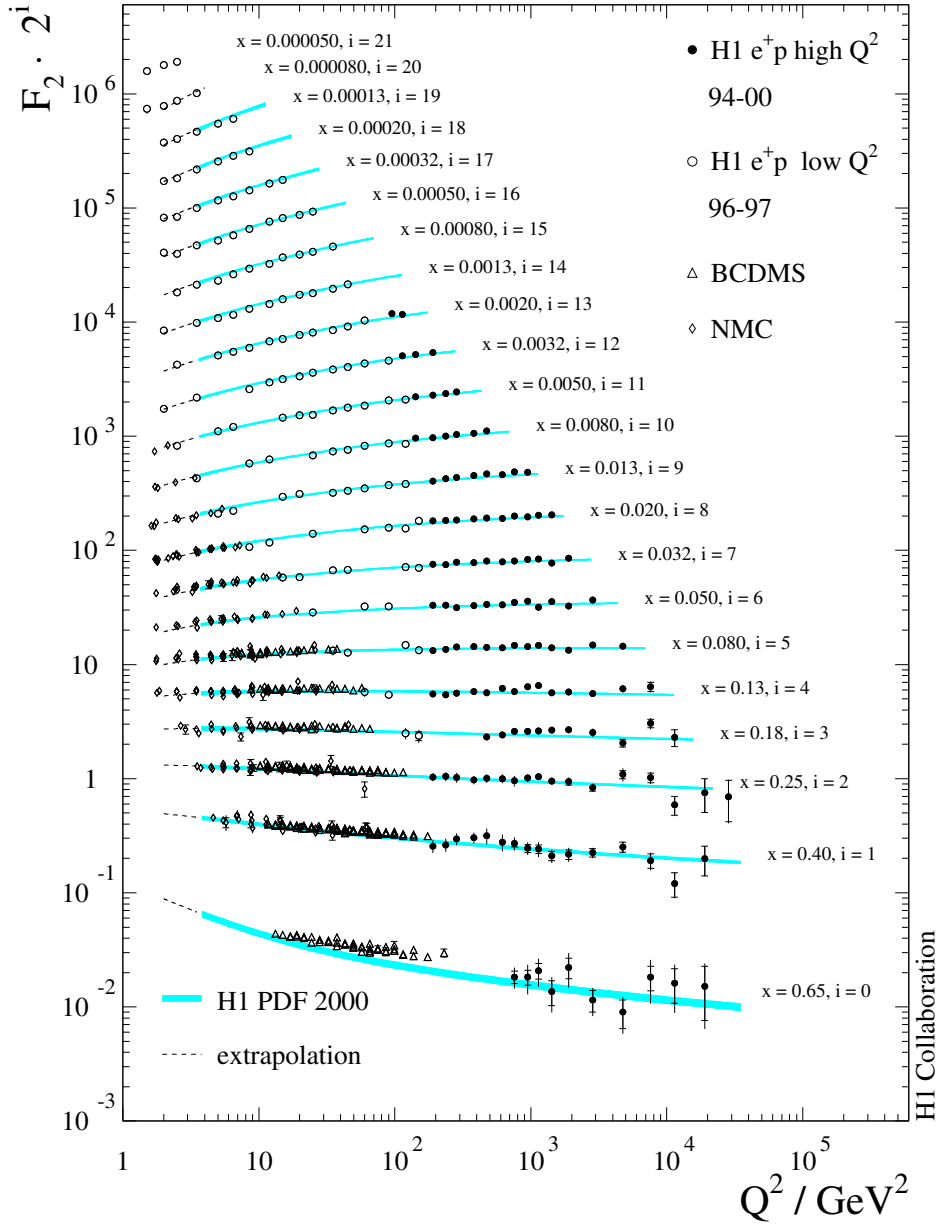


FIGURE 1.6: The proton structure function  $F_2$  as a function of  $Q^2$  for different values of  $x$  measured by the H1 collaboration and the fixed target experiments BCDMS and NMC. The results are compared with the corresponding Standard Model expectation determined from the H1 PDF 2000 fit indicated by the error bands. The figure is taken from [4].

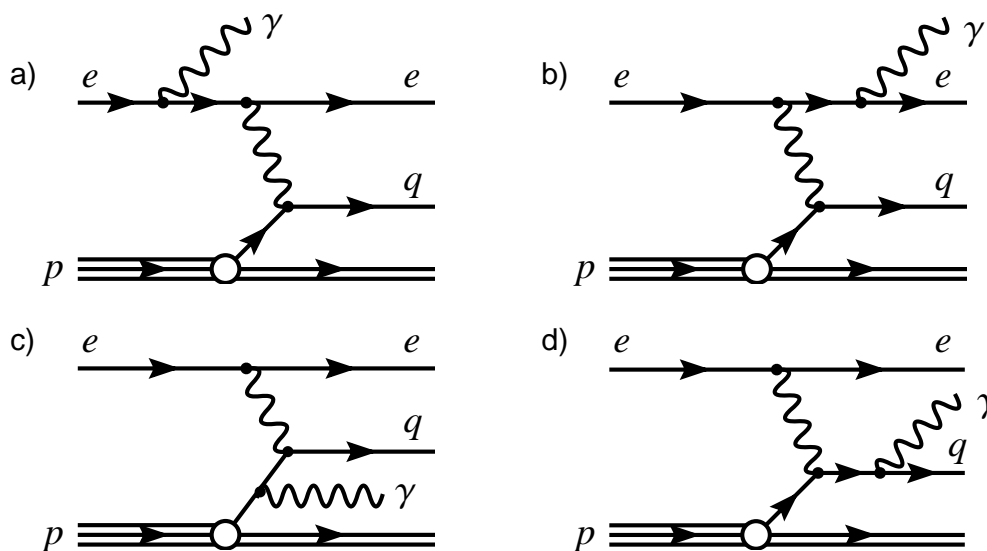


FIGURE 1.7: Leading order Feynman graphs for isolated photon production in DIS. The upper diagrams (a, b) illustrate the isolated photon production by radiation from the electron line ( $LL$ ), while the lower diagrams (c, d) correspond to the production via radiation from the quark (contribution from fragmentation is not shown).

The  $QQ$  contribution to the cross section is obtained by squaring the sum of the amplitudes for radiation off the incoming and outgoing quark, figure 1.7 a) and b), and the  $LL$  contribution accordingly corresponds to the squared sum of the amplitudes for radiation from the initial or final state electron, figure 1.7 c) and d). The  $QL$  contribution represents their interference which is odd under lepton charge exchange.

Besides the direct radiation of a photon from the quark, the  $QQ$  process also includes contributions from the quark-to-photon fragmentation function, corresponding to the transition of a hadronic jet (cf. section 4.5) into a highly energetic photon carrying a large fraction of the jet energy, as shown in figure 1.8. Whereas the direct radiation of a photon can be perturbatively calculated, the fragmentation contribution is based on a long distance process, which is not accessible within perturbation theory and needs to be determined from data.

Apart from the fragmentation contribution the cross section contains already at leading order a divergence caused by the emission of photons collinear to the primary quarks. Similar to the absorption of soft gluon radiation into the parton distribution functions as described in section 1.2.4, these collinear divergences can be factorised into the process independent fragmentation function defined at some factorisation scale  $\mu_{F,\gamma}$  (cf. section 1.3.1).

Although the measurement of photons in the final state has the advantage of small hadronisation uncertainties, the separation of the described hard photons in the final state from comoving multiple photons, emerging from the decay of neutral hadrons, is experimentally challenging. Such neutral hadrons are produced numerously within the hadronisation of jets. It is therefore convenient to apply an isolation requirement to the definition of a photon.

In the present work an infrared-safe isolation requirement within the so-called *democratic procedure* [15, 16] is defined, in contrast to the cone-based isolation criterion used in previous analyses [17, 1, 18]. The photon is clustered simultaneously with the other final state particles into jets by the jet algorithm (cf. section 4.5). The jet that contains the photon constitutes the so-called *photon-jet*. The isolation of the photon can be assured by requiring the fraction  $z$  of the transverse energy of the photon-jet  $E_T^{\text{photon-jet}}$  carried by the photon  $E_T^\gamma$  be greater than some cut-value  $z_{\min}$

$$z = \frac{E_T^\gamma}{E_T^{\text{photon-jet}}} > z_{\min}. \quad (1.23)$$

In order to guarantee the infrared finiteness of the observables a minimal amount of hadronic activity should be allowed close to the photon. In the present analysis the minimum fraction is chosen to be  $z_{\min} = 0.9$ . For stronger isolation constraints like  $z_{\min} = 0.95$ , it is unclear whether the resummed fragmentation functions allow reliable predictions [19]. It was thought that by imposing an isolation criterion the fragmentation contribution could be eliminated. However, the fragmentation and collinear contributions can at most be suppressed [2].

The definition of the virtuality as introduced in equation (1.2) is calculated by means of the initial and final state electron  $Q^2 = Q_{QQ}^2 = -(k - k')^2$ , which only holds for the  $QQ$  process. If a photon is radiated from the electron, the virtuality could correctly be defined by the incoming and outgoing quark  $Q_{LL}^2 = -(p_q - p'_q)^2$ . As the experimental measurement of  $Q^2$  in the present analysis (cf. section 4.3.2) is, however, based on the kinematics of the scattered electron, the experimental constraint of a minimum  $Q^2$  is equivalent to a cut only on  $Q_{QQ}^2$ . Therefore the true virtuality  $Q_{LL}^2$  of the exchanged photon in the  $LL$  process can become markedly small. Thus some care has to be taken in the choice of the factorisation scale for the pdf's inside the proton, where usually the four-momentum transfer squared  $Q^2$  is used.

In the present measurement of isolated photons in DIS, elastically produced photons from elastic QED Compton scattering or deeply virtual Compton scattering (DVCS) (cf. appendix C) are widely excluded from the analysis by imposing a cut on the minimum mass of the hadronic system  $W_X$ . In presence of final state photons, the definition of the hadronic final state  $X$  (cf. equation 1.6) needs to be carefully adjusted, not to include the four-momentum of the photon  $p_\gamma$ :

$$W_X^2 = (q + P - p_\gamma)^2 = (k + P - k' - p_\gamma)^2. \quad (1.24)$$

The invariant mass  $W_X$  can be fully determined from the incoming electron and proton and the outgoing electron and photon.

### 1.3.1 Fragmentation and Collinear Contribution

The radiation of a photon from a quark ( $QQ$  process) involves a non-perturbative long distance process in which the photon is produced through the fragmentation of a hadronic quark jet into a single photon carrying a large fraction  $z$  of the transverse jet energy. The probability of this transition is given by the process independent quark-to-photon fragmentation function



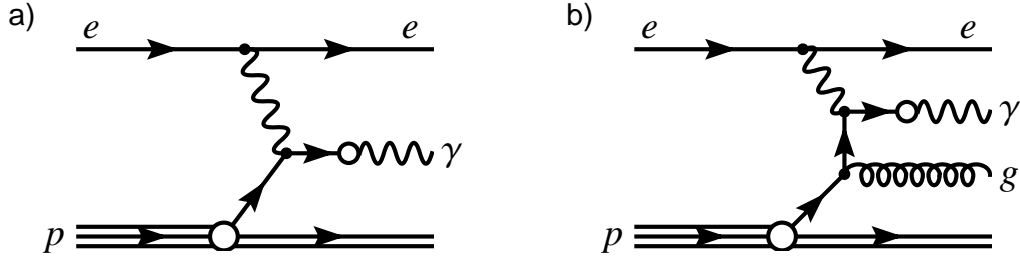


FIGURE 1.8: Feynman graphs for the quark fragmentation into a highly energetic photon in DIS. a) Fragmentation contribution at order  $O(\alpha^3)$ , exclusively contributing to the photon plus no jet sample (see text). b) Example for quark-fragmentation at order  $O(\alpha^3\alpha_s)$ .

$D_{q \rightarrow \gamma}(z)$ , which cannot be calculated perturbatively and must be derived from experimental data.

The cross section for the fragmentation contribution is obtained by convolution of the fragmentation function with the partonic cross section<sup>5</sup> for the  $2 \rightarrow 2$  electron-quark scattering process

$$q(p_q) + e(k) \rightarrow q(p_{q\gamma}) + e(k'), \quad (1.25)$$

such that the two outgoing quark and photon four-momenta are related by  $p'_\gamma = zp_{q\gamma}$  and  $p'_q = (1-z)p_{q\gamma}$ . The leading order contribution from fragmentation is visualised in figure 1.8 a).

It was mentioned in section 1.3 that already at leading order a collinear singularity appears in the photon emission by the quark. As physical cross sections are necessarily finite, the singularity may be factorised into the fragmentation function defined at the factorisation scale  $\mu_{F,\gamma}$ . Within the so-called *phase space slicing method* [20] a parameter  $y_{min}$  can be introduced, which separates the divergent collinear contribution ( $y_{q\gamma} < y_{min}$ ) from the finite contribution, where the outgoing quark and photon are still theoretically resolved ( $y_{q\gamma} > y_{min}$ ). In this context the variable  $y_{q\gamma} = p_{q\gamma}^2 / (p_q + k)^2$  is the dimensionless invariant mass of the quark-photon system. The final cross sections should be independent of  $y_{min}$ , which is an important cross check for QCD calculations.

The quark-to-photon fragmentation function at order  $\alpha$  is given by [2]

$$D_{q \rightarrow \gamma}(z) = D_{q \rightarrow \gamma}(z, \mu_{F,\gamma}) + \frac{\alpha e_q^2}{2\pi} \left( P_{q\gamma}^{(0)}(z) \ln \frac{z(1-z)y_{min}s_{eq}}{\mu_{F,\gamma}^2} + z \right), \quad (1.26)$$

where  $D_{q \rightarrow \gamma}(z, \mu_{F,\gamma})$  describes the non-perturbative transition  $q \rightarrow \gamma$  at the factorisation scale  $\mu_{F,\gamma}$ . The second term represents the finite part after absorption of the collinear quark-photon contribution into the bare fragmentation function separated by the parameter  $y_{min}$ . The variable  $e_q$  denotes the charge of quark  $q$  and  $s_{eq}$  the electron-quark centre-of-mass energy squared.

<sup>5</sup>The DIS cross section can be calculated from the partonic cross section by convolution with the proton quark density functions at an appropriate scale (e.g.  $Q^2$ ) summed over all contributing quark flavours.

In the second term also the LO quark-to-photon splitting function  $P_{q\gamma}^{(0)} = (1 + (1 - z)^2)/z$  contributes.

The variation of the fragmentation function  $D_{q\rightarrow\gamma}(z, \mu_{F,\gamma})$  with the scale  $\mu_{F,\gamma}$  can be predicted by an evolution equation analogue to the DGLAP evolution equations (1.20 and 1.21). The fragmentation function  $D_{q\rightarrow\gamma}(z, \mu_{F,\gamma})$  at the factorisation scale is related with the fragmentation function  $D_{q\rightarrow\gamma}(z, \mu_0)$  at the initial scale  $\mu_0$  by

$$D_{q\rightarrow\gamma}(z, \mu_{F,\gamma}) = \frac{\alpha e_q^2}{2\pi} P_{q\gamma}^{(0)}(z) \ln\left(\frac{\mu_{F,\gamma}^2}{\mu_0^2}\right) + D_{q\rightarrow\gamma}(z, \mu_0). \quad (1.27)$$

The fragmentation function  $D_{q\rightarrow\gamma}(z, \mu_0)$  and the corresponding initial scale  $\mu_0$  cannot be calculated and must consequently be determined from experiment. The first measurement was performed by the ALEPH collaboration [16], stated as

$$D_{q\rightarrow\gamma}(z, \mu_0) = \frac{\alpha e_q^2}{2\pi} \left( -P_{q\gamma}^{(0)}(z) \ln(1 - z)^2 - 13.26 \right) \quad (1.28)$$

at the scale  $\mu_0 = 0.14$  GeV.

It should be noted that the fragmentation contribution to the cross section is also of order  $\mathcal{O}(\alpha^3)$  if the above LO parametrisation of the fragmentation function is used. The partonic  $2 \rightarrow 2$  cross section enters here with  $\mathcal{O}(\alpha^2)$ . Besides the above LO parametrisation, further parametrisations exist, such as the next-to-leading order (NLO) fragmentation function derived from the ALEPH measurement [21] and the BFG fragmentation functions [22].

In the measurement of isolated photons in DIS, the fragmentation contribution enters in the exclusive observation of a photon jet in DIS (photon plus no-jet sample, cf. section 4.5) already at leading order. In this selection no other jet apart from the photon-jet is observed within the detector acceptance. If additional jets are observed, the fragmentation contribution is at least of order  $\mathcal{O}(\alpha^3 \alpha_s)$ . An example for such higher order fragmentation contributions is given in figure 1.8 b).

Because of the contribution at leading order, a measurement of the quark-to-photon fragmentation function in the exclusive photon-jet measurement in DIS at HERA is suggested by Gehrmann-De Ridder, Gehrmann and Poulsen [2].

## 1.4 Neutral Hadron Background

Various neutral hadrons like  $\pi^0$ ,  $\eta$ ,  $\eta'$  and others have photonic decay modes. At high transverse energies the decay photons are usually not resolved in the detector, but measured in a common electromagnetic cluster within the main calorimeter (cf. section 3.2.1), thus providing a very similar detector signature compared with photons from the hard interaction.

Since neutral hadrons are produced in great numbers during the fragmentation of coloured partons, they are typically found close to jets. An isolation requirement can therefore significantly reduce the background from neutral hadrons. However, a residual contribution of

roughly double the magnitude of the isolated photon signal remains in the present analysis. This remaining background is statistically subtracted by means of a dedicated shower shape analysis (see chapter 5).

Due to their light mass mostly pions are produced in the fragmentation of jets and the neutral hadron background consists after all selection steps to approximately 85 % of clusters induced by the light  $\pi^0$  meson. As an example, the kinematics of the neutral pion decay  $\pi^0 \rightarrow \gamma\gamma$  is discussed in further detail in appendix A. In this section also the non-separable background in asymmetric pion decays is discussed.

## 1.5 Recent Isolated Photon Research

Recent results on the production of isolated photons are presented. At first, former results in electron-proton scattering at HERA in both photoproduction and deep-inelastic scattering are reviewed, followed by results on the production of photons in hadronic collisions. Results on the production of isolated photons in  $e^+e^-$  collisions, which was studied by all four LEP experiments at CERN, are not included in this review. A measurement of the photon fragmentation function by the ALEPH collaboration is shortly discussed in section 1.5.3.

### 1.5.1 Results at HERA

At HERA inclusive isolated photon cross sections  $ep \rightarrow \gamma X$  have been measured in photoproduction by the ZEUS [23] and H1 [18] collaboration and compared to PYTHIA and HERWIG Monte Carlo predictions as well as to NLO calculations.

In figure 1.9 H1 and ZEUS cross sections<sup>6</sup> are shown as a function of the transverse energy  $E_T^\gamma$  and the pseudorapidity  $\eta^\gamma$  (see section 3.2) of the photon and compared to Monte Carlo predictions. The two measurements are consistent and reasonably described in shape, but the predictions by PYTHIA (HERWIG) are low by about 40 % (50 %) in normalisation. The cross sections are reasonably well described in shape by pQCD NLO calculations (not shown), but after corrections for multiple interactions and hadronisation the predictions are 30–40 % below the data.

The H1 measurement also presents isolated photon cross sections in association with jets<sup>7</sup> in photoproduction. The prompt photon cross sections with associated jet are somewhat better described by the NLO calculations. The better description together with the fact that NLO corrections are in average smaller than in the inclusive case, suggests that higher order corrections are of less importance if the prompt photon is accompanied by an energetic jet.

The production of prompt photons with associated jets in photoproduction is also studied by the ZEUS collaboration [24]. Differential cross sections  $d\sigma/dE_T^\gamma$  and  $d\sigma/d\eta^\gamma$  are shown in

<sup>6</sup>The ZEUS cross sections were corrected to the kinematic range used in the H1 analysis.

<sup>7</sup>A jet is required with  $E_T^{jet} > 4.5$  GeV.

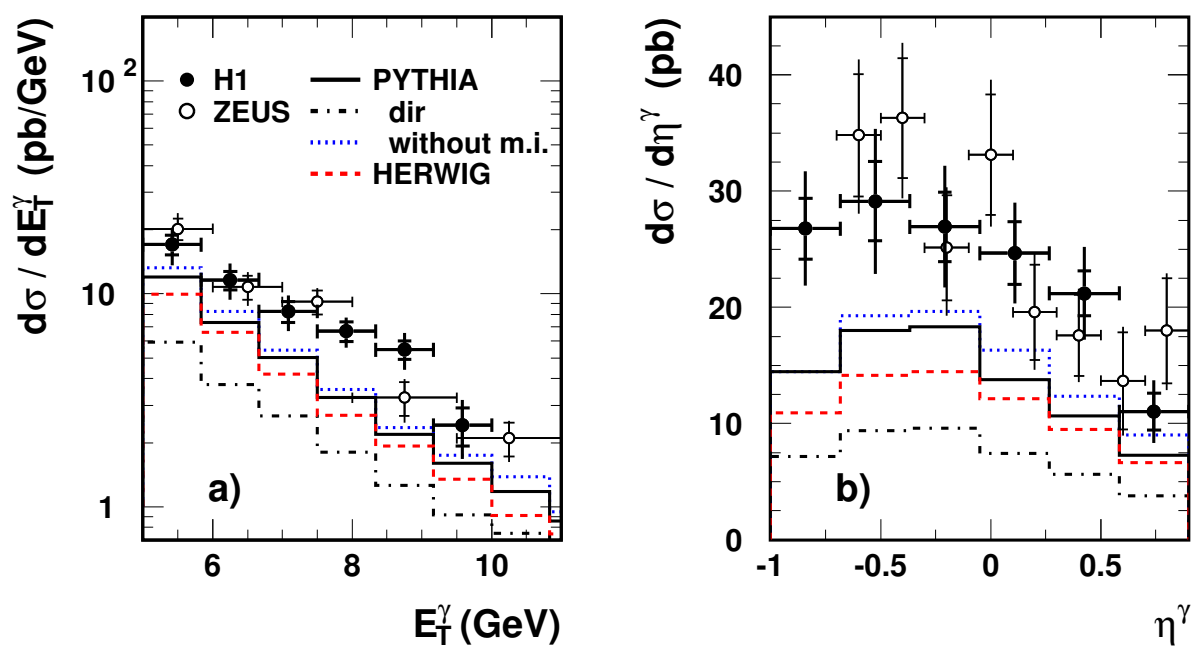


FIGURE 1.9: Inclusive prompt photon differential cross sections  $d\sigma/dE_T^\gamma$  (a) and  $d\sigma/d\eta^\gamma$  (b) in photo-production of the H1 [18] and ZEUS [23] measurement compared with predictions of PYTHIA and HERWIG. The cross sections of the ZEUS measurement were corrected to the kinematic range used in the H1 analysis, which is given by  $\sqrt{s} = 319$  GeV,  $0.2 < y < 0.7$ ,  $5 < E_T^\gamma < 10$  GeV and  $-1 < \eta^\gamma < 0.9$ .

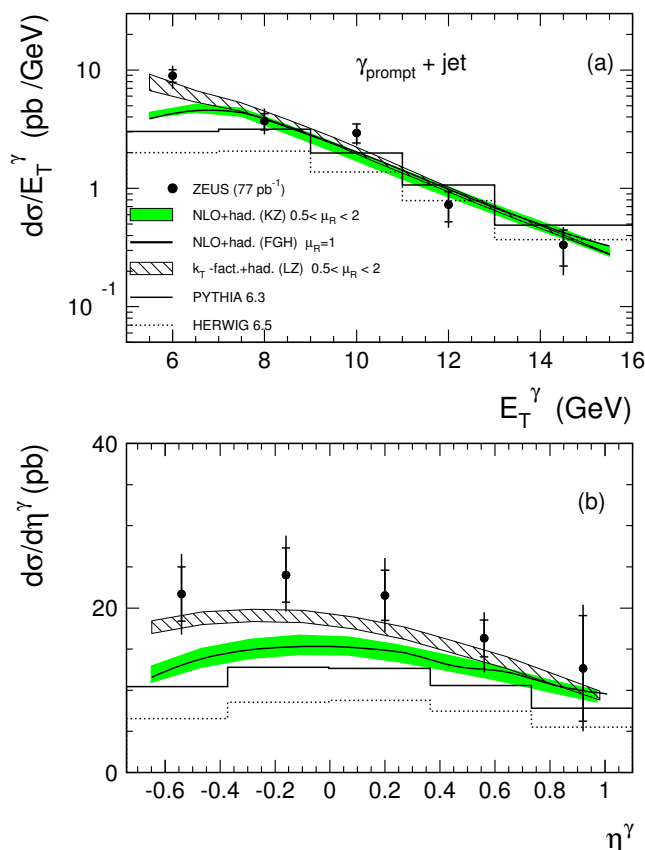


FIGURE 1.10: Isolated photon plus jet differential cross sections  $d\sigma/dE_T^\gamma$  (a) and  $d\sigma/d\eta^\gamma$  (b) measured by the ZEUS collaboration [24] for the kinematic range  $\sqrt{s} = 318$  GeV,  $0.2 < y < 0.8$ ,  $5 < E_T^\gamma < 16$  GeV,  $6 < E_T^{\text{jet}} < 17$  GeV,  $-0.74 < \eta^\gamma < 1.1$  and  $-1.6 < \eta^{\text{jet}} < 2.4$ . The cross sections are compared to the Monte Carlo predictions of PYTHIA and HERWIG and two NLO calculations as well as to one calculation based on a  $k_T$ -factorisation approach.

figure 1.10 and compared with the PYTHIA and HERWIG Monte Carlo predictions as well as with two NLO calculations and a calculation based on a  $k_T$ -factorisation approach. The data shows a steeper rise towards low  $E_T^\gamma$  than the Monte Carlo predictions. The shape is better described by the NLO calculations and the best description is obtained from the calculation based on the  $k_T$ -factorisation approach. For an increased minimum transverse energy of the photons to 7 GeV, the differential cross sections are well described by the NLO calculations and the  $k_T$  factorisation calculation.

In deep-inelastic scattering isolated photons have been measured by the ZEUS collaboration [1] in the kinematic range  $5 < E_T^\gamma < 10$  GeV,  $-0.7 < \eta^\gamma < 0.9$  and  $Q^2 > 35$  GeV<sup>2</sup> using an integrated luminosity of 121 pb<sup>-1</sup>. Inclusive differential isolated photon cross sections are shown in figure 1.11 and compared to the prediction of the PYTHIA and HERWIG Monte Carlo simulations. In this measurement contributions of photon radiation from the electron are neglected in the acceptance corrections as well as in the comparison to the Monte Carlo models. The differential cross sections  $d\sigma/dE_T^\gamma$  are reasonably described by the PYTHIA Monte Carlo when scaled by a factor 2.3 and HERWIG scaled by a factor 7.9. Cross sections have also been measured for photons accompanied by an additional jet and compared to a NLO calculation, where a fair level of agreement was found for the  $\eta^\gamma$  distribution. However, no

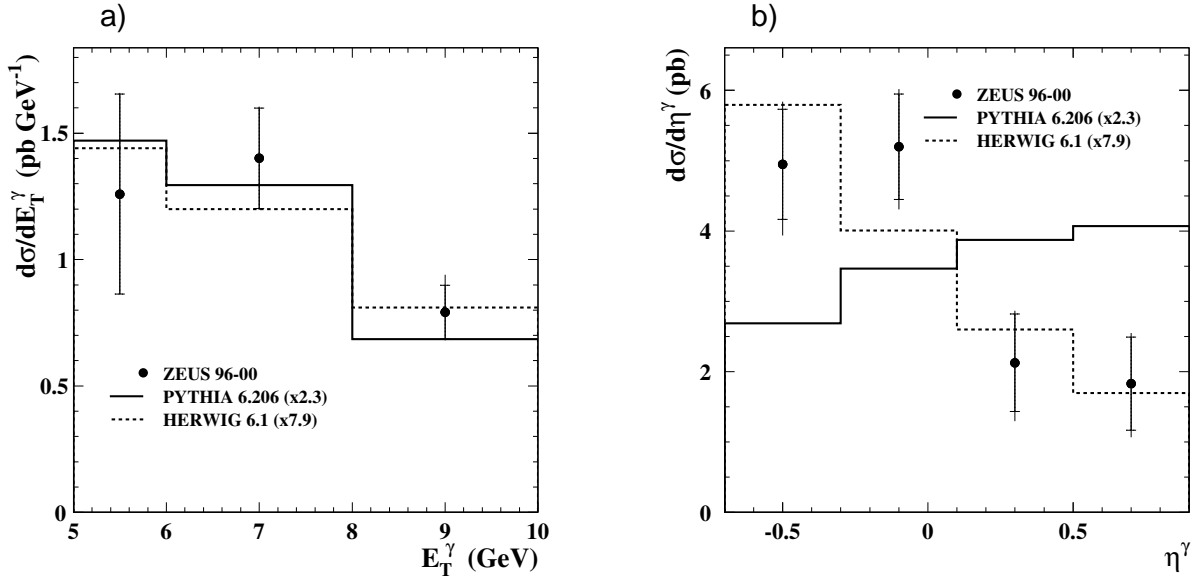


FIGURE 1.11: Inclusive differential isolated photon cross sections  $d\sigma/dE_T^\gamma$  (a) and  $d\sigma/d\eta^\gamma$  (b) measured by the ZEUS collaboration [1] in the kinematic range  $5 < E_T^\gamma < 10$  GeV,  $-0.7 < \eta^\gamma < 0.9$  and  $Q^2 > 35$  GeV<sup>2</sup>. The cross sections are compared with the PYTHIA and HERWIG Monte Carlo simulations scaled by a factor 2.3 and 7.9, respectively.

corrections for hadronisation were applied on the parton level calculation (see section 6.1.2).

A comparison of the measurement presented in this analysis to the ZEUS results is shown in section 7.2. The present analysis extends the kinematic range covered by the ZEUS measurement of isolated photons in DIS with respect to  $E_T^\gamma$ ,  $\eta^\gamma$  and  $Q^2$ , which leads to an increased total cross section expectation by approximately a factor 10.

## 1.5.2 Results in Hadronic Collisions

The production of isolated photons has as well been studied at various hadron colliders and fixed target experiments. Figure 1.12 shows a summary of results from photon production in  $pp$  and  $p\bar{p}$  collisions [25]. The results are given as a ratio of data to NLO calculation in dependence of the reduced variable  $x_T = 2E_T^\gamma/\sqrt{s}$ . The data are shown for a variety of experiments covering a large range of the centre-of-mass energy. These are the fixed target experiments WA70 ( $\sqrt{s} = 23$  GeV), UA6 ( $\sqrt{s} = 24.3$  GeV), E706 ( $\sqrt{s} = 31.6$  GeV and 38.8 GeV), the ISR<sup>8</sup> experiments ( $\sqrt{s} = 63$  GeV) at CERN<sup>9</sup> R110, R806, AFS, the CDF ( $\sqrt{s} = 1.8$  TeV) and D0 ( $\sqrt{s} = 1.96$  TeV) experiments at TEVATRON together with preliminary data from the PHENIX experiment ( $\sqrt{s} = 200$  GeV) at RHIC<sup>10</sup> (see [25] for references).

<sup>8</sup>Intersecting Storage Ring.

<sup>9</sup>The name CERN is derived from **C**onseil **E**uropéen pour la **R**echerche **N**ucléaire (European Council for Nuclear Research).

<sup>10</sup>Relativistic Heavy Ion Collider.

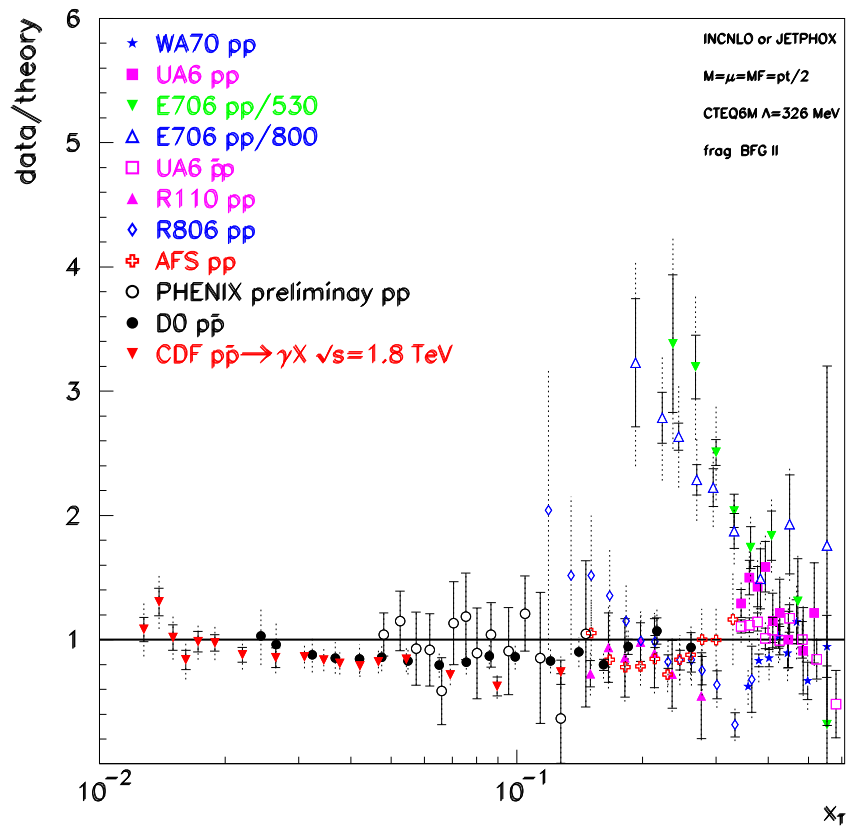


FIGURE 1.12: Ratios data/theory for collider and fixed target  $pp$  and  $p\bar{p}$  data with the scale  $\mu = E_T^\gamma/2$  (see [25] for details).

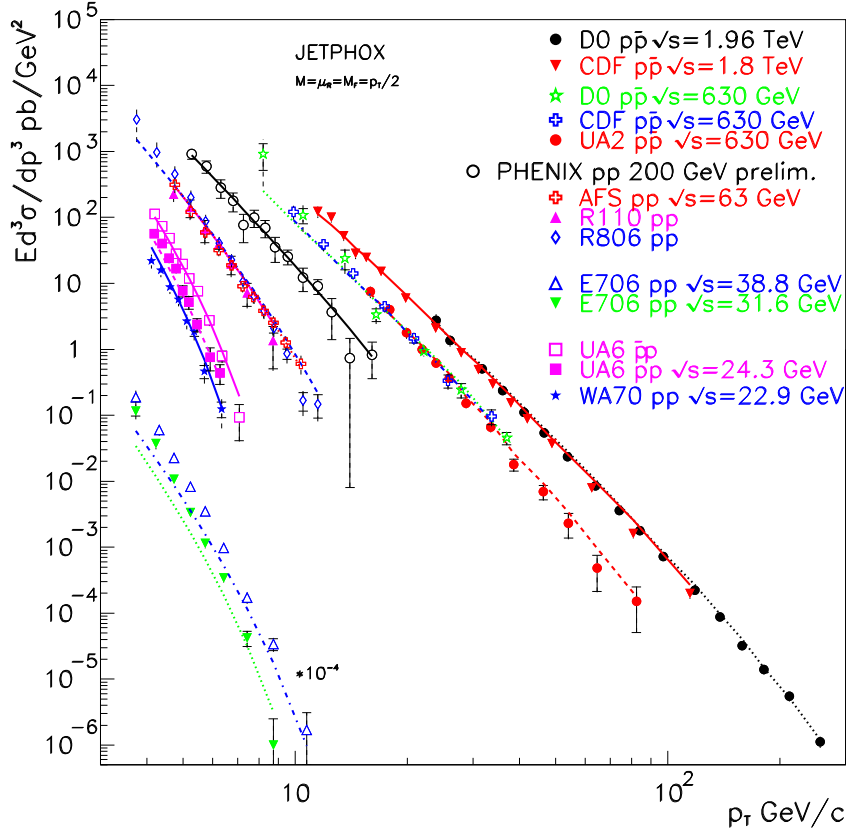


FIGURE 1.13: Photon production cross sections measured in  $pp$  and  $p\bar{p}$  collisions compared to NLO calculations (taken from [25]). The E706 data are scaled by a factor  $10^{-4}$ . For details refer to the reference.

Apart from the data measured by the E706 experiment, the data agree well with the NLO calculation in the entire range  $\sqrt{s} = 23$  GeV to 1.96 TeV with a weak indication of the  $x_T$  distribution predicted by the NLO calculation to be slightly less steep than the measurements (eg. CDF, R806). The E706 data decreases much stronger with  $x_T$  than the theory. Agreement could be achieved under the assumption of soft gluon radiation parametrised in terms of an effective  $\langle k_T \rangle$  that provides an additional transverse momentum to the incoming partons of the proton [26]. It should be noted that the smallest  $x_T$  values for the E706 data correspond to values of  $E_T^\gamma$  down to 3.5 GeV, similar to the lowest energies considered in the present analysis.

Figure 1.13 shows the  $E_T^\gamma$  distribution for the  $pp$  and  $p\bar{p}$  collision data together with the NLO calculations. The different slope of data and theory for the E706 experiment is clearly visible. A slight difference in slope can also be seen for the CDF data [27, 28], which extends to far lower  $E_T^\gamma$  than the D0 measurement [29]. The other measurements agree well with the calculations.



### 1.5.3 Measurement of the Photon Fragmentation Function at LEP

The ALEPH collaboration made a first measurement [16] of the quark-to-photon fragmentation function in hadronic  $Z^0$  decays, which was followed by a further measurement of the fragmentation function of the OPAL collaboration [30].

In the ALEPH measurement photons with transverse energies greater than 5 GeV are selected when carrying more than 70 % of the photon-jet energy and background from the decay of neutral hadrons is eliminated by a Monte Carlo subtraction method. The Monte Carlo prediction of the neutral pion production is cross-checked under the assumption of isospin symmetry in the production of charged pions. The ratio of observed charged pions to predicted charged pions in the Monte Carlo was found to be compatible with unity. The quark-to-photon fragmentation function is then determined in exclusive 2-jet events, where one of the jets is the photon-jet, by a fit to the differential cross sections as a function of the photon energy fraction carried by the photon-jet.

Results on the measurement of the quark-to-photon fragmentation function by the ALEPH collaboration are discussed and further compared to results of the present analysis in chapter 7.



# CHAPTER 2

## CALCULATIONS

---

The measured isolated photon cross sections will be compared to pQCD calculations as well as to Monte Carlo model predictions. Monte Carlo simulations are also used to correct the data for detector acceptances, inefficiencies and migrations. Moreover, the Monte Carlo simulation is used to correct the parton level QCD calculations for hadronisation effects. This chapter introduces the calculations and Monte Carlo models used in the present analysis.

### 2.1 Fixed Order QCD Calculations

In the following, two QCD calculations are presented: a LO calculation covering the inclusive isolated photon production as well as the exclusive photon plus jet and photon plus no-jets production (cf. section 4.5) and a NLO calculation for the exclusive photon plus jet production. The calculations are adjusted to the kinematic cuts as used in the present analysis and based on the same jet algorithm for the selection of exclusive final states. Furthermore, the same infrared-safe photon isolation definition is used, see equation (1.23), and also the same fraction of  $e^+p$  (52.1 %) and  $e^-p$  (47.9 %) collisions as in the experimental data set was assumed.

The calculations are performed on parton level. In order to obtain the corresponding  $ep$  cross sections, the partonic cross sections are convoluted with the CTEQ6L [11] proton pdf's. A variation of the proton pdf parametrisation is found to change the predictions by 5–10%. Hadronisation effects of the outgoing partons are corrected for by means of the Monte Carlo simulation. The correction factors  $f^{had}$  are defined as the ratio of the cross sections calculated from hadrons to those from partons and are determined from the scaled signal Monte Carlo (see section 2.2.2).

#### 2.1.1 Inclusive LO Calculation

The LO,  $O(\alpha^3)$ , calculation by Gehrmann-De Ridder, Gehrmann and Poulsen [31, 2] is compared to both the inclusive measurement of isolated photons in DIS and jet production in

association with isolated photons in DIS.

Up to leading order the underlying theory of isolated photon production in DIS has already been discussed in section 1.3. In contrast to predictions by Monte Carlo generators, the parton level calculation is based on the full leading order matrix element  $eq \rightarrow eq\gamma$ , which has been discussed along with equation (1.22). The final state photon is either radiated by the quark ( $QQ$  contribution) or the electron ( $LL$  contribution). The interference ( $LQ$ ) contributes only at a small fraction of roughly 3% and is included in the sum of the predictions but never shown separately. The fragmentation contribution in the  $QQ$  process is expressed by the ALEPH LO parametrisation [16] of the fragmentation function  $D_{q \rightarrow \gamma}(z)$ , which has been stated in equation (1.28).

In the photon plus no-jets production and also in the inclusive isolated photon production, both the fragmentation contribution and the collinear quark-photon divergence appear already at leading order. A NLO calculation will therefore encounter double unresolved partonic configurations, which are only expected at next-to-next-to-leading order (NNLO) in other DIS processes such as  $eq \rightarrow eq$  [2]. A NLO calculation for the inclusive isolated photon production is thus not available at present. In the production of isolated photons in association with hadronic jets, however, the divergence and fragmentation contribution enters only at NLO.

### 2.1.2 Exclusive Photon plus Jet NLO Calculation

In addition to the LO calculation, also the NLO,  $\mathcal{O}(\alpha^3\alpha_s)$ , QCD calculation for the exclusive production of isolated photons plus jet in DIS by Gehrmann-De Ridder, Kramer and Spiesberger [32] is compared to the present measurement.

The diagrams with the photon emitted from the initial or final state lepton are considered separately in this calculation, as they are explicitly gauge invariant. Therefore, the matrix element of the  $QQ$  contribution explicitly describes the interaction of the virtual photon  $\gamma^*$  with a quark  $q$  or gluon  $g$  of the proton. The contributing LO subprocess is consequently given by  $\gamma^*q \rightarrow \gamma q$ . By requiring a non-zero transverse momentum of the photon in the  $\gamma^*p$  centre-of-mass frame, the photon is automatically isolated from the quark-jet and hence the photon fragmentation does not contribute to this order.

At NLO, processes with an additional gluon have to be taken into account. The gluon can either be emitted into the final state or it can interact as incoming parton. The Feynman graphs of the corresponding two NLO sub-processes  $\gamma^*q \rightarrow q\gamma g$  and  $\gamma^*g \rightarrow q\gamma\bar{q}$  are displayed in figure 2.1. In addition, also virtual corrections to the LO process  $\gamma^*q \rightarrow \gamma q$  have to be considered. When the  $ee\gamma^*$  vertex is taken into account, all these processes are of order  $\mathcal{O}(\alpha^3\alpha_s)$  and can contribute to final states with either one or two hadronic jets in addition to the photon-jet, depending strongly on the jet algorithm.

In the production of photons with additional hadronic jets the fragmentation contribution enters in the sub-processes  $\gamma^*q \rightarrow gq$  and  $\gamma^*g \rightarrow q\bar{q}$ , where one of the final state partons fragments into a high-energetic photon (see figure 1.8 b). The partonic cross section is of order  $\mathcal{O}(\alpha^2\alpha_s)$  (including the  $ee\gamma^*$  vertex), while the non-perturbative fragmentation function

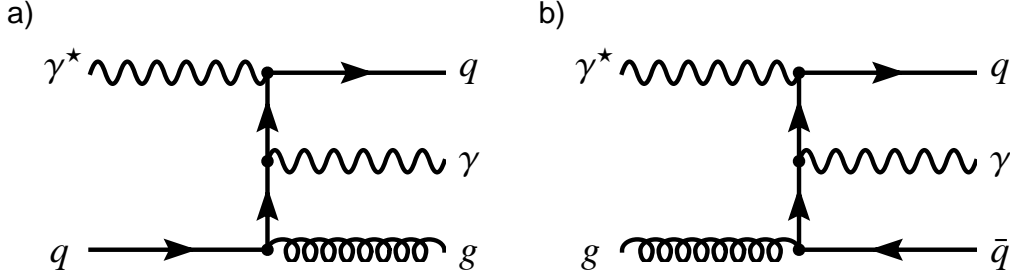


FIGURE 2.1: Feynman graphs for higher order processes in the isolated photon production in DIS. a)  $\gamma^* q \rightarrow g \gamma q$ . b)  $\gamma^* g \rightarrow q \gamma \bar{q}$ .

is formally of order  $\mathcal{O}(\alpha)$ , so that the fragmentation contribution is of the same order,  $\mathcal{O}(\alpha^3 \alpha_s)$ , as the direct NLO contribution. In the NLO calculation the fragmentation function of Bourhis, Fontannaz and Guillet (BFG) is taken [22]. Similar to the LO calculation infrared singularities occur also at NLO, which either cancel with virtual corrections to the LO contribution or have to be factorised into the renormalised proton pdf's or into the photon fragmentation function. Further details on the treatment of the singularities can be found in [32].

The renormalisation and factorisation scales are fixed by  $\mu_R = \mu_F = \sqrt{Q^2 + (P_T^{jet})^2}$ . Theoretical uncertainties are obtained from varying  $\mu_R$  and  $\mu_F$  independently by a factor two up and down. The uncertainties are found to be small and lower than the uncertainties from the choice of the proton pdf parametrisation.

## 2.2 Monte Carlo Simulations

In many fields of science even simple problems may be difficult or even impossible to solve analytically. In order to provide quantitative results the problem can either be approximated or translated to a stochastic description based on first principles. In such cases Monte Carlo (MC) methods<sup>1</sup> provide approximate solutions by performing statistical sampling experiments on a computer mostly based on random numbers<sup>2</sup> and typically a sequence description of the underlying process. MC methods are widely used in various fields, such as the numerical estimation of certain integrals or partial differential equations, the simulation of climate changes and earthquakes or option pricing and risk measurement in quantitative finance.

<sup>1</sup>The Monte Carlo method is named after the city in the Monaco principality, because of its relation to the roulette game, which is a simple generator of random numbers.

<sup>2</sup>Random numbers provided by many software packages are pseudorandom numbers. Pseudorandom numbers usually offer statistical randomness while the process of being generated is entirely deterministic.

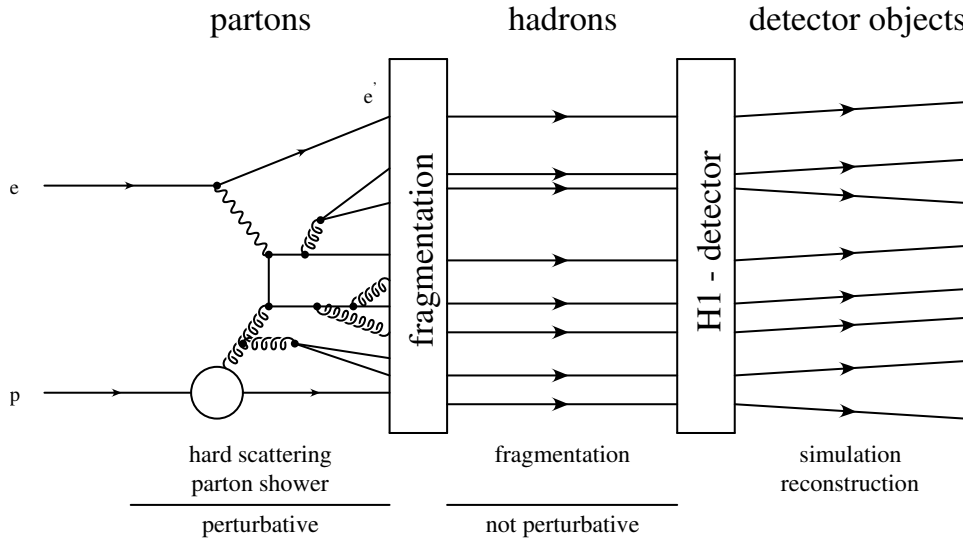


FIGURE 2.2: Schematic view of the event generation and detector simulation as implemented in modern Monte Carlo programs (Figure taken from [33]).

## 2.2.1 Event Generators

In high-energy physics so-called MC *event generators* apply MC methods to simulate the multi-particle final state of scattering events, as illustrated in figure 2.2, which should have the same average behaviour and fluctuations as the real data. In data events randomness arises from the quantum mechanics of the underlying theory, which is reflected in the modelling of all relevant variables according to their probability density distributions in the event generator.

The event generation includes various successive simulation steps. The hard scattering process is usually expressed by a LO matrix element, whereas in case of hadronic beams the incident partons are described by parton distribution functions. In processes that contain coloured objects gluon radiation in the initial or final state may give large corrections to the overall topology of the event. The two approaches most widely used for these perturbative corrections are the *Parton Showers* (PS) and the *Colour Dipole Model* (CDM). At decreasing energies and larger distances, QCD becomes strongly interacting and perturbation theory breaks down. In this fragmentation regime coloured partons are combined into colourless hadrons. Since the fragmentation process has yet to be understood in terms of fundamental QCD dynamics, phenomenological models are used for its description. Mostly used are the *string fragmentation* and the *cluster fragmentation*. In a last step the final state hadrons are passed to the detector simulation as described in section 3.2.6.

The comparison of event properties at parton, hadron and detector level allows for the extraction of detector acceptance corrections or for hadronisation corrections that can be applied to parton level calculations.

All MC simulations used in the present analysis and discussed throughout this chapter are based on the CTEQ6L proton parton densities. They are summarised in table 2.2. Before describing the simulation of the relevant signal and background contributions in more detail, the most relevant models for parton cascades and fragmentation are shortly explained.

### Parton Showers (PS)

Parton showers [34] are modelled in the leading log approximation through successive emission of quarks and gluons according to the splitting probability for quarks and gluons given by the four splitting functions  $P_{\alpha\beta}(x/z)$  introduced along with the DGLAP equations (1.20) and (1.21). In the resulting parton showers coherence effects are simulated by *angular ordering*, which restricts successive gluon emissions to decreasingly smaller angles. Unlike the Colour Dipole Model, the PS model allows for initial and final state radiation. Already the parton that enters the hard interaction can originate from parton splitting.

### Colour Dipole Model (CDM)

In the Colour Dipole Model (CDM), quarks are not treated as independent source of gluons, but each pair of coloured objects is treated as a colour dipole emitting a gluon, which results in two new dipoles radiating gluons themselves. In DIS, the QCD radiation starts from the colour dipole formed by the struck quark and the proton remnant.

### LUND String Fragmentation

The LUND String Fragmentation Model [35, 36] is based on the appearance of string-like colour fields between colour charges. According to this model diverging coloured objects lose kinetic energy which transforms into string potential energy. When the string energy exceeds twice the quark mass the string is split by creating a quark-antiquark pair. The coloured objects continue to diverge and consequently more quark-antiquark pairs are produced until the resulting partons combine to form colourless hadrons.

### Cluster Decay Fragmentation

In the Cluster Decay Fragmentation Model [37] all gluons produced in the parton showers are split into quark-antiquark pairs. Neighbouring quarks and antiquarks are then combined into colour neutral clusters, which are finally decayed into hadrons.

## 2.2.2 Isolated Photon Simulations

Isolated photons from the hard interaction are in LO DIS emitted from the scattering quark ( $QQ$ ) or the electron ( $LL$ ) as discussed in section 1.3. The simulation of these contributions involves two different event generators for the two contributions.

### Emission from Quark ( $QQ$ contribution)

The radiation from the struck quark is simulated with the PYTHIA [38] MC event generator in version 6.224. The generation is based on the LO QCD matrix elements for quark scattering with a transverse or longitudinal polarised virtual photon:  $q_i\gamma_T^* \rightarrow q_i\gamma$  and  $q_i\gamma_L^* \rightarrow q_i\gamma$ . Perturbative corrections are modelled using initial and final state parton showers in the leading log approximation. The fragmentation into hadrons is simulated using the LUND String Fragmentation Model as implemented in the JETSET program [39], which is now part of the PYTHIA software package.

Historically the PYTHIA model was developed for photoproduction, that is a real photon colliding with a hadron target. Only recently have virtual photons been added to the description as well [40, 41, 42], taking special care of the non-trivial transition region between photoproduction and DIS. In this approach the  $\gamma^*p$  cross section is divided into a VMD<sup>3</sup>, an anomalous, a direct and a DIS component. For low  $Q^2$  the DIS process is kinematically forbidden, while at very high  $Q^2$  all other processes are suppressed. At intermediate  $Q^2$  values the processes overlap, as they are equally valid descriptions of the same underlying physics. In order to avoid double counting in this transition region Sudakov style form factors are introduced for the DIS process, suppressing those parton configurations that are already covered by the direct processes.

As parton splitting can already occur in the initial state, the boson-gluon fusion (BGF) is included in the PYTHIA model as well, as shown in figure 2.1 b), and was found to contribute with roughly 40 % of the observed isolated photon events<sup>4</sup>. It should be noted that the PYTHIA simulation of the  $QQ$  contribution cannot easily be associated to the  $QQ$  contribution obtained from the LO calculation (section 2.1.1).

In addition to PYTHIA, also the HERWIG event generator [43] in version 6.505 is used to model the  $QQ$  subprocess. Since HERWIG models the fragmentation via the Cluster Decay Model it is used to extract an uncertainty on the fragmentation model in comparison to PYTHIA. However, HERWIG uses the equivalent-photon approximation for the incoming photon beam, which is not valid for  $Q^2$  above a few  $\text{GeV}^2$ . The comparison between PYTHIA and HERWIG is therefore done in a well defined phasespace region covered by both generators (cf. section 6.2).

### Emission from Electron ( $LL$ contribution)

The production of isolated photons in DIS radiated from the electron is simulated with the RAPGAP event generator [44]. RAPGAP is used to generate an inclusive DIS event sample based on the QPM matrix element in order  $\mathcal{O}(\alpha_s^0)$ ,  $\gamma^*q \rightarrow q$ , and on the order  $\mathcal{O}(\alpha_s^1)$  matrix elements for QCD-Compton scattering,  $\gamma^*q \rightarrow qg$ , and BGF,  $\gamma^*g \rightarrow q\bar{q}$ . As in PYTHIA,

<sup>3</sup>Vector Meson Dominance.

<sup>4</sup>The LO matrix element still describes the photon-quark scattering.



QCD cascades are simulated with initial and final state parton showers and the fragmentation is modelled in the LUND String Model.

In the RAPGAP simulation, QED radiation from the electron is explicitly included. By selecting DIS events on generator level that have a photon radiated from the electron within certain kinematic constraints<sup>5</sup>, a clean RAPGAP DIS sample of the  $LL$  contribution is obtained. For its radiative component this MC event sample is henceforth referred to as *RAPGAP (rad.)*.

### Combination of the Isolated Photon Monte Carlos

The  $QQ$  contribution as obtained from PYTHIA and the  $LL$  contribution from RAPGAP (rad.) are combined to form an isolated photon prediction, which is named *signal MC* in the following. The supposedly small contribution (cf. section 2.1.1) from interference between the processes ( $LQ$  contribution) is neglected in the MC simulation.

The signal MC does not well describe the measured cross sections (see chapter 7). However, the cross sections are reasonably described if PYTHIA is scaled by a factor 2.3, while RAPGAP (rad.) remains unscaled. This combined prediction is henceforth termed *scaled signal MC*. The scaled signal MC is used for the display of control distributions, corrections to the data and hadron corrections of the parton level calculations, whereas the unscaled MC prediction (signal MC) is used for comparison to the cross section measurements.

### 2.2.3 Neutral Hadron Background Simulation

The background from photon-like clusters induced by the decay of neutral hadrons as described in section 1.4 is also modelled by the RAPGAP generator. RAPGAP is again used to generate an inclusive DIS event sample, in which, however, the radiation from the electron is switched off. Additionally, events with QED radiation from the hard interacting quark<sup>6</sup> are rejected in order to have pure background contributions from neutral hadrons.

The RAPGAP neutral hadron background MC is named *RAPGAP (non-rad.)* in the following, since QED-radiative contributions are excluded. RAPGAP (non-rad.) will solely be used for illustrations in control distributions and for various cross checks. It does not enter the measurements.

Since RAPGAP (non-rad.) was observed to not well describe the DIS data, a reweighting in  $Q^2$  was applied in order to match the observed  $Q^2$  distribution in a DIS sample with at least one jet with transverse momentum  $P_T^{jet} > 7$  GeV. No photon or cluster selection was applied in the selection of these events and hence the contribution from isolated photons is negligible.

<sup>5</sup>The constraints should well include the phasespace of the cross section definition and be sufficiently restrictive to allow an efficient production of the desired events. In the selection of the RAPGAP  $LL$  contribution, the range of the photons transverse momentum and polar angle was required to be  $P_T^\gamma > 1.5$  GeV and  $\theta^\gamma < 160^\circ$ , respectively.

<sup>6</sup>Events are discarded if a photon is radiated from the hard interacting quark with a transverse energy  $P_T^\gamma > 2$  GeV and a polar angle  $16^\circ < \theta^\gamma < 148^\circ$ .

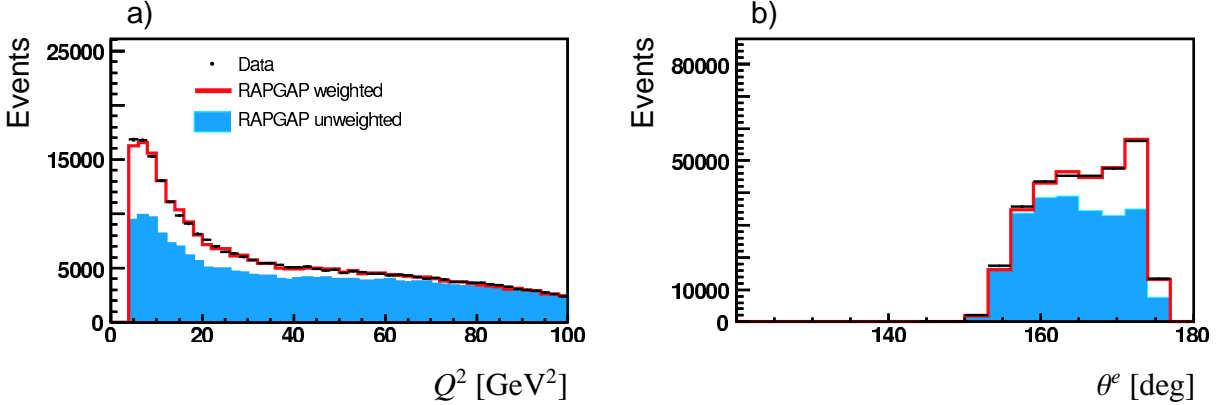


FIGURE 2.3: Distribution of  $Q^2$  (a) and the polar angle of the electron  $\theta^e$  (b) in DIS events with at least one jet of transverse momentum  $P_T^{\text{jet}} > 7$  GeV. The data are compared with the weighted and unweighted RAPGAP (non-rad.) MC.

The jet requirement was placed to guarantee sufficient hadronic activity in the events. The resulting reweighting factor decreases monotonically with  $Q^2$  and ranges between 1.95 for  $Q^2 = 4$  GeV and 0.9 for  $Q^2 = 150$  GeV. Figure 2.3 shows the observed data in comparison with RAPGAP (non-rad.) weighted and unweighted.

## 2.2.4 Single Particle Monte Carlo

The shower shape analysis described in chapter 5 requires high statistics samples of shower simulations in the whole phase space of energy and pseudorapidity. For this purpose the calorimeter signal produced by single photons and photons from decays of single neutral particles (*single particle* (SP) events) are simulated.<sup>7</sup>

Since various kinds of neutral particles may contribute to the background of photon-like clusters, some care has to be taken in the composition of the SP neutral hadrons. At first, clusters are selected in an inclusive DIS MC which fulfil the criteria of the standard cluster selection aiming at photon-like clusters as described in section 4.4. The linking from the selected cluster to the incident generated particle, which initiated the decay chain, allows the identification of the main contributors to the photon-like background clusters. Now, the relative contribution of the identified neutral hadrons is evaluated by counting the candidates in an inclusive DIS MC without any selection criteria applied. Again the decay chain of an observed candidate has to be followed up to the principal neutral hadron. The relative contributions are found in dependence of the transverse energy of the neutral hadrons.

In table 2.1 the contributing neutral hadrons are listed along with their relative contribution found in the unselected RAPGAP MC averaged over the transverse energy, as the energy dependence is found to be small. The last column of the table shows the relative contributions after the standard cluster selection including a restriction on the transverse cluster extent and

<sup>7</sup>In contrast to the SP events, the term *full event* MC refers to the simulation of the entire  $ep$  scattering process.

TABLE 2.1: Relative contribution of the relevant neutral hadrons to the background composition of photon-like clusters before and after the standard cluster selection (cf. section 4.4).

Neutral Hadron	Relative Contribution	
	Before Selection [%]	After Selection [%]
$\pi^0$	23.3	86.8
$\eta$	8.7	4.8
$\eta'$	5.0	0.3
$\omega$	16.1	1.6
$n$	2.9	0.1
$\bar{n}$	2.8	0.5
$K_L^0$	7.7	0.9
$K_S^0$	7.7	1.5
$\rho$	13.5	3.3
$K^*$	12.3	0.3

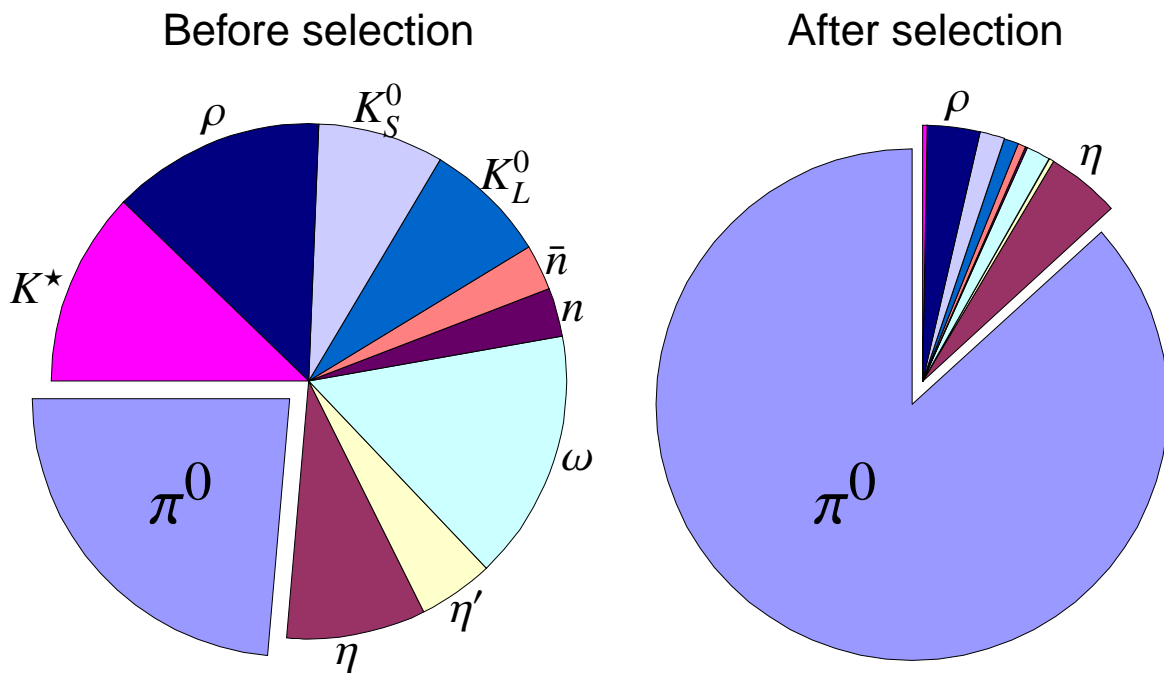


FIGURE 2.4: Illustration of the relative contribution of the relevant neutral hadrons to the background composition of photon-like clusters before and after the standard cluster selection (cf. section 4.4).

on the isolation of the cluster. Even though many neutral hadrons contribute considerably before the selection, after the selection mainly  $\pi^0$  and  $\eta$  contribute at a fraction of 86.8 % and 4.8 %, respectively. However, particles aside from  $\pi^0$  and  $\eta$  still have a sizeable share of roughly 10 %. The relative contributions before and after the standard cluster selection are also visualised in figure 2.4.

Besides a sample of *SP neutral hadrons* combined according to the relative contributions found in the RAPGAP MC, of which the average is listed in the second column of table 2.1, a sample of *SP photons* is used in the present analysis.

### 2.2.5 Photoproduction Background Monte Carlo

Due to migration and misidentification photoproduction events at small  $Q^2$  might pass the DIS selection and contribute to the measured cross sections. In order to estimate the contribution, Monte Carlo samples of such photoproduction events are used.

The simulation uses the PYTHIA event generator and consists of a 2-jet sample with two outgoing partons in the matrix element and a prompt photon sample based on the matrix element  $\gamma q \rightarrow \gamma q$ . Both samples cover processes with the exchanged photon interacting directly with the hard parton of the proton (*direct processes*) and processes in which the exchanged photon resolves before the hard interaction (*resolved processes*).

TABLE 2.2: Summary of used Monte Carlo event samples.

Generator	Purpose	Kin. Regime	Target Period	Luminosity [ $\text{pb}^{-1}$ ]		$N_{\text{Events}}[10^6]$
				total	unweighted	
PYTHIA	$QQ$	DIS	99/00	16740	2113	1.244
PYTHIA	$QQ$	DIS	04	14508	1860	1.138
PYTHIA	$QQ$	DIS	05	14368	2044	1.138
HERWIG	$QQ$	DIS	99/00	34449	3684	0.987
RAPGAP (rad.)	$LL$	DIS	99/00	771	771	0.158
RAPGAP (rad.)	$LL$	DIS	04	771	771	0.158
RAPGAP (rad.)	$LL$	DIS	05	771	771	0.158
RAPGAP (non-rad.)	Neutral Hadron BG	DIS	99/00	97	97	40.000
RAPGAP (non-rad.)	Neutral Hadron BG	DIS	04	97	97	40.000
RAPGAP (non-rad.)	Neutral Hadron BG	DIS	05	97	97	40.000
SP Photons	signal (Clusters)	-	99-05	-	-	0.540
SP Neutral Hadrons	BG (Clusters)	-	99-05	-	-	5.728
PYTHIA	2-jet BG	$\gamma p$ dir./res.	99-05	470	470	2.978
PYTHIA	prompt- $\gamma$ BG	$\gamma p$ dir./res.	99-05	2817	2817	0.374



## CHAPTER 3

# THE H1 EXPERIMENT AT HERA

---

The data for this analysis were collected with the H1 experiment in the years 1999–2005. After a brief overview of the HERA<sup>1</sup> accelerator, the H1 apparatus is described, focusing on the detector components relevant for the present measurement of isolated photons in deep-inelastic scattering.

### 3.1 HERA Storage Ring

The HERA storage ring is located at the DESY<sup>2</sup> research laboratory in Hamburg, Germany. HERA accelerates and stores *bunches* of electrons and protons in two separate underground storage rings and provides the unique opportunity to study high-energetic lepton-quark interactions.

The electrons and protons are pre-accelerated in linear accelerators (LINACs) and smaller storage rings (DESY II/III and PETRA<sup>3</sup>) before they are transferred to HERA. At HERA the counter rotating electron and proton beams are accelerated to meet their final energies of 27.6 GeV and 920 GeV, respectively, which allows for head-on collisions with a centre-of-mass energy of  $\sqrt{s} \approx 319$  GeV (cf. equation 1.1). At a rate of 10.4 MHz collisions take place at two opposite interaction regions, where the multi-purpose detectors H1 (north) and ZEUS (south) are installed. In addition, two fixed-target experiments, HERMES and HERA-B, are installed at HERA. A schematic layout of the HERA accelerator together with an enlarged view of the pre-accelerators and the four experiments is shown in figure 3.1.

---

<sup>1</sup>Hadron-Elektron-Ring-Anlage.

<sup>2</sup>Deutsches Elektronen Synchrotron.

<sup>3</sup>Positron-Elektron-Tandem-Ring-Anlage.

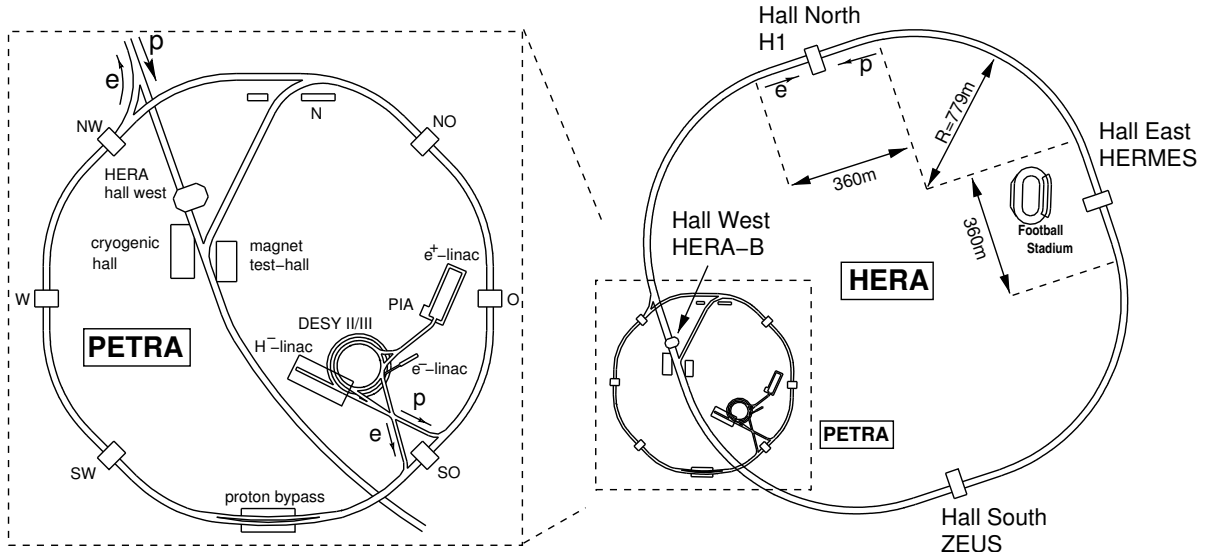


FIGURE 3.1: Schematic view of the HERA collider. On the left hand side, a more detailed view of the pre-accelerator system is shown.

### 3.1.1 Luminosity Upgrade Project for HERA

The accelerator performance finds itself summarised in the produced *integrated luminosity*  $L$ , which is proportional to the number of events expected in  $ep$  collisions  $N^{ep} = L \cdot \sigma^{ep}$  with  $\sigma^{ep}$  being the total  $ep$  cross section. The produced luminosity can also be understood as the time-integrated *instantaneous luminosity*  $\mathcal{L}$  ( $L = \int \mathcal{L} dt$ ), which itself depends on the pure accelerator specific bunch-crossing frequency as well as on the number of particles per bunch and the collimation of the beams. The luminosity is hence strictly limited by the accelerator design.

Figure 3.2 shows the integrated luminosity available for physics analyses at H1 in separate lines for the *HERA I* and *HERA II* running periods. It is obvious that between the first  $ep$  collisions in 1992 and the end of the HERA I running period in August 2000, the gradient of produced luminosity increased steadily and finally HERA exceeded its instantaneous design luminosity. Consequently a luminosity upgrade [45, 46, 47] was carried out from September 2000 on, aiming for an increase of the instantaneous design luminosity by approximately a factor five to  $\mathcal{L}_{nom}^{HERA II} = 7.4 \cdot 10^{31} \text{ cm}^{-2} \text{ s}^{-1}$ .

The upgrade project included the installation of two new super-conducting magnets close to the H1 experiment for a stronger electron beam focusing, which made major changes to the inner design of the H1 experiment necessary. The vacuum beam pipe had to be changed and now has an elliptic design. Further changes to the inner subdetector components were made, which are discussed in more detail in section 3.2. In addition to the new magnets, HERA is operated at the highest possible beam currents after the upgrade. The increased instantaneous



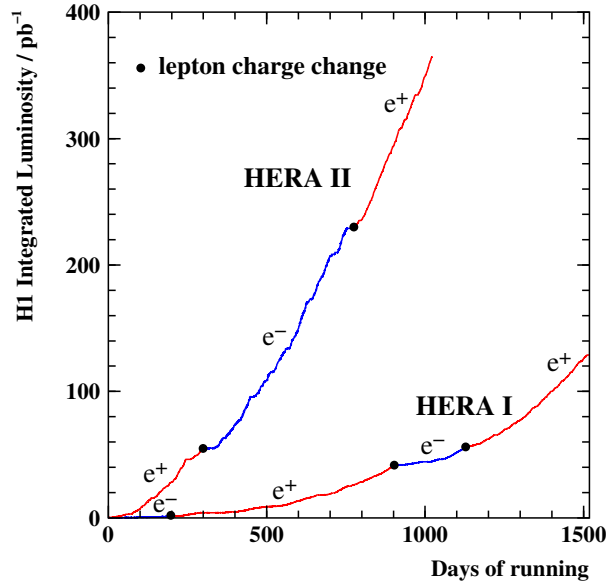


FIGURE 3.2: Development of the integrated luminosity available for physics analyses at H1 over the time of running. The two separate lines indicate the running periods HERA I and HERA II.

luminosity is reflected in the much steeper gradient of the collected luminosity during the HERA II running period (cf. figure 3.2).

## 3.2 H1 Detector

The H1 detector is an almost hermetic general purpose detector, designed to measure cross sections and final states for a wide spectrum of  $ep$  reactions. Its complex assembly of sub-detectors is built around the nominal interaction point IP of the electron and proton beam (cf. figure 3.1), allowing for a precise identification and reconstruction of the particles emerging from the interaction.

The right-handed *reference frame* at H1 is defined such that the positive  $z$ -axis points into the proton beam direction referred to as the *forward* direction. The positive  $x$ -axis points horizontally to the centre of the storage rings and the  $y$ -direction is vertically upwards. The polar angle  $\theta$  is measured with respect to the  $z$ -axis and the azimuthal angle  $\phi$  lies in the  $xy$ -plane<sup>4</sup>,  $\phi = 0$  corresponding to the positive  $x$ -axis. Often the pseudorapidity<sup>5</sup>  $\eta = -\ln \tan(\theta/2)$  is used instead of the polar angle  $\theta$ .

The markedly higher energy of the proton beam compared to the electron beam causes the

<sup>4</sup>also referred to as the *transverse* plane.

<sup>5</sup>For negligible particle masses, differences in the pseudorapidity are invariant under longitudinal Lorentz-boosts.

centre-of-mass frame to be boosted into the forward direction. Unlike most other colliding beam detectors, the H1 detector consequently features an asymmetric instrumentation with a more heavily equipped forward region. The *backward* region is less densely instrumented and dedicated predominantly to the reconstruction of the scattered electron.

As already mentioned, the H1 detector was also upgraded during the luminosity upgrade project (section 3.1.1). The Central Inner Proportional Chamber (CIP) with two layers and the Central Inner z-Chamber (CIZ) were replaced by a five-layer proportional chamber with high granularity (CIP2k) [48] in order to overcome the increased non- $ep$  background<sup>6</sup> situation. The luminosity system, the data acquisition, several subdetectors and the trigger system were adapted to the new running conditions. Furthermore the backward drift chamber was replaced by the backward proportional chamber and also the forward region of H1 was equipped with new detectors.

In figure 3.3 the H1 detector is illustrated with its major detector components. A detailed description of the H1 detector can be found in [49, 50]. The subdetectors relevant for the present work are now described in more detail.

### 3.2.1 Calorimetry

Calorimeters complement the momentum measurement of charged particles provided by tracking detectors and allow furthermore the detection and energy measurement of photons and neutral hadrons, which are not observable in tracking devices.

The calorimetry in the H1 experiment features four distinct detector components. The largest component is the *Liquid Argon* calorimeter (LAr), which covers the forward and central region. Energy leaking out of the LAr is detected by the tail catcher, which is installed in the instrumented iron. In the forward and backward region the LAr is complemented by the plug calorimeter and the *Spaghetti* calorimeter (SpaCal), respectively.

In the present analysis isolated photons are identified by their *electromagnetic showers* in the LAr. Before describing the calorimetric system in more detail, a short review on electromagnetic showers is given.

#### Electromagnetic Showers

When energetic photons or electrons traverse matter<sup>7</sup> they may initiate a cascade of further electrons and photons by alternating pair production ( $\gamma \rightarrow e^+e^-$ ) and bremsstrahlung processes ( $e \rightarrow e\gamma$ ). They induce a so-called electromagnetic shower.

---

<sup>6</sup>New focusing magnets close to the interaction point lead to stronger synchrotron radiation, which in turn evaporates particles from the surface of absorbers. The higher pressure of the residual gas in the beam pipe gives rise to more so-called *beam-gas* events in the backward region of H1, where protons scatter with the gas molecules.

<sup>7</sup>In calorimeters well-suited absorber materials are used.

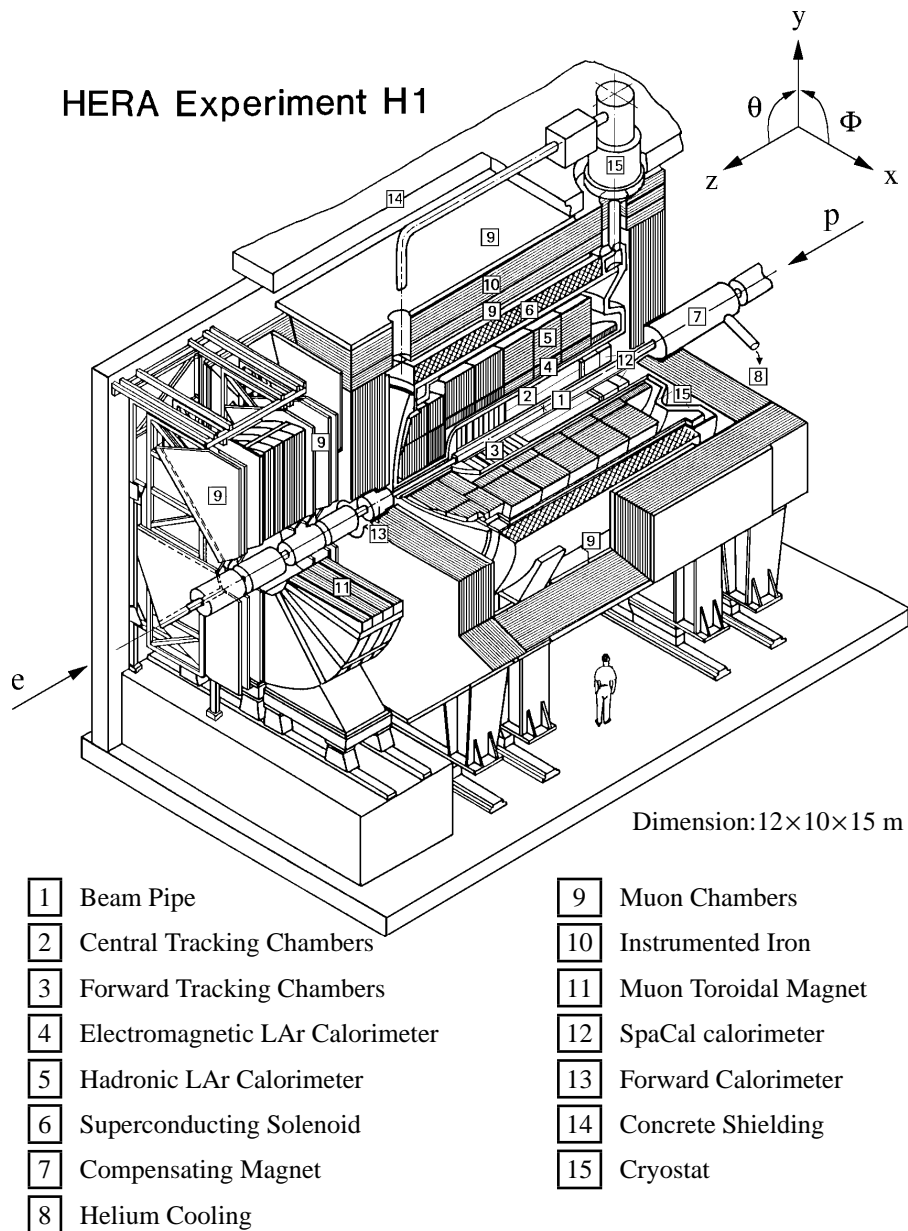


FIGURE 3.3: An isometric view of the H1 detector with its major detector components.

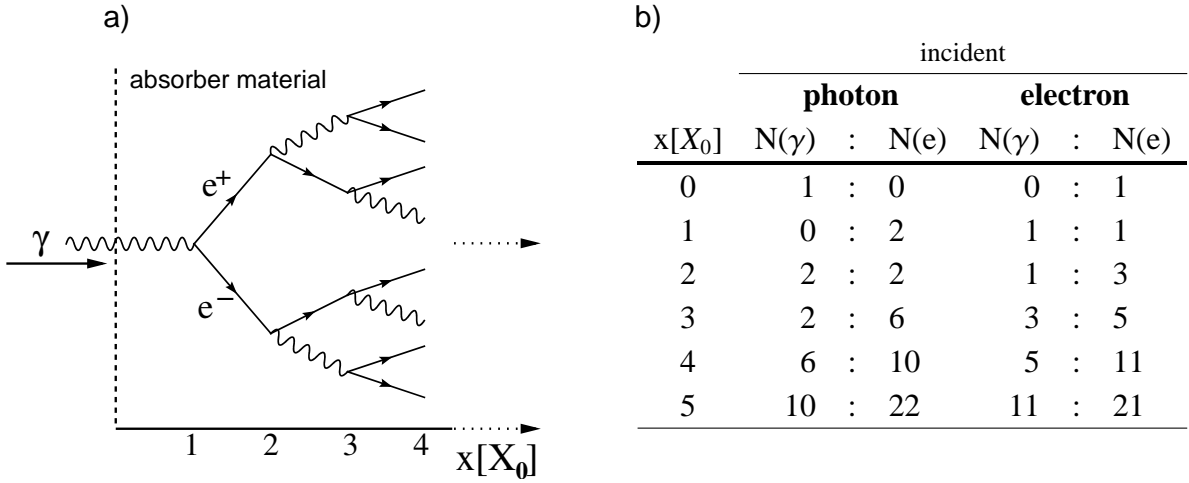


FIGURE 3.4: Simple model of an electromagnetic shower. In a) an incident photon from the left is shown, inducing an electromagnetic shower. Successive and equidistant bremsstrahlung and pair production processes produce an exponential increase of electrons, positrons and photons in the absorber material with increasing penetration depth  $x$ . Following this model, b) displays the number of produced photons versus the number of electrons plus positrons for different depths of penetration, which are stated in multiples of the radiation length  $X_0$ . The numbers are given for showers induced by a photon or electron.

The appropriate longitudinal scale for describing electromagnetic cascades is the material dependent *radiation length*  $X_0$ <sup>8</sup>, which is the mean distance over which a high-energy electron loses all but  $1/e$  of its energy by bremsstrahlung. A good approximation for the radiation length is [51]

$$X_0 = \frac{716.4 \text{ g/cm}^2 A}{Z(Z+1) \ln(287/\sqrt{Z})}, \quad (3.1)$$

where  $A$  is the atomic weight and  $Z$  the atomic charge. The radiation lengths obtained by this formula agree with a precise determination [52] to better than 2.5 % for all elements with  $Z > 2$ .

The main characteristics of an electromagnetic shower can already be deduced from a simple model as illustrated in figure 3.4. A photon entering matter converts into an  $e^+e^-$ -pair after the radiation length  $X_0$ . Within another radiation length the produced electron and positron emit bremsstrahlung-photons, which again produce electron-positron pairs. The continuing pair production and bremsstrahlung processes lead to an exponentially increasing number of particles  $N(x) = 2^x$  with the penetration depth  $x$  (measured in units of  $X_0$ ). As suggested by figure 3.4 (b), showers induced by electrons become fairly similar to photon showers after few radiation lengths.

<sup>8</sup>As an example, the radiation length for lead is  $X_0^{\text{Pb}} = 6.37 \text{ g/cm}^2$  in surface density units, which corresponds to  $X_0^{\text{Pb}} = 0.56 \text{ cm}$  [51].

TABLE 3.1: Longitudinal parameters of an electromagnetic shower [56] derived with Rossi's Approximation B [55]. The depth  $x_{max}$  of the maximum shower development and the longitudinal centre-of-gravity are given in units of the radiation length  $X_0$  for showers induced by photons or electrons.

	incident photon	incident electron
$x_{max}[X_0]$	$\ln E_0/E_c - 0.5$	$\ln E_0/E_c - 1.0$
centre-of-gravity $[X_0]$	$x_{max} + 1.7$	$x_{max} + 1.4$

The exponential particle growth continues as long as the energy of the shower particles is sufficiently high for more bremsstrahlung and pair production processes. The *critical energy*  $E_c$ , below which ionisation losses become dominant, can for heavy elements ( $Z > 13$ ) satisfactorily be approximated by [53]

$$E_c = \frac{550 \text{ MeV}}{Z}. \quad (3.2)$$

Under the assumption that the incident energy  $E_0$  is evenly distributed, the energy of the shower particles equals  $E(x) = E_0 \cdot 2^{-x}$ . The maximum number of shower particles is reached when  $E(x_{max}) = E_c$ , which in this simple model leads to

$$x_{max} \sim \ln\left(\frac{E_0}{E_c}\right). \quad (3.3)$$

A more involved approach leads to a more accurate parametrisation of the mean longitudinal profile of the energy deposition of an electromagnetic shower, which is given in the form [54]

$$\frac{dE}{dx} = E_0 b \frac{(bx)^{a-1} e^{-bx}}{\Gamma(a)}, \quad (3.4)$$

where  $a$  and  $b$  are energy dependent parameters. The longitudinal shower maximum and the centre-of-gravity, analytically derived using the assumptions of *Rossi's approximation B* [55], are summarised in table 3.1 for incident photons and electrons and show qualitative agreement with equation (3.3). A fraction of 98 % of the shower energy is contained within a depth of  $x = 2.5 \cdot x_{max}$  [56].

The transverse shower profile, which is not described within the framework of the former parametrisation, can also be understood qualitatively. In the first phase of the shower evolution the transverse expansion is characterised by small angle bremsstrahlung emission and in the second part, multiple scattering in the absorber material increasingly contributes with decreasing energy of the shower particles, thus gradually broadening the shower.

The lateral dimension of electromagnetic showers can conveniently be measured in terms of the *Molière radius*  $R_M$ , given by [57, 58]

$$R_M = \frac{21 \text{ MeV}}{E_c} X_0 [\text{g/cm}^2]. \quad (3.5)$$

Roughly 95 % of the shower energy is contained in a cylinder with radius  $2R_M$  around the shower axis [59]. While the longitudinal extent of the shower strongly depends on the energy of the incident particle, the Molière radius only changes with the absorber material. It should be noted that equation (3.5) only holds for homogeneous calorimeters. For *sampling calorimeters*, which consist of alternating sampling and absorber layers, the lateral extent is underestimated.

In the present analysis *Monte Carlo* methods (see section 2.2) are used to simulate the transverse and longitudinal shower development.

### The Liquid Argon Calorimeter

The *Liquid Argon* calorimeter (LAr) [60] provides full azimuthal acceptance and has an asymmetric polar angle coverage of  $4^\circ < \theta < 154^\circ$ . While the LAr, given its considerable coverage of the solid angle, is of vital importance for the reconstruction of the hadronic final state, its inner electromagnetic section also allows for a precise measurement of isolated photons and electrons.

Figure 3.5 shows a longitudinal cross section of the LAr with its segmentation into 8 *wheels*. Listed from the backward direction these are the *Backward Barrel* (BBE), three *Central Barrels* (CB1, CB2, CB3), two *Forward Barrels* (FB1, FB2) and an *Inner* and *Outer Forward* module (IF, OF).<sup>9</sup> Except for the BBE and the OF all wheels consist of an inner electromagnetic and an outer hadronic part. The BBE only provides an electromagnetic section, whereas the OF has two hadronic *stacks*. The transversal cross section in figure 3.6 displays the sectioning of the wheels along the azimuthal angle into 8 octants. Between the octants and also between the wheels the calorimeter has insensitive regions, which are referred to as  $\phi$ -*cracks* and  $z$ -*cracks*, respectively.

The LAr is a sampling calorimeter composed of alternating absorber layers and liquid argon filled gaps. The electromagnetic section consists of 2.4 mm thick lead absorber plates interspersed with 2.35 mm wide sampling layers of liquid argon. The liquid argon acts as active material between the high voltage and readout cells, which are mounted on the absorber plates. Shower particles crossing the sampling layer induce a signal by the ionisation of liquid argon atoms. The total depth of the absorber material in the electromagnetic section varies between 20–30  $X_0$  depending on the impact angle.

Since for most absorbers the nuclear interaction length  $\lambda$  is roughly one order of magnitude larger than  $X_0$ , hadronic showers penetrate much deeper into the absorber material than electromagnetic showers. The hadronic section therefore extends the electromagnetic part and features alternating 19 mm thick stainless steel absorbers and liquid argon gaps of twice 2.4 mm width, which add up to 5–8  $\lambda$  including the electromagnetic section.

As indicated in figure 3.5 the orientation of the absorber plates was chosen such that the angle of incidence is not smaller than  $45^\circ$ . The orientation of the plates is vertical in the

<sup>9</sup>For convenience the wheels are numbered 0 (BBE) to 7 (OF) from the backward to the forward direction.

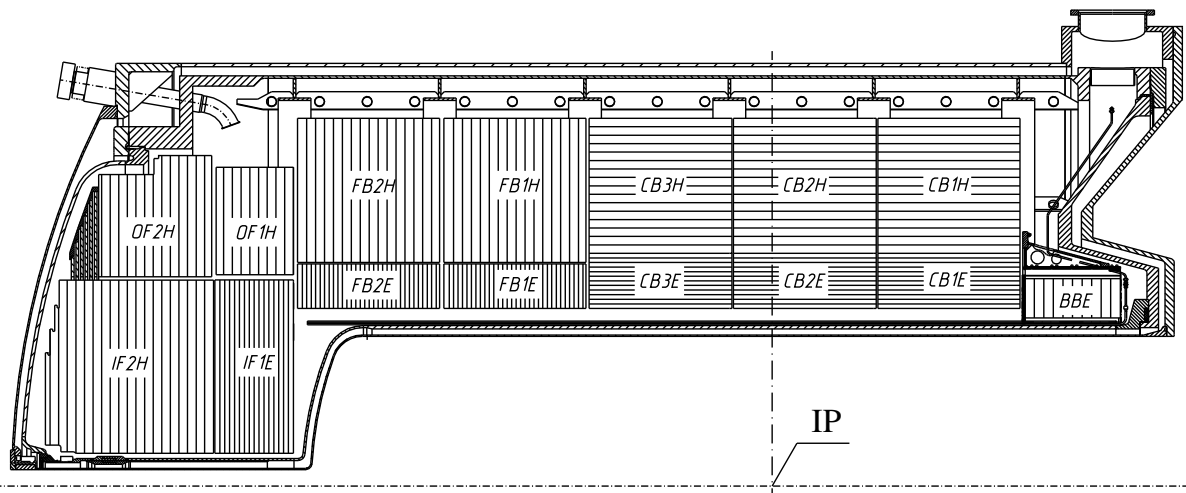


FIGURE 3.5: Longitudinal cross section of the Liquid Argon calorimeter showing its segmentation into eight wheels.

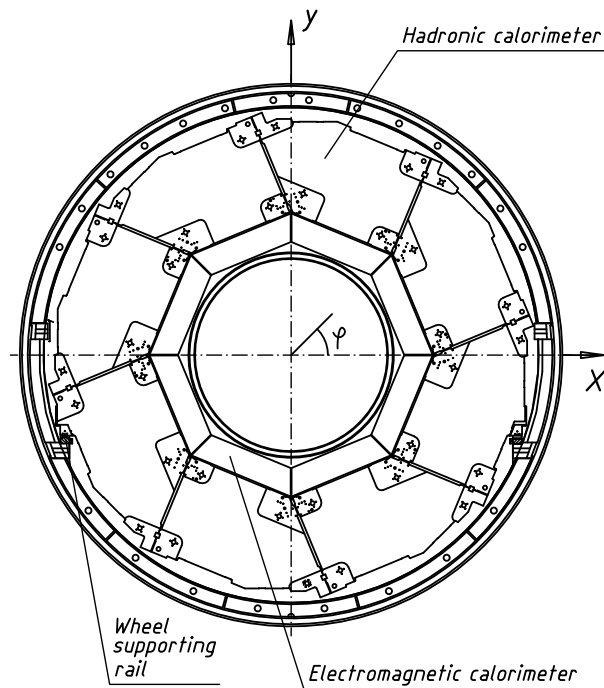


FIGURE 3.6: Transversal cross section of the Liquid Argon calorimeter showing its segmentation into eight octants along the azimuthal angle.

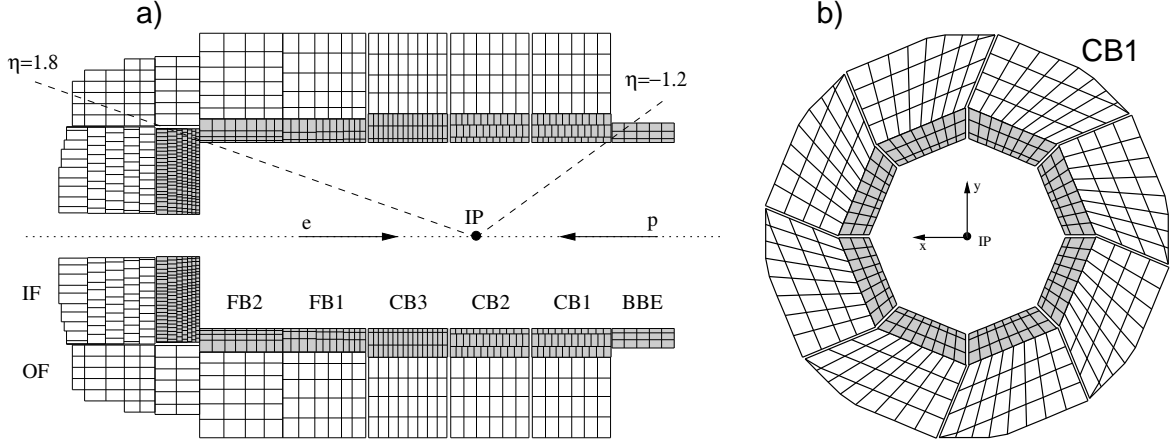


FIGURE 3.7: Longitudinal (a) and transversal (b) cross section of the Liquid Argon calorimeter illustrating the fine granularity of the readout system. The shaded area indicates the electromagnetic section of the calorimeter and the dashed lines represent the acceptance range for isolated photons of  $-1.2 < \eta^\gamma < 1.8$  used in the present analysis.

forward region and the BBE and parallel to the beam for the central barrels.

Both the electromagnetic and the hadronic section are highly segmented in the transverse and longitudinal direction with about 44000 cells in total, which is illustrated in figure 3.7. The cell granularity is finer in the forward direction on account of the higher particle concentration and in the electromagnetic section in order to resolve the compact electromagnetic showers induced by electrons and photons. The longitudinal segmentation varies from three (central) to four (forward) layers of cells in the electromagnetic section, where the first layer has a thickness of three to six radiation lengths, and from four to six layers in the hadronic section. Transversally a basic granularity of the electromagnetic readout cells of  $2R_M$  was chosen, measured at the entrance of the electromagnetic calorimeter. Only in the BBE, CB1 and CB2 the basic dimensions are approximately doubled. For particles incident from the interaction point, the laterally projected cell size in the electromagnetic stack ranges between  $5 \times 5 \text{ cm}^2$  in the forward and  $7 \times 13 \text{ cm}^2$  in the central wheels.

The isolated photons measured in the present analysis are restricted to the pseudorapidity range  $-1.2 < \eta^\gamma < 1.8$ , corresponding to the five wheels CB1 to FB2 as indicated by the dashed lines in figure 3.7.

In test beam measurements [61, 62], the energy resolution was found to be

$$\frac{\sigma^{el}(E)}{E} = \frac{12\%}{\sqrt{E/\text{GeV}}} \oplus 1\% \quad (3.6)$$



for electromagnetic showers and

$$\frac{\sigma^{had}(E)}{E} = \frac{50\%}{\sqrt{E/\text{GeV}}} \oplus 2\% \quad (3.7)$$

for hadronic showers.

The deposited energy in the readout cells of the LAr undergoes several subsequent steps during its reconstruction process. After an important *noise suppression* sequence, neighbouring cells are assigned to *clusters*, which are contiguous formations of cells that are likely to contain the cascade of a single incident particle. Clusters can then be classified into hadronic and electromagnetic clusters, depending on their extent and the position of the first deposited energy.

In hadronic showers a sizeable fraction of the energy is consumed in semi-stable final states that may delay the energy deposit by up to 10 minutes as well as in the production of nuclear fragments that do not reach the sampling layer and consequently remain hidden from detection. In a *non-compensating* calorimeter<sup>10</sup> as the LAr, such effects demand an offline correction based on a shower shape analysis. Electromagnetic showers as induced by photons are not affected by such nuclear effects.

### Spaghetti Calorimeter (SpaCal)

In the backward region, the LAr is complemented by the *Spaghetti* calorimeter (SpaCal) [63], which covers the angular range  $153^\circ < \theta < 177.5^\circ$ . The principal task of the SpaCal is the detection of electrons scattered at small angles (large polar angle  $\theta$ ), corresponding to measurements in the kinematic range of  $Q^2 < 150 \text{ GeV}^2$ .

Like the LAr, the SpaCal is a sampling calorimeter with an inner electromagnetic and an outer hadronic section. Both parts are fabricated of long scintillating fibres (hence the name “Spaghetti”) placed parallel to the beam axis and embedded in a lead matrix as absorber material. Charged shower particles in the induced showers are detected by the excitation of molecules in the scintillator material, which trigger light impulses in the fibres. The light is transmitted to *photomultiplier* tubes at the backward end of the fibres, where the impulses are converted into electrical signals.

The electromagnetic part consists of 1192 cells with a cell size of  $4.05 \times 4.05 \text{ cm}^2$ . The cell dimensioning corresponds to roughly double the Molière radius of 2.55 cm [64], which ensures a good spatial resolution. Most importantly, it allows for a good  $e/\pi$  separation based on the transverse shower extent. In test beam measurements [65], the energy resolution was found to be  $\sigma^{el}(E)/E = 7\% / \sqrt{E/\text{GeV}} \oplus 1\%$ . The longitudinal cell length of 25.5 cm corresponds to  $28 X_0$ . Electromagnetic showers are well contained in the electromagnetic section for incident electron energies of up to 30 GeV [65].

<sup>10</sup>An example for a *compensating* calorimeter is the uranium scintillator calorimeter of the ZEUS experiment, where interactions between neutrons and the uranium atoms compensate for the delayed or hidden energy deposits.

The hadronic section of the SpaCal only provides a coarse transverse granularity of 136 cells with a transversal cross section of  $11.9 \times 11.9 \text{ cm}^2$  each. Though the hadronic section has a limited spatial resolution, it allows to distinguish electromagnetic and hadronic showers. The longitudinal extent of the SpaCal amounts to roughly  $2\lambda$ , of which the electromagnetic section corresponds to one nuclear interaction length.

The SpaCal provides a precise *time-of-flight* measurement with a time resolution of better than 1 ns, permitting the suppression of non- $ep$  background, which is asynchronous to the nominal bunch crossings defined by the strict timing of  $ep$  collisions with a period of 96 ns.

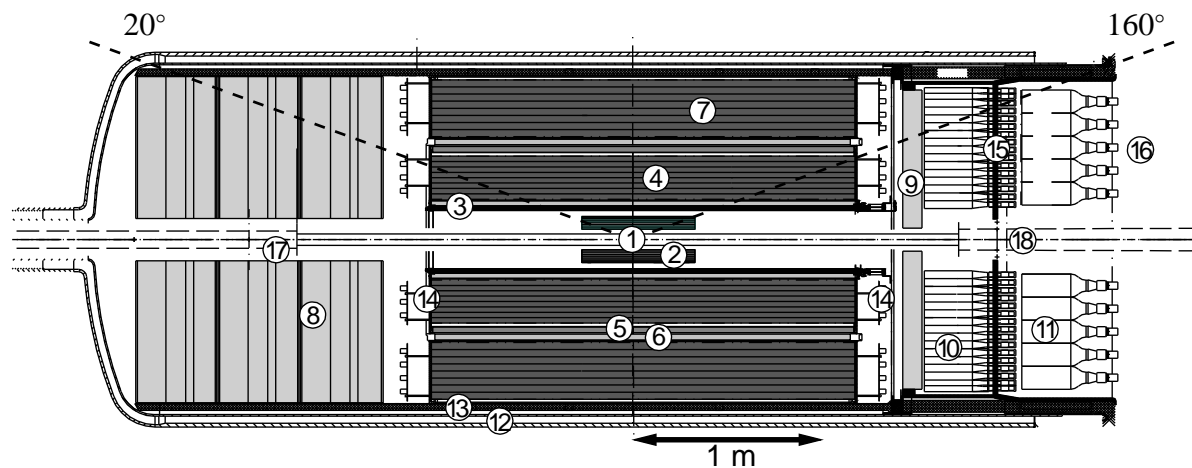
As mentioned earlier, a new focusing magnet was installed in the backward region of the H1 experiment for the HERA II running period (see section 3.1.1). For the installation of the new beam pipe some of the inner cells of the SpaCal had to be removed lowering the acceptance range of the SpaCal for the HERA II running period to  $153^\circ < \theta < 174^\circ$  [66].

### 3.2.2 Tracking

Enclosing the interaction region the H1 tracking system constitutes the innermost part of the H1 detector, allowing to track charged particle trajectories right from the  $ep$  collision vertex. In the tracking system three different detector technologies are employed: *drift chambers*, *multi-wire proportional chambers* and *silicon trackers*. The drift chambers allow for a precise measurement of particle trajectories, whereas the multi-wire proportional chambers (MWPCs) have a lower spatial resolution but a fast response time (10 ns). MWPCs are therefore predominantly used in triggering. The silicon detectors exceed the spatial resolution of the drift chambers and enhance the precision of the track measurement close to the interaction point, thus allowing to accurately reconstruct the primary vertex as well as any additional decay vertices.

Figure 3.8 shows the  $rz$ -view of the H1 tracking system, specifying all major detector components implemented during the HERA II running period. The chief difference in the tracking setup between the HERA I and HERA II running periods that applies to the present analysis, is the exchange of the *Backward Drift Chamber* (BDC) for the *Backward Proportional Chamber* (BPC). The backward chambers enhance the angle measurement of the scattered electron. Furthermore, the *Central Inner Proportional Chamber* (CIP) and the *Central Inner  $z$ -Chamber* (CIZ) have been replaced by a new MWPC (CIP2k) [48] in the transition of the running periods (cf. section 3.1.1) with minor impact on the present analysis. Figure 3.9 depicts the  $r\phi$ -view of the central tracking system for the HERA I and HERA II running periods.

Since only charged particles leave tracks in the tracking system, photons usually cross the tracking system undetected, provided that no conversion into lepton-antilepton pairs takes place. As the electromagnetic showers of electrons and photons in the calorimeters do not differ greatly (cf. section 3.2.1), a tracking veto is the favourable criteria for the separation of



1	Nominal interaction point	IP	Calorimetry	
Central Tracking			10	Spaghetti Calorimeter (em.) em. SpaCal
2	Central Silicon Tracker	CST	11	Spaghetti Calorimeter (had.) had. SpaCal
3	Central Inner Prop. Chamber	CIP2k	Miscellaneous	
4	Inner Central Jet Chamber	CJC1	12	CJC electronics
5	Central Outer z-Chamber	COZ	13	Cables
6	Central Outer Prop. Chamber	COP	14	LAr cryostat inner wall
7	Outer Central Jet Chamber	CJC2	15	em. SpaCal Photomultipliers
Forward Tracking			16	had. SpaCal Photomultipliers
8	Forward Tracking Detectors	FTD	17	Final Focusing Magnet GO
Backward Tracking			18	Final Focusing Magnet GG
9	Backward Prop. Chamber	BPC		

FIGURE 3.8: Longitudinal cross section of the H1 tracking system as it was implemented in the HERA II running period. The dashed lines indicate the central region of  $20^\circ < \theta < 160^\circ$ .

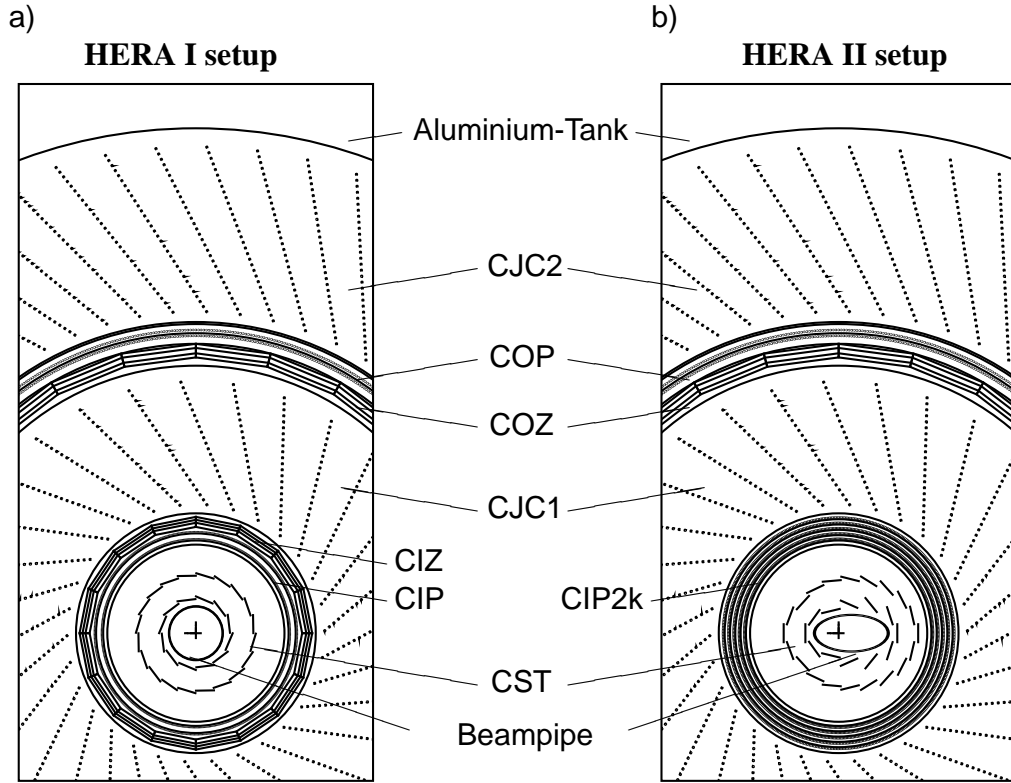


FIGURE 3.9: Transverse view of the central tracking detectors. The setup as it was implemented during the HERA I running period is shown in a), while b) shows the central tracking setup as it was installed during the HERA II running period. It should be noted that the depicted setups refer to the years of data taking that are used in the present analysis and do not encompass all distinct setups that were in use during the full HERA I and HERA II running period.

photons from electrons.<sup>11</sup> The tracking veto in this analysis applies to the *Central Jet Chamber* (CJC), which is described in more detail below.

In few cases the track information is complemented by track measurements in the Forward Tracking Detector (FTD). The FTD extends the tracking acceptance into the forward direction and covers the polar angle range  $7^\circ < \theta < 25^\circ$ .

### Central Tracker

The Central Jet Chambers (CJC1 and CJC2) [67] have an active length of 220 cm along the  $z$ -direction and consist of two concentric drift chambers, the inner CJC1 ( $20.3 < r < 45.1$  cm) and the outer CJC2 ( $53.0 < r < 84.4$  cm). The CJC1 (CJC2) is azimuthally segmented into

<sup>11</sup>A tracking veto usually implies the requirement that no track trajectory is allowed within a certain distance of closest approach (DCA) to the barycentre of the electromagnetic shower in the calorimeter.

30 (60) drift cells with 24 (32) sense wires per cell that are spanned parallel to the beam axis. Incident charged particles are traced by their ionising of gas atoms<sup>12</sup>, where the emerging ionisation electrons are detected by the anode sense wires after a short drift-time. The drift cells are inclined by  $30^\circ$  with respect to the radial direction in order to correct for the Lorentz angle. As ionisation electrons drifting towards the anode wire are deflected by the magnetic field, the inclination is chosen such that the drift is effectively perpendicular to the anode wire plane, resulting in an enhanced track resolution.

The spatial resolution in the  $r\phi$ -plane is based on a drift-time measurement of the ionisation electrons, while the  $z$ -coordinate is obtained from charge division. The 3-dimensional space point measured by one single sense wire is referred to as *hit*, which is measured with an accuracy of  $\sigma_{r\phi} \approx 170 \mu\text{m}$  in the transverse direction and  $\sigma_z \approx 3 \text{ cm}$  in the longitudinal direction. The  $z$ -resolution of measured tracks can be significantly improved by the *Central Inner/Outer z-Chambers (CIZ/COZ)*<sup>13</sup>. These two thin drift chambers situated inside and outside of the CJC1 have a polygonal wire structure perpendicular to the beam pipe (see figure 3.9), which leads to an improved  $z$ -resolution of typically  $300 \mu\text{m}$ . The transverse momentum of a particle is determined from the track curvature, reconstructed from a fit to all measured track hits. The resolution degrades with increasing momentum and is given by  $\sigma(P_T)/P_T = 0.01 \text{ GeV}^{-1} P_T$ .

The nearest detector component to the interaction point is the Central Silicon Tracker (CST). In two layers of silicon strip detectors with an inner radius of  $r_i = 5.75 \text{ cm}$  and an outer radius of  $r_o = 9.75 \text{ cm}$ , hits are measured with an accuracy of  $\sigma_{r\phi} = 12 \mu\text{m}$  and  $\sigma_z = 22 \mu\text{m}$ . The high precision allows for the reconstruction of secondary decay vertices of long-lived particles with decay lengths in the order of  $\mathcal{O}(100 \mu\text{m})$ .

### Backward Chamber

During the HERA I running period the *Backward Drift Chamber (BDC)* [68] was situated in front of the SpaCal at  $z = -145 \text{ cm}$  having the same polar angle acceptance as the SpaCal of  $153^\circ < \theta < 177.5^\circ$ . For the HERA II running period the BDC has been replaced by the *Backward Proportional Chamber (BPC)* [69], which provides a larger inner radius in order to account for the larger beam pipe. The BPC approximately covers the modified acceptance of the SpaCal in the HERA II running period (cf. section 3.2.1) of  $153^\circ < \theta < 174^\circ$ . Due to the structural design the BPC has a roughly  $8 \text{ cm}$  wide insensitive region along the  $x$ -axis. The backward chambers are used to enhance the angle measurement of the scattered electron at low  $Q^2$ .

### 3.2.3 Luminosity System

The H1 luminosity system (figure 3.10) makes use of the well known cross section of the Bethe-Heitler process  $ep \rightarrow e\gamma$ , which is predicted in QED with high accuracy. The electron

<sup>12</sup>In the CJC a gas mixture of Ar, CO<sub>2</sub> and CH<sub>4</sub> is used.

<sup>13</sup>The CIZ was installed only in the HERA I running period.

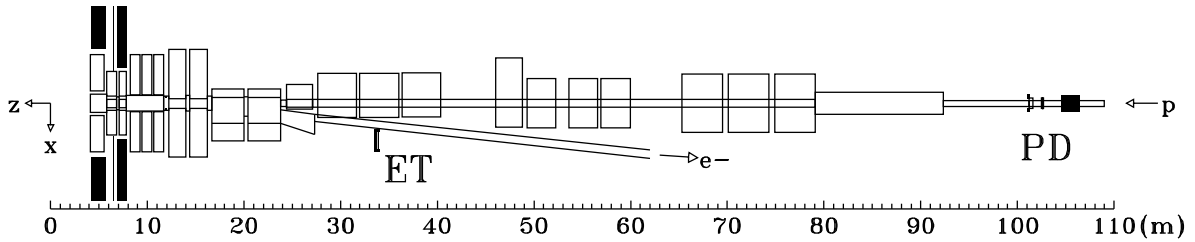


FIGURE 3.10: The H1 luminosity system. Photons and electrons are detected at very small scattering angles. The electron tagger (ET) is placed at  $z = -33.9$  m and the photon tagger (PT) at  $z = -102.9$  m.

and photon are mostly scattered at small angles and leave the detector through the backward beampipe. They are finally detected in coincidence in two small angle calorimeters, the electron tagger (ET) at  $z = -33.9$  m and the photon tagger at  $z = -102.9$  m. Both calorimeters are situated very close to the beampipe. The main background for the luminosity measurement is from bremsstrahlung in electron scattering with residual gas atoms  $eA \rightarrow eA\gamma$ . After corrections, an uncertainty on the luminosity measurement of better than 1.5 % is achieved.

### 3.2.4 Time-of-Flight System

The Time-of-Flight (ToF) system consists of plastic scintillators installed at various places within the H1 experiment. The ToF system delivers precise timing information used to reject non- $ep$  background events which are asynchronous to the strict 96 ns-period of  $ep$  collisions at HERA. In particular two scintillators of the *veto-wall* at  $z = -8.1$  m and  $z = -6.5$  m reject events with a significant time offset to the HERA clock.

### 3.2.5 Trigger System and Data Acquisition

When comparing the bunch crossing rate of 10.4 MHz with the technically possible rate of  $\mathcal{O}(10$  Hz) at which events can be recorded for physics analyses, it is obvious that an efficient trigger logic is needed for the rate reduction.

The H1 trigger system has an input rate of several 100 kHz depending on the beam quality of which roughly 1 kHz originates from  $ep$  collisions, the input rate is hence clearly dominated by various kinds of non- $ep$  background as well as detector noise. Moreover, the trigger logic has to reliably select *interesting*  $ep$  events according to predefined priorities, since events once rejected are irrecoverable. The rate is subsequently reduced in four trigger levels, of which all but the third trigger level were active during the data taking periods relevant for this analysis. Figure 3.11 shows a schematic view of the trigger system.

The first trigger level (L1) is based on a fast decision from hardware components. During the decision time of  $2.3 \mu\text{s}$  (corresponding to 24 bunch-crossings) all subdetector information

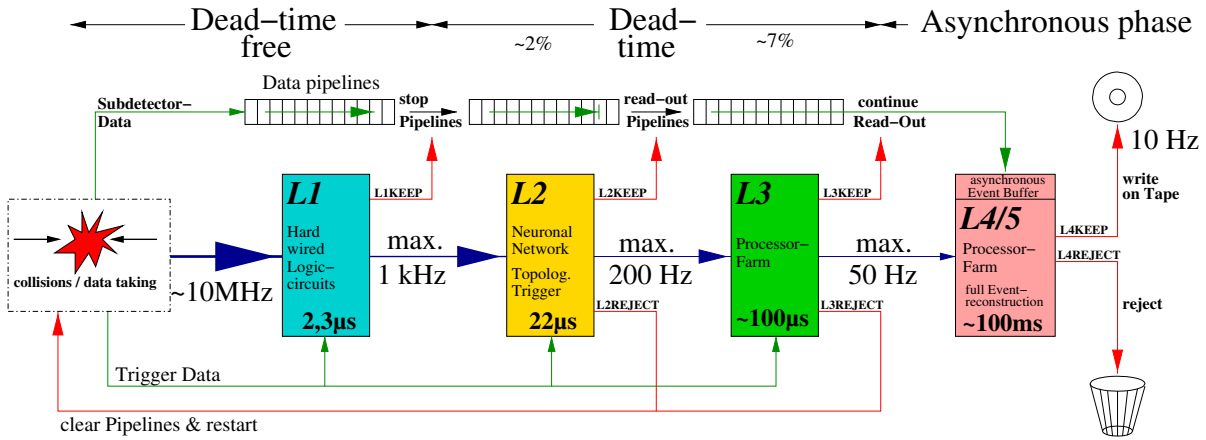


FIGURE 3.11: Data flow in the designed H1 trigger system layout.

of incoming events is buffered in a circular pipeline. By this means, the delayed readout of an accepted event is always assured within the decision time, thus allowing the first trigger level to operate *dead-time free*. The central trigger logic (CTL) combines 256 trigger elements, which are derived from various subdetector measurements, to 128 different subtriggers resembling specific physics processes. As soon as an event passes the criteria of one of these subtriggers, the readout pipeline is stopped and the event is passed to the next trigger level. Some subtriggers might, however, still deliver very high rates and, depending on the priorities, a subtrigger might be subject to downscaling. Technically the downscaling is realised by means of *trigger bits*. Any event accepted by subtrigger  $i$  receives the *raw* subtrigger bit, of which only the fraction  $1/d_i$  ( $d_i$  is the downscaling factor) additionally receive the *actual* subtrigger bit. An event is passed to the next trigger level, as soon as an actual subtrigger bit is set. In the data analysis the observed number of events needs to be corrected for such downscale factors, which becomes more involved when different downscaled subtriggers are used in combination (cf. section 4.2.1).

According to the trigger design the event rate needs to be reduced in the second trigger level (L2) to 200 Hz within roughly 20  $\mu$ s using more complex algorithms. Since the third trigger level has, however, not been in use during the data taking period relevant for this analysis, L2 has to reduce the event rate down to the maximum level four input rate of 50 Hz. On the second trigger level correlations between different detector components are matched. For this purpose two trigger concepts are provided: the topological trigger (L2TT) and the neural network trigger (L2NN). The topological trigger L2TT searches for spatial correlations and expected patterns, whereas the L2NN performs cuts in the multi-dimensional phasespace defined by global event quantities, which are calculated from the collected subdetector information by preprocessing units of the L2NN system. A L2 decision to reject the event restarts the readout pipelines. If the event is accepted by L2, the full event is read out which takes roughly 1–2 ms.

During this readout time the pipeline remains stopped and dead-time accumulates.

The third trigger level (L3) is designed to reduce the input rate by approximately a factor 4 based on software algorithms running on a multi-processor system. Until mid-2006 the third trigger level was, however, not in use and events were passed from L2 forthwith to the fourth trigger level (L4), where a full reconstruction and classification of the event is carried out on a processor farm. Events passing L4 undergo another downscaling procedure similar to the downscaling in L1, where the rate of frequent *soft physics processes* (low  $P_T$ , low  $Q^2$ ) is reduced by *downscaling*<sup>14</sup>.

Events passing all precedent trigger levels are permanently written to tape in two different data formats, *Production Output Tapes* (POTs) and *Data Summary Tapes* (DSTs). The POTs contain the complete event data including *raw* and *reconstructed* information, while on DSTs only a subset of predominantly reconstructed quantities is stored, which is sufficient for most physics analyses. DSTs occupy roughly 10 kB per event of disk space, which is an order of magnitude smaller than the data volume of the POTs. In the offline analysis of the *ep* scattering data, calibration constants to the subdetector measurements, as well as information on the detector alignment, are extracted. After the so-called *reprocessing*, the corrected measurements are written to a further generation of DSTs. In the present analysis only reprocessed data is used.

### 3.2.6 Detector Simulation

The H1SIM software package [70], based on the GEANT program [71], simulates the detector response of generated Monte Carlo particles. The GEANT description of the detector includes all instrumentation as well as passive material. In complex calculations the energy deposits by the particles in the active material of the detector are evaluated.

The shower simulation in the LAr as provided by GEANT is a time-consuming iteration. Therefore, usually a certain parametrisation, H1FAST [72], is used for analyses that do not depend on a detailed shower description. The GEANT shower simulation was, however, found to be more reliable and thus used in a former analysis on isolated photons [18, 73]. Meanwhile the H1FAST parametrisation has improved markedly [74] and was found to give reliable results also in the detailed description of shower profiles. In the present analysis, the new H1FAST parametrisation is hence used for the simulation of electromagnetic showers in the LAr.

Monte Carlo events that underwent the simulation by H1SIM are treated like data events and are passed to the same reconstruction program, H1REC [50].

---

<sup>14</sup>Downscaling means that a number of events is represented by a single event that receives a corresponding weight. The other events are hence discarded.



# CHAPTER 4

## EVENT SELECTION

---

This chapter describes the selection of DIS events with an isolated photon candidate. At first the selection of DIS events concentrates primarily on the identification of the scattered electron and on the rejection of photoproduction background. In a next step, a subsample of events with an isolated photon candidate in the LAr calorimeter is selected. The candidates still contain a sizeable fraction of neutral hadron background after the selection. The actual photon content is therefore extracted by a multivariate shower shape analysis described in chapter 5. The extracted photon signal is then used to determine isolated photon cross sections (cf. chapters 5 and 7).

Before describing the selection of DIS events, the used data samples are introduced and the data preselection and the triggering are explained.

### 4.1 Data Taking Periods and Preselection

The present analysis is based on data taken with the H1 experiment in the years 1999–2005 and covers parts of both the HERA I and HERA II data taking periods. Table 4.1 gives a detailed overview of the used data samples. The total analysed integrated luminosity amounts to  $227 \text{ pb}^{-1}$  with fractions of 52.1 %  $e^-p$  and 47.9 %  $e^+p$  scattering data. In the H1 data taking, a HERA fill of electron and proton bunches is organised in H1 runs of approximately 1–2 hours, which have a stable trigger strategy setup and an unaltered readout status. Any H1 run is subject to a quality classification. H1 runs in which detector defects or other malfunctions occur may be classified as *poor* runs. Such runs are excluded from the data sets. Additionally, it is required that in any selected event the high voltage (HV) of the following subdetectors was at nominal settings and their readout be functional: CJC1, CJC2, Luminosity system, LAr, SpaCal, BPC and ToF.

In order to reduce background originating from non- $ep$  collisions the  $z$ -position of the reconstructed collision vertex is required to be within a range of  $\pm 40$  cm of the nominal run vertex. For the determination of the correct integrated luminosity of the analysed data sets as

TABLE 4.1: Summary of analysed data samples.

Data Taking Period	Year	$\sqrt{s}$	Beams	H1 Run Range	$\int \mathcal{L} dt$
HERA I	1999	319 GeV	$e^- p$	231721 – 241649	10.2 pb <sup>-1</sup>
	1999	319 GeV	$e^+ p$	244968 – 259461	13.9 pb <sup>-1</sup>
	2000	319 GeV	$e^+ p$	262204 – 279215	46.5 pb <sup>-1</sup>
HERA II	2004	319 GeV	$e^+ p$	367257 – 392241	48.1 pb <sup>-1</sup>
	2005	319 GeV	$e^- p$	401617 – 436893	108.1 pb <sup>-1</sup>

listed in table 4.1, the employed  $z_{vtx}$  constraint as well as the HV and readout requirements have to be taken into account.

Beside background events resulting from collisions with residual gas molecules and beam pipe material, there is also a considerable background from cosmic rays and beam-halo muons. Beam-halo muons originate from the decay of charged pions produced at some distance to the detector. While the ToF system rejects a large fraction of such background by timing constraints at the trigger level, the event time reconstructed offline from the drift chamber measurement is used to further reject the remaining non- $ep$  background. Only events with a timing of  $\pm 4.8$  ns around the nominal interaction time are selected.

In figure 4.1, the event yield for a selection of DIS events with a photon candidate as described throughout this chapter is shown. The event yield is stable<sup>1</sup> with an average of about 60 events per pb<sup>-1</sup> of integrated luminosity and is slightly higher in the HERA I data taking period due to a different downscaling strategy on the trigger level described in section 4.2.1.

## 4.2 Triggering

On the first trigger level L1 various subtriggers are dedicated to the triggering of DIS events with  $Q^2$  up to approximately 150 GeV<sup>2</sup>, which are usually triggered by the energy deposition of the scattered electron in the SpaCal. Since these subtriggers tend to produce comparatively high rates, they are subject to downscaling as described in section 3.2.5. In addition, most of them are further constrained by requirements on the second trigger level L2. In the present analysis various subtriggers are used simultaneously in order to diminish the event loss due to the downscaling. The evaluation of correction factors for a combined use of downscaled subtriggers is explained in section 4.2.1.

In table 4.2 the used subtriggers are listed for different years of data taking along with their

<sup>1</sup>The measured cross sections were also cross-checked for a possible run range dependence. The cross sections were found to be stable throughout the HERA I and HERA II data taking periods.

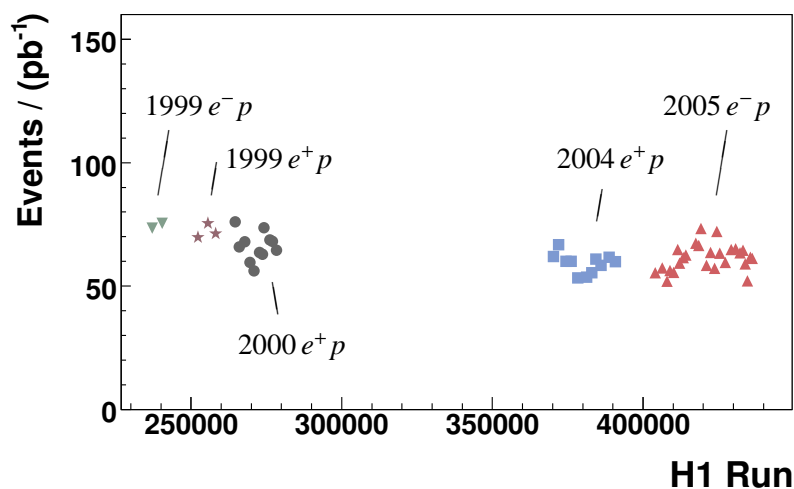


FIGURE 4.1: Event yield for the selection of DIS events with a photon candidate. Single points correspond to an integrated luminosity of  $4 \text{ pb}^{-1}$ .

L1 and L2 conditions and average downscale correction factors<sup>2</sup>. All considered subtriggers contain at least one element of the *inclusive electron trigger* (IET) [75], which compares compact energy depositions in the SpaCal with predefined energy thresholds. Energy depositions in the innermost trigger region in the SpaCal are associated to a different trigger element than the outer regions<sup>3</sup>. Only the subtriggers s4 and s61 include the inner trigger region. The L1 definition of subtrigger s61 requires in addition to the IET element also a track in the CJC with a transverse momentum of at least 900 MeV. This track trigger element is delivered by the *DC- $r\phi$*  trigger [76] up to 2004 and by the Fast Track Trigger (FTT) [77] from 2005 on.

### 4.2.1 Downscaled Subtriggers

The mechanism of downscaling was already shortly introduced in section 3.2.5. An event that passes a subtrigger condition sets the raw subtrigger bit, which is then subject to downscaling by a run dependent downscaling factor. For events that survive the downscaling, the actual subtrigger bit is set and the L1 decision is given as an OR of all actual subtrigger bits.

In case only one downscaled subtrigger  $i$  is used, the appropriate weight to correct to the original event rate is simply given by the downscale factor  $d_i$ . If more subtriggers are considered and an event is also accepted by more than one of these subtriggers, the weight decreases and may be calculated as suggested in [78]. The calculation of weights for an exclusive downscaling on the first trigger level is explained in the following.

<sup>2</sup>So-called global options, which are additional veto conditions to reject beam induced background, are not listed.

<sup>3</sup>The innermost trigger region in the SpaCal corresponds to a square of  $8.1 \times 8.1 \text{ cm}^2$  and contains the intersection with the beam axis.

TABLE 4.2: The used subtriggers listed for different years of data taking. Apart from global options, the L1 and L2 definitions are listed together with the average downscale factor  $\bar{d}_i$  during the respective period.  $E^{IET}$  refers to the energy measured by the inclusive electron trigger.  $E^{IET}(outer)$  neglects energy depositions in the innermost trigger region, whereas  $E^{IET}(all)$  takes into account depositions in any trigger region of the IET.  $R_{SpaCal}$  is the distance of the energy deposition in the SpaCal to the  $z$ -axis. The L2 condition of the s9 subtrigger changed in the year 2005 to  $R_{SpaCal} > 40$  cm from Run 421376 on.

## HERA I

Subtrigger $i$	L1 condition	L2 condition	$\bar{d}_i$
s0	$E^{IET}(outer) > 6 \text{ GeV}$	–	3.24
s1	$E^{IET}(outer) > 6 \text{ GeV}$	$R_{SpaCal} > 30 \text{ cm}$	1.71
s3	$E^{IET}(outer) > 6 \text{ GeV}$	$R_{SpaCal} > 30 \text{ cm}$	1.38
s4	$E^{IET}(all) > 6 \text{ GeV}$	–	3.83
s9	$E^{IET}(outer) > 2 \text{ GeV}$	$R_{SpaCal} > 30 \text{ cm}$	1.89
s61	$E^{IET}(all) > 6 \text{ GeV}$ and track in CJC ( $P_T > 900 \text{ MeV}$ )	–	1.02

## HERA II

Subtrigger $i$	L1 condition	L2 condition	$\bar{d}_i$
s0	$E^{IET}(outer) > 6 \text{ GeV}$	$R_{SpaCal} > 20 \text{ cm}$	1.69
s3	$E^{IET}(outer) > 9 \text{ GeV}$	$R_{SpaCal} > 30 \text{ cm}$	1.00
s9	$E^{IET}(outer) > 2 \text{ GeV}$	$R_{SpaCal} > 30(40) \text{ cm}$	2.08
s61	$E^{IET}(all) > 6 \text{ GeV}$ and track in CJC ( $P_T > 900 \text{ MeV}$ )	–	1.02

For subtrigger  $i$ ,  $r_{ij}$  denotes the raw subtrigger bit in event  $j$  and  $d_{ik}$  the downscale factor in run  $k$ . Then the probability that subtrigger  $i$  triggers the event  $j$  in run  $k$  is given by

$$P_{ijk} = \frac{r_{ij}}{d_{ik}}. \quad (4.1)$$

Consequently the probability that in any of  $N$  subtriggers the actual subtrigger bit is set in event  $j$  and run  $k$  is

$$P_{jk} = 1 - \prod_{i=1}^N \left(1 - \frac{r_{ij}}{d_{ik}}\right). \quad (4.2)$$

The inverse of this probability  $1/P_{jk}$  is already the weight to be applied for each event to obtain the original rate, as though no downscaling was used. In a given run a certain subtrigger pattern will always obtain the same weight, which tends to be the smaller the more subtriggers have accepted the event. However, for heavily varying downscale factors, the weight for a certain subtrigger pattern can change strongly from run to run resulting in statistical uncertainties that are larger than necessary. The fluctuations can be substantially reduced if the trigger probability is averaged over a preferably large run range with constant subtrigger definitions. The weight is then independent of the run and given by

$$w_j = \frac{\sum_{k=1}^{N_{runs}} L_k}{\sum_{k=1}^{N_{runs}} L_k P_{jk}}, \quad (4.3)$$

where  $L_k$  denotes the integrated luminosity of run  $k$ . The weight  $w_j$  is constant for a given pattern of raw subtrigger bits throughout the considered run range. In the present analysis weights are averaged for each of the five distinct run ranges listed in table 4.1.

### 4.2.2 Trigger Efficiency

The trigger efficiency is determined by means of an independent *monitor* trigger. For the considered SpaCal and track based signal subtriggers (cf. table 4.2) independent trigger elements based on energy depositions in the LAr are ideally suited as monitor triggers. Therefore, the subtrigger s67 is used as monitor in the present analysis. The s67 is dedicated to the triggering of scattered electrons in the LAr in high  $Q^2$  DIS events. Although this trigger is optimised for electrons it also responds to high energetic jets [79] and to the showers induced by energetic neutral particles [73]. The trigger efficiency is given by the fraction of events that were triggered by the monitor trigger and have a raw subtrigger bit set in at least one of the signal subtriggers ( $N_{signal \wedge monitor}$ ) to all events triggered by the monitor trigger ( $N_{monitor}$ ):

$$\epsilon = \frac{N_{signal \wedge monitor}}{N_{monitor}}. \quad (4.4)$$

The trigger efficiency is evaluated for events passing the entire DIS and isolated photon candidate selection as described throughout this chapter and will be given for the combined set of signal subtriggers.

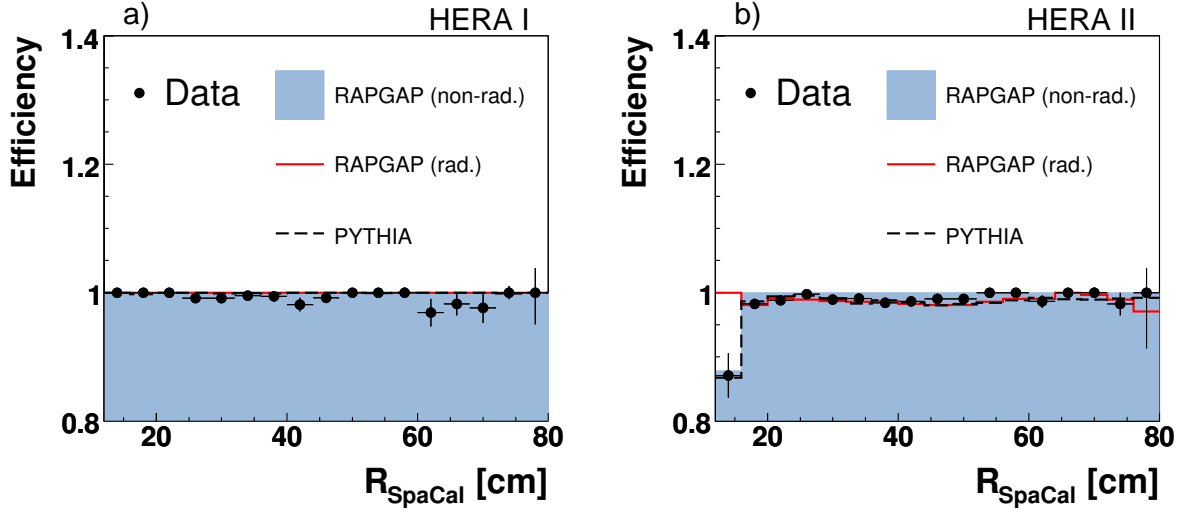


FIGURE 4.2: Trigger efficiency as function of the distance  $R_{\text{SpaCal}}$  of the electron cluster in the SpaCal to the  $z$ -axis for data and MC predictions. a) HERA I data taking period. b) HERA II data taking period.

The L1 and L2 trigger decisions are also simulated in the MC sample. Figure 4.2 shows the trigger efficiency separately for the HERA I and HERA II data set as a function of the distance  $R_{\text{SpaCal}}$  of the electron cluster in the SpaCal to the  $z$ -axis for data and MC predictions. Except for small  $R_{\text{SpaCal}}$  in the HERA II data set, the efficiency is above 98 % and is in agreement with the MC predictions for both photons and neutral hadron background. The efficiency drop in the inner region of the SpaCal ( $R_{\text{SpaCal}} \lesssim 20$  cm) for HERA II is due to the modified acceptance of the SpaCal after the luminosity upgrade (cf. section 3.2.1) and the lack of overlapping triggers in this region. Only the s61 contributes at  $R_{\text{SpaCal}} < 20$  cm in HERA II without L2 constraint, which is restricted by an additional track requirement. However, also in this region the efficiency is in agreement with the MC predictions of PYTHIA and RAPGAP (non-rad.). The RAPGAP (rad.) MC suffers from small statistics in the inner SpaCal region because of the comparatively small cross section of  $LL$  events at large polar angles of the electron<sup>4</sup>.

Figure 4.3 shows the trigger efficiency for the entire data set in addition to  $R_{\text{SpaCal}}$  as a function of the maximum transverse momentum observed in all CJC tracks  $P_T^{\text{max}}(\text{track})$ ,  $E'_e$  and  $Q^2$ . No strong dependence of the trigger efficiency is observed. The efficiency is well described by the MC predictions and remains above 98 %. The total trigger efficiencies for data and MC predictions are listed in table 4.3 for the entire data set and also separately for the HERA I and HERA II data taking periods. In data the total trigger efficiency for DIS events with a photon candidate averaged over the entire data taking period amounts to 99.0 %.

<sup>4</sup>A large polar angle of the electron implies a larger minimum distance from the radiated photon, which is suppressed in the  $LL$  process.

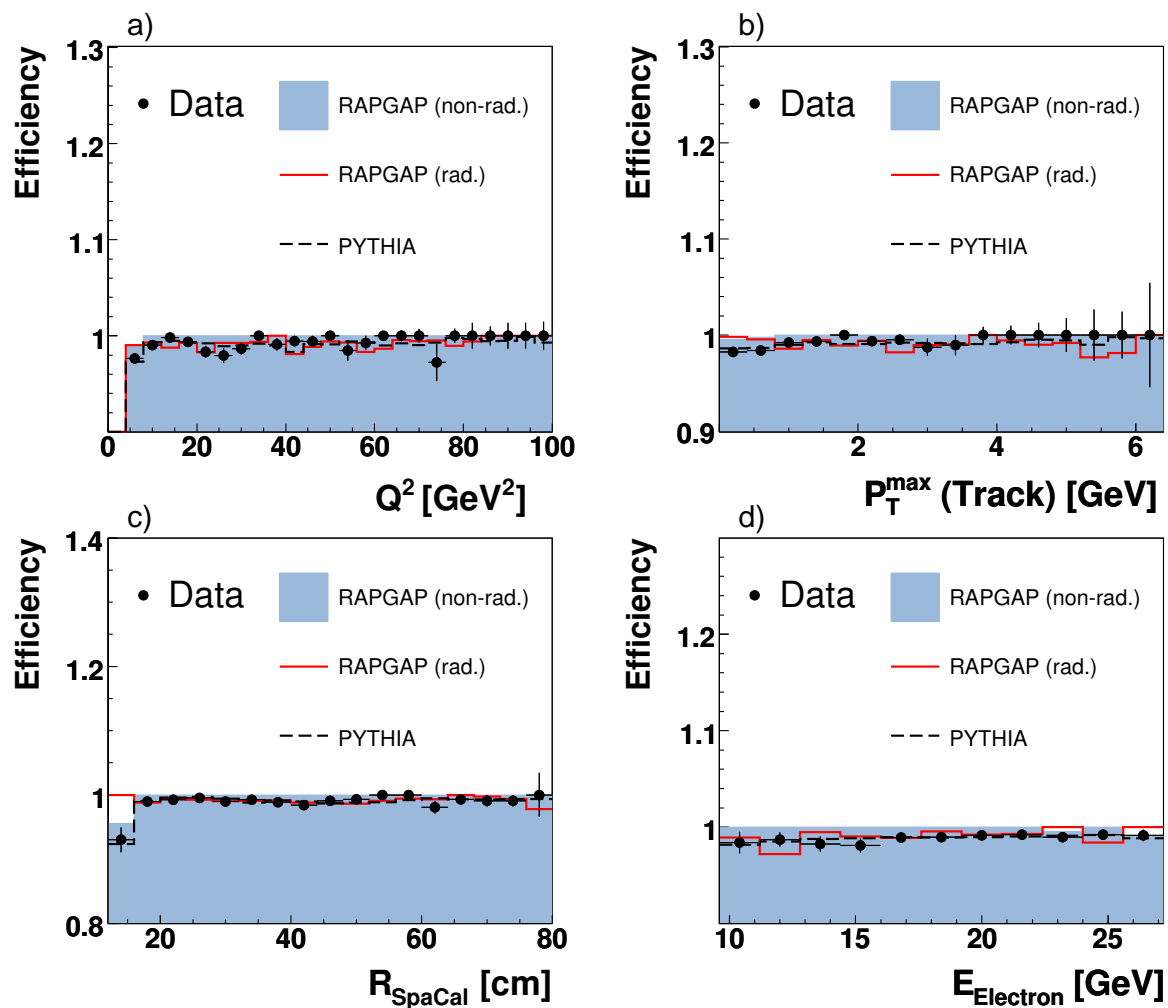


FIGURE 4.3: Trigger efficiency as function of  $Q^2$  (a), the maximum transverse momentum observed in all good CJC tracks  $P_T^{\max}(\text{track})$  (b),  $R_{\text{SpaCal}}$  (c) and  $E_e'$  (d) for data and MC predictions shown for the entire data set.

TABLE 4.3: Total trigger efficiencies separately for the data taking periods HERA I and HERA II and for the entire data set.

	Total Trigger Efficiencies		
	HERA I	HERA II	HERA I+II
Data	99.3 %	98.7 %	99.0 %
PYTHIA	99.9 %	98.5 %	99.0 %
RAPGAP(rad.)	100.0 %	98.7 %	99.1 %
RAPGAP(non-rad.)	100.0 %	99.8 %	99.9 %

## 4.3 Selection of DIS Events

### 4.3.1 Electron Reconstruction

The scattered electron is identified as an electromagnetic cluster with an energy

$$E'_e > 10 \text{ GeV} \quad (4.5)$$

and a polar angle

$$\theta^e < 177^\circ \quad (4.6)$$

in the SpaCal. The lower polar angle of the electron is constrained by the SpaCal acceptance ( $\theta^e \gtrsim 153^\circ$ ). The scattering angle of the electron is determined from the measured impact position in the BDC (BPC for HERA II) and the position of the energy cluster in the SpaCal together with the reconstructed primary vertex. In standard H1 analyses of DIS events the scattered electron is usually associated to the electromagnetic cluster with the highest transverse momentum. In the presence of energetic final state photons, this assumption is often mistaken and needs to be adjusted, making use of the fact that the DIS cross section decreases with  $Q^2$ . Hence, among two or more electromagnetic clusters with an energy above 8 GeV and no associated track the electromagnetic cluster that reconstructs the lowest  $Q^2$  relates to the scattered electron. The reconstruction of  $Q^2$  from the kinematics of the scattered electron is described in the next section (4.3.2).

In addition to the high minimum energy of the scattered electron, further requirements on the electromagnetic cluster of the electron are used to suppress the background from photoproduction ( $\gamma p$ ) events, in which the electron escapes through the beam pipe and a hadron fakes the signature of an electron in the detector. The cluster is required to be compact, i.e. the radius  $R_e$  of the cluster should be small, and the energy in the hadronic part of the SpaCal should be limited:

$$R_e < 4 \text{ cm}, \quad (4.7)$$

$$E_{e,had} < 0.5 \text{ GeV}. \quad (4.8)$$

In order to reject background from neutral hadrons in the SpaCal, in HERA I at least four hits in the BDC are required to be associated to the electron with a *distance of closest approach* (DCA) of less than 2.5 cm between the track trajectory and the barycentre of the cluster. In HERA II, due to the limited acceptance of the BPC, three hits in the BPC are required only for electron energies below 18 GeV. Above 18 GeV the background contribution is found negligible. The background from  $\gamma p$  events after the entire selection is estimated with PYTHIA (cf. section 2.2.5). Less than 0.5% of all selected photon candidates (cf. section 4.4) can be accounted for by misidentified  $\gamma p$  events, most of which contribute at non photon-like clusters in the shower shape analysis (cf. chapter 5).

Moreover, dead cells in the SpaCal and cells with poor trigger efficiency are excluded from the analysis. The calibration of the electron energy is discussed in section 4.7.1.



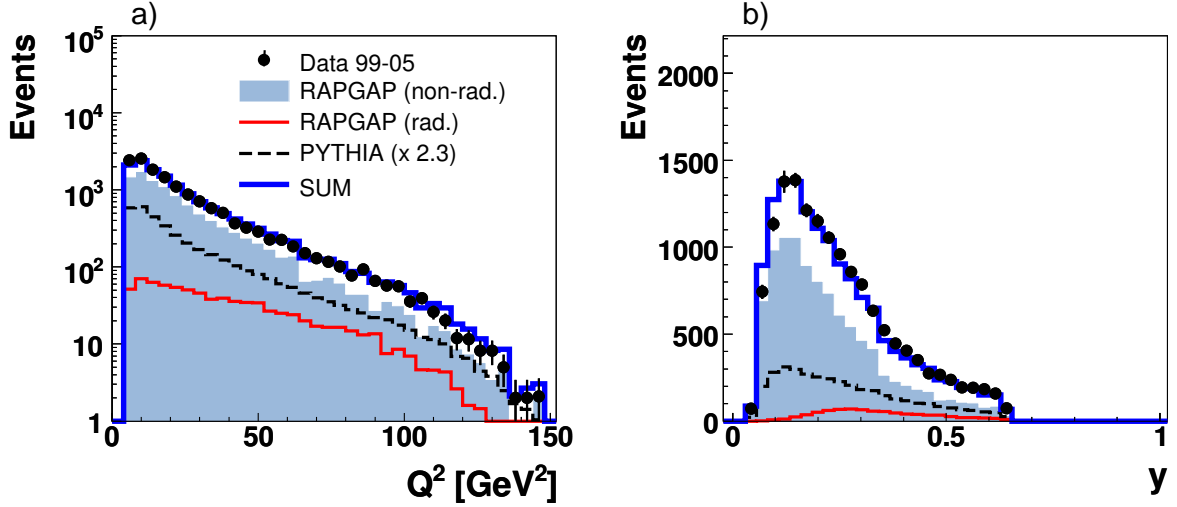


FIGURE 4.4: Distributions of (a)  $Q^2$  and (b)  $y$  for isolated photon candidates after the entire selection described in this chapter. Data are shown as points with error bars. The bold solid histogram shows the sum of the expectation from RAPGAP (non-rad.) for neutral hadron background (shaded), from PYTHIA for radiation from the quark scaled by a factor 2.3 (dashed line) and from RAPGAP (rad.) for radiation from the electron (solid line). The unshaded area corresponds to the expected isolated photon contribution.

### 4.3.2 Kinematic Selection

In DIS events the event kinematics is preferably reconstructed from the scattered electron:

$$Q^2 = 2E_e E'_e (1 + \cos \theta^e), \quad y = 1 - \frac{E'_e}{2E_e} (1 - \cos \theta^e). \quad (4.9)$$

Compared to the so-called *hadron method*, this method is largely unaffected by calorimeter noise or energy losses in inactive detector material [80]. However, at small  $y$  the  $x$  resolution degrades and radiative corrections become large. Therefore a phasespace cut of

$$y > 0.05 \quad (4.10)$$

is applied. The covered range of the four-momentum transfer squared is motivated by the angular SpaCal acceptance:

$$4 < Q^2 < 150 \text{ GeV}^2. \quad (4.11)$$

The distributions of  $Q^2$  and  $y$  reconstructed with the electron method as defined in equation (4.9) are shown in figure 4.4.

In addition, at least one *good track*<sup>5</sup> in the CJC is required with a polar angle  $30^\circ < \theta < 150^\circ$  not associated to the electron.<sup>6</sup> This requirement assures a good trigger efficiency of the sub-

<sup>5</sup>The criteria applied in the selection of good tracks are listed in table D.1.

<sup>6</sup>The track requirement has been added a further  $P_T$  threshold to cross-check for systematic effects. No significant effect on the measured cross sections was found.

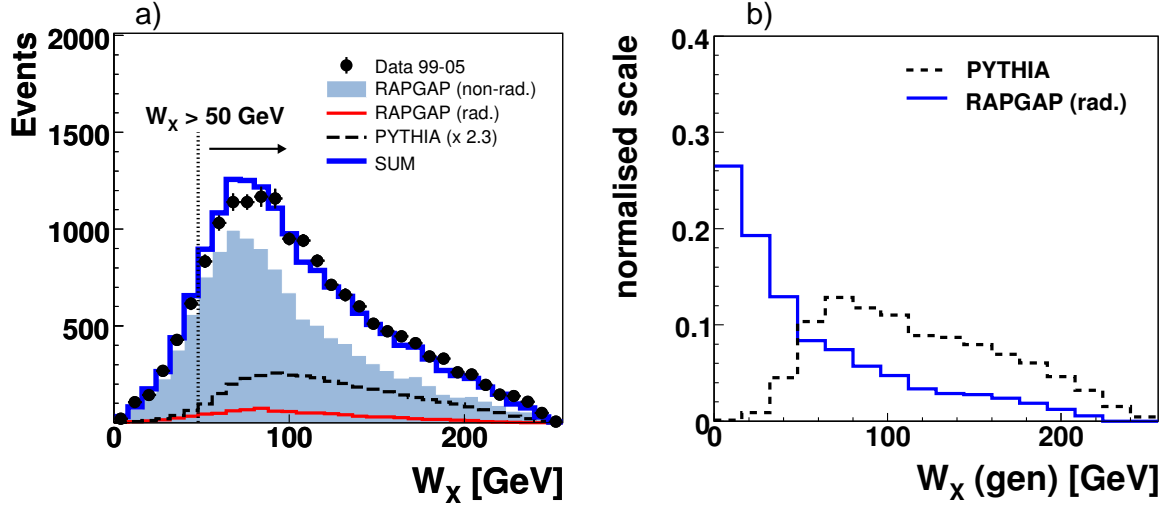


FIGURE 4.5: The mass of the hadronic system  $W_X$ . a) Shown after the entire selection as described in this chapter apart from the cut on  $W_X$ . The data are compared to the MC predictions, as described in the figure 4.4 caption. b) Shown as generated for PYTHIA and RAPGAP (rad.) after all cuts on generator level according to the phase space definition (see table 7.2), apart from the cut on  $W_X$ .

trigger s61 and further rejects contributions from elastic Compton scattering ( $p+e \rightarrow p+e+\gamma$ ) as well as non- $ep$  background.

In addition the invariant mass of the final state hadronic system  $X$  without the final state photon is required to be

$$W_X > 50 \text{ GeV}. \quad (4.12)$$

According to equation 1.24 the mass of the hadronic system is calculated from the beam energies, the reconstructed scattered electron and the reconstructed final state photon (see section 4.4).

The distribution of  $W_X$  is shown in figure 4.5 a). After the entire selection described in this chapter the constraint on  $W_X$  rejects only a minor fraction of the photon signal and mainly affects the neutral hadron background. However, a large fraction of photons radiated by the electron contributes at low masses of the generated hadronic system as can be seen in figure 4.5 b). Such events correlate strongly with low track multiplicities in the reconstructed event and typically do not pass the track requirement, which can be understood from figure 4.6. Particularly visible in RAPGAP (rad.), events with generated hadronic masses below 50 GeV mostly do not provide a central track in the reconstructed event. Hence, the requirement of a minimum mass of the hadronic system allows the mapping of the track requirement to the phase space definition and also allows for an efficient rejection of elastic contributions in both the phase space definition and the reconstructed events.

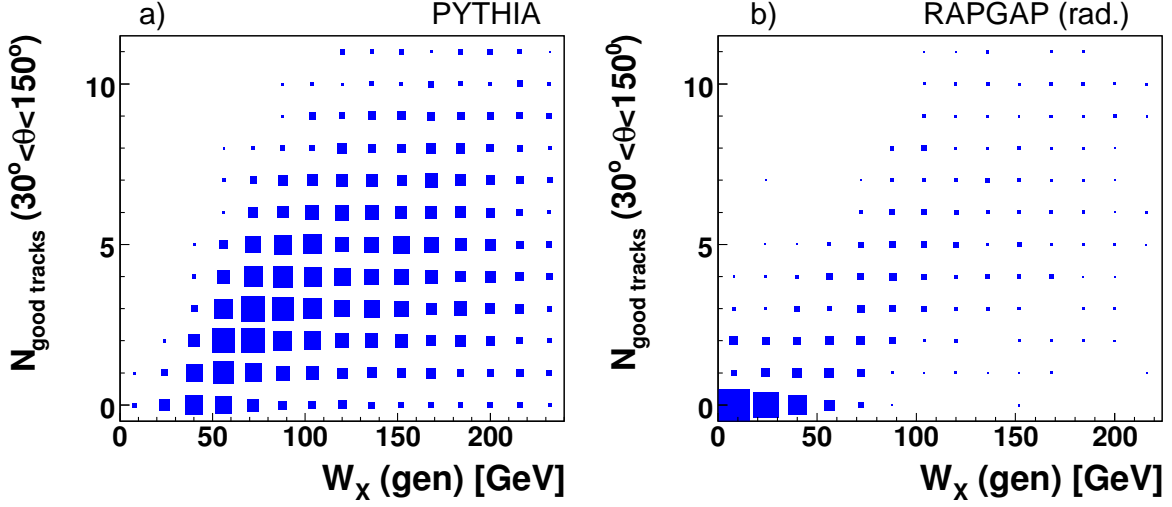


FIGURE 4.6: The mass of the generated hadronic system  $W_X(\text{gen})$  after all cuts on generator level (see table 7.2), apart from the cut on  $W_X$ , against the number of reconstructed central good tracks in the polar angle range  $30^\circ < \theta < 150^\circ$  on detector level for (a) PYTHIA and (b) RAPGAP (rad.).

### 4.3.3 Hadronic Final State

The hadronic final state (HFS) is reconstructed from energy deposits in the LAr and the SpaCal calorimeters combined with tracking information of the Central Tracker. Tracks and clusters are merged to so-called *combined objects*, which form the particles of the reconstructed HFS [81, 82]. The scattered electron is by definition not included in the HFS.<sup>7</sup> For the HFS it is convenient to introduce the quantity  $\Sigma^{\text{had}}$ , the transverse momentum  $P_T^{\text{had}}$  and the inclusive hadronic angle  $\theta^{\text{had}}$  defined by

$$\Sigma^{\text{had}} = \sum_i (E_i - p_{z,i}), \quad P_T^{\text{had}} = \sqrt{(\sum_i p_{x,i})^2 + (\sum_i p_{y,i})^2}, \quad \tan \frac{\theta^{\text{had}}}{2} = \frac{\Sigma^{\text{had}}}{P_T^{\text{had}}} \quad (4.13)$$

Here  $E_i$ ,  $p_{x,i}$ ,  $p_{y,i}$  and  $p_{z,i}$  are the respective four-momentum components of particle  $i$ . The summation includes all HFS particles.

### 4.3.4 Rejection of $\gamma p$ Events

Photoproduction ( $\gamma p$ ) events are further rejected by the requirement that the difference between the total energy and the longitudinal momentum summed over all final state particles including the scattered electron  $\Sigma^{\text{tot}} = \Sigma^{\text{had}} + E'_e - p'_{z,e}$  be in the range

$$35 < \Sigma^{\text{tot}} < 70 \text{ GeV}. \quad (4.14)$$

<sup>7</sup>The final state photon is usually included in the general HFS. Throughout the present analysis the hadronic system  $X$  is defined not to include the photon.

$\Sigma^{tot}$  is a conserved quantity and can be calculated from the initial state. If no particles are lost in the backward region it is twice the electron beam energy ( $\Sigma^{tot} \approx 2E_e \approx 55$  GeV) apart from uncertainties of the energy and momentum measurement.

## 4.4 Selection of Photon Candidates

As discussed in appendix A, a thorough separation of photons from neutral hadrons is not possible in a cut based selection due to the non-separable fraction of the background. Although the selection described in this section aims at isolated photons, the selected candidates are still dominated by neutral hadrons because of their high production rates in the fragmentation of coloured partons. The reconstructed photon-like particles will therefore be referred to as photon candidates. The content of isolated photons is evaluated in a second step by means of a shower shape analysis described in chapter 5.

Photon candidates are identified as clusters in the electromagnetic section of the LAr calorimeter with energies

$$3 < E_T^\gamma < 10 \text{ GeV} \quad (4.15)$$

and a pseudorapidity in the range

$$-1.2 < \eta^\gamma < 1.8, \quad (4.16)$$

which corresponds to the five wheels of the Central and Forward Barrel in the LAr calorimeter (see figure 3.7). Clusters close to the cracks of the calorimeter suffer from distorted shower shapes and mismeasured energies. Therefore, clusters are rejected if more than 95 % of their energy is deposited in cells adjacent to cracks. The most energetic cell of a cluster (*hottest cell*) is furthermore required to be in the wheel that contains most of the cluster's energy. A cluster is therefore unambiguously assigned to one of the five wheels in the LAr calorimeter.

Background from hadronic showers, predominantly induced by charged pions, is largely rejected by a cut on the energy fraction in the first two layers of the electromagnetic section of the LAr calorimeter. The energy fraction is shown in figure 4.7 for charged pions and photons. The cut depends on the polar angle of the cluster and is indicated by the line in figure 4.7 a). The background of charged particles is further reduced by the requirement that no track<sup>8</sup> is allowed to geometrically match the electromagnetic cluster with a DCA to the cluster's barycentre of less than 20 cm. A detailed MC study showed that under the assumption of isospin symmetry,  $N_{produced}(\pi^\pm) \approx N_{produced}(\pi^0)$ , the charged pions account for less than 0.3 % of the photon candidates after passing all selection criteria.

Neutral hadrons that decay into multiple photons constitute the main background. Since in most cases such decay photons are merged into one electromagnetic cluster that tends to have

<sup>8</sup>Vertex-fitted and non-vertex-fitted CJC track hypotheses are considered for the track veto. The track information can be complemented by tracking information of the Forward Tracker.

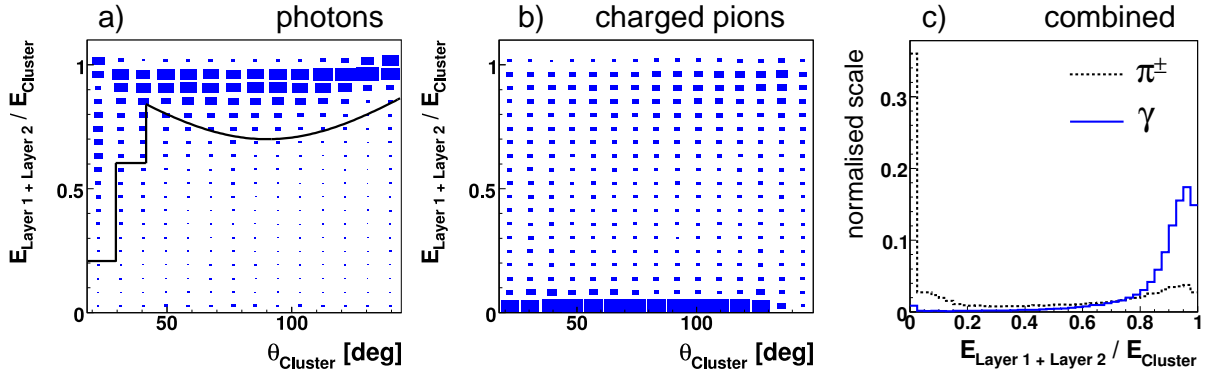


FIGURE 4.7: Energy fraction of the candidate cluster in the first two layers of the LAr calorimeter. a) and b) show the energy fraction versus the polar angle of the cluster for the single photon and single charged pion simulation without any selection applied. c) shows the projections along the polar angle. The line in a) indicates the polar angle dependent threshold below which clusters are considered as hadronic showers.

a wider transverse extent than that of a single photon, a cut is applied on the transverse radius<sup>9</sup> of the photon candidate cluster of

$$R_T < 6 \text{ cm.} \quad (4.17)$$

The cut is illustrated in figure 4.8 a). The  $R_T$  distribution is well described throughout the entire range and according to the signal and background simulations almost only contributions from neutral hadrons are rejected by this requirement. Figure 4.8 b) shows the normalised  $R_T$  distribution for the PYTHIA and RAPGAP (non-rad.) MC simulations for photons and neutral hadrons in comparison with the SP photons and SP neutral hadrons. The SP photons resemble well the PYTHIA distribution. The SP neutral hadrons underestimate the RAPGAP (non-rad.) prediction at large  $R_T > 6$  cm, which was found to be consistent with the occurrence of overlaps between clusters from distinct incident particles. Such an overlap is not included in the SP description of the neutral hadrons. The restriction to lower  $R_T$  eliminates most of such overlap effects, which are discussed in more in detail in section 5.3.1. The overshoot of SP neutral hadrons at lower  $R_T$  is due to the normalisation of the histogram and the undershoot at higher  $R_T$ .

Furthermore, the invariant mass  $M_{\gamma\gamma}$  of the cluster, when combined with the closest neighbouring electromagnetic cluster having an energy above 80 MeV, is constrained by

$$M_{\gamma\gamma} > 0.3 \text{ GeV.} \quad (4.18)$$

This requirement rejects candidates that originate from  $\pi^0$  decays with two photons reconstructed in separate clusters and is motivated in appendix A. The invariant mass is well described by the MC simulation as can be seen in figure 4.9. If all selected photon candidates are taken into account (figure 4.9 a)), no clear contribution from the  $\pi^0$  decay is visible. When

<sup>9</sup>For a definition of the transverse radius  $R_T$  see section 5.1.1.

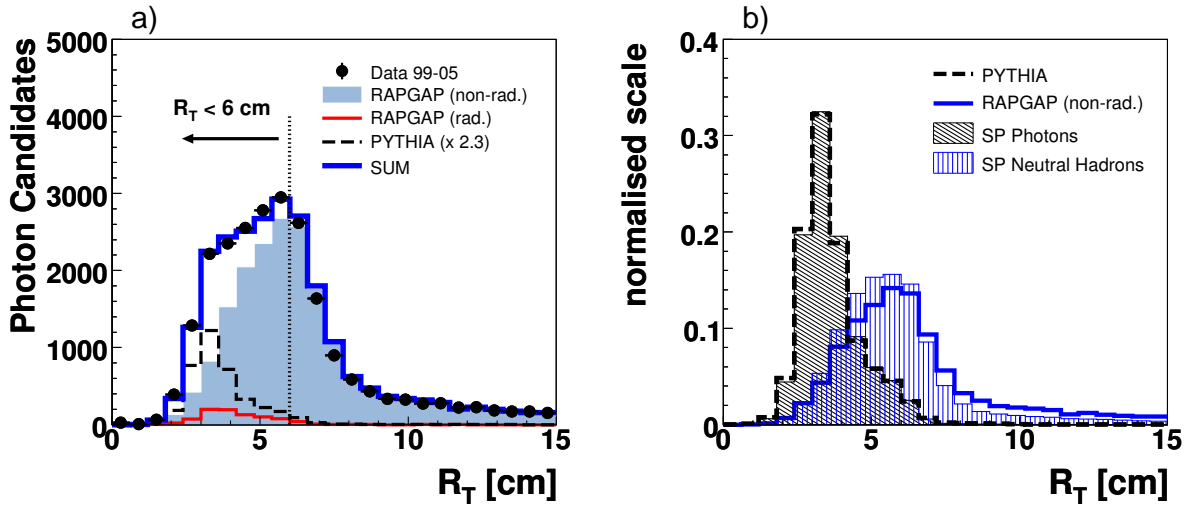


FIGURE 4.8: Distributions of the transverse cluster radius  $R_T$ . a) Isolated photon candidates in DIS events are shown after the entire selection as described in this chapter apart from the cut on the transverse radius. The data are compared to the MC predictions, as described in the figure 4.4 caption. b) The normalised distribution is shown for the full event MCs PYTHIA and RAPGAP (non-rad.) compared to the respective SP predictions.

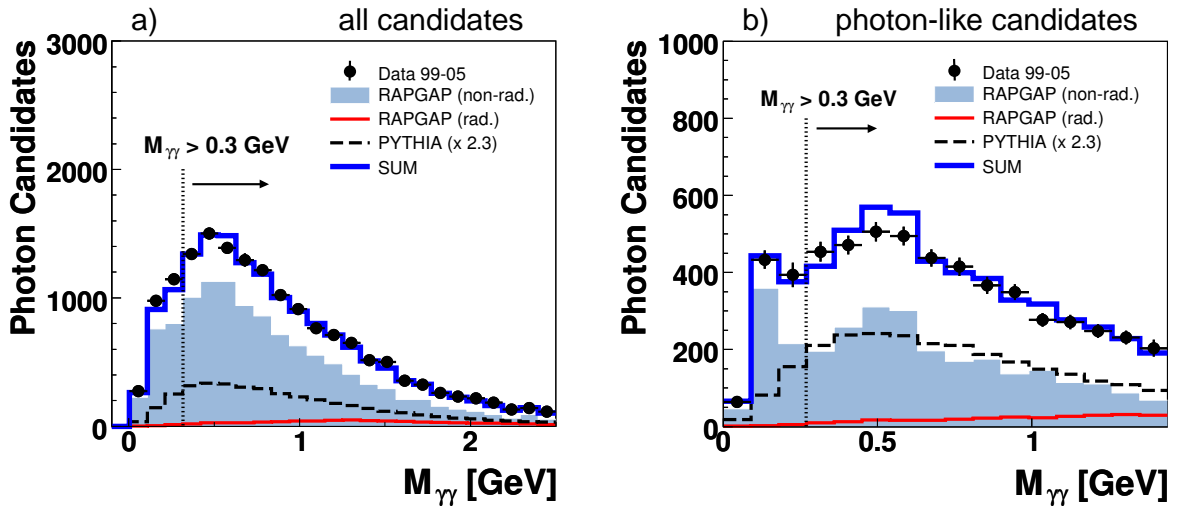


FIGURE 4.9: The invariant mass  $M_{\gamma\gamma}$  of the photon candidate cluster combined with the closest neighbouring electromagnetic cluster having an energy above 80 MeV. The data are compared to the MC predictions as described in the figure 4.4 caption. a) All photon candidates after the entire selection described in this chapter. b) Photon-like candidates according to the shower shape analysis (see text).

selecting explicitly photon-like clusters<sup>10</sup> (figure 4.9 b)), clear signals in the  $M_{\gamma\gamma}$  distribution are observed at roughly 150 MeV and 550 MeV corresponding to the masses of the  $\pi^0$  and  $\eta$  meson, respectively. Hence, mostly such clusters originating from  $\pi^0$  decays are discarded which classify as photon-like in the shower shape analysis (cf. chapter 5).

Only events with exactly one photon candidate passing all above requirements are accepted.

## 4.5 Jet Algorithm and Isolation Requirement

Perfect correlation between the initial partons carrying colour and the emerging colour neutral hadrons, which are finally observed in the detector, cannot be established. Jet algorithms, however, group final state particles into jets, which can be compared to the partonic configuration. Any jet algorithm should reduce the effect of hadronisation and be infrared safe. The replacement of two collinear particles with one particle of the same momentum as the sum of the two particles should not affect the outcome of the algorithm.

Following the democratic procedure introduced in section 1.3, the photon candidate along with the other particles of the HFS is combined into jets using the  $k_T$  algorithm [83] in the HERA laboratory frame. The algorithm combines particles into jets until all particles are merged. Consequently any particle is unambiguously assigned to a jet at the end of the algorithm, while in a cone-algorithm (e.g. [84]) particles can belong to more than one overlapping jet and might need special treatment. The iterative procedure of the algorithm is as follows:

1. Calculate  $d_i$  for each particle and  $d_{ij}$  for each pair of particles with

$$d_i = P_{T,i}^2 \quad d_{ij} = \min(d_i, d_j) \cdot \Delta R_{ij}^2 / R_0^2,$$

where  $R_{ij}^2 = (\Delta\eta_{ij})^2 + (\Delta\phi_{ij})^2$  is the distance of the two particles in the  $\eta\phi$ -plane squared and  $R_0$  is the resolution parameter of order 1.

2. Find the smallest  $d_i$  and  $d_{ij}$ . If  $d_i^{min} < d_{ij}^{min}$ , then particle  $i$  is identified as a jet and removed from the clustering algorithm. If  $d_i^{min} > d_{ij}^{min}$ , particles  $i$  and  $j$  are merged into a new fictive particle.
3. Continue from start as long as particles are left to be associated to jets.

The resolution parameter<sup>11</sup> is set to  $R_0 = 1$  as suggested in [85] and the merging of particles is done in a  $P_T$ -weighted recombination scheme:

$$P_{T,ij} = P_{T,i} + P_{T,j}, \quad \eta_{ij} = \frac{P_{T,i}\eta_i + P_{T,j}\eta_j}{P_{T,ij}}, \quad \phi_{ij} = \frac{P_{T,i}\phi_i + P_{T,j}\phi_j}{P_{T,ij}}. \quad (4.19)$$

<sup>10</sup>Here photon-like clusters are selected with discriminator values of  $D > 0.5$ . The discriminator is the result of a shower shape analysis and described in chapter 5. Photon-like clusters typically have values close to  $D \rightarrow 1$ , while background accumulates at  $D \rightarrow 0$ .

<sup>11</sup>For studies of photons in the vicinity of jets the resolution parameter has been varied in the range  $0.1 < R_0 < 2$ . The results are shown in section 7.4.

A schematic representation of the iterative steps of the algorithm is shown in figure 4.10. The final jets are massless and ordered in  $P_T$ . Jets are accepted with a transverse momentum  $P_T^{jet} > 2.5$  GeV and a pseudorapidity in the range  $-2.0 < \eta^{jet} < 2.1$ . Due to the harder kinematic cuts for the photon candidate there is always a jet containing the photon candidate, called the *photon-jet*. All remaining jets classify as hadronic jets. For hadronic jets the  $\eta^{jet}$  range is restricted to  $-1.0 < \eta^{jet} < 2.1$ . The transverse momentum and polar angle of the hadronic jet with the highest transverse momentum are shown in figure 4.11.

To ensure isolation of the photon the fraction  $z$  of the transverse energy of the photon-jet carried by the photon candidate is required to be

$$z = \frac{E_T^{\text{photon candidate}}}{E_T^{\text{photon-jet}}} > 0.9. \quad (4.20)$$

This definition of the isolation is stable against infrared divergences and thus well-suited for comparisons with perturbative QCD calculations. The cut is illustrated in figure 4.12.

The jet algorithm is applied to all reconstructed particles except for the scattered electron. However, the measurements and the parton level predictions are best compared on hadron level and therefore need corresponding corrections. In the MC simulations the jet algorithm is hence also applied to the particles of the parton and hadron level, which allows for the extraction of the desired correction factors. The hadronic jets are found to be well correlated to the partonic jets even at low transverse momenta as shown in figure 4.13.

Events with either no hadronic jet or at least one hadronic jet are called *photon plus no-jets* and *photon plus jet*, respectively.

## 4.6 Selection Summary

Table 4.4 shows a summary of all cuts applied during the entire selection. Since there is no requirement for additional jets apart from the photon-jet, the constraints on the hadronic jets do not affect the inclusive measurement of isolated photons. They only affect the observed jet multiplicities and therefore the exclusive photon plus no-jets and photon plus jet measurements.

The overall selection efficiency for isolated photons in DIS, given as the fraction of events generated in the selected kinematic region passing all cuts on detector level, is 38 % as predicted by PYTHIA<sup>12</sup>. According to PYTHIA the DIS selection accounts for a loss of roughly 28 % and the photon candidate selection for a loss of roughly 31 % of the events. In the DIS selection most events are lost, because the electron misses the acceptance range of the SpaCal. The isolation requirement rejects approximately 3 % of the events. Less than 1 % of the events are rejected because more than one photon candidate is found. In total 14670 DIS events

<sup>12</sup>In section 6.1.1 detailed information on the selection efficiencies and acceptances can be found.



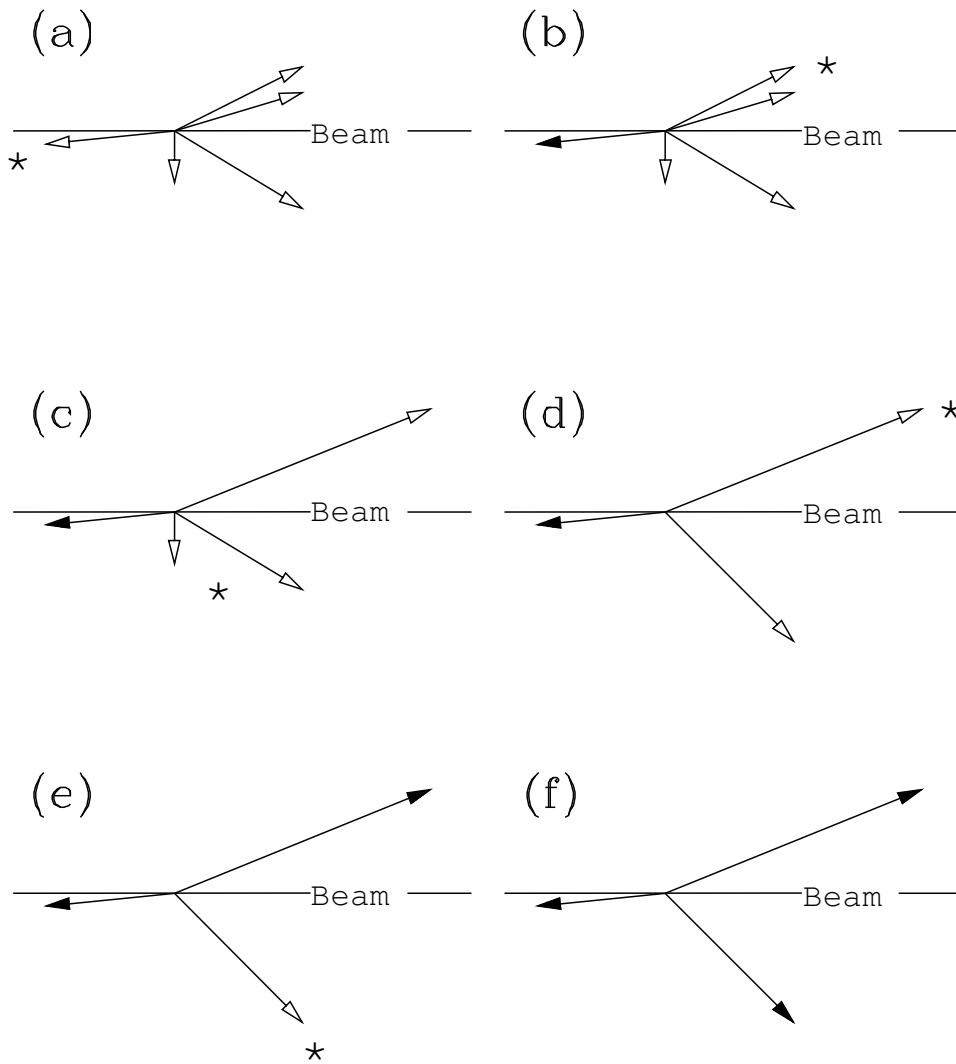


FIGURE 4.10: Schematic representation of the  $k_T$  algorithm. Open arrows represent the objects still to be associated to jets, and the solid arrows represent the final jets. The six diagrams show successive iterations of the algorithm. The asterisk marks the object(s) corresponding to the minimum distance  $d_i$  or  $d_{ij}$  for each step. Figure taken from [84].

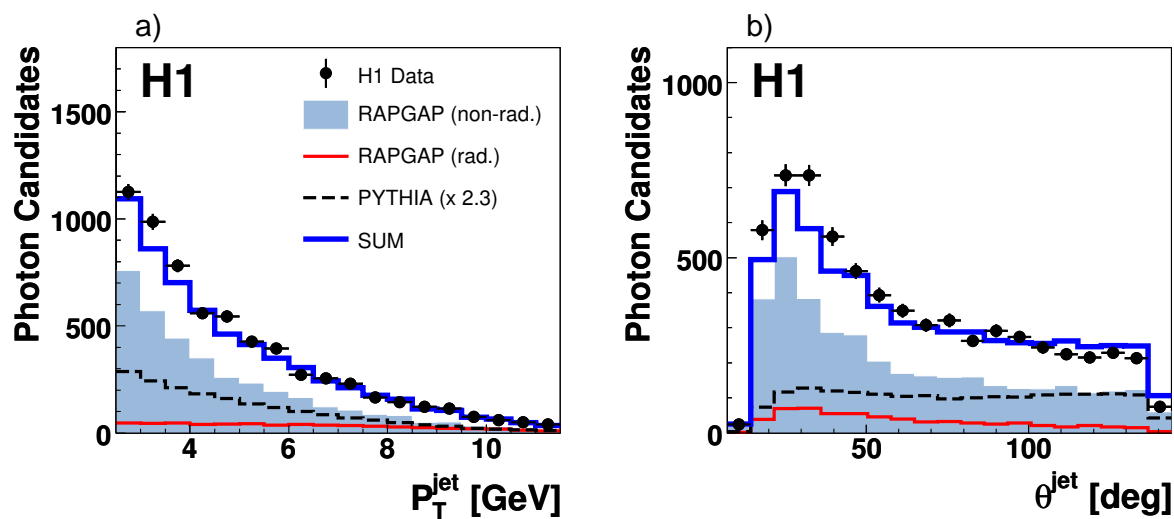


FIGURE 4.11: Distributions of (a) the transverse momentum and (b) the polar angle of the hadronic jet with the highest transverse momentum in events with an isolated photon candidate. The data are compared to the MC predictions, as described in the figure 4.4 caption.

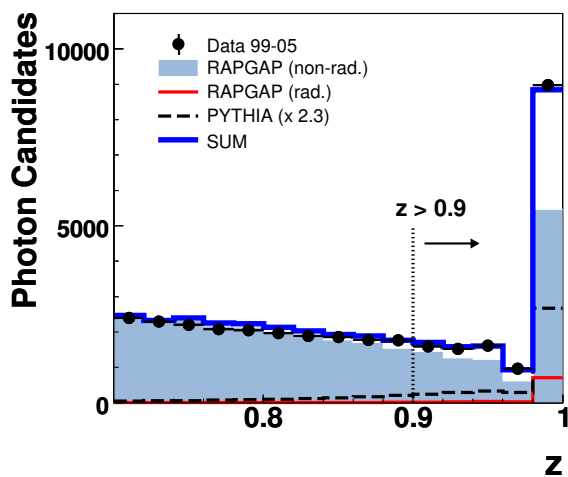


FIGURE 4.12: Distribution of the fraction  $z$  of the transverse energy of the photon-jet carried by the photon candidate in DIS events after the entire selection as described in this chapter apart from the cut on  $z$ . The data are compared to the MC predictions, as described in the figure 4.4 caption.

TABLE 4.4: Summary of selection requirements. The constraints on the hadronic jets do not affect the inclusive selection of events, only the jet multiplicity is affected.

<b>Preselection</b>
H1 Run quality, HV on, $ z_{vtx}  < 40$ cm, CJC timing
<b>Triggers</b>
subtriggers: s0,s1,s3,s4,s9,s61 (in HERA I) subtriggers: s0,s3,s9,s61 (in HERA II)
<b>DIS Selection</b>
electromagnetic cluster in the SpaCal $35 < \Sigma^{tot} < 70$ GeV electron kinematics: $E'_e > 10$ GeV, $\theta^e < 177^\circ$ electron quality: $R_e < 4$ cm, $E_{e,had} < 0.5$ GeV, fiducial cuts electron linked to track in BDC/BPC (in HERA II only for $E'_e < 18$ GeV) phasespace: $4 < Q^2 < 150$ GeV <sup>2</sup> , $y > 0.05$ , $W_X > 50$ GeV good track in CJC with polar angle $30^\circ < \theta < 150^\circ$
<b>Photon Candidate Selection</b>
electromagnetic cluster in the LAr photon kinematics: $3 < E_T^\gamma < 10$ GeV, $-1.2 < \eta^\gamma < 1.8$ energy fraction in first two layers of LAr ( $\theta^\gamma$ dependent cut) reject clusters close to calorimeter cracks $DCA_{\text{Cluster-Track}} > 20$ cm $R_T < 6$ cm $M_{\gamma\gamma} > 0.3$ GeV
<b>Photon Candidate Isolation</b>
$z = E_T^{\text{photon candidate}} / E_T^{\text{photon-jet}} > 0.9$
<b>Jet Requirements</b>
$P_T^{Jet} > 2.5$ GeV $-1.0 < \eta^{Jet} < 2.1$ (hadronic jets) $-2.0 < \eta^{Jet} < 2.1$ (photon-jet)

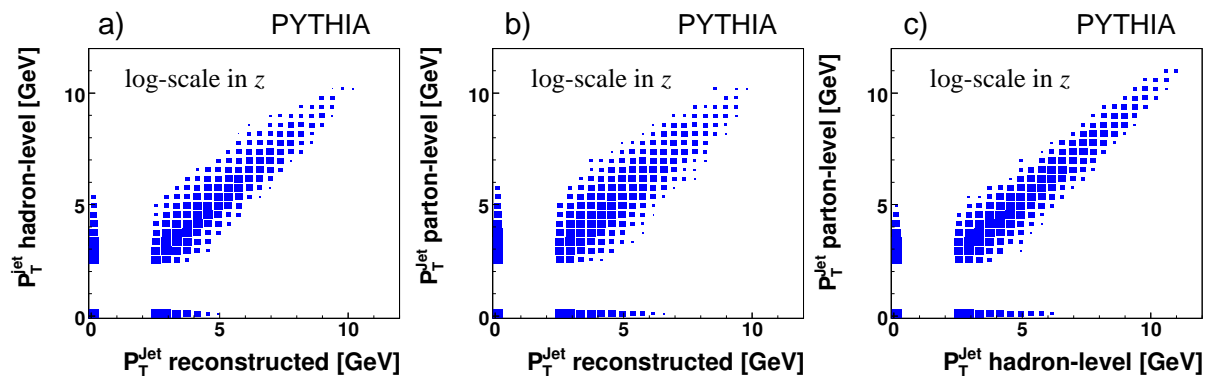


FIGURE 4.13: Correlations of the transverse momentum of the hadronic jet with the highest transverse momentum between different MC generation steps in PYTHIA: parton-level, hadron-level and reconstructed particles.

with an isolated photon candidate are selected, out of which 6495 have at least one additional hadronic jet.

Figure 4.14 and figure 4.15 show control distributions of variables relevant to the DIS selection and variables related to the selected photon candidates after the entire selection, respectively. The distributions still include a sizeable contribution from the decay of neutral hadrons. In chapter 5 the extraction of the isolated photon content from the selected photon candidates is discussed.

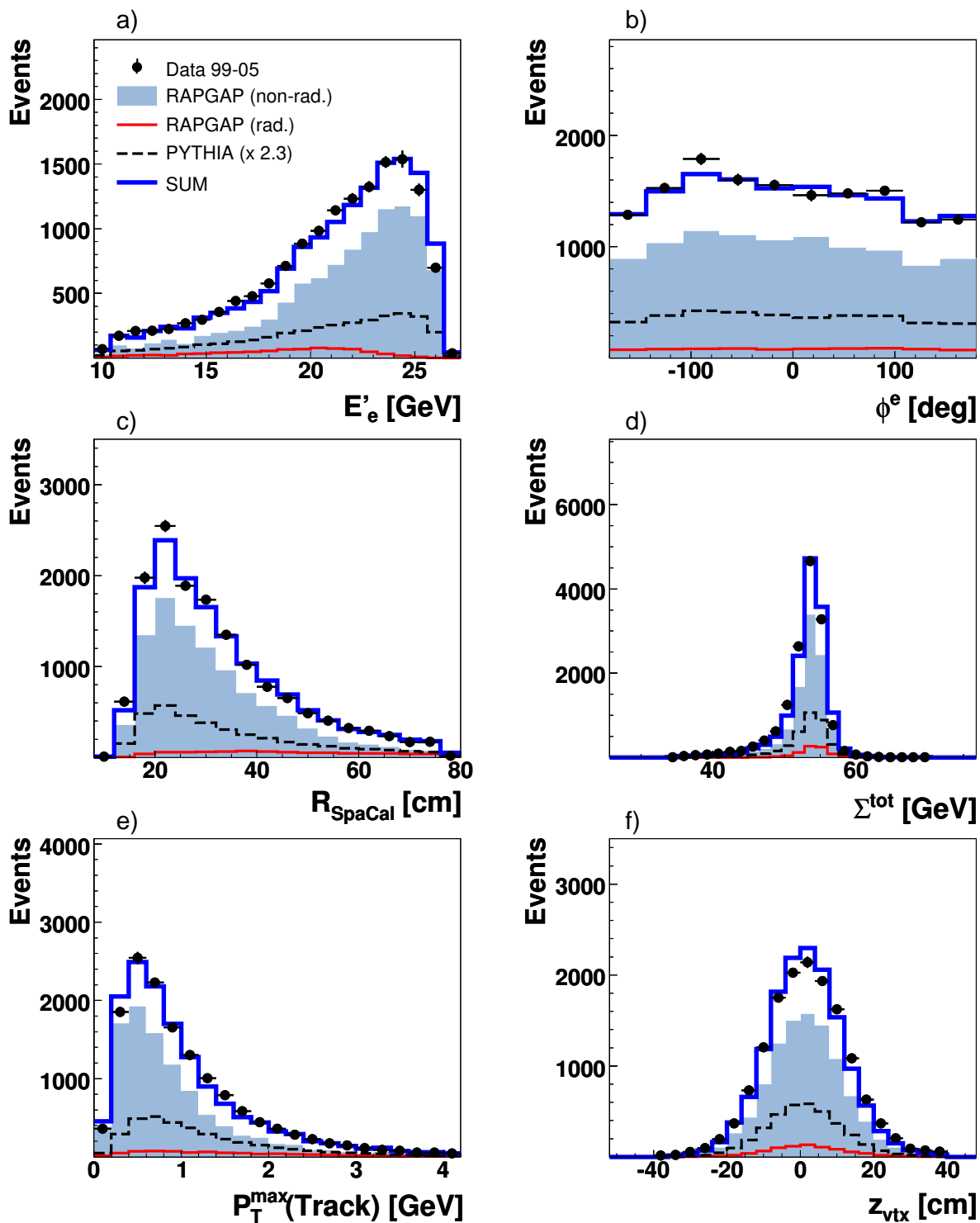


FIGURE 4.14: Distributions of variables relevant to the selection of DIS events after the entire selection described in this chapter: (a) energy of the scattered electron, (b) azimuthal angle of the electron, (c) distance of the scattered electron to the  $z$ -axis, (d) inclusive variable  $\Sigma^{tot}$ , (e) maximum transverse momentum observed in all good CJC tracks  $P_T^{max}(track)$  and (f) the  $z$ -position of the event vertex. The data are compared to the MC predictions as described in the figure 4.4 caption.

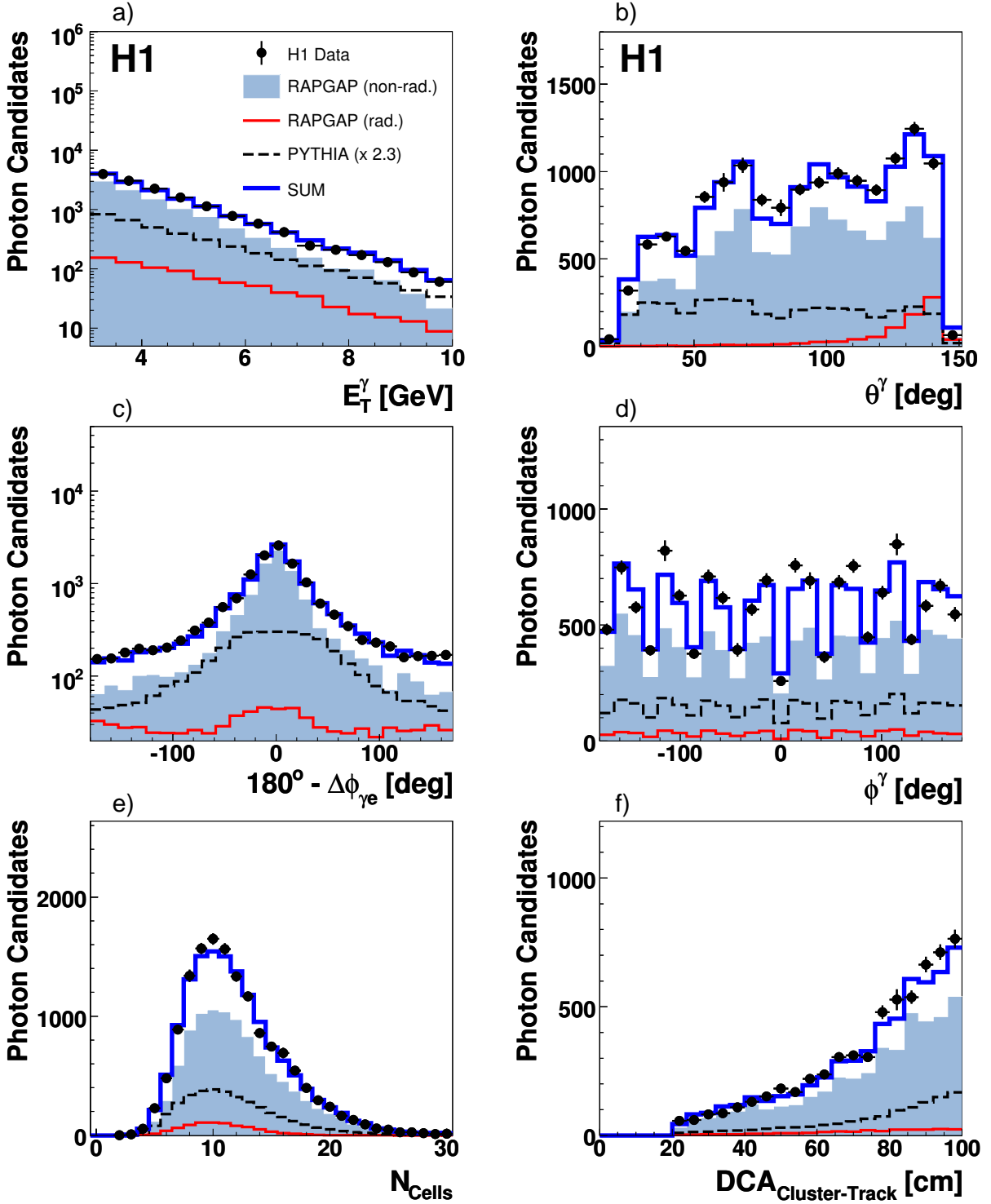


FIGURE 4.15: Distributions of variables related to the photon candidates after the entire selection described in this chapter: (a) transverse energy, (b) polar angle, (c) acoplanarity with the scattered electron, (d) azimuthal angle, (e) number of cells in the cluster and (f) the DCA to the closest vertex-fitted track. The data are compared to the MC predictions as described in the figure 4.4 caption.

## 4.7 Energy Calibration

In this section the energy calibration of the scattered electron as an electromagnetic cluster in the SpaCal and the energy calibration of the final state photon as an electromagnetic cluster in the LAr calorimeter are discussed.

### 4.7.1 Electron Energy Calibration

The kinematics in  $ep$  scattering experiments is overdetermined. The so-called *double angle* (DA) method [86] describes the kinematic variables in terms of the electron beam energy  $E_e$ , the polar angle of the scattered electron  $\theta^e$  and the inclusive hadronic angle  $\theta^{had}$ . The electron energy reconstructed with the DA method  $E_{DA}$  is given by

$$E_{DA} = \frac{2E_e \sin \theta^{had}}{\sin \theta^{had} + \sin \theta^e - \sin(\theta^{had} + \theta^e)} \quad (4.21)$$

and can be used as a reference energy for the calibration of the electron energy as originally proposed in [87]. The determination of  $E_{DA}$  is to first order independent of the energy measurements in the LAr and SpaCal. The DA method provides a good resolution for medium values of  $y$  ( $0.05 < y < 0.2$ ) [88].

During the reprocessing of the data a cell-wise DA calibration of the electron energy measurement in the SpaCal is performed. Usually only events are accepted for the calibration which are measured at medium hadronic angles  $15^\circ < \theta^{had} < 80^\circ$ . The lower limit suppresses energy losses in the forward region of the detector and the upper limit restricts  $y$  to maximum values of roughly 0.15.

In the present analysis the provided calibration is again checked with the DA method for the entire data set. First of all, the reliability of the DA estimation is investigated in the MC simulation. Figure 4.16 a) shows the relative deviation of the DA energy  $E_{DA}$  from the generated electron energy  $E'_{e,gen}$  in dependence of the inclusive hadronic angle as given by PYTHIA. At low  $\theta^{had}$ ,  $E_{DA}$  agrees well with  $E'_{e,gen}$ . With increasing  $\theta^{had}$ , however,  $E_{DA}$  overestimates  $E'_{e,gen}$  and the resolution degrades, which is clearly visible in figure 4.16 b). The figure shows the relative energy deviation for the angular ranges  $15^\circ < \theta^{had} < 80^\circ$  and  $\theta^{had} > 80^\circ$ .

For data events with  $15^\circ < \theta^{had} < 80^\circ$  passing a loose DIS and photon candidate selection<sup>13</sup>, the relative deviation of  $E_{DA}$  from the measured electron energy  $E'_e$  is shown in figure 4.17 a). A Gaussian fit yields a relative deviation of  $0.3 \pm 3.2\%$  between the energies proving a well calibrated electron energy. For events passing the full selection as described in this chapter, the mean inclusive hadronic angle is  $\theta^{had} = 127^\circ \pm 32^\circ$ . For such large hadronic angles a shift

<sup>13</sup>In the loose selection only weak requirements are applied on the selection of DIS events ( $E'_e > 8$  GeV,  $35 < \Sigma^{tot} < 70$  GeV,  $Q^2 > 3$  GeV<sup>2</sup>) along with a loose photon candidate selection neglecting the cuts on the transverse radius of the cluster and on the isolation from tracks. The minimum transverse energy of a photon candidate cluster is reduced to  $E_T = 2.2$  GeV. The standard photon candidate selection is described in section 4.4.

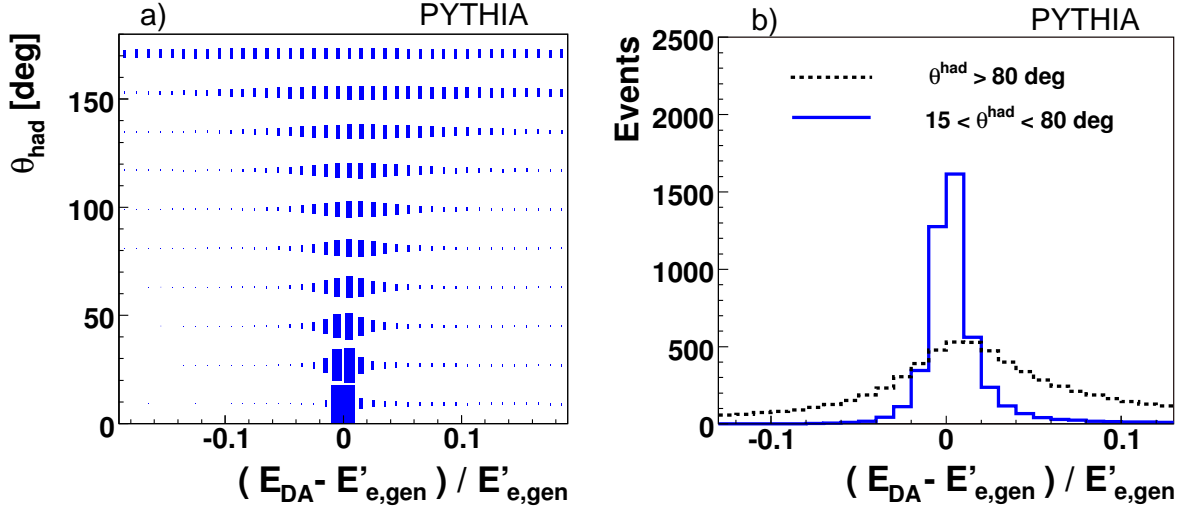


FIGURE 4.16: Relative deviation of the DA energy  $E_{\text{DA}}$  from the generated electron energy  $E'_{e,\text{gen}}$  as given by PYTHIA. a) The deviation in dependence of the inclusive hadronic angle. b) The deviation for different ranges of the hadronic angle. A Gaussian fit yields a deviation of  $0.2 \pm 1.0\%$  for  $15^\circ < \theta^{\text{had}} < 80^\circ$  and  $1.2 \pm 3.7\%$  for  $\theta^{\text{had}} > 80^\circ$ .

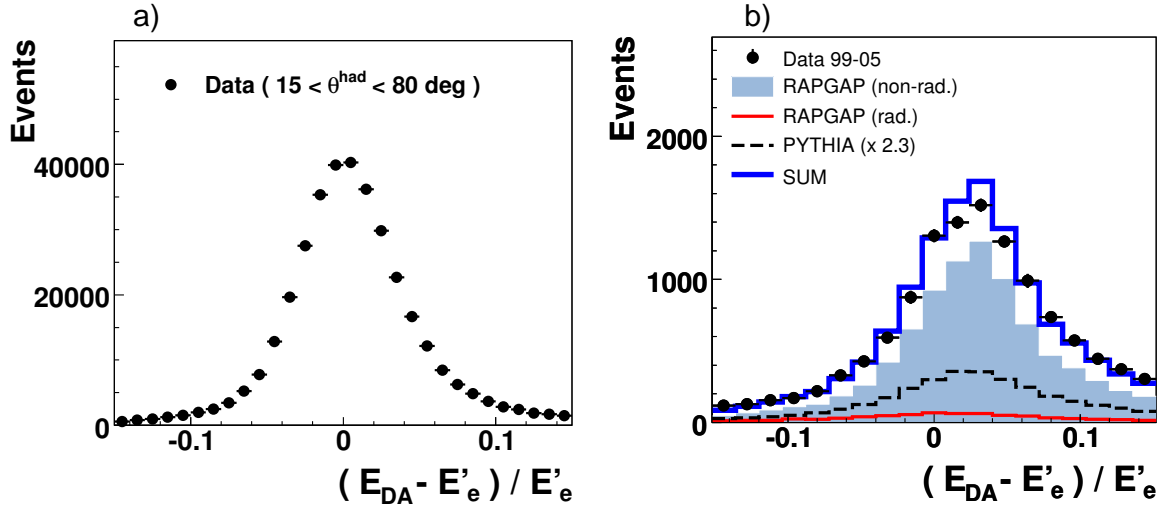


FIGURE 4.17: Relative deviation of the DA energy  $E_{\text{DA}}$  from the energy of the scattered electron  $E'_e$ . a) Data events with  $15^\circ < \theta^{\text{had}} < 80^\circ$  passing a loose DIS selection and photon candidate selection. b) Data events passing the entire DIS and photon candidate selection described in this chapter together with the MC predictions. Gaussian fits yield mean deviations of  $2.7 \pm 4.4\%$  and  $2.6 \pm 4.0\%$  for the data and the MC simulation, respectively.



between  $E_{DA}$  and  $E'_e$  is expected, which is effectively visible in figure 4.17 b). The shift and the resolution are well described by the calibrated MC simulations.

For the MC simulation, no cell-wise DA calibration is performed. By correlating the electron energy distribution<sup>14</sup>, the  $\Sigma^{tot}$  and the  $(E_{DA} - E'_e)/E'_e$  distributions between data and MC simulation, overall calibration constants for the simulation were derived: The electron energy is smeared by 2 % and shifted by 1.0 %, 3.0 %, 2.5 % for the years 1999/2000, 2004 and 2005, respectively. In data the cell-wise DA calibration has been checked and the electron energy is found to be well calibrated in the entire data set used in the present analysis.

### 4.7.2 Photon Energy Calibration

Originally, the LAr has been calibrated in test beam measurements [62]. In addition, a precise DA calibration of the electromagnetic energy measurement similar to the method described in section 4.7.1 has been performed using electrons in high  $Q^2$  neutral current events [89]. The extracted calibration factors depend on the running period and the polar and azimuthal angle of the deposited energy.

In the present analysis, the provided calibration has been reinspected using electrons in Bethe-Heitler (BH) events and photons in predominantly deeply virtual Compton scattering (DVCS) events (cf. appendix C), which provide sufficient statistics down to transverse energies of roughly  $E_T^{e,\gamma} \approx 2$  GeV. Photons in DVCS events can be compared to the DA energy expectation of the photon, which is given by  $E_{T,DA}^\gamma = E_{DA} \sin \theta^e$  with  $E_{DA}$  taken from equation (4.21). The comparison is shown in figure 4.18 a) and yields a mean deviation of below 0.5 %. Furthermore, the transverse energy of the electron cluster in BH events is compared to the transverse momentum of the track measurement, which is precisely measured at low energies (cf. section 3.2.2). The comparison is performed separately for different ranges of the transverse energy and for the five wheels of the LAr used in the present analysis. An agreement to better than 1 % was found in the first four wheels. In the FB2 the statistics of BH events is not sufficient to provide reliable estimates. The overall agreement of the energy measurement of electron track and cluster in BH events for cluster energies in the range  $2 < E_T < 10$  GeV is shown in figure 4.18 b). The mean deviation is  $-0.4$  %.

The same cross-check has been performed on simulated SP electron events. It was found that the simulated electromagnetic cluster needed an additional wheel-wise transverse energy dependent calibration of typically 1–2 %. The overall agreement of the energy measurement of electron track and cluster in the recalibrated SP electron events is shown in figure 4.18 c).

Figure 4.19 a) shows the effect of the calibration on isolated photons in the PYTHIA MC over the entire data sample. Differences between the transverse energies of the generated photon and the reconstructed photon are shown in dependence of the generated transverse photon energy. A good agreement to better than 1 % is observed for the calibrated photon

<sup>14</sup>In the electron energy distribution especially the kinematic peak of the distribution close to the electron beam energy is considered.

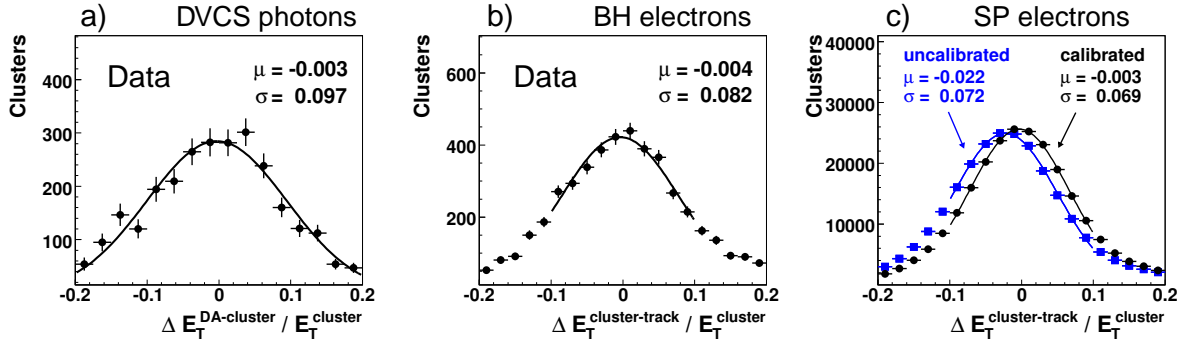


FIGURE 4.18: Cluster transverse energy compared to the DA transverse energy expectation for photons in DVCS events (a) and compared to the track measurement for electrons in (b) Bethe-Heitler events and (c) simulated SP events.

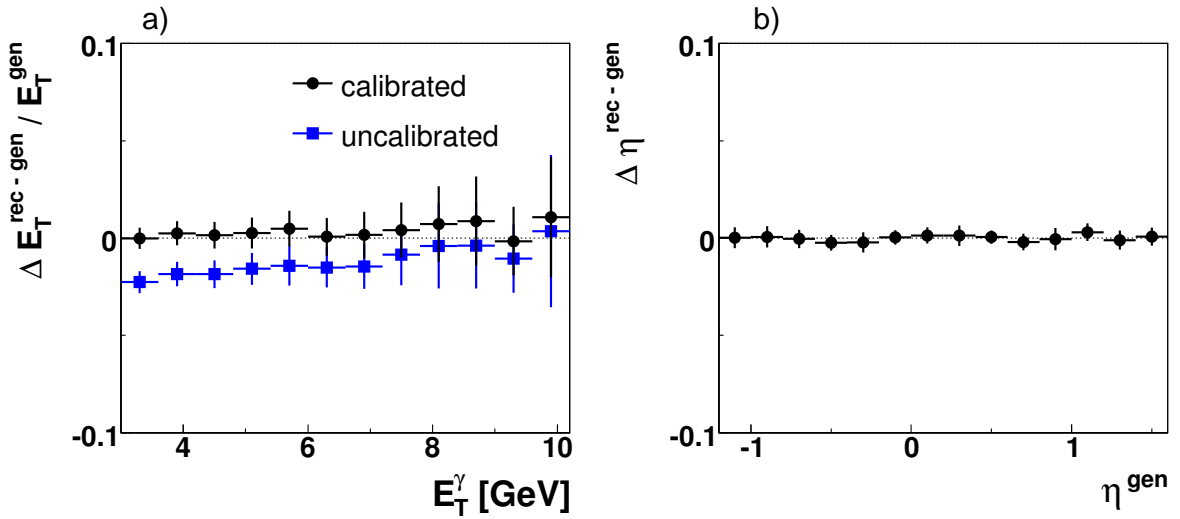


FIGURE 4.19: Mean value (calibrated values shown as solid points, uncalibrated as solid squares) and resolution (error bars) of the transverse energy (a) and pseudorapidity (b) of isolated photons in the PYTHIA MC in dependence of the generated transverse energy and the generated pseudorapidity of the photons, respectively.

clusters. The comparison of the transverse energies also involves a good measurement of the polar angle of the photon. The  $\eta$  resolution is shown in figure 4.19 b).

The systematic uncertainties on the energy measurement of electromagnetic clusters mainly depend on the available statistics of electrons in high  $Q^2$  neutral current events or BH events, respectively. Therefore the systematic error increases towards the forward direction of the calorimeter, where the statistics becomes sparse. In the studied range the photon energy is found to be well calibrated. However, due to the somewhat lower transverse energies of the photons compared to the otherwise considered electron clusters in high  $Q^2$  events (cf. [89]), slightly increased systematic errors are assumed. They are estimated as 1 % in CB1, 2 % in CB2 and CB3, 3 % in FB1 and 4 % in FB2.



## CHAPTER 5

# PHOTON SIGNAL EXTRACTION

---

The selected isolated photon candidates still contain background from neutral hadrons and their photonic decay products (cf. chapter 4). The decay photons are usually reconstructed in a single electromagnetic cluster similar to the detector response of a single incident photon.

The extraction of the photon signal exploits the fine granularity of the electromagnetic part of the LAr calorimeter. In order to discriminate between signal photons and the background from neutral hadrons and their decay products the calorimeter cluster corresponding to the isolated photon candidate is further analysed. Differences in the shower profile are quantified by means of six shower shape variables calculated from the measurements of the individual cells composing the cluster. The variables will be introduced in section 5.1 and combined in section 5.2 to form a classifier using multivariate classification methods, from which the pure single photon content is extracted by a least-squares fit in section 5.3.

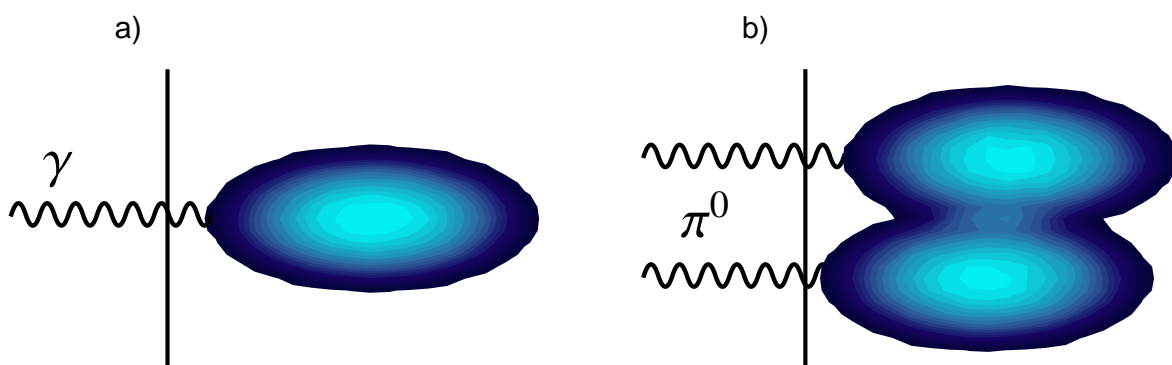


FIGURE 5.1: Schematic representation of the different shower profiles of clusters induced by (a) single photons or (b) multiple photons. The black line indicates the calorimeter surface.

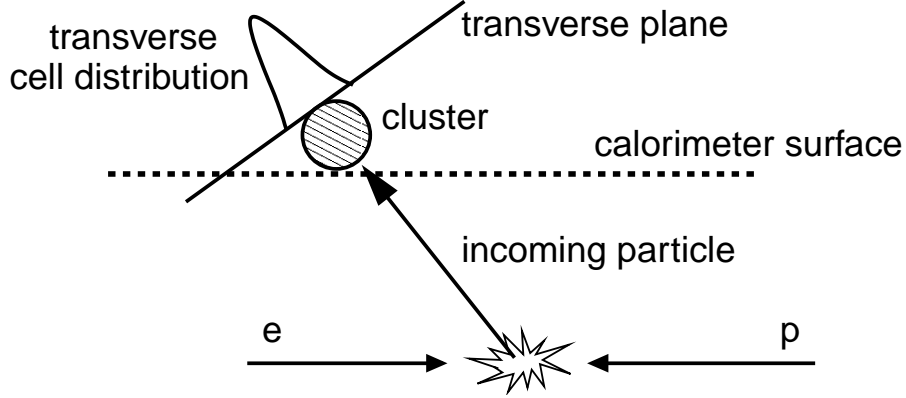


FIGURE 5.2: Illustration of the transverse plane in the context of shower shape variables. The transverse plane is defined as perpendicular to the direction of the incoming particle.

## 5.1 Shower Shape Variables

Figure 5.1 illustrates in a schematic representation the different shower profiles of clusters induced by single photons or multiple photons. Since the decay photons of neutral hadrons have a minimum opening angle (see appendix A), the multi-photon clusters are typically less compact, transversely wider and more asymmetric. For multiple photons the shower is likely to start closer to the calorimeter surface, as the probability of conversion increases with the number of incident photons. In the following, six shower shape variables are introduced describing these differences.

### 5.1.1 Variables

The first three shower shape variables quantify the transverse dimension of the clusters (transverse radius, kurtosis and symmetry), where in the context of the shower shape analysis the transverse plane is defined as perpendicular to the direction of the incoming particle as illustrated in figure 5.2. The remaining three variables describe the compactness (hot core fraction and hottest cell fraction) and the longitudinal shower profile (first layer fraction).

In the description of the transverse dimension of the cluster, higher central transverse moments of the cell distribution are employed, defined as

$$\mu_{T,k} = \langle |\vec{r}_T - \langle \vec{r}_T \rangle|^k \rangle, \quad (5.1)$$

where  $\vec{r}_T$  is the transverse projection of the cell vector and  $\langle \vec{r}_T \rangle = (\sum_i E_i \vec{r}_{T,i}) / \sum_i E_i$  is the energy weighted average of the transverse cell positions.

#### 1. Transverse Radius $R_T$

The transverse radius is defined as the square root of the second central transverse mo-

ment

$$R_T = \sqrt{\mu_{T,2}}. \quad (5.2)$$

Compact showers induced by single photons have small values of  $R_T$ .

## 2. Transverse Kurtosis $K_T$

The transverse kurtosis  $K_T$  is defined as the ratio of the fourth and squared second moment of the transverse energy distribution of cluster cells

$$K_T = \frac{\mu_{T,4}}{(\mu_{T,2})^2} - 3. \quad (5.3)$$

The kurtosis defines how strongly the energy distribution is peaked. It is zero for a Gaussian distribution. A distribution with a pronounced peak ( $K_T > 0$ ) is called leptokurtic, a flat-topped one ( $K_T < 0$ ) is called platykurtic [90, 91].

## 3. Transverse Symmetry $S_T$

The transverse symmetry  $S_T$  of a cluster is defined as the ratio of the spread (defined by root mean squared) of the transverse cell distributions along the two principal axes. The eigenvectors of the  $3 \times 3$  matrix

$$S_{kl} = \langle (r_{T,k} - \langle r_{T,k} \rangle) (r_{T,l} - \langle r_{T,l} \rangle) \rangle = \langle r_{T,k} r_{T,l} \rangle - \langle r_{T,k} \rangle \langle r_{T,l} \rangle, \quad (5.4)$$

where  $r_{T,1} = r_{T,x}$ ,  $r_{T,2} = r_{T,y}$  and  $r_{T,3} = r_{T,z}$  are the Cartesian coordinates of the transverse cell vector  $\vec{r}_T$ , constitute the principal axes of the transverse cell distribution. Since the transverse cell distribution is flat, one of the eigenvalues vanishes and the remaining eigenvalues  $\lambda_1$  and  $\lambda_2$  with  $\lambda_1 > \lambda_2$  yield the squared radii along the two meaningful principal axes. The symmetry is then calculated as

$$S_T = \sqrt{\lambda_2/\lambda_1}. \quad (5.5)$$

A photon cluster is expected to have a symmetric cluster, whereas multi-photon clusters are typically more asymmetric. Due to the finite granularity and the geometry of the calorimeter, clusters of few cells may approximate a line in the transverse projection. In such cases, the transverse symmetry is close to zero.

## 4. Hottest Cell Fraction

The hottest cell fraction (HCeF) is the energy fraction of the electromagnetic cluster contained in the cell with the largest energy deposit (*hottest cell*).

## 5. Hot Core Fraction

The hot core fraction (HCF) of the cluster energy is contained in four or eight (depending on the granularity of the calorimeter) contiguous cells in the first two calorimeter layers. The cells include the hottest cell and are chosen to maximise the energy which

they contain (*hot core*). Both, the hot core and hottest cell fraction, are sensitive to the compactness of the cluster in the calorimeter. They yield larger values for photons than for the background.

## 6. First Layer Fraction

The first layer fraction (FLF) is the fraction of the cluster energy detected in the first calorimeter layer (*layer 1*). The probability of conversion is proportional to the number of incident photons, hence the energy deposited in the first layer of the calorimeter is expected to be larger on average for multi-photon clusters than for those initiated by a single photon.

The six shower shape variables are shown for isolated photon candidates in figure 5.3. The measured distributions are compared with the sum of the background and scaled signal MC predictions. A good agreement is observed. In the measured data the shower shapes were found to be stable throughout the entire data taking relevant to the present analysis.

Figure 5.4 shows a comparison in the shower shape variables between the SP predictions for photons and neutral hadrons and the corresponding full event MCs, PYTHIA and RAPGAP (non-rad.). The SP events are reweighted so as to match the  $E_T^\gamma$  and  $\theta^\gamma$  distributions of the full event MCs. The SP distributions follow the shower shape description of the full event MCs. In Figure 5.4 e) a discrepancy at large radii between the two background predictions is observed. The difference between the full event MCs and the SP simulation due to possible overlaps of clusters is discussed in section 5.3.1. It should be noted that the SP events are passed through the same photon candidate selection (section 4.4 and 4.5) as the full event MCs including the isolation criteria based on the jet algorithm.

The discriminant power of signal and background becomes weaker at high transverse energies, where the multi-photon clusters become more similar to a single photon cluster. Therefore, events with  $E_T^\gamma > 10$  GeV are excluded from the measurement as presented in section 4.4.

### 5.1.2 Correlations

Six variables describing the shower shape of an electromagnetic cluster are likely to be correlated. Certain correlations between the shower shape variables may occur in either the signal or the background clusters or they may already be implied in the definition of the variables and hence occur in both signal and background clusters.

Figure 5.5 shows correlation plots of the variables for SP photons and SP neutral hadrons. Some clear correlations are visible, however no substantial correlation is observed which may indicate an apparent redundancy in the chosen set of variables.

The correlation coefficient  $\rho$  can furthermore give quantitative information on the significance of a linear correlation hypothesis. The covariance between the variables  $u$  and  $v$  is given



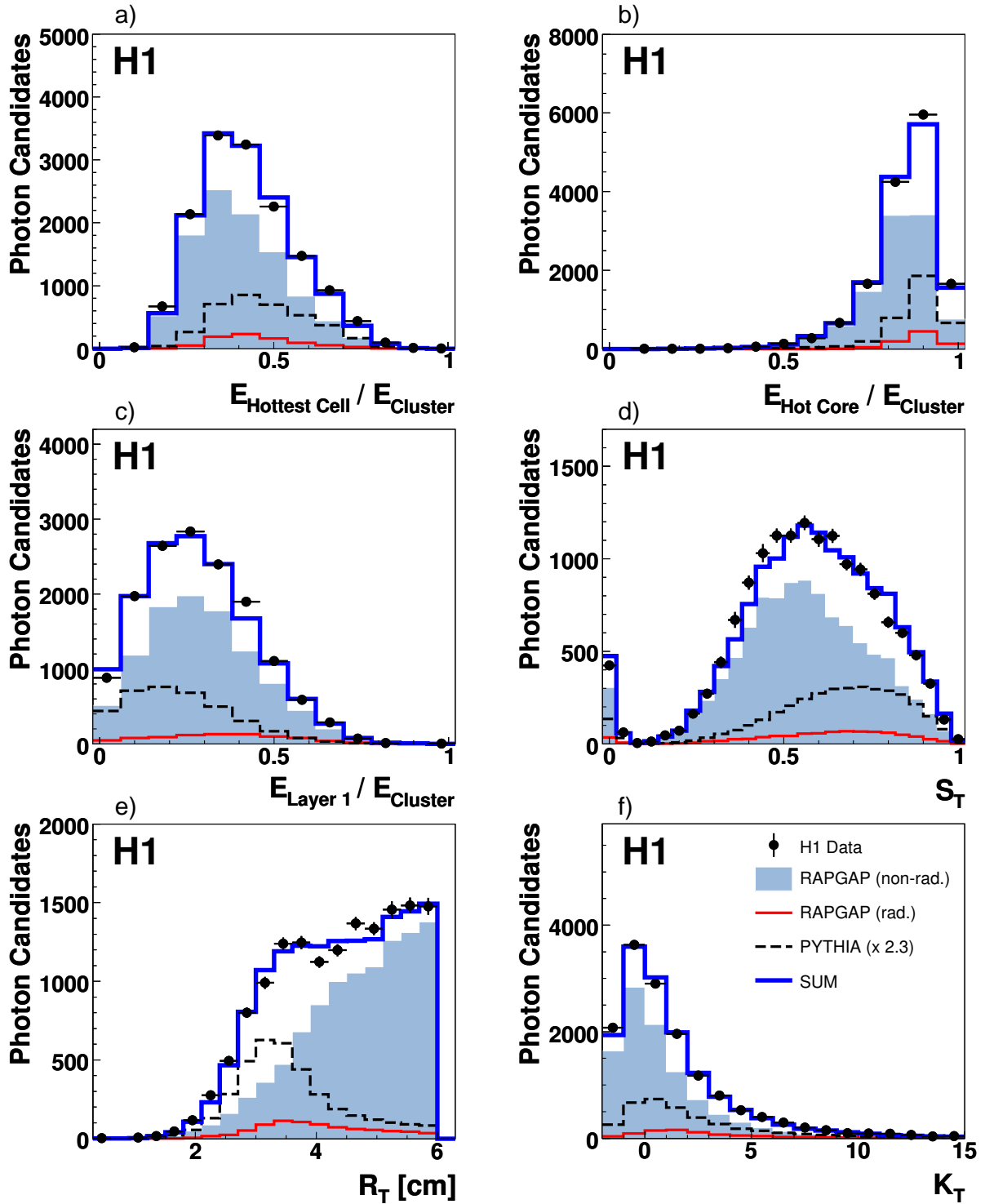


FIGURE 5.3: Distributions of the six shower shape variables that are used to define the classifiers for the isolated photon identification: (a) hottest cell fraction, (b) fraction of the hot core, (c) first layer fraction, (d) transverse symmetry, (e) transverse radius and (f) the transverse kurtosis. The data are shown with the MC predictions described in the caption to figure 4.4. The shape difference between RAPGAP (rad.) and PYTHIA arises from the different distributions in phase space (see figure 4.15 b).

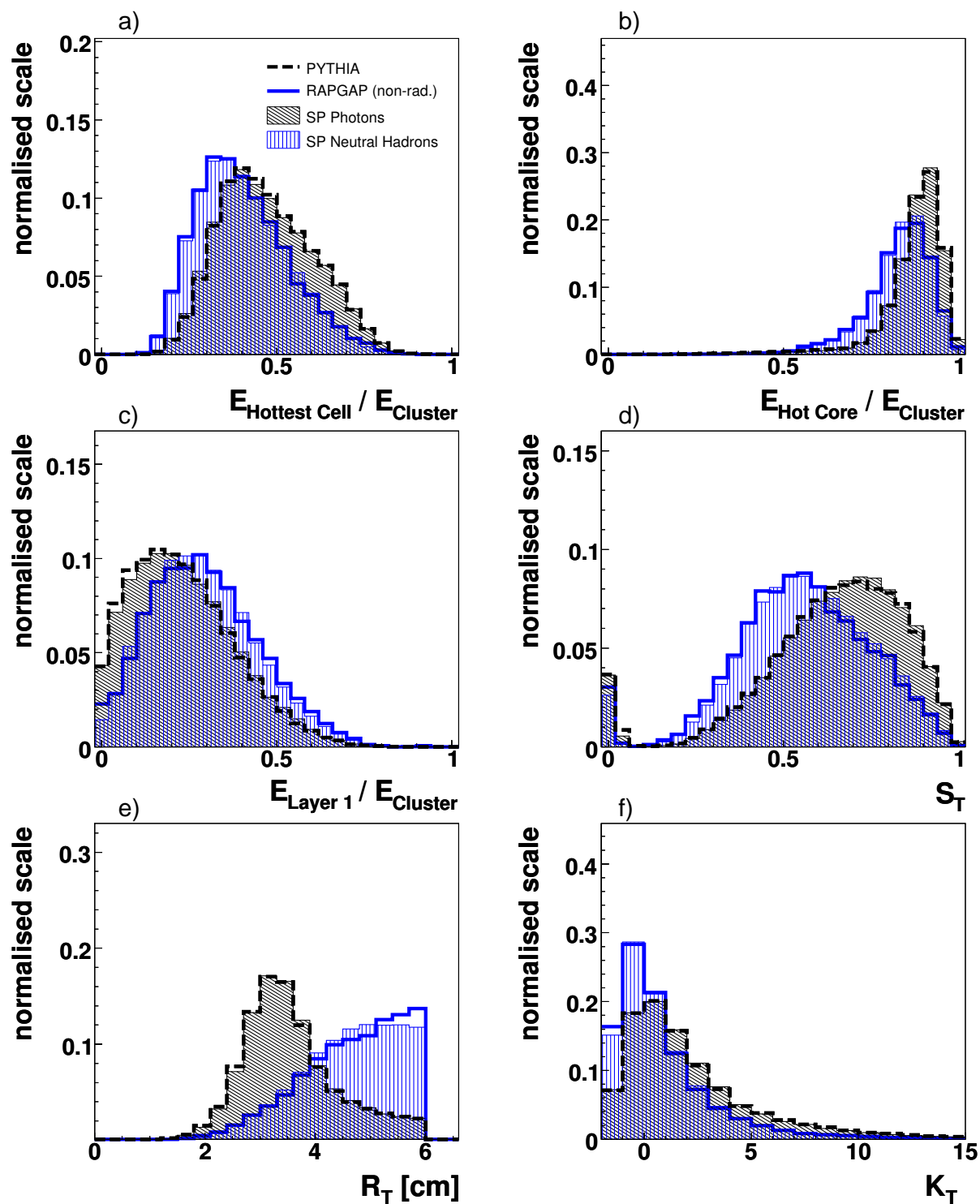
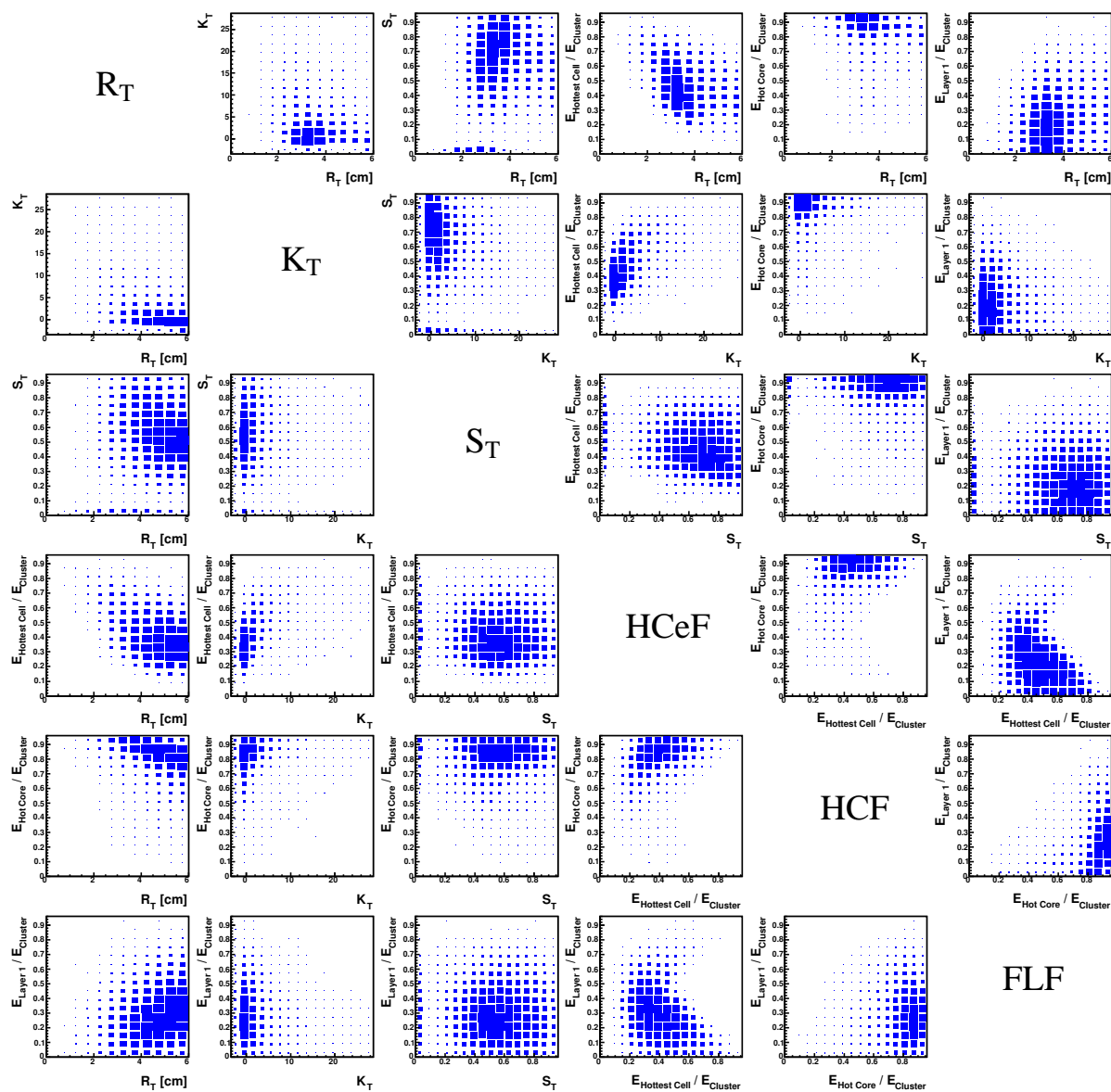


FIGURE 5.4: Comparison between the single particle MCs for photons and neutral hadron background with PYTHIA and RAPGAP (non-rad.) in the six shower shape variables. All histograms are normalised.

## SP photons



## SP neutral hadrons

FIGURE 5.5: Two dimensional correlation plots between the six shower shape variables for SP photons (top-right triangle) and SP neutral hadrons (bottom-left triangle).

by

$$\sigma_{uv} = \langle u - \langle u \rangle \rangle \langle v - \langle v \rangle \rangle \quad (5.6)$$

$$= \langle uv \rangle - \langle u \rangle \langle v \rangle, \quad (5.7)$$

where  $\langle u \rangle = (\sum_i w_i u_i) / (\sum_i w_i)$  is the weighted average of variable  $u$  over all events in the considered sample. With the standard deviation  $\sigma_u$  being the square root of the variance defined as

$$\sigma_u^2 = \sigma_{uu} = \langle u - \langle u \rangle \rangle^2 = \langle u^2 \rangle - \langle u \rangle^2, \quad (5.8)$$

the correlation coefficient reads

$$\rho_{uv} = \frac{\sigma_{uv}}{\sigma_u \sigma_v} = \frac{\sigma_{uv}}{\sqrt{\sigma_{uu} \sigma_{vv}}}. \quad (5.9)$$

The correlation coefficient varies in the range  $-1 < \rho < 1$ . A negative coefficient indicates a decreasing relationship, while a positive coefficient indicates an increasing relationship. The closer the absolute value  $|\rho|$  is to one, the stronger the dependency of the variables. For independent variables the correlation coefficient is zero. The converse, however, is not valid since the coefficient detects only linear dependencies between two variables.

Table 5.1 lists the correlation coefficients between the six variables for SP photons and neutral hadrons. The highest correlation coefficient is observed between the hottest cell fraction and the transverse kurtosis with a value of 0.55 for both signal and background clusters. The smallest linear correlation is observed between the transverse symmetry and the first layer fraction, where the coefficient almost vanishes. The smallest overall correlations with the other variables are found for the transverse symmetry.

In the present analysis the variable with the highest significance in the signal-background separation is the transverse radius. Correlations with the transverse radius therefore enter strongest in the multivariate classification described in the next section. When considering the systematic uncertainties due to the shower shape description (see section 6.2), the correlations of the hottest cell fraction and the hot core fraction with the transverse radius are explicitly taken into account.

## 5.2 Classifiers

The extraction of the photon signal is done by a fit (see section 5.3) of signal and background models to the measured data in some distribution that features a preferably distinct shape for signal and background events and hence provides comparatively high separation power. Such distributions are usually found in the classifier output of multivariate methods, which try to maximise the separation power from the given set of input variables. The fit result has a smaller uncertainty for classifiers that provide higher separation power, but the fit procedure does not strongly depend on the actual performance of the multivariate method. In typical

TABLE 5.1: Correlation coefficients as defined in equation (5.9) between the six shower shape variables for SP photons (top-right triangle) and SP neutral hadrons (bottom-left triangle).

	$R_T$	$K_T$	$S_T$	HCeF	HCF	FLF	
$R_T$		-0.20	0.17	-0.38	-0.26	0.21	} SP Photons
$K_T$	-0.33		-0.09	0.55	0.09	-0.06	
$S_T$	-0.09	0.10		-0.20	-0.12	-0.02	
HCeF	-0.40	0.55	-0.04		0.20	-0.43	
HCF	-0.44	0.29	0.04	0.41		0.29	
FLF	0.26	-0.07	-0.00	-0.38	0.04		
<hr style="width: 50%; margin: 0 auto;"/> SP Neutral Hadrons							

classification problems as in the L2NN neural network, which is used in the second trigger level (cf. section 3.2.5), the performance of the method is crucial, since misidentified signal events may be irretrievably lost.

In the fit, the high statistics SP photon and SP neutral hadron samples are used as signal and background models. They are also used for the statistical learning in the multivariate methods. In order to avoid any bias between the fit result and the multivariate method the samples are split. A fraction of 60% of the SP events is used for the statistical learning and the remaining fraction of 40% for the modelling of the signal and background classifier distributions that enter the fit.

In the present analysis three multivariate classification methods are employed: a *naïve Bayes classification*, an *artificial neural network* and a *range search*. The methods and their implementation are discussed in appendix B.

For the final extraction of the photon content the *naïve Bayes classifier*, henceforth termed discriminator  $D$ , is used. The results of the further two multivariate methods are used to cross-check for possible bias induced by the method. Since the signal and background shower shapes are expected to vary significantly as a function of the energy of the photon candidate and the granularity of the LAr calorimeter, the multivariate methods are set up in 15 entities. For any of the 5 wheels and 3 bins of transverse energy (3–4 GeV, 4–6 GeV, 6–10 GeV) a single entity is trained.<sup>1</sup> In section 5.3 the same kinematic bins are used for the signal extraction. They are listed in table E.1. The output distributions of the multivariate methods are shown in figure 5.6 for data and compared to the MC predictions. In all three output distributions the photon signal is enhanced towards high classifier values and the neutral hadron background towards

<sup>1</sup>For the neural network, the performance of 15 separate networks was compared to the performance of a single network, which also encompasses the polar angle and the transverse energy of the photon candidate as additional variables. The set of separate networks was found to give better separation power.

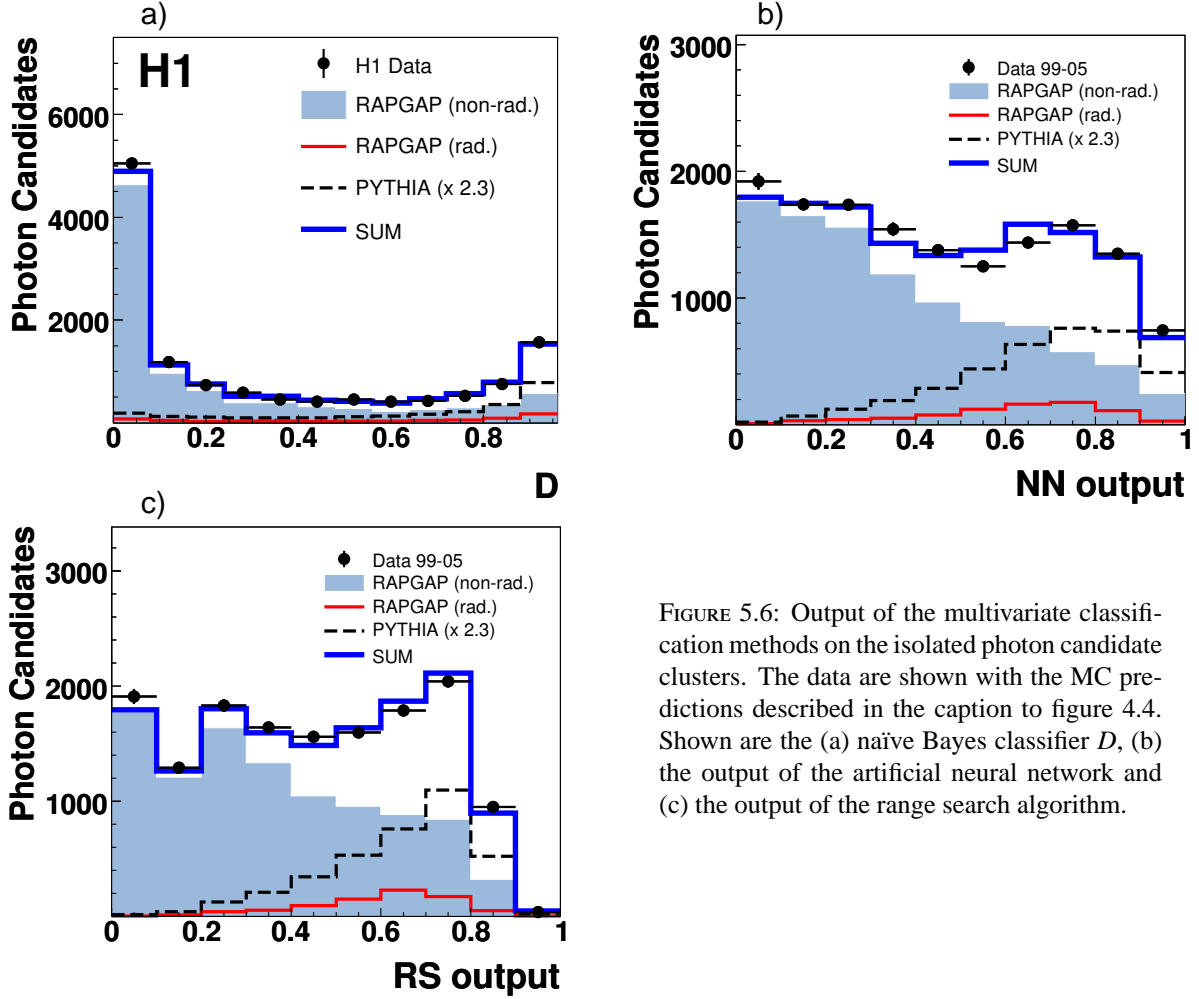


FIGURE 5.6: Output of the multivariate classification methods on the isolated photon candidate clusters. The data are shown with the MC predictions described in the caption to figure 4.4. Shown are the (a) naïve Bayes classifier  $D$ , (b) the output of the artificial neural network and (c) the output of the range search algorithm.

low values. The performance of the methods is further discussed in the following section.

### 5.2.1 Performance

In order to compare different classifiers the signal efficiency  $\epsilon_S$  and background rejection  $1 - \epsilon_{BG}$  is determined for any possible cut in the output distributions. In figure 5.7 the resulting graph of the signal efficiency versus background rejection is shown for the three multivariate methods. In principle, the further the graph tends towards the upper right corner at high signal efficiency and high background rejection for a certain classifier the better the method. The graph shows that all three classifiers perform about equally well.

However, none of the methods provides a full background rejection ( $1 - \epsilon_{BG} \approx 1$ ) at finite signal efficiencies, which is due to the non-separable background discussed in appendix A. For strongly asymmetric photonic decays of the neutral hadrons the photon candidate cluster cannot be distinguished from a cluster induced by a single photon. By definition, no multivari-

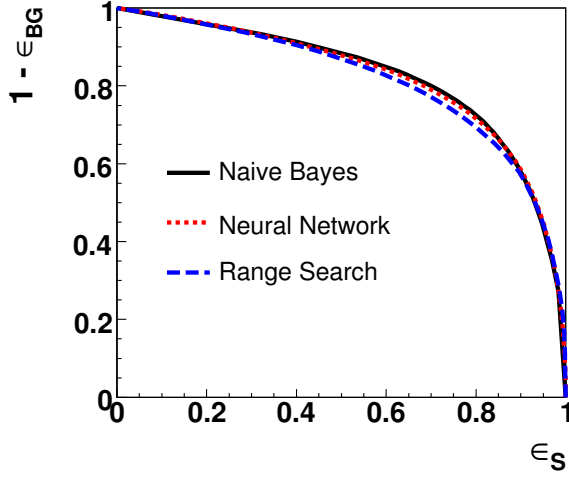


FIGURE 5.7: Signal efficiency versus background rejection graph for the three multivariate classification methods and for the entire kinematic range.

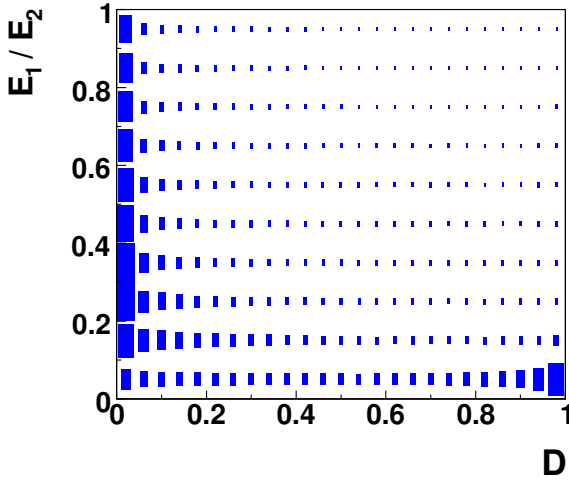


FIGURE 5.8: The discriminator  $D$  (naïve Bayes output) in dependence of the decay symmetry for single particle neutral pions. The decay symmetry is given by the energy ratio  $E_1/E_2$  of the two decay photons with  $E_1 < E_2$ .

ate classifier can overcome this intrinsic background. Figure 5.8 illustrates the naïve Bayes output in dependence of the decay symmetry for  $\pi^0$  background. As expected, photon-like classifications can be associated with asymmetric decays.

The efficiency versus rejection graphs are also shown in figure 5.9 for the kinematic bins in which the different entities of the multivariate methods are set up. Apart from the tendency of the naïve Bayes approach to better perform at higher energies and in the forward region, the methods provide comparable separation power throughout the considered phasespace. The separation power is best in the CB3 and FB1 due to a finer granularity in the calorimeter.

In addition to the efficiency-rejection graph the maximum separation power  $S_{max}$  and the minimum fraction of misclassification  $M_{min}$  may be used to compare the different classifiers. They are given by

$$S_{max} = \max(\epsilon_S / \epsilon_{BG}), \quad M_{min} = \min\left(\frac{1 - \epsilon_S + \epsilon_{BG} \frac{N_{BG}}{N_S}}{1 + \frac{N_{BG}}{N_S}}\right), \quad (5.10)$$

where  $N_S$  and  $N_{BG}$  are the total number of signal and background events expected. The quanti-

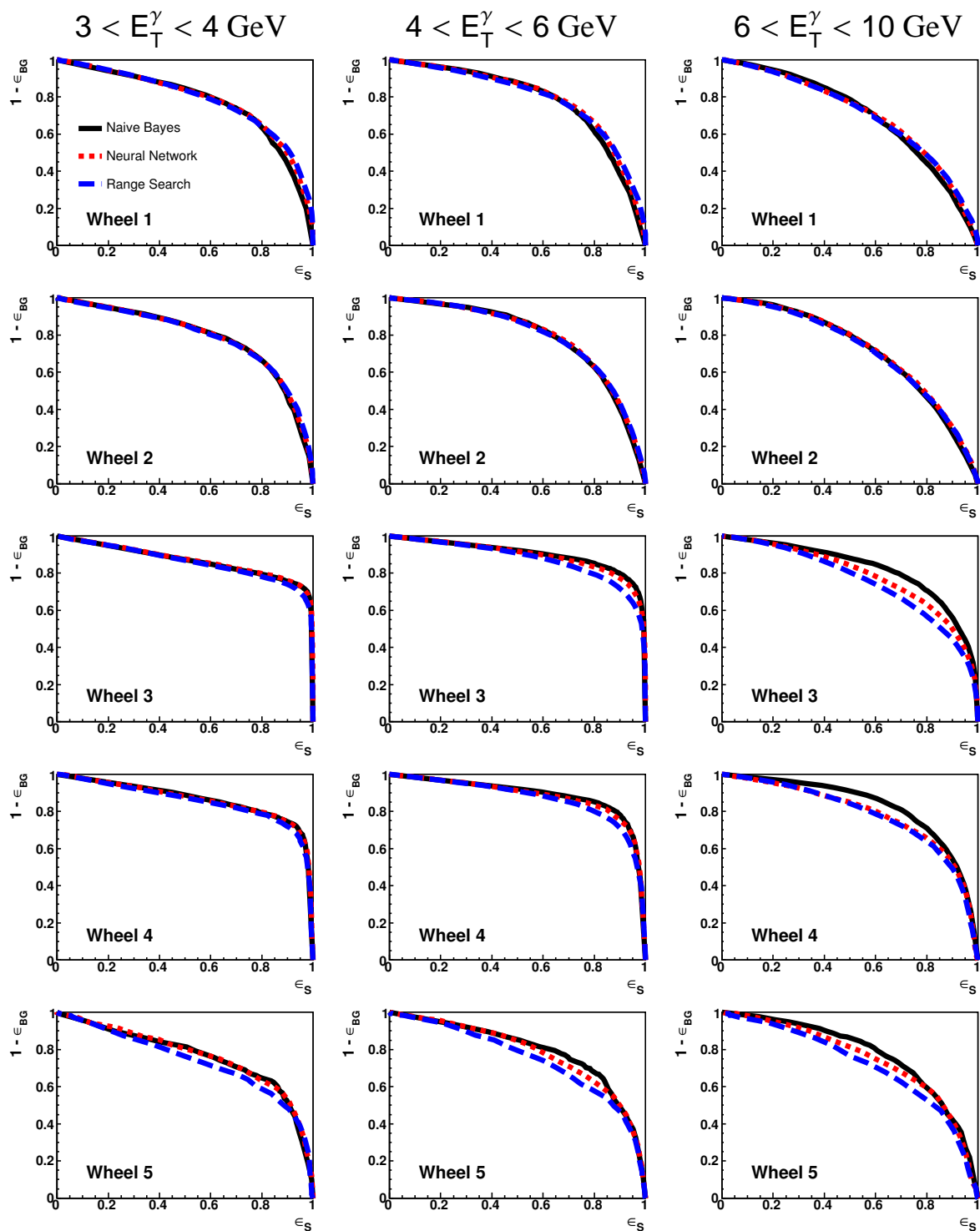


FIGURE 5.9: Signal efficiency versus background rejection graphs for the three multivariate classification methods shown for the different considered kinematic bins (see table E.1).



TABLE 5.2: The maximum separation power  $S_{max}$  and the minimum fraction of misclassification  $M_{min}$  for the three multivariate classification methods together with the corresponding classifier output and working point.

	$S_{max}$	output	$\epsilon_S$	$1 - \epsilon_{BG}$	$M_{min}$	output	$\epsilon_S$	$1 - \epsilon_{BG}$
Naïve Bayes	4.8	0.98	0.32	0.93	0.24	0.46	0.81	0.71
Neural Network	6.1	0.94	0.05	0.99	0.24	0.50	0.81	0.71
Range Search	5.6	0.86	0.05	0.99	0.25	0.50	0.80	0.70

ties  $S_{max}$  and  $M_{min}$  are listed in table 5.2 for the three methods under the assumption  $N_S \approx N_{BG}$  together with the corresponding working points. As the methods yield very similar classification results and because of its simple definition, henceforth solely the naïve Bayes discriminator  $D$  is used in the measurement of isolated photons. In section 5.3 the other two methods will again be employed for cross-checking the results of the actual photon signal extraction.

### 5.3 Signal Extraction

Figure 5.10 shows the shape of the naïve Bayes discriminator for SP photons and SP background separately for the kinematic ranges in which entities of the multivariate methods were trained. As already mentioned, the shower shape densities vary significantly as a function of energy and granularity of the LAr calorimeter, which equally affects the discriminator.

The photon signal is thus extracted in the same 15 bins of  $(E_T^\gamma, \eta^\gamma)$ , the intervals in  $\eta^\gamma$  corresponding to different wheels of the calorimeter (see table E.1). The contribution of photons and neutral hadrons in any of the 15 analysis bins is determined by independent minimum- $\chi^2$  fits of the signal and background discriminator distributions to the data distribution, separately for the inclusive sample and the photon plus no-jets as well as the photon plus jet subsamples. The  $\chi^2$  function is defined as

$$\chi^2 = \sum_i \frac{(N_{data,i} - N_{bg}d_{bg,i} - N_{sig}d_{sig,i})^2}{\sigma_{data,i}^2 + N_{bg}^2 \sigma_{bg,i}^2 + N_{sig}^2 \sigma_{sig,i}^2} \quad (5.11)$$

in each of the  $(E_T^\gamma, \eta^\gamma)$  bins, where the sum runs over the bins of the discriminator distributions.  $N_{data,i}$  is the number of data events in the  $i$ 'th bin.  $d_{sig,i}$  and  $d_{bg,i}$  denote the  $i$ 'th bin content of the signal and background discriminator distribution, respectively, normalised to unity. The  $\sigma_i$  represent the associated statistical errors.  $N_{sig}$  and  $N_{bg}$ , representing the number of signal and background events, respectively, are the parameters that are determined by the fit. If the content in any histogram bin is small ( $N_{data,i} < 7$ ), adjacent bins are merged.

The total number of isolated photons is obtained by summing  $N_{sig}$  over all analysis bins. It is listed for the inclusive sample and the photon plus no-jets and photon plus jet subsamples in

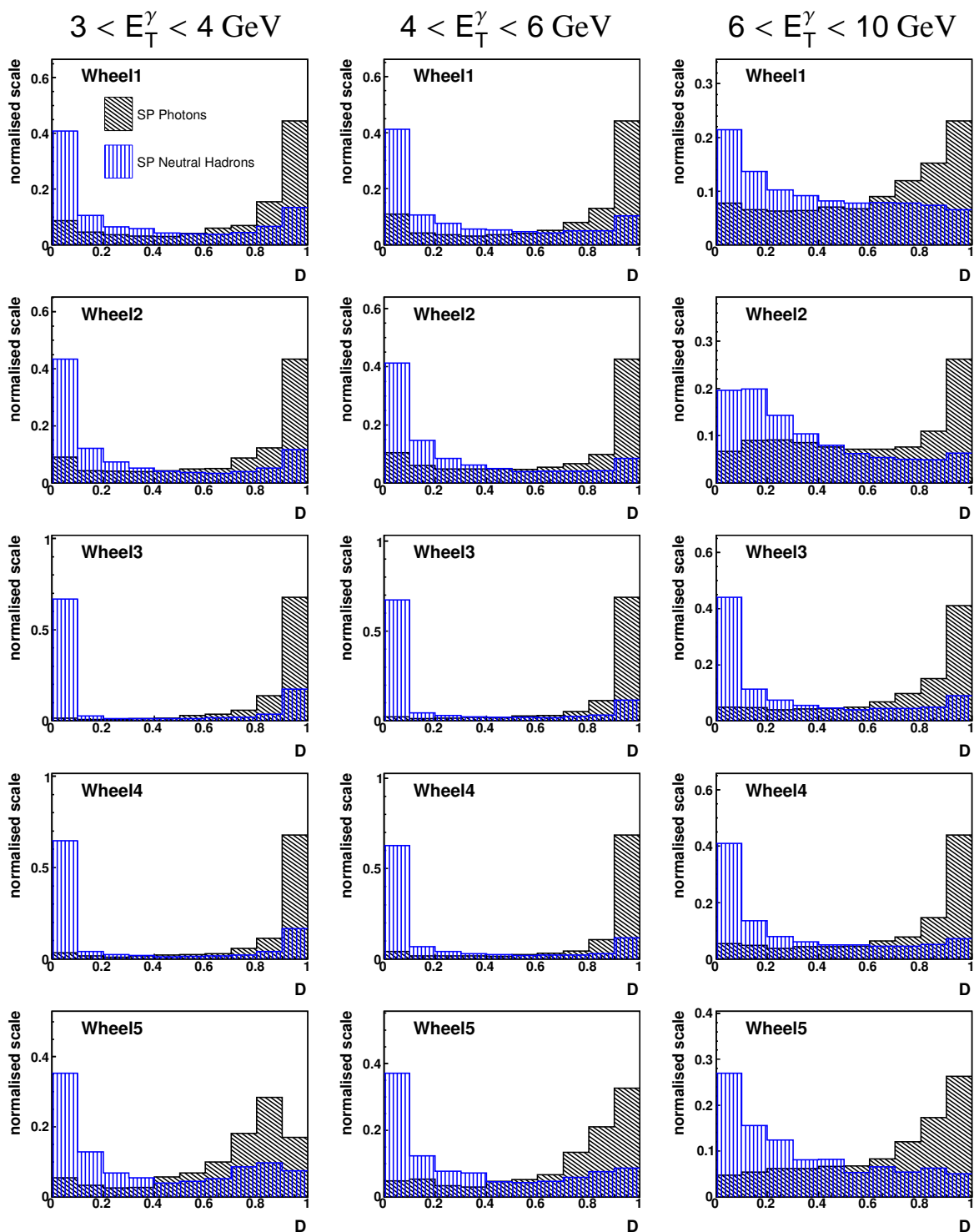


FIGURE 5.10: Normalised distributions of the discriminator  $D$  (naïve Bayes output) for SP photons and SP neutral hadrons shown for the 15 analysis bins (see table E.1).

TABLE 5.3: Total number of signal events for the considered event samples along with the corresponding number of photon candidates as presented in section 4.6 and the signal fraction.

	# photon candidates	# photons	signal fraction
inclusive	14670	$4372 \pm 145$	30 %
photon plus no-jets	8175	$1755 \pm 106$	21 %
photon plus jets	6495	$2606 \pm 95$	40 %

table 5.3 along with the corresponding number of photon candidates as presented in section 4.6 and the signal fraction defined as ratio of extracted photons to photon candidates. The signal fraction is 21 % for the photon plus no-jets and 40 % for the photon plus jet sample, showing that the jet multiplicity for events with isolated photons is higher than for background events. The photon signal is also extracted in five different bins of  $Q^2$  (see table E.1). In these fits the signal and background distributions in  $E_T$  and  $\eta$  of the single particles used for the discriminator distribution are assumed to follow the  $E_T$  and  $\eta$  dependence of signal and background extracted from the fit in the 15 bins. Variations of the  $E_T$  and  $\eta$  dependence with  $Q^2$  were found to be negligible.

The numbers of extracted photons are listed in table 5.4 for any considered analysis bin together with the minimum  $\chi^2$  achieved by the fit and the number of degrees of freedom (NDF), which is given by the number of histogram bins minus the number of parameters to be fitted. The discriminator histogram is used with five bins. Hence, three degrees of freedom are available if no merging of bins is taking place. As an example, in figure 5.11 the discriminator distributions in the 15 bins of  $(E_T^\gamma, \eta^\gamma)$  of the inclusive sample are shown along with the SP photon and neutral hadron distributions scaled according to the fit results.

### 5.3.1 Consistency Checks

The consistency of the signal extraction method is surveyed with respect to the chosen set of shower shape variables, the employed multivariate method and the SP signal and background simulation.

#### Dependence on the Shower Shape Variables

The extracted photon signal should be largely independent of the chosen set of shower shape variables. In order to test potentially strong dependences on specific variables in the set, the discriminator is redefined from only five of the six variables. Table 5.5 shows the relative change of the extracted number of photons for sets with any one variable being left out. No strong dependence on any of the variables is observed. The relative change of the extracted signal is well below 5 % and in the order of the statistical uncertainty.

TABLE 5.4: Fit results for any considered analysis bin in the photon signal extraction. Listed are the extracted number of photons, the minimum  $\chi^2$  achieved by the fit and the number of degrees of freedom.

Fit results in bins of $(E_T^\gamma, \eta^\gamma)$						Fit results in bins of $Q^2$					
Wheel	$E_T^\gamma$ range [GeV]		# photons	$\chi^2$	NDF	$Q^2$ range [GeV <sup>2</sup> ]		# photons	$\chi^2$	NDF	
Inclusive						Inclusive					
1 (CB1)	3.0	4.0	418.6 ± 57.0	13.9	3	4.0	10.0	988.0 ± 83.4	15.8	3	
1 (CB1)	4.0	6.0	606.4 ± 48.6	1.2	3	10.0	20.0	1222.8 ± 76.2	16.3	3	
1 (CB1)	6.0	10.0	298.8 ± 37.0	4.3	3	20.0	40.0	1068.2 ± 62.4	5.5	3	
2 (CB2)	3.0	4.0	478.8 ± 61.3	2.6	3	40.0	80.0	844.8 ± 47.2	14.8	3	
2 (CB2)	4.0	6.0	566.9 ± 49.8	1.7	3	80.0	150.0	249.3 ± 23.5	6.6	3	
2 (CB2)	6.0	10.0	371.9 ± 43.7	17.8	3	Photon plus no-jets					
3 (CB3)	3.0	4.0	386.5 ± 50.2	1.1	3	4.0	10.0	438.5 ± 65.3	10.2	3	
3 (CB3)	4.0	6.0	499.4 ± 33.8	1.3	3	10.0	20.0	476.9 ± 58.5	30.6	3	
3 (CB3)	6.0	10.0	250.9 ± 24.1	5.1	3	20.0	40.0	462.9 ± 47.1	1.9	3	
4 (FB1)	3.0	4.0	125.6 ± 23.5	1.1	3	40.0	80.0	290.0 ± 31.6	15.1	3	
4 (FB1)	4.0	6.0	135.3 ± 18.9	8.8	3	80.0	150.0	86.8 ± 14.0	13.3	3	
4 (FB1)	6.0	10.0	126.2 ± 16.9	2.5	3	Photon plus jet					
5 (FB2)	3.0	4.0	30.9 ± 12.0	5.3	3	4.0	10.0	545.4 ± 51.1	6.5	3	
5 (FB2)	4.0	6.0	64.9 ± 15.8	1.4	3	10.0	20.0	757.1 ± 47.7	1.6	3	
5 (FB2)	6.0	10.0	11.2 ± 10.3	8.2	3	20.0	40.0	593.9 ± 39.8	8.0	3	
Photon plus no-jets						40.0	80.0	548.3 ± 34.4	2.4	3	
1 (CB1)	3.0	4.0	209.8 ± 45.3	12.9	3	80.0	150.0	157.6 ± 18.8	0.6	3	
1 (CB1)	4.0	6.0	242.4 ± 32.9	1.0	3						
1 (CB1)	6.0	10.0	89.6 ± 22.5	7.3	3						
2 (CB2)	3.0	4.0	245.0 ± 49.0	3.0	3						
2 (CB2)	4.0	6.0	250.9 ± 35.9	2.2	3						
2 (CB2)	6.0	10.0	106.2 ± 25.4	3.8	3						
3 (CB3)	3.0	4.0	180.4 ± 41.9	3.1	3						
3 (CB3)	4.0	6.0	190.9 ± 23.1	0.3	3						
3 (CB3)	6.0	10.0	72.3 ± 13.9	3.6	3						
4 (FB1)	3.0	4.0	55.3 ± 14.5	3.0	3						
4 (FB1)	4.0	6.0	33.3 ± 10.9	5.2	3						
4 (FB1)	6.0	10.0	24.2 ± 8.8	3.1	3						
5 (FB2)	3.0	4.0	9.9 ± 7.3	4.1	2						
5 (FB2)	4.0	6.0	29.2 ± 10.5	0.6	3						
5 (FB2)	6.0	10.0	15.3 ± 10.3	1.2	1						
Photon plus jet											
1 (CB1)	3.0	4.0	210.0 ± 31.2	6.2	3						
1 (CB1)	4.0	6.0	343.7 ± 33.3	8.1	3						
1 (CB1)	6.0	10.0	210.4 ± 29.1	2.7	3						
2 (CB2)	3.0	4.0	240.9 ± 33.9	4.7	3						
2 (CB2)	4.0	6.0	316.5 ± 33.0	1.0	3						
2 (CB2)	6.0	10.0	259.3 ± 34.5	16.0	3						
3 (CB3)	3.0	4.0	215.3 ± 26.2	3.8	3						
3 (CB3)	4.0	6.0	306.4 ± 23.8	2.8	3						
3 (CB3)	6.0	10.0	173.0 ± 19.2	6.3	3						
4 (FB1)	3.0	4.0	67.5 ± 17.9	4.9	3						
4 (FB1)	4.0	6.0	98.8 ± 14.7	7.2	3						
4 (FB1)	6.0	10.0	103.0 ± 14.2	2.2	3						
5 (FB2)	3.0	4.0	12.7 ± 8.4	3.5	2						
5 (FB2)	4.0	6.0	33.4 ± 10.3	1.2	3						
5 (FB2)	6.0	10.0	14.8 ± 8.7	5.6	2						

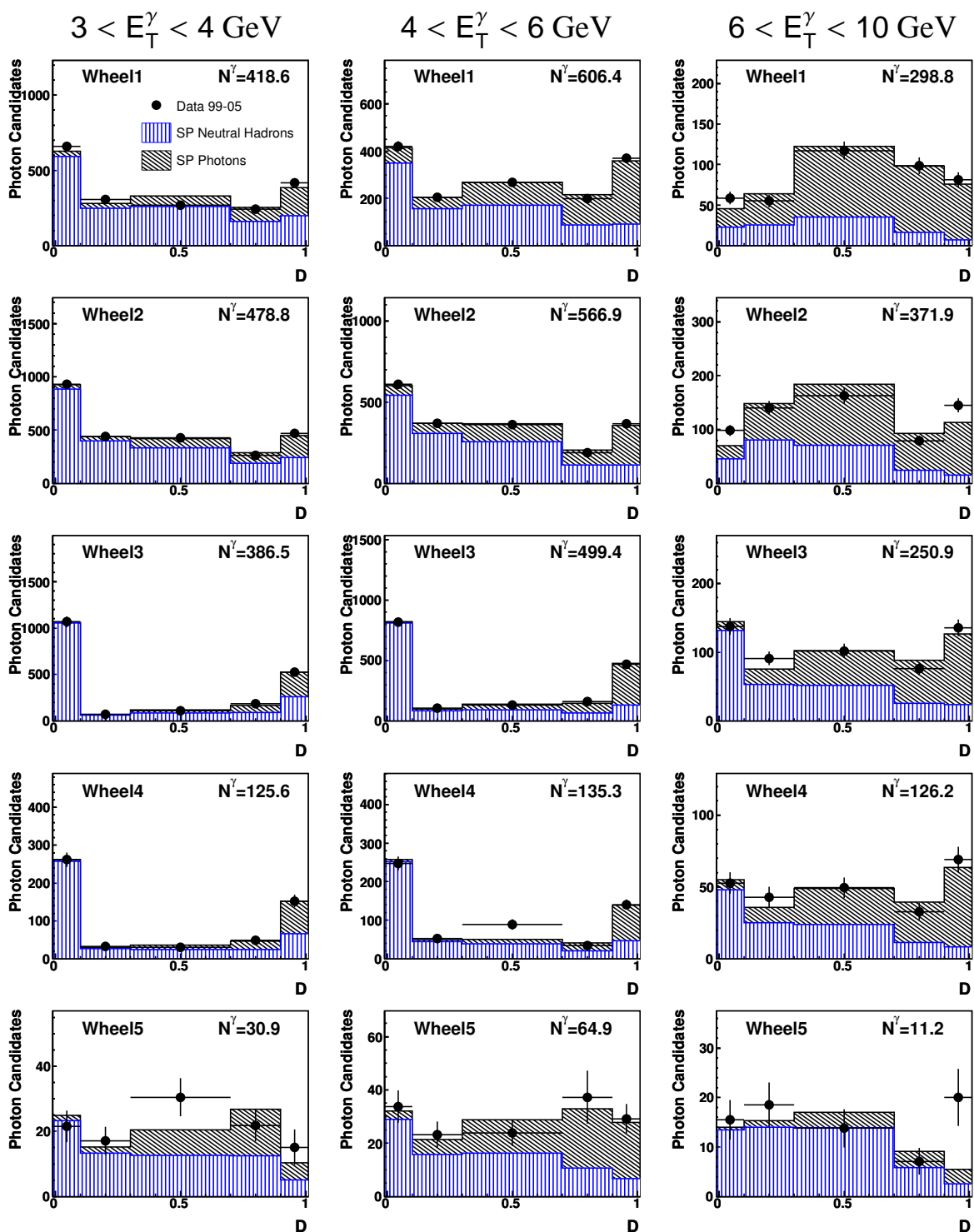


FIGURE 5.11: Distributions of the discriminator  $D$  (naïve Bayes output) along with SP photons and SP neutral hadrons scaled according to the fit results (cf. table 5.4) shown for the 15 inclusive analysis bins (see table E.1). The SP photon distributions are drawn stacked on top of the SP neutral hadron distributions.

TABLE 5.5: Effect of the redefined discriminator made up from only five of the six shower shape variables on the extracted photon signal.

<u>neglected variable</u>	<u>photon signal change</u>
$R_T$	0.9 %
$K_T$	3.1 %
$S_T$	3.6 %
HCeF	0.5 %
HCF	-4.1 %
FLF	2.7 %

TABLE 5.6: Total number of photons extracted for the three different multivariate methods. The deviation from the naïve Bayes method is given in the last column.

	<u># photons</u>	<u>relative deviation</u>
nominal (naïve Bayes)	$4372 \pm 145$	—
Neural Network	$4420 \pm 145$	1.1 %
Range Search	$4284 \pm 150$	-2.0 %

In general, the separation power is diminished for the redefined discriminator made of five variables, which is reflected in a slightly increased statistical error of the extracted photon signal.

### Dependence on Multivariate Methods

Instead of the naïve Bayes classifier, the neural network and range search classifiers can be used in equation (5.11) for the extraction of the photon signal. The number of signal photons extracted with the three methods are shown in figure 5.12 for the 15 analysis bins. The results obtained with the different multivariate methods vary by an amount of the order of the statistical error. No systematic shift is observed. The total number of photons extracted with these methods are listed in table 5.6. The neural network based result differs by 1.1 % and the range search based result by -2.0 % from the nominal result based on fits to the naïve Bayes discriminator.

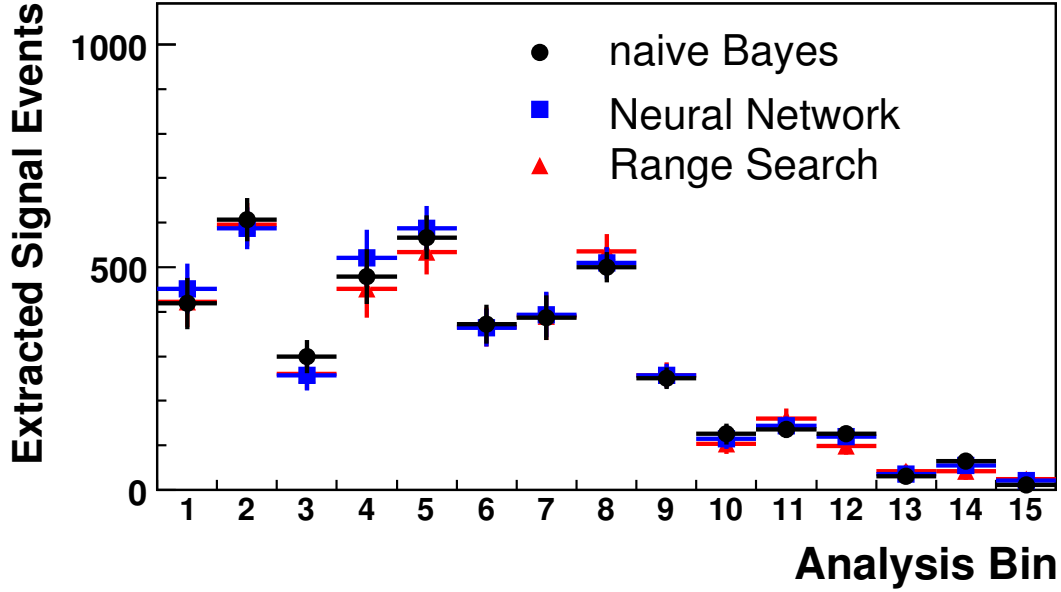


FIGURE 5.12: Number of photons extracted for the three multivariate methods shown in 15 ( $E_T^\gamma$ ,  $\eta^\gamma$ ) analysis bins (see table E.1).

### Consistency in the Simulation: Cluster Overlap

In the  $\chi^2$  function defined in equation (5.11) the discriminator distributions of SP photons and SP neutral hadrons are used as signal and background histograms. As the use of SP events may induce a bias due to missing features in the shower shape description, the extraction method is cross-checked with the full event MCs PYTHIA and RAPGAP (non-rad.) as signal and background models in a kinematic range where the full event MCs provide sufficient statistics.<sup>2</sup>

It is observed that at lowest energies the signal extraction based on the SP simulation yields systematically 10% higher signal counts than the extraction based on the full event MCs. In order to study this effect, the energy of the photon candidate cluster over the generated energy of the incident neutral particle for photons and neutral hadron background without any restriction on the cluster's transverse radius is shown in figure 5.13. For photons the ratio is centred close to one and consistent between the PYTHIA MC and the SP simulation. For neutral hadrons at lowest cluster energies the ratio for the SP simulation is centred slightly below one, which is due to the contribution of asymmetric decays where one of the decay photons does not contribute to the cluster. The RAPGAP (non-rad.) simulation, however, predicts a markedly larger ratio implying a significantly larger cluster energy compared to the energy of the generated incident neutral particle. The effect is most pronounced at low energies

<sup>2</sup>The comparison is performed in the first three wheels (CB1, CB2, CB3) and in the lowest two energy bins ( $3 < E_T^\gamma < 4$  GeV and  $4 < E_T^\gamma < 6$  GeV).

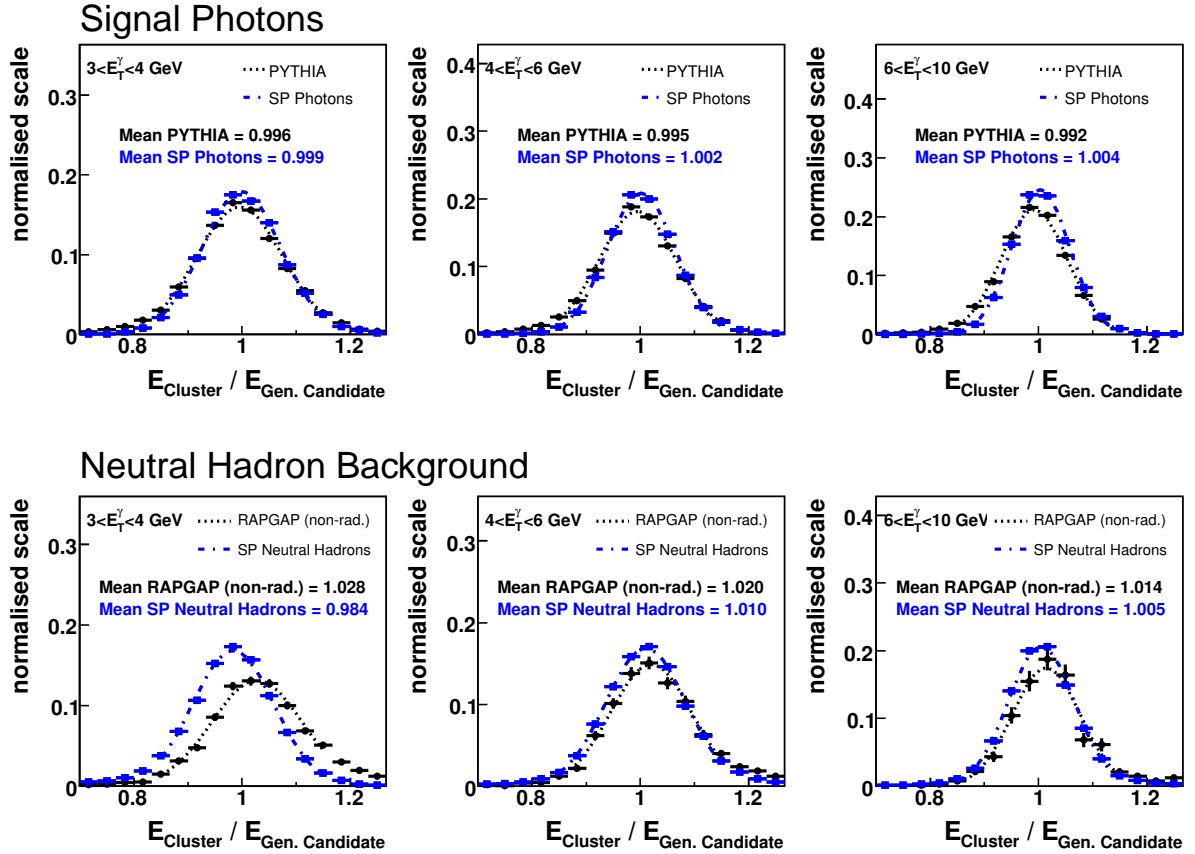


FIGURE 5.13: Energy of the photon candidate cluster divided by the generated energy of the incident neutral particle for photons (top row) and neutral hadron background (bottom row) without any restriction on the transverse radius of the cluster. The ratio is compared between the full event MCs and the SP simulation and shown for different energy bins. From left:  $3 < E_T^\gamma < 4$  GeV,  $4 < E_T^\gamma < 6$  GeV and  $6 < E_T^\gamma < 10$  GeV.



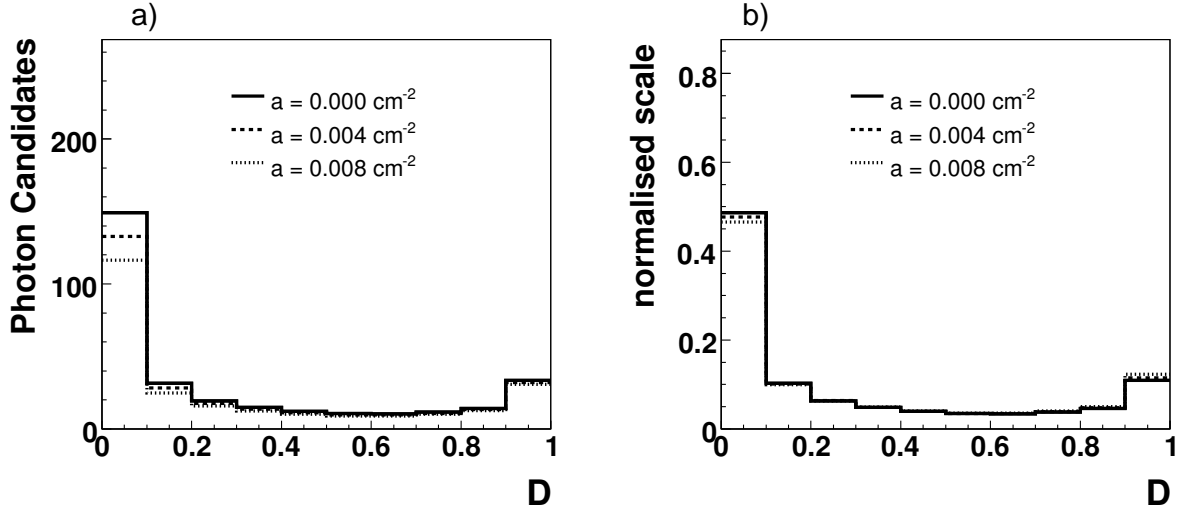


FIGURE 5.14: Naïve Bayes discriminator distribution for the SP neutral hadron background with modelled cluster overlap is shown for different values of the constant  $a$ . a) Not-normalised. b) Normalised to one.

and observed neither in the SP simulation nor in any of the photon simulations.

The higher cluster energy in the RAPGAP (non-rad.) sample may be explained by additional energy contributions from neighbouring incident particles. These are expected to contribute stronger for clusters of large transverse extent where an overlap is more probable. Since high-energetic neutral hadron clusters become increasingly compact, these overlaps would mainly affect low energetic neutral hadron induced clusters and leave high-energetic clusters and narrow photon clusters largely unaffected.

Following the assumption of such cluster overlaps, in the following the effect is modelled in a simple approach for the SP neutral hadron simulation, which leads to a consistent signal extraction when compared to the full event MCs (see below). An overlap probability  $P_{co}$  is assumed to be proportional to the transverse area of the cluster:

$$P_{co} = a \cdot R_T^2, \quad (5.12)$$

where  $a$  is a constant which needs to be estimated for the specific hadronic environment of DIS events. If an overlap occurs, the transverse radius of the cluster is assumed to exceed the upper limit of 6 cm required in the analysis (see section 4.4). Since the overlap probability increases with larger transverse radii and thus towards more background-like clusters, the relative contribution of photon-like clusters with low transverse radius is enhanced in the background event sample. The discriminator distribution for the SP neutral hadron background with modelled cluster overlap is shown for different values of the constant  $a$  in figure 5.14. In the normalised distribution a slight increase of the bin content at high discriminator values and at the same time a small decrease at low values with the constant  $a$  can be observed, which leads to a smaller extracted signal when used in the fit.

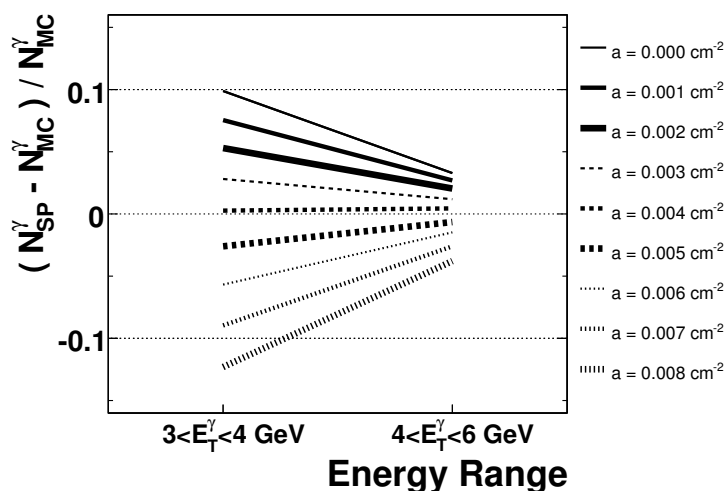


FIGURE 5.15: Relative deviation of the number of signal photons extracted using the SP simulation  $N_{SP}^{\gamma}$  from the number of signal photons extracted using the full event MCs  $N_{MC}^{\gamma}$ . The deviation is shown for different values of the constant  $a$  and for the two lower energy bins used in the analysis. Straight lines between the measurements in the two energy bins are drawn for visualisation. The numbers  $N_{SP}^{\gamma}$  and  $N_{MC}^{\gamma}$  are summed over the first three wheels: CB1, CB2, CB3.

The extracted photon signal based on the SP simulation with modelled cluster overlap for the neutral hadrons can now again be compared to the extraction result when using the full event MCs PYTHIA and RAPGAP (non-rad.) in the mentioned kinematic range where the full event MCs provide sufficient statistics. Figure 5.15 shows the relative deviation in the two lowest energy bins summed over the first three wheels for different values of the constant  $a$ . For values of the constant ranging in  $0 < a < 8 \cdot 10^{-3} \text{ cm}^{-2}$ , the deviation varies between +10% and -12% at lowest energies and between +3% and -4% for medium energies. At higher energies ( $E_T^{\gamma} > 6 \text{ GeV}$ ) the effect of the cluster overlap modelling becomes negligible.

A consistency in the signal extraction between the full event MCs and the SP simulation is achieved at a value of the constant  $a = 0.004 \text{ cm}^{-2}$ , which is henceforth used in the present measurement of isolated photons in DIS. Any results presented in this chapter so far were already based on the SP simulation with cluster overlap modelling applied. The overlap modelling leads to a correction of at most 10% at low cluster energies.

In the SP photon simulation the cluster overlap was found to be of no major importance as can be seen in figure 5.13. If the cluster overlap modelling is applied to the SP photons, no strong effect can be observed due to the small transverse extent of the photon clusters. Therefore the modelling is only applied to the background clusters.

A further cross-check was done for the cluster overlap modelling. Instead of rejecting the event in case of an overlap, the radius can as well be increased by a certain amount, which also leads to the rejection of the event in most cases if the cut on the transverse radius is applied. However, if the radius cut is not applied, the transverse radius distribution of the SP neutral hadrons with applied overlap modelling can be compared to the RAPGAP (non-rad.) MC with close attention to the description of high cluster radii, which are usually underestimated in the SP simulation as seen in figure 4.8. In the cross-check, the radius was increased by a Gaussian-smearred value around 5 cm in case of an overlap. The radius distribution was found to be much more consistent at all radii between the SP and full event simulation.

# CHAPTER 6

## CROSS SECTION MEASUREMENT AND SYSTEMATIC UNCERTAINTIES

---

### 6.1 Cross Section Measurement

Cross sections are measured in 15 bins of  $(E_T^\gamma, \eta^\gamma)$  and in five bins of  $Q^2$  as given in table E.1 for any of the three selected samples: inclusive, photon plus no-jets and photon plus jet.

In each bin  $i$ , the bin averaged cross section  $\sigma_i$  is computed from the number of events with photons resulting from the photon signal extraction (cf. chapter 5) as

$$\sigma_i = \frac{N_i^{sig}}{\mathcal{L} \cdot \mathcal{A}_i}, \quad (6.1)$$

where  $\mathcal{L}$  is the luminosity. The acceptance factor  $\mathcal{A}_i$  is discussed in detail in section 6.1.1.

The total cross section in each sample is obtained by summing the results in all 15 bins of  $(E_T^\gamma, \eta^\gamma)$ . The cross sections  $d\sigma/dE_T^\gamma$  and  $d\sigma/d\eta^\gamma$  are obtained accordingly by summing all corresponding bins in  $\eta^\gamma$  and  $E_T^\gamma$ , respectively.

#### 6.1.1 Acceptance Corrections

The acceptance factor  $\mathcal{A}_i$  as well as the purity  $\mathcal{P}_i$  and stability  $\mathcal{S}_i$  for bin  $i$  are calculated using the scaled signal MC<sup>1</sup>. They are defined as

$$\mathcal{A}_i = N_i^{rec} / N_i^{gen} \quad (6.2)$$

$$\mathcal{P}_i = N_i^{rec+gen} / N_i^{rec} \quad (6.3)$$

$$\mathcal{S}_i = N_i^{rec+gen} / N_i^{gen+sel}, \quad (6.4)$$

where

---

<sup>1</sup>The scaled signal MC was introduced in section 2.2.2 and is composed of the PYTHIA MC scaled by a factor 2.3 and the unscaled RAPGAP (rad.) MC.

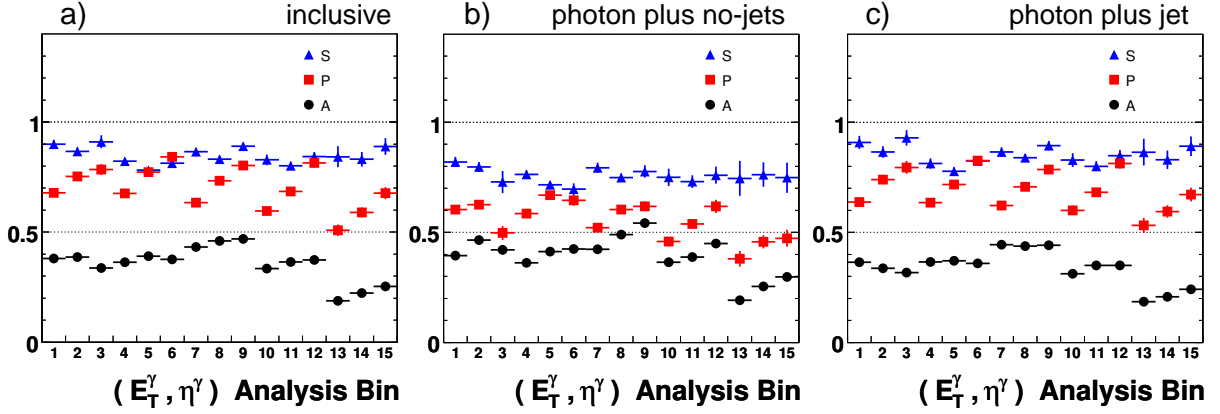


FIGURE 6.1: Acceptance factor  $\mathcal{A}$ , purity  $\mathcal{P}$  and stability  $\mathcal{S}$  for the 15 analysis bins in  $(E_T^\gamma, \eta^\gamma)$  defined in table E.1. The quantities are shown for (a) the inclusive sample, (b) the photon plus no-jets and (c) the photon plus jet subsamples.

- $N_i^{\text{rec}}$  is the number of events reconstructed in bin  $i$ .
- $N_i^{\text{gen}}$  is the number of events generated in bin  $i$ .
- $N_i^{\text{rec+gen}}$  is the number of events generated and reconstructed in bin  $i$ .
- $N_i^{\text{gen+sel}}$  is the number of events generated in bin  $i$  and passing the entire selection (i.e. reconstructed in any bin).

The number of generated events refers to events passing the selection cuts on hadron level. Consequently, the three quantities take into account the acceptance, trigger and reconstruction efficiencies and migration between the bins. They are shown separately for the inclusive sample and the photon plus no-jets and photon plus jet subsamples in figure 6.1 and figure 6.2 for the analysis bins in  $(E_T^\gamma, \eta^\gamma)$  and the analysis bins in  $Q^2$ , respectively.

The purity is found to be above 50 % in most of the analysis bins, while the stability remains well above 70 %. Migration between the bins is hence in an acceptable range. The acceptance factor  $\mathcal{A}_i$  varies between 20 % and 55 %. The highest corrections apply for low factors  $\mathcal{A}_i$  and can be found towards the forward direction, where an increasing number of conversions affect the selection efficiency, and in the low and high  $Q^2$  domain. In the lowest  $Q^2$  bin the selection efficiency is affected by the fiducial cuts and the missing innermost SpaCal region for the HERA II data taking period. Towards higher  $Q^2$  the acceptance is increasingly diminished due to electrons missing the SpaCal and being reconstructed in the LAr. The acceptance range of the SpaCal enters the phase space definition (see table 7.2) in the allowed polar angle range of the scattered electron of  $153^\circ < \theta^e < 177^\circ$ . However, the polar angle range is adjusted to the nominal interaction vertex and for forward shifted collision vertices the electron may pass outside the SpaCal also at  $\theta^e > 153^\circ$ . The probability for an electron to miss the outer

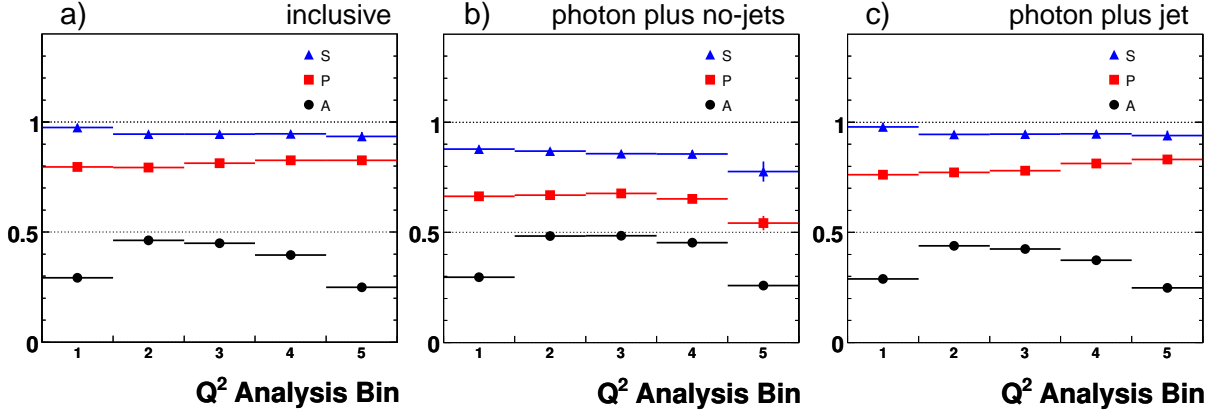


FIGURE 6.2: Acceptance factor  $\mathcal{A}$ , purity  $\mathcal{P}$  and stability  $\mathcal{S}$  for the 5 analysis bins in  $Q^2$  defined in table E.1. The quantities are shown for (a) the inclusive sample, (b) the photon plus no-jets and (c) the photon plus jet subsamples.

boundary of the SpaCal increases with  $Q^2$  and is zero for  $Q^2 \lesssim 40 \text{ GeV}^2$ .<sup>2</sup> Within the wheels of the LAr calorimeter the acceptance factor is approximately constant with a slight tendency to increase towards higher photon energies. Although the selection efficiency increases with  $E_T^\gamma$ , usually implying a higher acceptance factor, immigration at low  $E_T^\gamma$  largely outweighs the smaller selection efficiency and leaves only a slight increase of the acceptance factor with  $E_T^\gamma$ .

The statistical error of the acceptance factor due to the finite statistics in the MC samples is included in the statistical error of the final cross sections and is below 1 % in any analysis bin.<sup>3</sup>

### 6.1.2 Hadron Corrections

Since the cross sections are corrected to the generated hadron level by equation (6.1), also the parton level calculations need to be corrected to the hadron level for a meaningful comparison. Similar to the acceptance factor described in section 6.1.1, the hadron correction factors  $f_i^{had}$  are determined in the same analysis bins using the scaled signal MC. The correction factor for bin  $i$  is defined as

$$f_i^{had} = N_i^{\text{gen, had}} / N_i^{\text{gen, pt}}, \quad (6.5)$$

where

- $N_i^{\text{gen, had}}$  is the number of events generated in bin  $i$  on hadron level.
- $N_i^{\text{gen, pt}}$  is the number of events generated in bin  $i$  on parton level.

The obtained correction factors are listed for any considered analysis bin in tables F.1 to F.4. The highest corrections apply for low energies of the photon ( $3 < E_T^\gamma < 4 \text{ GeV}$ ) with a factor

<sup>2</sup>An electron missing the SpaCal's outer boundary at  $Q^2 \lesssim 40 \text{ GeV}^2$  requires  $z_{vtx} > +40 \text{ cm}$  or  $E_e' < 10 \text{ GeV}$ .

<sup>3</sup>In the analysis of less isolated photons presented in section 7.4 higher errors of the acceptance factors occur.

of down to  $f^{had} \approx 0.70$  and they are smallest for high photon energies ( $E_T^\gamma > 6$  GeV), where the correction factor approaches one. At low energies, hadron level jets can be extremely wide, which increasingly affects the resolution in  $z$ . The correction also increases towards the forward direction.

The uncertainty of the correction factor is estimated by comparing the correction factors obtained from PYTHIA with those from HERWIG. The correction for the total inclusive cross section is in average -14 % with an associated uncertainty of 5 %. The combined uncertainties of the theoretical predictions from hadronisation corrections and proton parton distributions amount to up to 11 % (cf. section 2.1).

## 6.2 Systematic Uncertainties

For the determination of systematic errors two additional event samples are used which provide clean signatures of photons (DVCS sample) and electrons (BH sample) in the LAr calorimeter. The samples are discussed in appendix C. For comparison SP photons and SP electrons are reweighted in order to match the phase space distribution of the measured DVCS photons and BH electrons, respectively.

The effect of different systematic errors on the cross section is evaluated by applying variations to the MC simulation. The considered uncertainties are listed in the following.

### Shower Shapes

The uncertainties on the description of the shower shapes by the simulation are estimated by distorting the shower shape variables of the SP photons and SP electrons by a stretching factor  $k$ :

$$v^{\text{stretched}}(k) = v \cdot \left(1 + \frac{k}{100}\right), \quad (6.6)$$

where  $v$  represents any of the six shower shape variables (cf. section 5.1).<sup>4</sup> The measured shower shape variables in the BH and DVCS event samples are then compared to the distorted shower shapes in the simulation. As an example, figure 6.3 shows the shape comparison of SP and DVCS photons for the hottest cell fraction in wheel 2 (CB2) of the LAr calorimeter for different stretching factors. The simulated shape evidently tends towards higher values of the hottest cell fraction for an increasing stretching factor.

For each factor  $k$  the  $\chi^2$  can be calculated between the histograms of data and SPs as  $\sum(b_d - b_{SP})^2 / (\sigma_d^2 + \sigma_{SP}^2)$ , where the sum runs over the non-empty bins of the histograms and  $b_{d,SP}$  and  $\sigma_{d,SP}$  denote the content and error of the bins in the data (d) and SP histogram, respectively. The number of non-empty bins in the histogram corresponds to the number of

<sup>4</sup>Instead of stretching, any kind of distortion could in principle be applied. However, due to the already good description of the shower shape variables more complicated distortions are not expected to provide better estimations of the uncertainty.

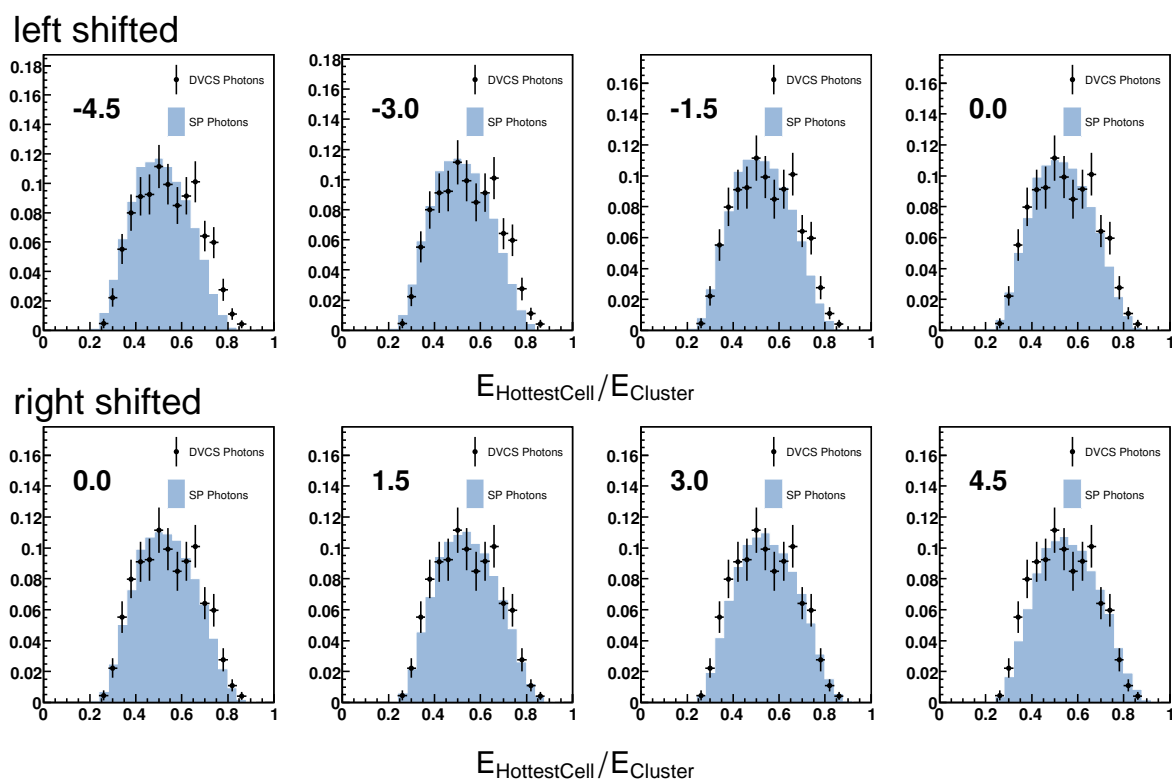


FIGURE 6.3: Hottest cell fraction of DVCS photons in CB2 compared to distorted SP photons (top row - left shifted, bottom row - right shifted). The stretching factor  $k$  increases from left to right and is stated in the top left corner of the histogram areas.

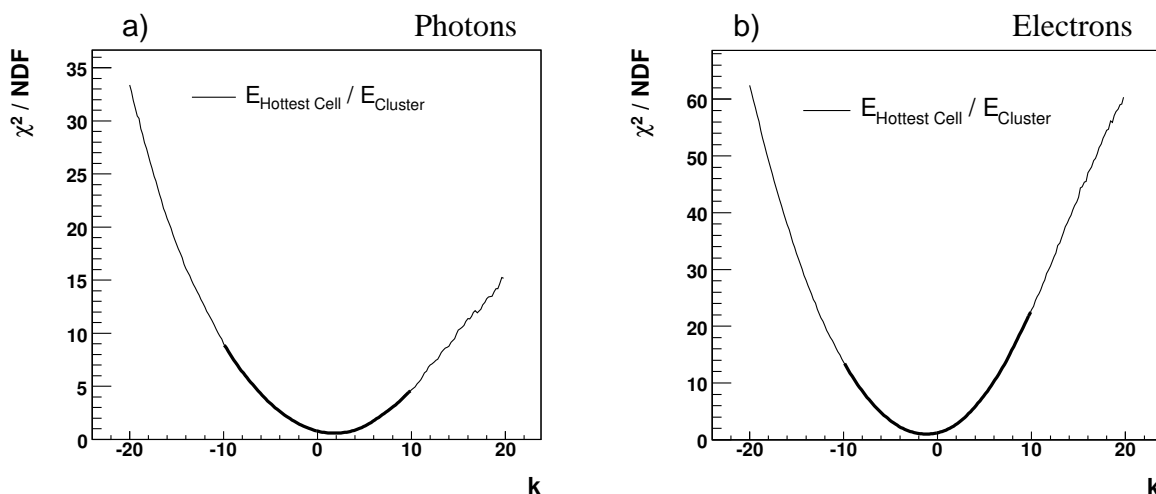


FIGURE 6.4:  $\chi^2/\text{NDF}$  distribution in dependence of the stretching factor  $k$  for the hottest cell fraction in wheel 2. a) Distribution for a comparison of DVCS photons with distorted SP photons. b) Distribution for a comparison of BH electrons with distorted SP electrons.

degrees of freedom (NDF). In figure 6.4 the  $\chi^2/\text{NDF}$  distribution in dependence of the stretching factor  $k$  is shown for the comparison of photons and electrons again for the hottest cell fraction in wheel 2. Clear minima are observed, which are found by a polynomial fit to be at  $k = 1.8$  for the photons and  $k = -1.2$  for the electrons

As statistical and systematic effects are involved, the  $k$  range defined by  $\min(\chi^2) \pm 1$  does not correspond to the desired uncertainty of the shower shape simulation. As an indicator for the uncertainty, the  $k$ -range given by  $\min(\chi^2) \pm \text{NDF}$  is used, which is  $[-3.6, 1.2]$  for the electron clusters and  $[-2.2, 5.6]$  for the photon clusters in the considered example. The calculation of these ranges is, however, in most cases biased by the limited statistics of the BH and DVCS samples and therefore the final uncertainties are instead estimated by close examination of the histogram comparisons taking the evaluated ranges as guidance. In cases where the photon and electron comparison leads to different ranges, more weight is given to the photon simulation. In the example of the hottest cell fraction in wheel 2, a  $k$ -range of  $[-3.0, 3.0]$  is finally taken as the uncertainty. Such ranges are derived for all six shower shape variables and separately for any wheel. They are listed in table 6.1. The effect of the stretching factor depends on the shape of the distribution. When comparing different variables, a higher stretching factor can hence not necessarily be associated with a higher uncertainty.

The fits for the signal extraction (cf. section 5.3) are repeated with the distorted input distributions. Due to the correlation of the variables the transverse radius (up/down), the hottest cell fraction (down/up) and the hot core fraction (down/up) are varied simultaneously, as motivated in section 5.1.2. The resulting systematic error on the total inclusive cross section is  $+10.2\%$  and  $-12.8\%$ . It varies between  $11\%$  and  $25\%$  for the single differential cross sections. The error increases with increasing  $E_T^\gamma$  and towards large  $\eta^\gamma$  and is independent of  $Q^2$ .



TABLE 6.1: Derived uncertainties of the shower shape variables in terms of the stretching factor  $k$ .

		Wheel				
		1	2	3	4	5
$R_T$	+	2.0	5.0	1.0	4.5	0.0
	-	4.0	1.8	4.0	3.0	9.0
$K_T$	+	3.0	5.0	2.0	4.0	8.0
	-	7.0	10.0	9.0	8.0	8.0
$S_T$	+	1.5	1.7	3.0	4.0	4.0
	-	3.0	5.0	1.7	3.0	4.0
HCeF	+	4.0	3.0	6.0	2.0	1.0
	-	1.8	3.0	2.0	8.0	2.0
HCF	+	1.6	1.5	1.2	1.5	8.0
	-	0.0	0.2	0.2	1.0	4.0
FLF	+	10.0	10.0	10.0	15.0	8.0
	-	0.0	0.0	2.0	0.0	9.0

### Photon Energy

The photon energy calibration is discussed in section 4.7.2. The uncertainty on the photon energy measurement is estimated using the BH and DVCS control samples. For the BH events the cluster transverse energy is compared with the track measurement. For DVCS events, the energy is compared to the energy calculated using the double angle method. The photon energy scale uncertainty estimated with this method varies for the different wheels of the LAr calorimeter. The uncertainties amount to 1 % in CB1, 2 % in CB2 and CB3, 3 % in FB1 and 4 % in FB2. The resulting error on the total inclusive cross section is +3.6 % and -2.6 %.

### Photon Angle

The uncertainty of the polar angle of the photon is found by comparing the polar angle measurements of the track and cluster in BH electrons. An uncertainty of 3 mrad (4 mrad in FB2) is attributed to the polar angle measurement of the photon. The resulting error on the total inclusive cross section is +0.1 % and -0.7 %.

### Electron Energy and Angle

An uncertainty varying from 1 % ( $E'_e = 27.6$  GeV) to 2 % ( $E'_e = 10.0$  GeV) is attributed to the energy of the scattered electron [92] and an uncertainty of 2 mrad to the measurement of the

scattering angle. This affects the total inclusive cross section by +1.9 % and -2.9 %.

### Hadronic Final State

A 3 % uncertainty is attributed to the energy of hadronic final state objects [93]. The resulting error on the total inclusive cross sections is +1.2 % and -0.7 %.

### Cluster Overlap Modelling

A 5 % uncertainty is applied for the cluster overlap modelling in the SP neutral hadron background which corresponds to half the size of the maximum correction.

### Model Dependence

The model dependence of the acceptance corrections is derived from the differences between the PYTHIA and HERWIG simulation. Therefore, PYTHIA is reweighted in  $Q^2$  and  $y$  to the restricted phase space simulated by HERWIG. A resulting error of 5 % is found for the inclusive and photon plus jet and 10 % for the photon plus no-jets cross sections.

### LL/QQ Ratio

The uncertainty of the ratio of the  $LL$  and  $QQ$  contributions for the acceptance corrections is taken into account by varying the scaling factor for PYTHIA from 1.5 to 3. The resulting error on the total inclusive cross section is +1.4 % and -0.8 %. For the double differential cross section, a systematic error of up to 5 % is found. In regions with  $\eta^\gamma > -0.6$ , the systematic error is below 1 %.

### Trigger Efficiency

An uncertainty of 1 % is attributed to the simulation of the trigger efficiency, which was studied in section 4.2.2.

### Track Reconstruction Efficiency

The track reconstruction efficiency has been studied in NC DIS events [73] and for combined BH and DVCS events [94].<sup>5</sup> A track reconstruction inefficiency affects the rejection of background from charged particles and is taken as 1 %, which results in an error of  $\pm 0.3$  % for the total inclusive cross section.

---

<sup>5</sup>In combined BH and DVCS events, clusters are selected with associated hits in the CIP. The fraction of events with a track in the CJC defines the track reconstruction efficiency.

### Photon Conversion Probability

In H1 two methods were used to study the description of the dead material in front of the calorimeter. The first method uses the innermost tracking chamber CIP to identify photons by requiring no signal in any CIP plane. The conversion probability between the CIP and the LAr was found to be well described by the simulation [94]. The second method identifies converted photons by reconstructing the tracks of the electron positron pair and their displaced vertex [95]. The dead material between the nominal vertex and the LAr was found to be well described for HERA I while some dead material in the CIP was missing for HERA II. The missing material was traced back to a bug in the simulation describing the geometry of the readout cables in the CIP. The missing dead material underestimates the conversion probability in HERA II by at most 2 % [96]. The missing dead material is not corrected, but accounted for in the systematic error. The resulting systematic error on the cross sections is 2 %.

### Luminosity Measurement

The uncertainty on the luminosity measurement is 2 %.

In each analysis bin the individual effects of these experimental uncertainties are combined in quadrature. The systematic uncertainty obtained on the total inclusive cross section is +13.6 % and -15.5 %. The largest contribution to this uncertainty arises from the systematic effect attributed to the description of the shower shapes, which is partially correlated among measurement bins.



# CHAPTER 7

## RESULTS

---

In this chapter results are presented for the production of isolated photons in deep-inelastic scattering based on data taken with the H1 detector in the years 1999–2005 ( $227 \text{ pb}^{-1}$ , 52.1 %  $e^-p$  and 47.9 %  $e^+p$ ). The differential cross sections are compared with the signal MC predictions (section 2.2.2) as well as LO and NLO calculations (sections 2.1.1 and 2.1.2). The predictions used for comparison to the cross sections are shortly listed in table 7.1. Unless otherwise stated, the cross sections presented in this chapter are given for the phase space defined in table 7.2.

Inclusive cross sections are presented for the entire phase space (section 7.1) as well as for an increased minimum  $Q^2$  (section 7.2). For the latter also a comparison with the measurement of inclusive isolated photon production by the ZEUS collaboration [1] is shown. Exclusive cross sections for the photon plus no-jets and photon plus jet subsamples are shown in section 7.3.

Less isolated photons in the close vicinity of jets are also studied and cross sections at lower  $z$  values and in dependence of the jet resolution parameter  $R_0$  are presented in section 7.4.

### 7.1 Inclusive Isolated Photon Production

The measured inclusive isolated photon cross section for the kinematic range specified in table 7.2 is

$$\sigma(ep \rightarrow e\gamma X) = 50.3 \pm 1.7 \text{ (stat)} \begin{matrix} +6.8 \\ -7.8 \end{matrix} \text{ (syst) pb.}$$

The LO calculation predicts a cross section of 28.6 pb, while the signal MC expectation is 26.4 pb. Both predictions significantly underestimate the total inclusive cross section by almost a factor of two.

Bin averaged differential cross sections  $d\sigma/dE_T^\gamma$ ,  $d\sigma/d\eta^\gamma$  and  $d\sigma/dQ^2$  are presented in figure 7.1 (table F.1). For all measurement bins the total uncertainty is dominated by systematics. The measurements are compared to the predictions by the signal MC and the LO calculation.

TABLE 7.1: Predictions used for comparison to the measured cross sections.

	MC	Calculations
Isolated Photons ( $z > 0.9$ )		
Inclusive	signal MC	LO
Photon plus no-Jets	signal MC	LO
Photon plus Jet	signal MC	LO + NLO
Photons in Jet Vicinity		
Inclusive	scaled signal MC	–
Photon plus no-Jets	scaled signal MC	–
Photon plus Jet	scaled signal MC	–
MC Predictions		
signal MC	PYTHIA ( $QQ$ ) + RAPGAP (rad.) ( $LL$ )	
scaled signal MC	PYTHIA $\times 2.3$ ( $QQ$ ) + RAPGAP (rad.) ( $LL$ )	

The correction factor  $f^{had}$  for the correction of the LO calculation to hadron level is listed in all the cross section tables in appendix F.

The LO calculation lies furthest below the data at low  $Q^2$ . It provides a reasonable description of the shapes of the data distributions in  $E_T^\gamma$  and  $\eta^\gamma$ , with some tendency to lie further below the data at high transverse energies and central and forward rapidities ( $\eta^\gamma > -0.6$ ) of the photon. The  $LL$  and  $QQ$  contributions are shown separately in figure 7.1. Their relative contributions depend strongly on  $\eta^\gamma$  and  $Q^2$ . For backward photons ( $\eta^\gamma < -0.6$ ), close to the scattered electron, the  $LL$  contribution is of similar magnitude to that of  $QQ$ . For forward and central photons ( $\eta^\gamma > -0.6$ ) the  $QQ$  contribution dominates. The interference contribution  $LQ$  is included in the sum, but not shown separately as it amounts to a few percent of the total cross section only.

The cross section predicted by the signal MC agrees reasonably well with the LO calculation. The PYTHIA prediction follows the shape of the  $QQ$  contribution, whereas the RAPGAP prediction follows the  $LL$  contribution. In the following the measured cross sections are only compared to the LO calculations, as the signal MC and LO give similar predictions.

Figure 7.2 (table F.2) presents the  $E_T^\gamma$  dependence of the cross section in five different bins in  $\eta^\gamma$ , corresponding to the wheel structure of the LAr calorimeter. For backward photons ( $\eta^\gamma < -0.6$ ), the  $LL$  and the  $QQ$  terms are of similar magnitude. As the  $LL$  contribution is very small for  $\eta^\gamma > -0.6$ , the underestimation of the data by the LO calculation by roughly a factor two can be attributed mainly to an underestimated  $QQ$  contribution. However, the shape of the distributions is found to be reasonably reproduced.

TABLE 7.2: Phase space region in which isolated photon cross sections are measured together with the definition of jets. Kinematics is defined in the H1 laboratory frame.

### Isolated Photon Cross Section Phase Space

Inclusive cross section
-------------------------

$$\begin{aligned}
 &3 < E_T^\gamma < 10 \text{ GeV} \\
 &-1.2 < \eta^\gamma < 1.8 \\
 &z = E_T^\gamma / E_T^{\text{photon-jet}} > 0.9 \\
 &E_e' > 10 \text{ GeV} \\
 &153 < \theta_e < 177^\circ \\
 &4 < Q^2 < 150 \text{ GeV}^2 \\
 &W_X > 50 \text{ GeV} \\
 &y > 0.05 \\
 &\sqrt{s} = 319 \text{ GeV}
 \end{aligned}$$

Jet definition
----------------

$$\begin{aligned}
 &k_T \text{ algorithm with } P_T\text{-weighted} \\
 &\text{recombination scheme, } R_0 = 1 \\
 &P_T^{\text{jet}} > 2.5 \text{ GeV} \\
 &-1.0 < \eta^{\text{jet}} < 2.1 \text{ (hadronic jet)} \\
 &-2.0 < \eta^{\text{photon-jet}} < 2.1 \text{ (photon-jet)}
 \end{aligned}$$

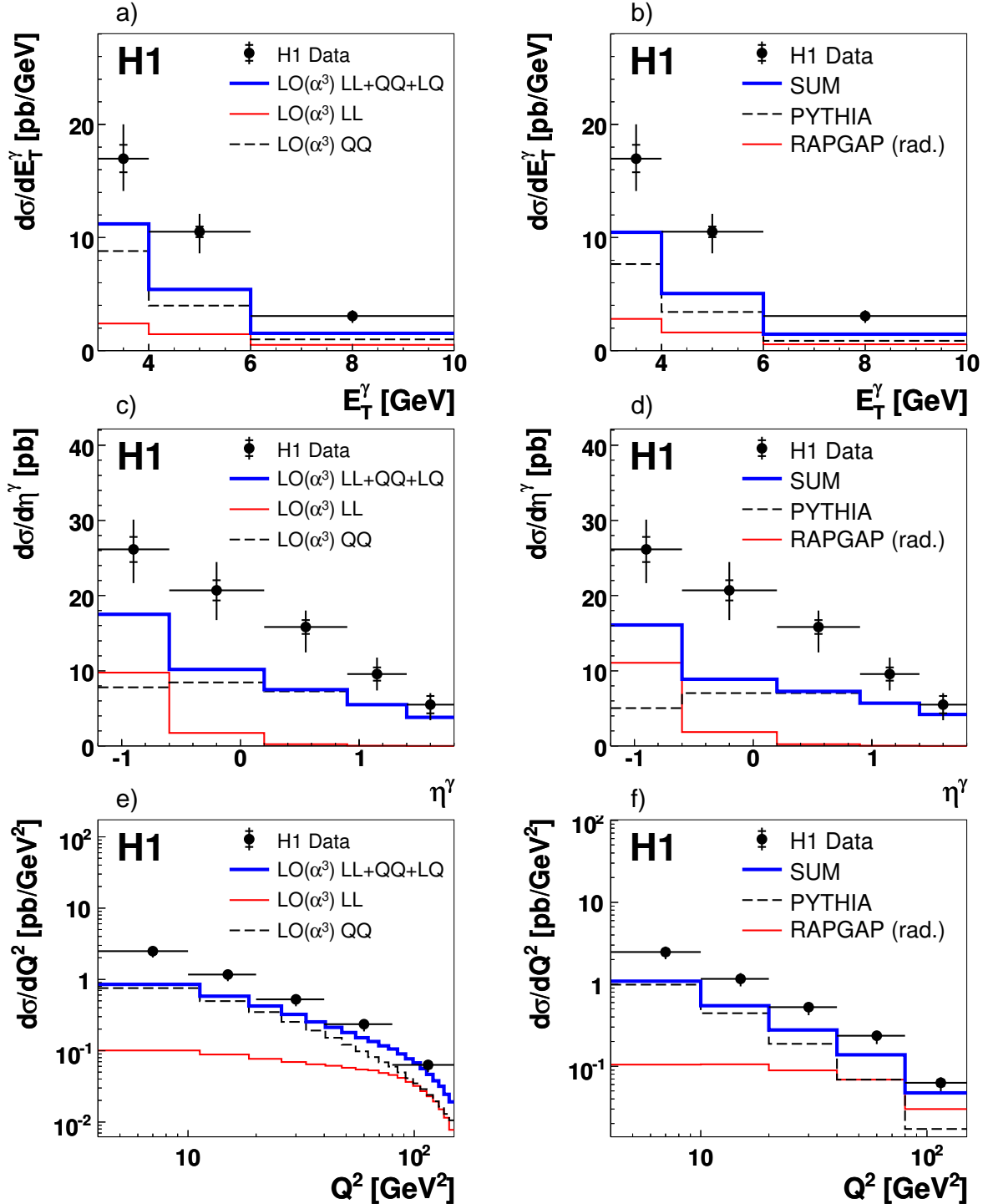


FIGURE 7.1: Differential cross sections for inclusive isolated photon production  $d\sigma/dE_T^\gamma$ ,  $d\sigma/d\eta^\gamma$ , and  $d\sigma/dQ^2$  in the kinematic range specified in table 7.2. The inner error bars on the data points indicate the statistical error, the full error bars contain in addition the systematical errors added in quadrature. The cross sections in (a, c, e) are shown together with a leading order,  $O(\alpha^3\alpha_s^0)$ , calculation corrected for hadronisation effects, *LL* corresponding to radiation from the electron and *QQ* to radiation from the quark. The same cross sections are shown in (b, d, f) together with the prediction from PYTHIA for photon emission from the quark and from RAPGAP (rad.) for emission from the electron.



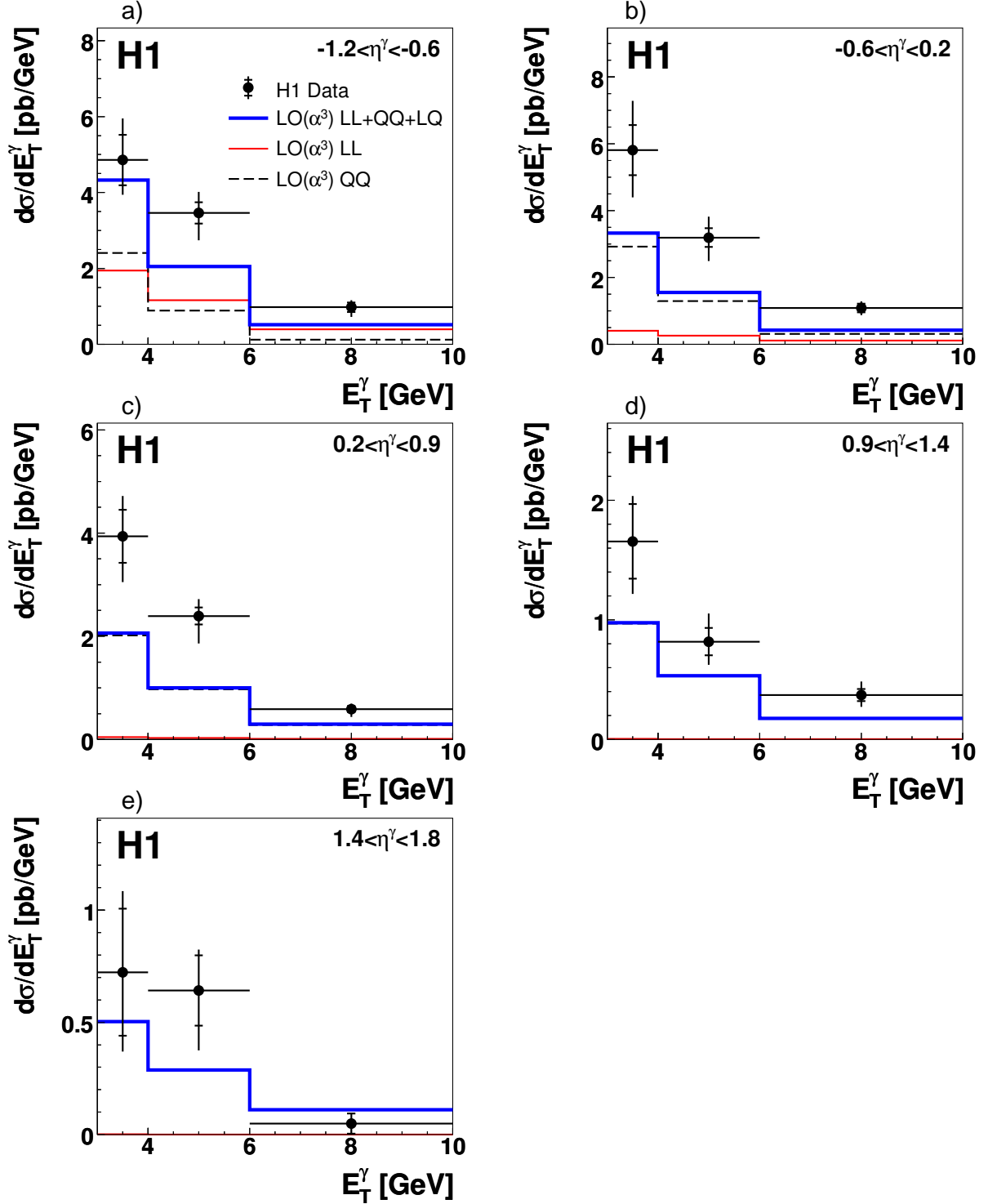


FIGURE 7.2: Differential cross sections  $d\sigma/dE_T^\gamma$  for inclusive isolated photon production in the kinematic range specified in table 7.2, in  $\eta^\gamma$  bins corresponding to the wheel structure of the LAr calorimeter (see table E.1). The  $LL$  contribution is negligible for  $\eta^\gamma > 0.2$ . The measurements are compared to a leading order calculation, as described in the figure 7.1 caption.

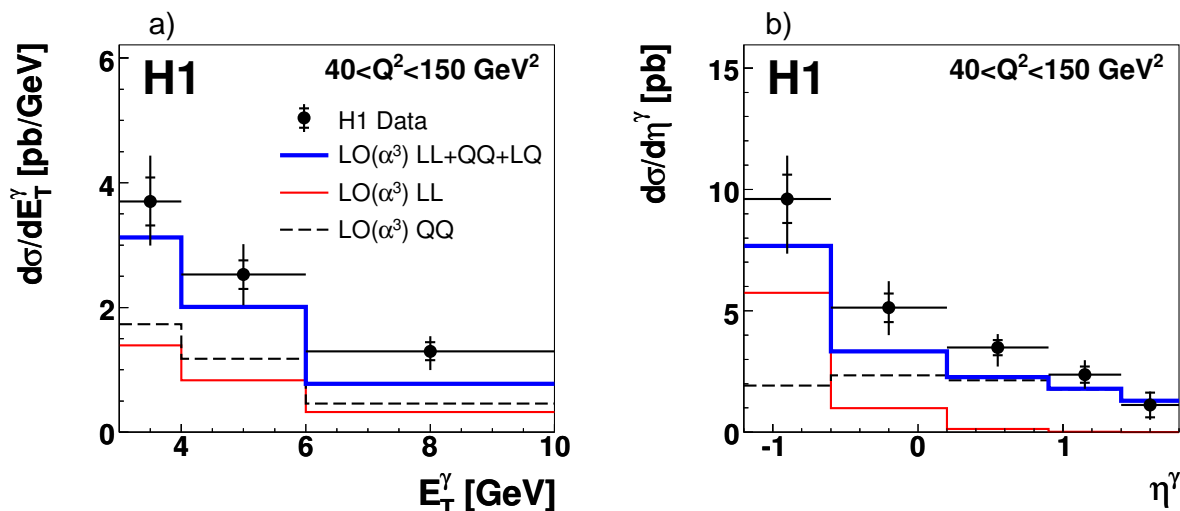


FIGURE 7.3: Differential inclusive cross sections  $d\sigma/dE_T^\gamma$  (a),  $d\sigma/d\eta^\gamma$  (b) for isolated photon production in the kinematic range specified in table 7.2 and the additional criterion  $40 < Q^2 < 150 \text{ GeV}^2$ . The cross sections are compared to a leading order,  $\mathcal{O}(\alpha^3\alpha_s^0)$ , calculation as in figure 7.1.

## 7.2 Isolated Photons at high $Q^2$

At  $Q^2 > 40 \text{ GeV}^2$  the measurements agree better with the LO predictions, as can be seen in figure 7.3 (table F.3).

The total inclusive cross section for  $Q^2 > 40 \text{ GeV}^2$  is

$$\sigma(ep \rightarrow e\gamma X) = 14.0 \pm 0.8 \text{ (stat)} \text{ }^{+2.2}_{-2.1} \text{ (syst)} \text{ pb.}$$

The LO (10.3 pb) prediction is about 30 % below the data. The shapes of the  $d\sigma/dE_T^\gamma$  and  $d\sigma/d\eta^\gamma$  distributions are well reproduced. According to the prediction the relative contribution of  $LL$  is higher than at low  $Q^2$ . Whereas in the  $QQ$  process the measured  $Q^2$  corresponds to the virtuality of the exchanged photon, in the  $LL$  process the measured  $Q^2$  is typically larger than the virtuality of the exchanged photon (see section 1.3). Therefore, the measured  $Q^2$  distribution falls less steeply in the  $LL$  process and the relative contribution of  $LL$  is expected to increase for kinematic reasons.

The present measurement is extrapolated to the phase space of the analysis performed by the ZEUS collaboration [1] ( $Q^2 > 35 \text{ GeV}^2$ ,  $y > 0$ ,  $E'_e > 10 \text{ GeV}$ ,  $139.8 < \theta_e < 171.9^\circ$  and  $5 < E_T^\gamma < 10 \text{ GeV}$ ). The extrapolation is not possible for  $\eta^\gamma < -0.6$ , since for  $\eta^\gamma < -0.6$  the allowed polar angle range of photon and electron would overlap when otherwise extrapolating to the kinematic range used in the ZEUS analysis and the separation of photon and scattered electron could not be guaranteed. In the present analysis as well as in the ZEUS analysis isolation between the electron and photon is assured by well separated ranges of the allowed

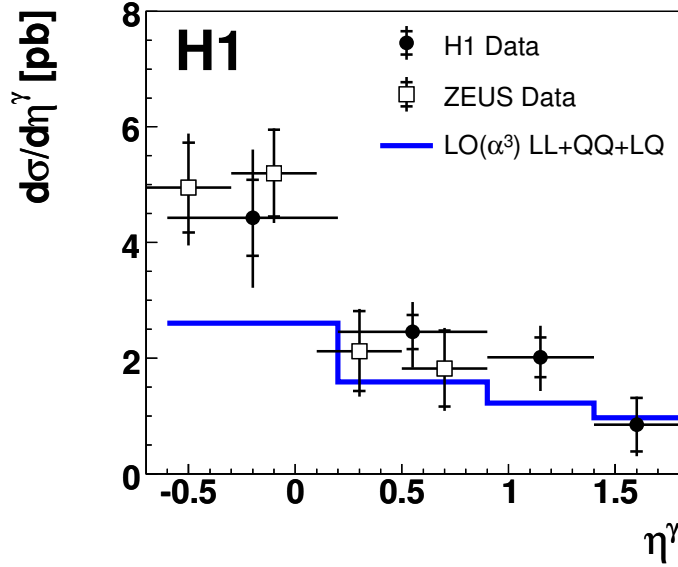


FIGURE 7.4: Differential cross sections  $d\sigma/d\eta^\gamma$  for the inclusive isolated photon production in comparison to the previous measurement by ZEUS [1] for  $Q^2 > 35 \text{ GeV}^2$ ,  $E'_e > 10 \text{ GeV}$ ,  $139.8^\circ < \theta_e < 171.9^\circ$  and  $5 < E_T^\gamma < 10 \text{ GeV}$ . The additional condition  $W_X > 50 \text{ GeV}$  is used in this analysis only. The cross sections are compared to a leading order,  $\mathcal{O}(\alpha^3\alpha_s^0)$ , calculation as in figure 7.1. The calculation is corrected for hadronisation effects in contrast to the comparison in [31].

polar angles for the electron and photon.

Figure 7.4 shows the comparison of the differential cross section  $d\sigma/d\eta^\gamma$ . A good agreement between the two measurements is observed. In the ZEUS analysis photon radiation from the electron is neglected in the acceptance corrections, and in addition no  $W_X$  cut is applied. A rough estimate shows that with the  $W_X$  cut used by H1 and the acceptance calculation with the combination of PYTHIA and RAPGAP, the ZEUS cross sections are expected to be lower by about 10 – 30 %. A different photon isolation criterion is used in the ZEUS analysis which is not corrected for. The ZEUS analysis requires  $E_T^\gamma/E_T^{cone} > 0.9$ , where  $E_T^{cone}$  is the transverse energy within a cone in  $\eta$ - $\phi$  of radius one around the photon candidate. Studies of isolated photons in photoproduction indicate that the two different isolation criteria give very similar results [94]. The measurement in the present analysis significantly extends the kinematical region probed by ZEUS in transverse energy, pseudorapidity and  $Q^2$ .

### 7.3 Photons plus Jet and Photons plus no-Jets

The cross section for jet production in association with isolated photons is studied. The measurement is performed in the phase space defined for the inclusive cross section with an additional jet requirement or veto as shown in table 7.2.

The total cross section for photon plus no-jets is measured as

$$\sigma(ep \rightarrow e\gamma Y) = 18.8 \pm 1.2 \text{ (stat)}^{+3.3}_{-3.4} \text{ (syst) pb,}$$

where  $Y$  contains no accepted hadronic jet. The prediction of the LO calculation is 11.7 pb. The cross section for the photon plus at least one jet is measured as

$$\sigma(ep \rightarrow e\gamma \text{ jet } X) = 31.6 \pm 1.2 \text{ (stat)}^{+4.2}_{-4.8} \text{ (syst) pb.}$$

The prediction of the LO calculation is 16.7 pb. For both samples the predictions are significantly lower than the data. The observed ratio of data to LO prediction is very similar to the inclusive measurement for both samples. As in the inclusive sample similar conclusions are found for the MC predictions.

A comparison to a NLO calculation is possible for the photon plus jet cross sections. The NLO calculation predicts a cross section for photon plus jet of  $20.2 \pm 0.6$  pb, about 20 % higher than the LO prediction but still roughly 35 % lower than the data. A higher cut on  $P_T^{\text{jet}} > 4$  GeV does not significantly improve the description of the data.

The measured differential cross sections for the photon plus no-jets and photon plus jet selections are presented in table F.4. They are compared with the LO predictions in figure 7.5. For both samples the LO prediction describes the shapes of the  $d\sigma/dE_T^\gamma$  and  $d\sigma/d\eta^\gamma$  distributions reasonably well and is furthest below the data at low  $Q^2$ , where the  $QQ$  term dominates. All four diagrams in figure 1.7 contribute to the photon plus no-jets and photon plus jet sample, but the  $LL$  contribution is largely suppressed for the photon plus no-jets sample due to the cut on  $W_X$ . Since, at leading order, the fragmentation contribution to the cross section enters only the photon plus no-jets sample, the observed excess can not solely be attributed to an underestimation of that contribution. The cross section for photon plus jet production is roughly two times higher than for photon plus no-jets. This is in contrast to the inclusive  $ep \rightarrow eX$  cross section, where topologies with an additional jet are suppressed by  $O(\alpha_s)$ . The similar cross sections for photon events with or without jets can be explained by the fact that both topologies correspond to the same order in the perturbative QCD.

In addition, the differential cross sections  $d\sigma/dE_T^\gamma$ ,  $d\sigma/d\eta^\gamma$  and  $d\sigma/dQ^2$  for the photon plus jet selection are compared to the NLO prediction (figure 7.5 right). On average, the NLO prediction for the photon plus jet sample is higher than the LO prediction, most significantly at low  $Q^2$ , but is still lower than the data by roughly 35 %. The shapes of all three differential cross sections are described well by the NLO prediction.

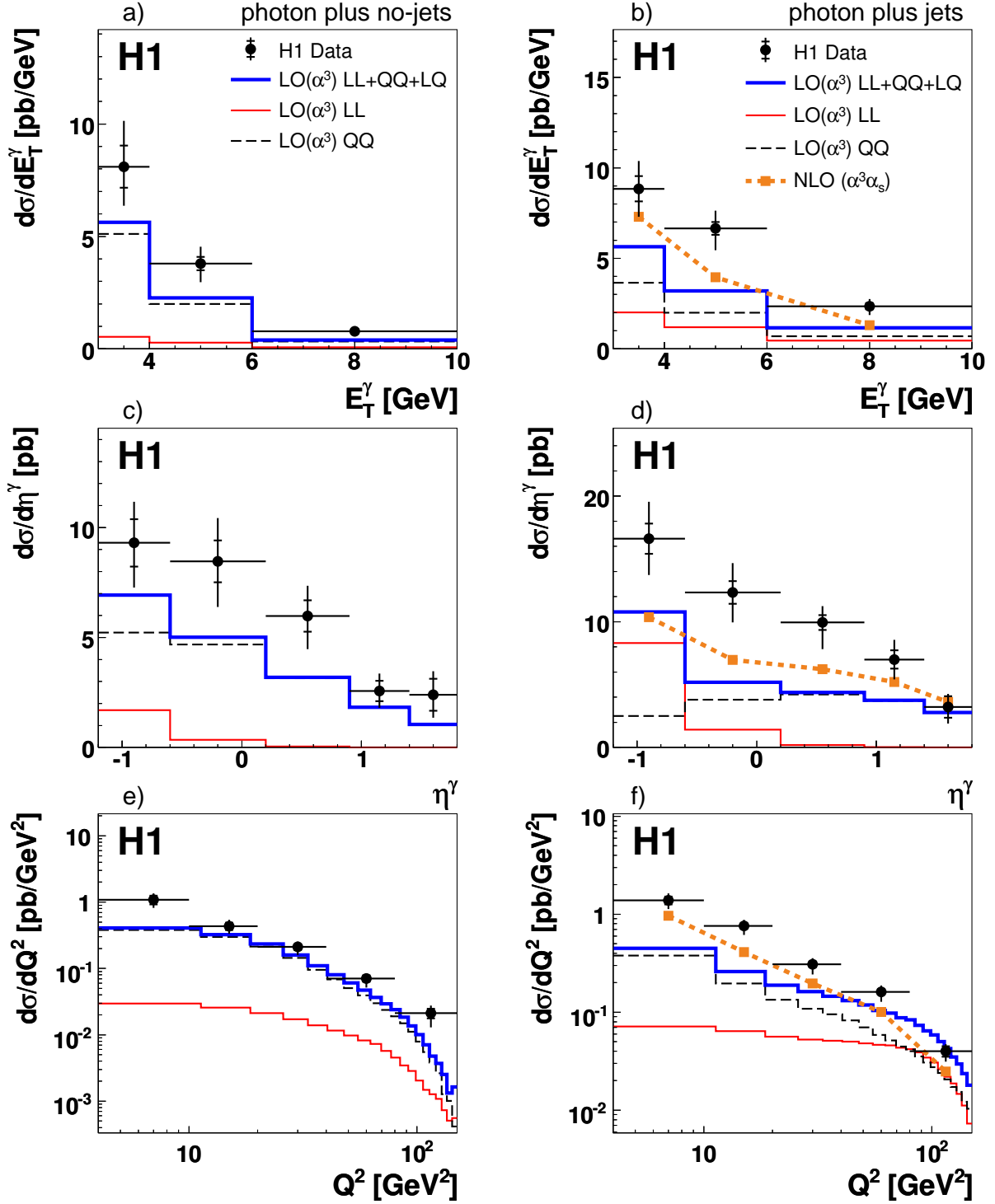


FIGURE 7.5: Differential cross sections  $d\sigma/dE_T^\gamma$ ,  $d\sigma/d\eta^\gamma$  and  $d\sigma/dQ^2$  for photon plus no-jets (a, c, e), and photon plus jet (b, d, f) production in the kinematic range specified in table 7.2. The cross sections are compared to a leading order,  $\mathcal{O}(\alpha^3\alpha_s^0)$ , calculation as in figure 7.1. The photon plus jet sample is additionally compared to a NLO ( $\alpha^3\alpha_s$ ) calculation. Both, LO and NLO predictions are corrected for hadronisation effects. The points in the NLO calculation indicate the bin averaged cross section. The scale uncertainties for the NLO calculation are smaller than 3% and not shown in the comparisons.

## 7.4 Photons in Jet Vicinity

The production of isolated photons in DIS involves a non-perturbative long distance process, in which the photon is produced through the fragmentation of a hadronic quark jet. The probability of this transition is described by the quark-to-photon fragmentation function, which is not predictable within perturbation theory and needs to be determined from experimental data (cf. section 1.3.1).

The contribution of final state photons produced in the fragmentation of hadronic jets is expected to strongly increase with diminishing isolation of the photons. In order to select photons in a close hadronic vicinity the isolation requirement (cf. section 4.5) can be altered in two ways. A measurement of photons at smaller  $z$  values is presented in section 7.4.1 or as an alternative the jet resolution parameter  $R_0$  is varied while the  $z$  constraint remains unchanged. The measurement of photons in dependence of  $R_0$  is presented in section 7.4.2.

This chapter presents the first measurement of less isolated photons in close hadronic vicinity at HERA. The presented systematic errors are not evaluated in comparable detail as in the measurement of isolated photons presented in the previous sections of this chapter and should be considered as estimates.

The LO calculation for less isolated photons was not available for the implemented jet algorithm (see section 4.5). Since the jet algorithm strongly affects the isolation definition, the MC prediction is used for comparison with the measured cross sections.

### 7.4.1 Measurement at low $z$

The measurement of isolated photons for the phase space defined in table 7.2 is repeated for lower values of  $z = E_T^\gamma / E_T^{\text{photon-jet}}$  down to  $z = 0.5$ . In these measurements the shower shape description and the acceptance corrections need to be reconsidered.

#### Measurement

For photon candidates in a close hadronic vicinity the cluster overlap is expected to contribute stronger than for well isolated photon candidates. Figure 7.6 shows the normalised transverse radius (a) and discriminator distribution (b) for neutral hadron background as predicted by RAPGAP (non-rad.) for strongly isolated photon candidates ( $z > 0.9$ ) and less isolated photon candidates ( $0.6 < z < 0.7$ ). As expected for more frequent cluster overlaps, less isolated photon candidates are found to be more photon-like (cf. section 5.3.1), since background-like clusters with larger transverse radii are more likely to overlap with surrounding clusters and to exceed the maximum transverse radius allowed ( $R_T < 6$  cm). According to RAPGAP (non-rad.) the effect occurs already at  $z < 0.9$  and does not grow significantly stronger down to values of  $z \approx 0.5$ . In the SP neutral hadron background used for the fit the cluster overlap is hence modelled with an increased constant  $a = 0.009 \text{ cm}^{-2}$  for the photon signal extraction at  $z < 0.9$  (cf. equation (5.12)).

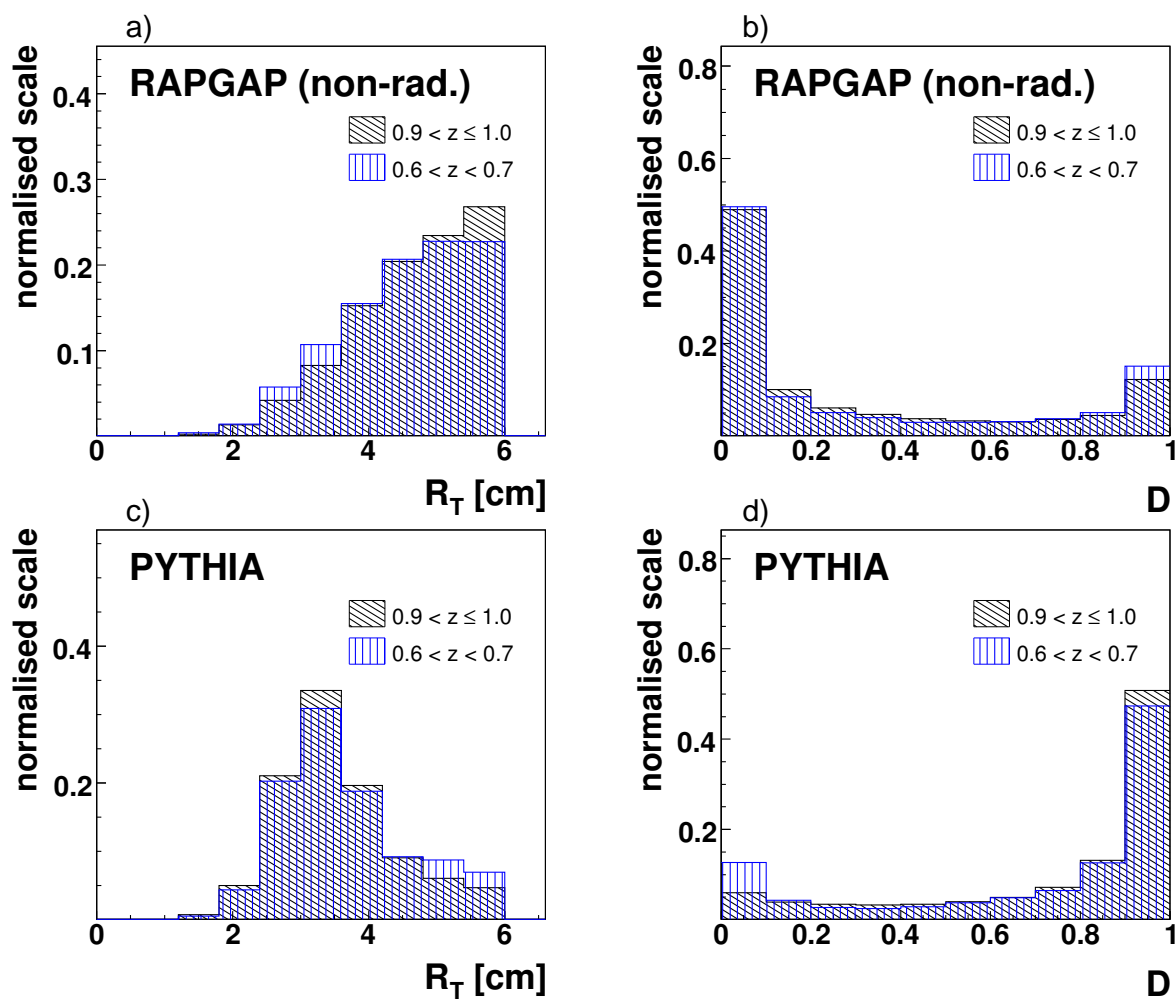


FIGURE 7.6: Comparison of the normalised distributions of the transverse radius (a, c) and the discriminator (b, d) for well isolated ( $z > 0.9$ ) and less isolated ( $0.6 < z < 0.7$ ) photon candidates shown for RAPGAP (non-rad.) neutral hadron background (a, b) and PYTHIA photons (c, d).

Figure 7.6 c) and d) show the same comparison of strongly isolated and less isolated photon candidates for the photon signal as predicted by PYTHIA. Apparently the cluster overlap alters the signal distributions towards more background-like distributions, which cannot be accounted for in the employed simple cluster overlap model<sup>1</sup> and may lead to a slight underestimation of the cross sections. However, due to an increased background fraction in the selected photon candidates at  $z < 0.9$ , the shower shape description of the signal becomes less important and the signal extraction mainly relies on a good description of the background.

Table 7.3 lists the number of photon candidates, the extracted photon signal and the signal fraction for five different  $z$  bins in the inclusive event sample and the photon plus no-jets and photon plus jet subsamples. In all samples the signal fraction drops considerably for values  $z < 0.9$  to roughly 10 % and remains approximately constant down to values of  $z \approx 0.5$ . The signal fraction tends to be slightly higher for the photon plus jet sample than for the photon plus no-jets sample, which has already been observed at  $z > 0.9$  where the difference is most prominent.

For the measurement at small  $z$  values less isolated photons have been enriched in the PYTHIA MC samples. Since the cross section predicted by PYTHIA strongly decreases with decreasing  $z$  values, the available statistics of the PYTHIA samples at  $z < 0.8$  is, however, still not sufficient for a reliable estimation of the acceptance factors. Furthermore, due to the strong decrease of the PYTHIA prediction towards smaller values of  $z$  the migration from higher  $z$  values is overestimated and would need further corrections. As the extracted photon signal only slightly increases with falling  $z$  values for  $z < 0.9$  (see table 7.3), for the extraction of the cross sections at  $z < 0.8$  the same acceptance factors as in the range  $0.8 < z < 0.9$  are assumed. The ratio of the cross section for the range  $z > 0.9$  to the cross section for the range  $0.8 < z < 0.9$  is well described by the PYTHIA prediction (see below), giving some confidence in the evaluation of the acceptance correction at low  $z$ . The RAPGAP (rad.) prediction of photons radiated from the electron is negligible at  $z < 0.9$ .

Figure 7.7 shows the acceptance factors as well as the purities and stabilities for the 15 analysis bins (see table E.1) in the range  $0.8 < z < 0.9$ . Mainly due to migration from higher  $z$  values the purity drops to values of about 20 % to 50 % compared to typically more than 50 % for  $z > 0.9$ . As a consequence, the average acceptance factor is increased with respect to the high  $z$  region. The  $E_T^\gamma$  distribution as predicted by PYTHIA is falling significantly steeper at lower  $z$  than for  $z > 0.9$ . Hence, the migration affects higher photon energies strongest, which is reflected in the markedly increased acceptance factor for higher energies.

The systematic errors of the cross section for  $z > 0.9$  have been taken as a basis for the estimation of the systematic errors for less isolated photons. Due to the stronger sensitivity of the signal extraction to the background shower shape description and because of the assumption of constant acceptance factors for  $z < 0.9$ , the systematic error evaluated at  $z > 0.9$  was

<sup>1</sup>The change of the signal distributions towards more background-like clusters may be described in the SP photons by an extended cluster overlap model as discussed towards the end of section 5.3.1. Instead of rejecting the event in case of an overlap the radius is increased by a certain random-smear amount, which may depend on the target  $z$ -range and the transverse radius before the overlap.



TABLE 7.3: Number of photon candidates, number of extracted photons and the signal fraction defined as the ratio of the photon candidates to the number of extracted photons for the considered  $z$  ranges and samples.

sample	$z$	# photon cand.	# photons	signal fraction
<b>Inclusive</b>	0.5 0.6	12481	$1422 \pm 110$	11 %
	0.6 0.7	12801	$1282 \pm 112$	10 %
	0.7 0.8	11015	$1080 \pm 108$	10 %
	0.8 0.9	9278	$932 \pm 100$	10 %
	0.9 1.0	14670	$4372 \pm 145$	30 %
<b>Photon plus no-Jets</b>	0.5 0.6	7300	$836 \pm 81$	11 %
	0.6 0.7	7823	$700 \pm 86$	9 %
	0.7 0.8	6957	$611 \pm 84$	9 %
	0.8 0.9	5783	$445 \pm 78$	8 %
	0.9 1.0	8175	$1755 \pm 106$	21 %
<b>Photon plus Jet</b>	0.5 0.6	5181	$512 \pm 67$	10 %
	0.6 0.7	4978	$556 \pm 69$	11 %
	0.7 0.8	4058	$465 \pm 65$	11 %
	0.8 0.9	3495	$452 \pm 59$	13 %
	0.9 1.0	6495	$2606 \pm 95$	40 %

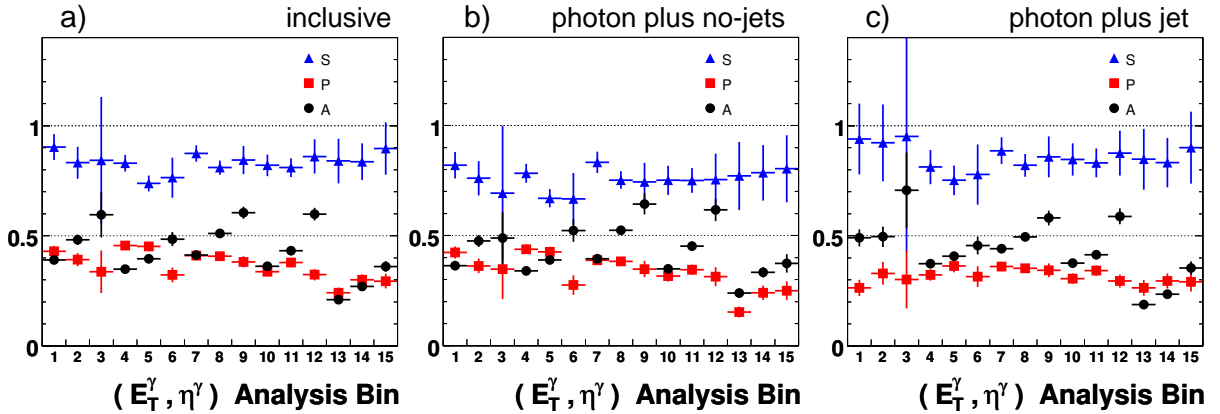


FIGURE 7.7: Acceptance factor  $\mathcal{A}$ , purity  $\mathcal{P}$  and stability  $\mathcal{S}$  for the range  $0.8 < z < 0.9$  shown for the 15 analysis bins in  $(E_T^\gamma, \eta^\gamma)$ , see table E.1. The quantities are shown for (a) the inclusive sample, (b) the photon plus no-jets and (c) the photon plus jet subsamples.

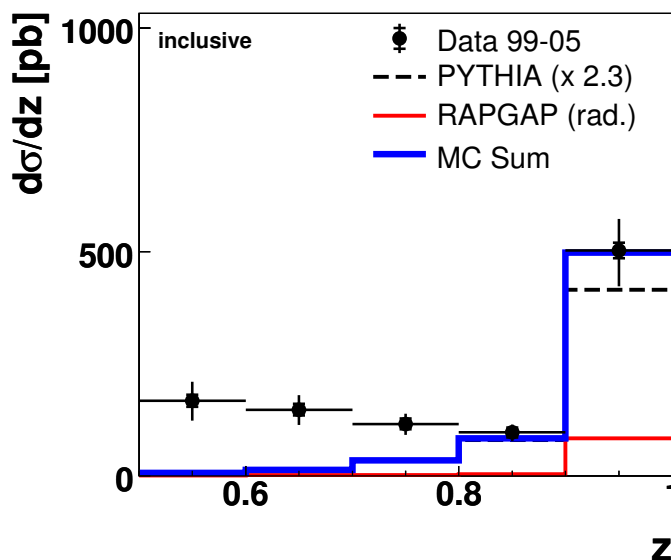


FIGURE 7.8: Differential inclusive cross sections  $d\sigma/dz$  for isolated photon production in the kinematic range specified in table 7.2 (altered  $z$  range). The cross sections are compared with the prediction from PYTHIA (scaled by a factor 2.3) for photon emission from the quark and from RAPGAP (rad.) for emission from the electron.

added in quadrature another 5% (10%, 15%, 20%) for the cross section in the  $z$  range 0.8–0.9 (0.7–0.8, 0.6–0.7, 0.5–0.6).

## Results

The measured differential cross sections  $d\sigma/dz$  for isolated photon production are shown for the inclusive sample in figure 7.8 (table F.5) and compared to the scaled signal MC.<sup>2</sup> Compared to strongly isolated photons at  $z > 0.9$  the differential cross sections are significantly smaller for  $z < 0.9$ . The measured cross sections are slightly falling in the range  $0.5 < z < 0.9$  with increasing  $z$  values and strongly increase in the last bin at  $z > 0.9$ . The scaled signal MC yields a good description of the differential cross sections for  $z > 0.8$ , but fails at  $z < 0.8$  where the prediction is significantly underestimating the measured cross sections. The shortcoming of the scaled signal MC at  $z < 0.8$  may indicate the missing fragmentation contribution in the scaled signal MC. As mentioned above the contribution of photons radiated from the electron as predicted by RAPGAP (rad.) essentially vanishes for  $z < 0.9$ .

Exclusive cross sections  $d\sigma/dz$  are shown in figure 7.9 (table F.5) for the photon plus no-jets

<sup>2</sup>In contrast to the signal MC previously used for comparison to the cross sections in this chapter, here the PYTHIA prediction is scaled by a factor 2.3 in order to obtain the possibly best matching prediction for isolated photons ( $z > 0.9$ ).

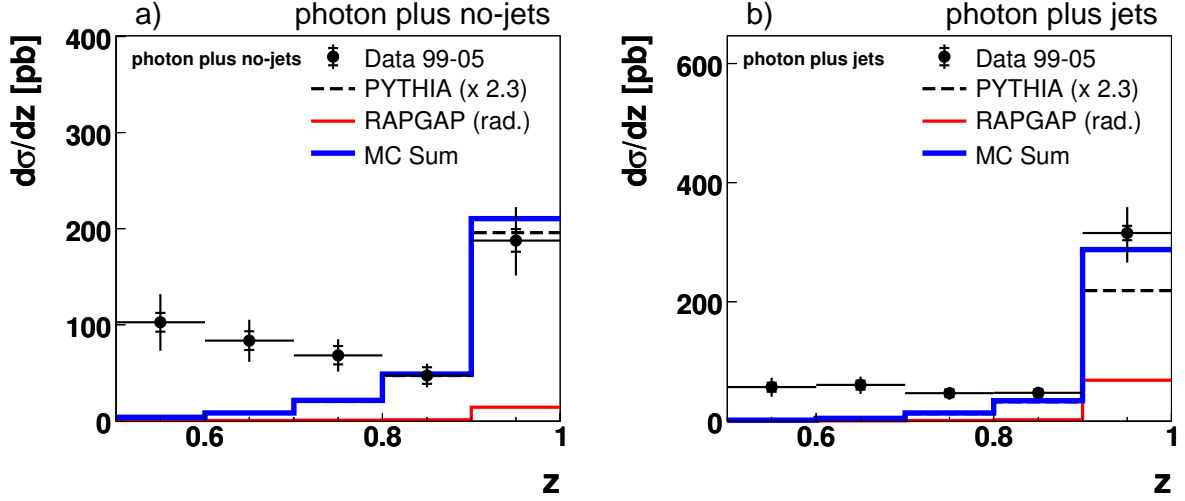


FIGURE 7.9: Differential cross sections  $d\sigma/dz$  for photon plus no-jets (a) and photon plus jet (b) production in the kinematic range specified in table 7.2 (altered  $z$  range). The measurements are compared to the scaled signal MC, as described in the figure 7.8 caption.

and photon plus jet subsamples. In both samples the cross sections are reasonably described by the scaled signal MC for  $z > 0.8$  and largely underestimated at  $z < 0.8$ . While in the photon plus jet sample the measured differential cross sections are approximately constant for less isolated photons in the range  $0.5 < z < 0.9$ , the cross sections are clearly falling in this  $z$  range with increasing  $z$  for the photon plus no-jets sample. Since the quark-to-photon fragmentation fully contributes already at leading order in the photon plus no-jets sample and only at higher orders in the photon plus jet sample, the rise of the cross sections towards low  $z$  may indicate an enhanced fragmentation contribution.

Because of the contribution at leading order, a measurement of the quark-to-photon fragmentation function in the exclusive photon plus no-jets sample in DIS was suggested by Gehrmann-De Ridder, Gehrmann and Poulsen [2].

The observed exclusive photon plus no-jets and photon plus jet cross sections can be compared to the ALEPH measurement [16] of  $d\sigma/dz_\gamma$  in exclusive 2-jet and 3-jet event samples<sup>3</sup> (as in the present analysis the photon-jet is considered as jet). The cross sections are measured in the range  $0.7 < z_\gamma < 1.0$  and shown in figure 7.10. In the 2-jet sample an increase towards low  $z_\gamma$  is observed, while for higher jet multiplicities the cross sections further decrease towards low  $z_\gamma$  values. The prominent contribution of isolated photons at  $z \approx 1$  was also observed at any jet multiplicity. The exclusive 2-jet cross sections were used for an extraction of the quark-to-photon fragmentation function. Figure 7.11 shows the 2-jet cross sections together with different parametrisations of the fragmentation function. For these cross sections

<sup>3</sup>In the ALEPH measurement  $z_\gamma$  is defined as the photon energy fraction carried by the photon-jet as opposed to the transverse energy fraction used in the present analysis.

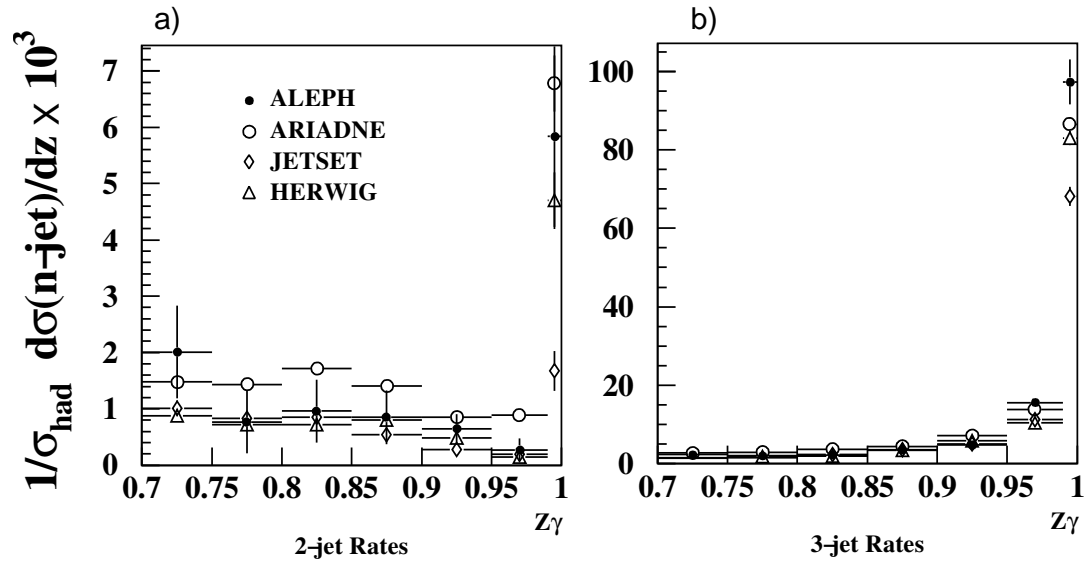


FIGURE 7.10: Differential cross sections of exclusive 2-jet (a) and 3-jet (b) events, where one of the jets is the photon-jet, as a function of  $z_\gamma$  measured by the ALEPH collaboration [16] for  $y_{\text{cut}} = 0.01$  (black dots) together with different predictions from MC simulations in order to compare the fragmentation contribution of different parton shower models.

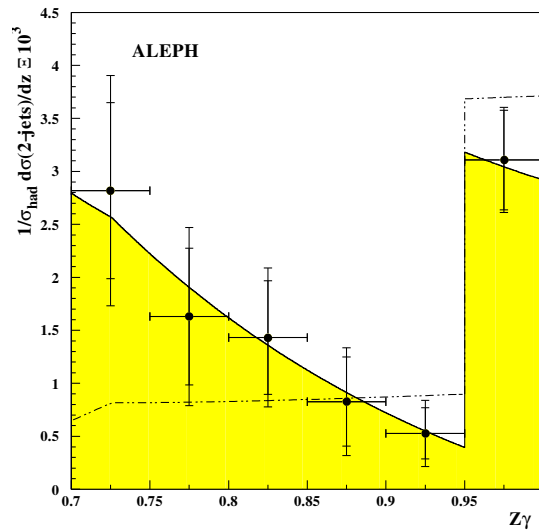


FIGURE 7.11: Differential cross sections of exclusive 2-jet events, where one of the jets is the photon-jet, as a function of  $z_\gamma$  measured by the ALEPH collaboration [16] for  $y_{\text{cut}} = 0.06$  (black dots) together with different parametrisations of the quark-to-photon fragmentation function (solid and dashed lines).

a larger jet resolution<sup>4</sup> parameter was used than for the cross sections shown in figure 7.10.

### 7.4.2 Measurement at small $R_0$

As an alternative to the measurement at lower  $z$  values the isolation requirement can be loosened by decreasing the jet resolution parameter  $R_0$  of the jet algorithm while keeping the constraint  $z > 0.9$ . The jet resolution parameter has been varied in the range  $0.1 < R_0 < 2.0$  and the total cross section for any value of  $R_0$  is compared to the prediction of the scaled signal MC. Small values of  $R_0$  allow contributions of photons in close hadronic vicinity, whereas large values of  $R_0$  impose a strong isolation requirement. As photons which fulfil the isolation requirement for large values of  $R_0$  will also fulfil the requirement at lower values of  $R_0$  the inclusive cross section is bound to decrease with increasing  $R_0$ .

The systematic errors of the cross section for  $R_0 = 1.0$  have been taken as a basis for the estimation of the systematic errors for varied jet resolution parameters. Even though weakly isolated photons contribute increasingly at smaller  $R_0$ , the extracted photon signal always includes a considerable fraction of well isolated photons. In order to account for the uncertainties due to the shower shape description and the extraction of acceptance factors for less isolated photons, the systematic errors are added in quadrature another 5 % in the range  $0.5 < R_0 < 1.0$  and 10 % for  $R_0 < 0.5$ . For  $R_0 > 1.0$  the same systematic errors as in the measurement of  $R_0 = 1.0$  are assumed.

Figure 7.12 (table F.5) shows the total inclusive cross section in dependence of  $R_0$ . As expected the measured total inclusive cross section decreases with increasing  $R_0$  from 90.4 pb at  $R_0 = 0.1$  to 25.8 pb at  $R_0 = 2.0$ . The measured cross sections are well described by the scaled signal MC in the range  $0.8 < R_0 < 2.0$ , while at lower  $R_0$  the measured cross section is increasingly underestimated, which may indicate the missing fragmentation contribution in the scaled signal MC.

Figure 7.13 (table F.5) shows the total exclusive isolated photon cross section in the photon plus no-jets and photon plus jet sample in dependence of  $R_0$ . The measured photon plus no-jets cross section is decreasing even more steeply with  $R_0$  than the inclusive cross section, while the photon plus jet cross section increases in the range  $0.1 < R_0 < 1.0$  and decreases for larger values of  $R_0$ . In both samples the cross sections are reasonably described in the range  $0.8 < R_0 < 2.0$  by the scaled signal MC and underestimated for lower  $R_0$ . Towards small  $R_0$  the final state is resolved in an increasing number of jets, which eventually fall short of the required  $P_T$  threshold. Hence, events which are reconstructed in the photon plus jet sample at intermediate  $R_0$  partly migrate to the photon plus no-jets sample for small  $R_0$ . The cross section for the photon plus jet production is thus not bound to be strictly decreasing with  $R_0$ .

For the variation of  $R_0$  the fragmentation contribution in leading order cannot be clearly associated to the photon plus no-jets sample anymore, since for small values of  $R_0$  the parton

<sup>4</sup>The ALEPH analysis uses the DURHAM E0 jet algorithm and presents results for variations of the jet resolution parameter  $y_{cut}$ .

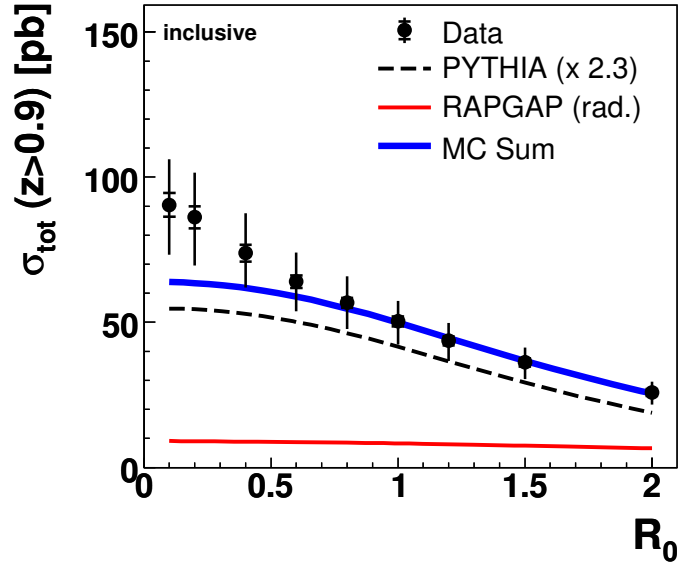


FIGURE 7.12: Total inclusive cross section for the isolated photon production in the kinematic range specified in table 7.2 in dependence of the jet resolution parameter  $R_0$ . The measurements are compared to the scaled signal MC, as described in the figure 7.8 caption.

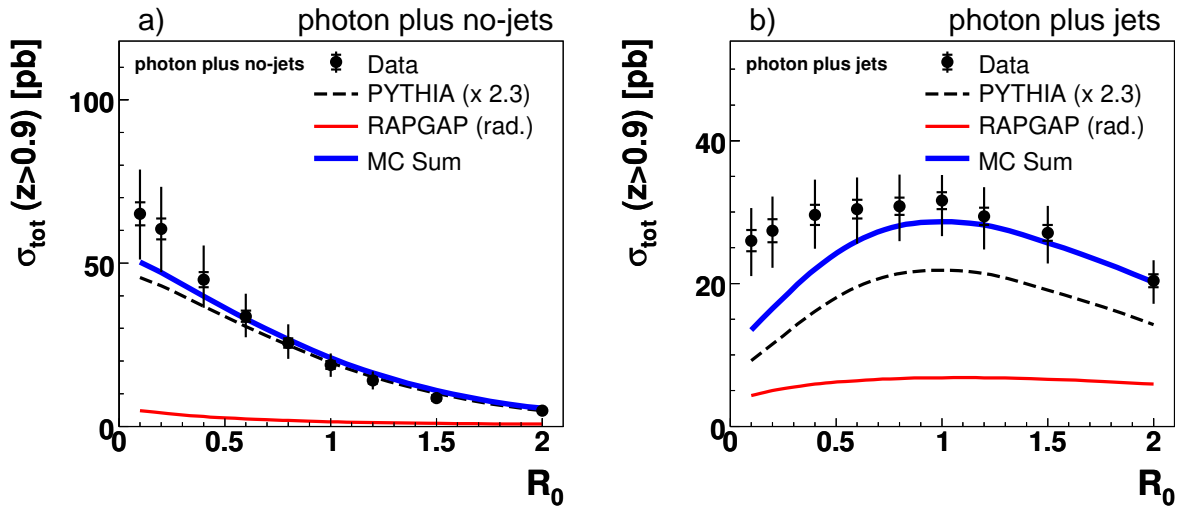


FIGURE 7.13: Total cross section for photon plus no-jets (a) and photon plus jet (b) production in the kinematic range specified in table 7.2 in dependence of the jet resolution parameter  $R_0$ . The measurements are compared to the scaled signal MC, as described in the figure 7.8 caption.

---

level jet multiplicity is not well correlated to the jet multiplicity on hadron level, which makes comparisons at small  $R_0$  with parton level calculations particularly difficult.





# CHAPTER 8

## CONCLUSIONS AND OUTLOOK

---

The cross section of isolated photon production in deep-inelastic scattering is measured using data taken with the H1 detector in both the HERA I and HERA II data taking periods with an integrated luminosity of  $227 \text{ pb}^{-1}$ . Compared to the previous ZEUS measurement [1] the range of  $Q^2$ ,  $E_T^\gamma$  and  $\eta^\gamma$  is largely extended. The present work represents the first measurement of isolated photons in deep-inelastic scattering at the H1 experiment. Furthermore, for the first time at HERA, cross sections in deep-inelastic scattering for less isolated photons in the vicinity of hadronic jets have been measured.

Isolated photons originating from the hard interactions involving hadrons are a sensitive probe for precision tests of perturbative QCD, since photons, unlike coloured partons, are widely unaffected by non-perturbative hadronisation effects. The background situation for the measurement of final state photons is, however, more difficult. A multivariate analysis of the shapes of photon and multi-photon showers in the LAr calorimeter has been presented and employed for the separation of the photon signal from the neutral hadron background.

Isolated photon cross sections in deep-inelastic scattering are measured in the kinematic region  $4 < Q^2 < 150 \text{ GeV}^2$ ,  $y > 0.05$  and  $W_X > 50 \text{ GeV}$ . The cross sections receive contributions from photon radiation by the quark ( $QQ$ ) as well as wide angle bremsstrahlung of the initial and final leptons ( $LL$ ) and their interference. A measurement of the photon distribution in the proton under the assumption of observing exclusively photons radiated from the electron [97] is therefore not considered.

The data are compared to a LO calculation, which is shown to underestimate the measured cross section by roughly a factor two. The prediction is most significantly below the measured data at low  $Q^2$ , while the shapes of the  $d\sigma/dE_T^\gamma$  and  $d\sigma/d\eta^\gamma$  distributions are described reasonably well. The cross sections in different bins of  $\eta^\gamma$  show that for  $\eta^\gamma > -0.6$ , where the  $LL$  contribution is small, the difference can mainly be attributed to an underestimation of the  $QQ$  contribution. The data are further compared to predictions from the MC generators PYTHIA, for the simulation of photons radiated by the quark, and RAPGAP for photons radiated from the electron. The MC predictions are very similar to the predictions from the LO calculation and show the largest discrepancy at low  $Q^2$ .

Jet production in events with isolated photons is also studied. The cross sections for events with no or at least one hadronic jet are underestimated by the LO prediction by a similar factor as in the inclusive measurement. Again the expectations are furthest below the data at low  $Q^2$ . The total photon plus jet cross section is roughly double the photon plus no-jets cross section as expected from the calculations. The NLO prediction for the photon plus jet production is higher than the LO prediction, most significantly at low  $Q^2$ , but still underestimates the data. The NLO calculation describes the shapes of the differential cross sections reasonably well.

The present measurement of isolated photons indicates the need for further clarification of the theoretical description of isolated photon phenomena in deep-inelastic  $ep$  scattering. A NLO calculation is needed also for the inclusive and photon plus no-jet production.

Cross sections in deep-inelastic scattering for less isolated photons in the vicinity of hadronic jets are also measured. Differential cross sections as function of  $z$ , the transverse energy fraction of the photon-jet carried by the photon, are presented in the range  $0.5 < z \leq 1.0$  and compared to the scaled MC prediction from PYTHIA (scaled by factor 2.3) and RAPGAP (not scaled). In this comparison PYTHIA is scaled by a factor 2.3 in order to give the possibly best description of the isolated photon cross section. The scaled MC prediction shows agreement with the measured cross sections for  $z > 0.8$ , but strongly underestimates at smaller  $z$  values. The discrepancy is largest in the photon plus no-jets production and increases towards smaller  $z$ , which may be attributed to the missing quark-to-photon fragmentation contribution in the MC prediction. The extracted differential cross sections are similar in shape to the measurement of the ALEPH collaboration [16] for  $0.7 < z \leq 1$  and may be used for an estimation of the quark-to-photon fragmentation function.

In addition, the total isolated photon cross section is measured in dependence of the jet resolution parameter  $R_0$ . For decreasing  $R_0$  weakly isolated photons increasingly contribute, since the isolation constraint applies to jets of smaller extent. The cross sections are well described by the scaled MC prediction for values of  $R_0$  larger than 0.8. At smaller values of  $R_0$  the data is increasingly underestimated, which may again be attributed to the missing fragmentation contribution in the MC prediction.

## Outlook

Further insight in the production of isolated photons in deep-inelastic  $ep$  scattering may be gained by an analysis of the total available HERA luminosity of roughly  $480 \text{ pb}^{-1}$ . With additional statistics the measurement of differential distributions at increased  $Q^2$  and  $E_T^\gamma$  would become possible and allow for a better understanding of the discrepancies between data and theory. Further data would, however, bring only limited improvement to the measurements presented in this work as most of the errors are dominated by systematic uncertainties. The systematic errors could be more accurately estimated with higher statistics, particularly in the additional Bethe-Heitler and deeply virtual Compton scattering event samples. A better theoretical understanding of the inclusive isolated photon production in deep-inelastic scattering is expected from a next-to-leading order calculation, which is not available at present.

A dedicated measurement with reduced systematic errors of photons in the vicinity of jets in deep-inelastic scattering may allow for an extraction of the quark-to-photon fragmentation function. The precise measurement of such less isolated photons requires a further understanding of the overlap of clusters from separate incident particles in the hadronic environment at values of  $z$  smaller than 0.9. Furthermore, the extraction of the acceptance correction factors needs the simulation of photons at low  $z$  with high statistics and a reliable estimation of the migration between bins of  $z$ .

A good understanding of the production of isolated photons is desirable, which is particularly true in view of the upcoming experiments at LHC, which are about to take first data. Isolated photons produced in the hard interaction are background to many searches for new phenomena, such as searches for the Higgs by its di-photon decay ( $H \rightarrow \gamma\gamma$ ).

In the past century photons played a major role in the transition from classical to modern physics. Soon, photons may again shed light on still unanswered questions of the fundamental principles.



# APPENDIX A

## KINEMATICS OF THE NEUTRAL PION DECAY

---

The pseudoscalar  $\pi^0$  meson is short-lived and decays almost exclusively in the di-photon decay channel as can be seen from table A.1. In the following only the  $\pi^0 \rightarrow \gamma\gamma$  decay will be considered.

The coordinate system is chosen, such that the  $\pi^0$  propagates along the  $z$ -axis and  $\theta_1^*$  defines the angle of the first photon to the  $z$ -axis in the rest frame. Since the  $\pi^0$  is a spinless particle, its decay is isotropic in the rest frame and the decay rate is therefore a flat function of  $\cos \theta_1^*$ :

$$\frac{dN}{d \cos \theta_1^*} = \frac{1}{2}. \quad (\text{A.1})$$

Momentum conservation requires the photons to emerge back-to-back in the rest frame and their momentum  $P_{1/2}^*$  and energy  $E_{1/2}^*$  in the rest frame is given by half the pion mass  $M_\pi/2$ . The energy of the photons in the laboratory frame is then derived by Lorentz transformation along the  $z$ -axis

$$E_1 = \gamma E_1^* + \gamma \beta P_{1,z}^* \quad (\text{A.2})$$

$$= \gamma \frac{M_\pi}{2} (1 + \beta \cos \theta_1^*). \quad (\text{A.3})$$

TABLE A.1: Parameters of the neutral pion  $\pi^0$  [51]. Stated are the mass ( $M_\pi$ ), the mean life time ( $\tau$ ) and the branching ratio for the decay in the two photon decay channel.

$\pi^0$	$J^{PC} = 0^{-+}$
Mass ( $M_\pi$ )	$134.9766 \pm 0.0006 \text{ MeV}$
Mean Life ( $\tau$ )	$8.4 \pm 0.6 \cdot 10^{-17} \text{ s}$
$\Gamma(\gamma\gamma)/\Gamma_{\text{tot}}$	$98.798 \pm 0.032 \%$

The so-called *Lorentz-boost* is specified by  $\gamma = E_\pi/M_\pi$  and  $\beta = P_\pi/E_\pi$ , where  $E_\pi$  and  $P_\pi$  are the energy and momentum of the pion, respectively. Thus we obtain

$$\frac{d \cos \theta_1^*}{dE_1} = \frac{2}{P_\pi}. \quad (\text{A.4})$$

Furthermore, the energy distribution in the laboratory frame can be related with the decay angle in the rest frame by

$$\frac{dN}{dE_1} = \frac{dN}{d \cos \theta_1^*} \frac{d \cos \theta_1^*}{dE_1} = \frac{1}{2} \frac{d \cos \theta_1^*}{dE_1}, \quad (\text{A.5})$$

where in the second step equation (A.1) was used. When inserting equation (A.4) into equation (A.5), the energy distribution in the laboratory frame

$$\frac{dN}{dE_1} = \frac{1}{P_\pi} \quad (\text{A.6})$$

is obtained. The distribution is flat with limiting values of  $(E_\pi \pm P_\pi)/2$ , which follows from equation (A.3).

More interesting than the energy spectrum, however, is the dependence on the opening angle  $\alpha$  between the two decay photons in the laboratory frame, since the opening angle is directly related to the transverse size of the electromagnetic shower in the calorimeter or, at larger opening angles, to the probability of finding the two photons resolved in separate clusters. If the four-momenta of the two photons are denoted as  $p_1$  and  $p_2$ , respectively, the photon energies can be related with the opening angle by

$$M_\pi^2 = (p_1 + p_2)^2 = 2E_1E_2(1 - \cos \alpha) = 4E_1E_2 \sin^2\left(\frac{\alpha}{2}\right). \quad (\text{A.7})$$

Moreover, using  $E_1 + E_2 = E_\pi$ , the opening angle can be stated as

$$\alpha = 2 \arcsin \left( \frac{M_\pi}{2 \sqrt{E_1 E_\pi - E_1^2}} \right). \quad (\text{A.8})$$

Obviously there is a minimum opening angle  $\alpha_{\min} = 2 \arcsin(M_\pi/E_\pi)$  for the symmetric decay  $E_1 = E_2 = E_\pi/2$ , which corresponds to  $\cos \theta_1^* = 0$ . In the rest frame the photons are emerging transverse to the pion direction.

The maximum opening angle  $\alpha_{\max} = \pi$  is found for a configuration at which in the rest frame the photons emerge along the  $z$ -axis. In this case one of the photons travels backwards at speed of light and the Lorentz boost to the laboratory frame cannot overcome this. The decay is hence the most asymmetric in the laboratory frame with photon energies  $E_{1/2} = (E_\pi \pm P_\pi)/2$ . These two extreme configurations are summarised in table A.2.

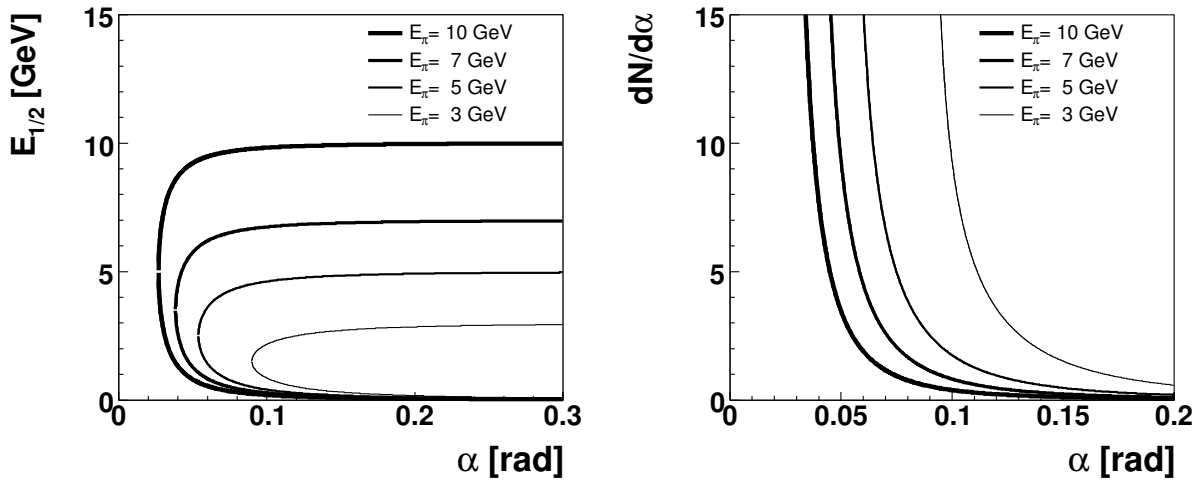


FIGURE A.1: Properties of the  $\pi^0 \rightarrow \gamma\gamma$  decay in dependence of the opening angle  $\alpha$  between the two photons. **Left:** The energies of the two decay photons are shown as a function of  $\alpha$  for several pion energies  $E_\pi$ . **Right:** The opening angle distribution for separate pion energies is shown.

In order to derive the opening angle spectrum  $dN/d\alpha$ , it may be written as

$$\frac{dN}{d\alpha} = \frac{dN}{dE_1} \frac{dE_1}{d\alpha}, \quad (\text{A.9})$$

where the first factor is given by equation (A.6) and the second factor is calculated from equation (A.8). The opening angle spectrum then results in

$$\frac{dN}{d\alpha} = \frac{M_\pi}{4P_\pi \sin^2(\alpha/2)} \frac{\cos(\alpha/2)}{\sqrt{\frac{E_\pi^2}{M_\pi^2} \sin^2(\alpha/2) - 1}}. \quad (\text{A.10})$$

Figure A.1 shows the energies of the decay photons as a function of the opening angle  $\alpha$  and the opening angle distribution as given by equation (A.10). Both are shown for different energies of the incident  $\pi^0$ . It should be noted that the decay is most likely close to the minimum opening angle  $\alpha_{\min}$ , which itself increases with decreasing pion energies. It is also visible that the decay already becomes notably asymmetric for opening angles slightly smaller than  $\alpha_{\min}$ .

In the energy range relevant for this analysis ( $3 < E_T^\gamma < 10$  GeV) decays of pions close to the minimum opening angle produce two approximately equal energetic photons, which are reconstructed in a single electromagnetic cluster of the main calorimeter. Such clusters carry the full energy of the incident pion, but are transversely wider than clusters from a single photon, because of the non-vanishing opening angle. This allows for a statistical separation of single photon clusters from *multi-photon* clusters by means of a shower shape analysis. The minimum distance of the two photons in the calorimeter can be approximated for small

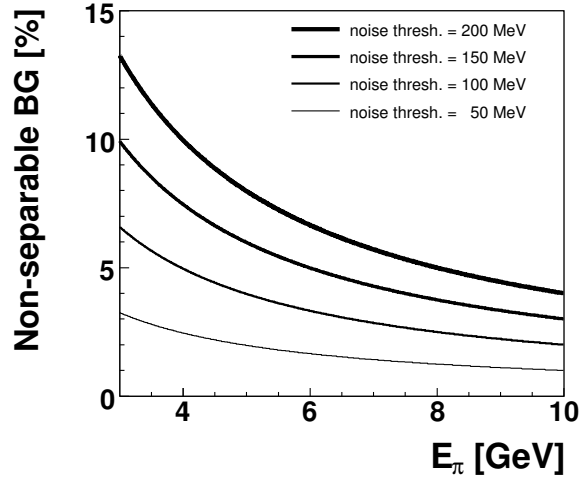


FIGURE A.2: Fraction of non-separable background from  $\pi^0 \rightarrow \gamma\gamma$  decays as a distribution of the pion energy. The non-separable background is defined as pion decays, at which one of the decay photons has an energy below the noise threshold. The distributions are shown for different noise thresholds. In the present analysis a noise threshold of 80 MeV is relevant for the background identification.

opening angles  $\alpha_{\min}$  with

$$d_{\gamma\gamma}^{\min} \approx \frac{R_{cal}\alpha_{\min}}{\sin\theta^\pi} \approx \frac{2R_{cal}M_\pi}{E_{T,\pi}}, \quad (\text{A.11})$$

where  $R_{cal} = 1.05$  m is the inner radius of the LAr calorimeter. For a  $\pi^0$  in the transverse energy range  $3 < E_{T,\pi} < 10$  GeV the minimum distance  $d_{\gamma\gamma}^{\min}$  between the two decay photons varies in the range 2.8–9.5 cm.

For larger opening angles between the two photons, two clusters of unequal energies are induced in the calorimeter, both of which are perfectly *photon-like*. The two photons are typically resolved in separate clusters for distances  $d_{\gamma\gamma} \gtrsim 20$  cm. Usually the more energetic cluster is identified as a single photon and cannot be separated by a shower shape approach. However, the invariant mass of the two clusters can be used to identify the pion decay. In the present analysis the invariant mass is calculated for any photon candidate cluster with the closest electromagnetic neighbour cluster above 80 MeV. Candidate pairs with an invariant mass covering well the pion mass ( $0 < M_{\gamma\gamma} < 300$  MeV) are excluded from the selection.

By means of the invariant mass cut, a considerable amount of otherwise non-separable background is rejected. However, as soon as the energy of the less energetic cluster declines below the calorimeter-dependent noise threshold, the pion decay remains hidden. In this case exactly one perfectly photon-like cluster is found in the detector, which cannot be traced back to the pion decay. The fraction of this non-separable background is shown in figure A.2 as a function of the pion energy for several possible noise thresholds. As opposed to simple cuts, the statistical subtraction based on reliable models is the only possibility to correct for the non-



separable background. At low cluster energies ( $E_T \approx 3 \text{ GeV}$ ) the fraction of non-separable background at an 80 MeV noise threshold amounts to roughly 5 %.

The former conclusions on the kinematics of the pion decay can also be transferred to the  $\eta \rightarrow \gamma\gamma$  decay, taking into account the higher mass of the  $\eta$  meson  $M_\eta = 547.51 \pm 0.18 \text{ MeV}$  [51]. However, the  $2\gamma$  decay accounts only for  $54.74 \pm 0.19 \%$  of the neutral modes, whereas the theoretically more involved  $\eta \rightarrow 3\pi^0$  decay contributes with  $45.20 \pm 19 \%$  of the neutral decay modes [51].

TABLE A.2: Extreme configurations in the  $\pi^0 \rightarrow \gamma\gamma$  decay. The first row represents the symmetric decay with a minimum opening angle between the photons in the laboratory frame. The second row shows the most asymmetric decay.

$\theta_1^*$	$\cos \theta_1^*$	$\theta_2^*$	$\cos \theta_2^*$	$E_1$	$E_2$	$\alpha$	$dN/d\alpha$
$\pi/2$	0	$\pi/2$	0	$E_\pi/2$	$E_\pi/2$	$\alpha_{\min}$	$\infty$
0	1	$\pi$	-1	$(E_\pi + P_\pi)/2$	$(E_\pi - P_\pi)/2$	$\pi$	0

# APPENDIX B

## MULTIVARIATE CLASSIFICATION METHODS

---

Multivariate classification methods try to model the functional dependence between input variables in the so-called *feature space* and a *classifier* as output by statistical learning from examples. In the present analysis, a classification based on the six shower shape variables (cf. section 5.1) into photon signal clusters and neutral hadron background clusters is desired. Modern classification methods do not only deliver the discrete output 0 (background) and 1 (signal) representing the class an event belongs to, but they provide a continuous output in the range  $[0, 1]$  which can be interpreted as a signal probability. A discrete classification can then be achieved by a cut in the classifier distribution, which allows for the customised adjustment of the *signal efficiency* versus the *background rejection*.

### Naïve Bayes Classifier

The naïve Bayes classifier (eg. [98]), which is also referred to as *maximum likelihood*, is derived from *Bayes theorem*, which relates the *posterior probability*  $P(C|\vec{x})$  for class  $C$  ( $C = 0$  for background,  $C = 1$  for signal) given the input vector  $\vec{x}$  with the *class-conditional probability density*  $P(\vec{x}|C)$  and the *prior probability*  $P(C)$ :

$$P(C|\vec{x}) = \frac{P(\vec{x}|C)P(C)}{P(\vec{x})}. \quad (\text{B.1})$$

The posterior probability  $P(C|\vec{x})$  can be interpreted as the probability that the input vector  $\vec{x}$  indeed belongs to category  $C$ . The class-conditional probability density  $P(\vec{x}|C)$  on the other hand expresses the chance to observe the feature vector  $\vec{x}$  in a random sample of category  $C$ . The prior probability  $P(C)$  introduces a relative frequency of the class contributions.

Now, the naïve Bayes assumption postulates the independence of the input variables. Under this assumption the probability density factorises as

$$P(\vec{x}|C) = \prod_i P(x_i|C) \quad (\text{B.2})$$

and therefore

$$P(C|\vec{x}) \sim P(C) \prod_i P(x_i|C), \quad (\text{B.3})$$

where the  $x_i$  are the components of input vector  $\vec{x}$ . Although the assumption that the variables are independent is not accurate in most cases, it simplifies the classification problem drastically, as it allows the class-conditional probability densities  $P(x_i|C)$  to be calculated separately for each variable. A multidimensional density estimation task is reduced to several one-dimensional density estimations.

The one-dimensional probability densities  $P(x_i|C)$  can be estimated from normalised signal and background histograms. In case of rather limited statistics some smoothing of the histograms might be necessary, which requires special care in the treatment of boundaries, tails and narrow structures in the distributions. In the present analysis SP events are produced in high statistics, such that an additional smoothing is not required and the probability densities are taken from the normalised histograms.

A classifier which is henceforth termed *discriminator*  $D$  can be defined as

$$D = \frac{P(C = 1|\vec{x})}{P(C = 1|\vec{x}) + P(C = 0|\vec{x})}. \quad (\text{B.4})$$

For the naïve independence assumption and the assumption that the prior probabilities for signal and background are equal, the discriminator is given by

$$D = \frac{\prod_i P(x_i|C = 1)}{\prod_i P(x_i|C = 1) + \prod_i P(x_i|C = 0)}. \quad (\text{B.5})$$

The discriminator varies in the range  $0 \leq D \leq 1$  and produces in general larger values for isolated photons than for the decay photons. The discriminator distribution for the selected photon candidates is shown in figure 5.6 a). The data are well described by the sum of the MC predictions.

Since correlations between the variables are not taken into account, the naïve Bayes classifier is believed to underperform in most situations, which gave rise to the development of many classifiers that exist in statistical theory nowadays. Empirical comparisons between naïve Bayes and decision tree algorithms, which take correlations into account, showed that naïve Bayes predicts equally well [99, 98]. This was explained by the cancellation of dependencies under certain circumstances [100].

### Artificial Neural Networks

Artificial Neural Networks (ANNs) [101, 102] are an attempt to model information processing capabilities of biological nervous systems like the brain. They consist of multiple highly interconnected processing elements, so-called *neurons*, operating conjointly to tackle specific problems. Like biological systems, ANNs learn by example. A biological neuron that is rarely

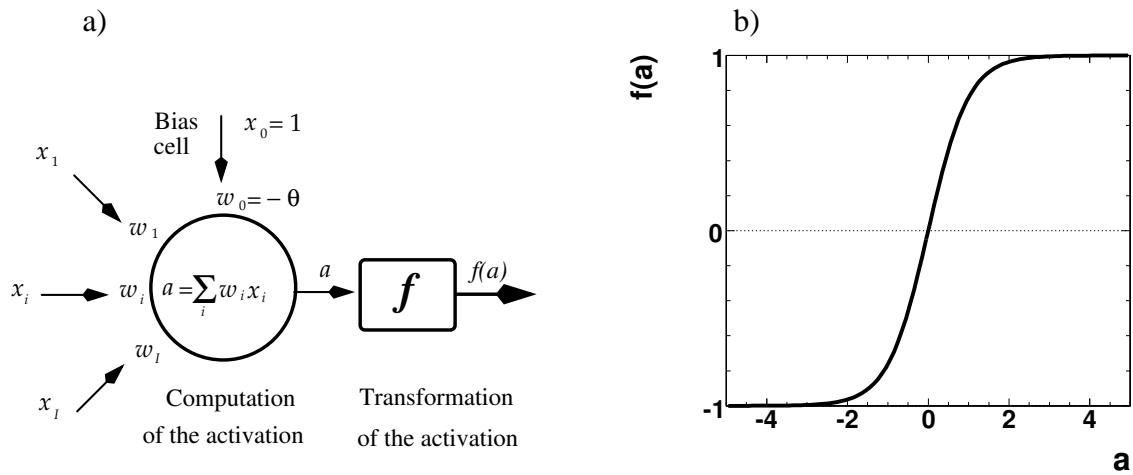


FIGURE B.1: a) Artificial neuron summing up the weighted input as the activation (taken from [103]). b) The activation is transformed by the activation function  $f(a) = \tanh(a)$ .

activated loses its ability to emit an action potential itself. The learning process in biological systems also involves the modulation of the synaptic connections between the neurons, which is equally true for artificial networks.

The principal unit of an ANN is the artificial neuron illustrated in figure B.1 a). The transmission of information between neurons is processed in two stages. First the neuron calculates its *activation*  $a$  as the sum of weighted input signals and then the output is emitted as a function  $f(a)$  of the activation. If the input signals are denoted as  $x_i$  with corresponding weights  $w_i$ , the output signal of a neuron can be written as

$$out = f\left(\sum_i w_i x_i - \theta\right), \quad (\text{B.6})$$

where  $\theta$  is the *activation threshold*, which can be represented by an imaginary *threshold neuron* with  $x_0 = 1$  and  $w_0 = -\theta$ . As activation function the hyperbolic tangent

$$f(a) = \tanh(a) = \frac{e^a - e^{-a}}{e^a + e^{-a}} \quad (\text{B.7})$$

is used in the present analysis, illustrated in figure B.1 b), with the advantage of being anti-symmetric.<sup>1</sup>

Despite the simple definition rules of single artificial neurons their combination in neural networks provides powerful tools for classification and pattern recognition. In the simplest kind of networks, neurons are organised in layers. Neurons in a certain layer receive the input

<sup>1</sup>For the neurons in the input layer the identity  $f(a) = a$  is used. The Fermi function  $f(a) = 1/(1 + e^{-a})$  is often implemented as activation function as well.

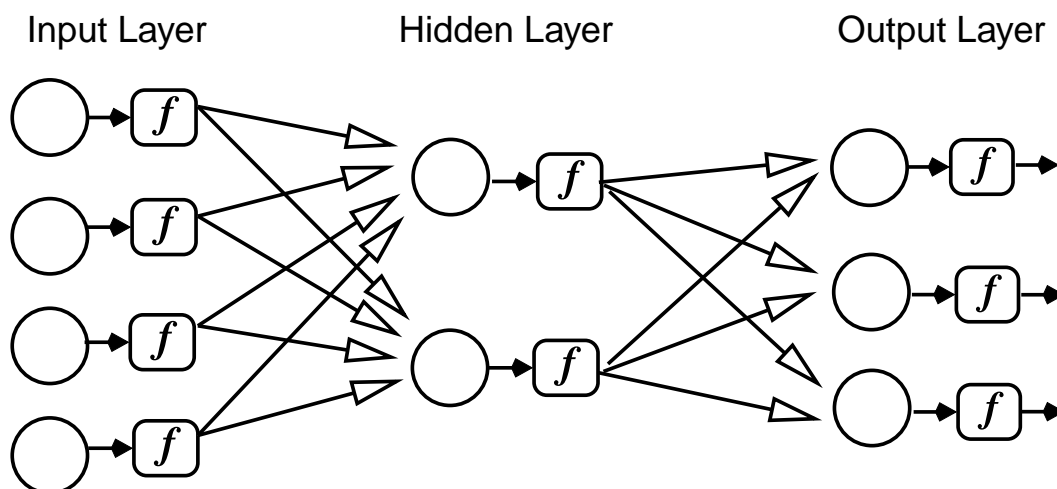


FIGURE B.2: Topology of a fully connected feed-forward neural network with one hidden layer (taken from [103]).

from neurons of the preceding layer and send the output to the succeeding layer. Such networks are termed *multi-layer neural networks* and the sequential layer-wise propagation of the activation is termed *feed-forward* operation. Multi-layer neural networks consist of an input layer, hidden layers and a final output layer as shown in figure B.2. The input layer is fed with the external information while the output layer delivers the classification decision. The number of hidden layers is in principle not limited. In the present analysis only one hidden layer is used, which is motivated by a general theorem [104] claiming that any continuous function can be represented by a neural network with one hidden layer provided that the number of neurons is sufficiently large. The topology of the employed neural network therefore consists of one input layer with six neurons corresponding to the six shower shape variables, 17 neurons in one hidden layer and one neuron in the output layer, which delivers a classification output between 0 and 1.

The training of the multi-layer neural network is done by means of an *error backpropagation* algorithm [105, 106]. The weights of the inter-neuron connections are optimised in an iterative procedure so as to best classify a set of training data of which the true class is known, such as the SP photon and SP neutral hadron clusters in the present analysis. The deviation of the network output from the true class defines an error  $E$ , which is used to update the weights depending on the error-function's partial derivative  $\Delta w \sim \partial E / \partial w$ .

To avoid *over-training* an additional validation set of training data is used. The training is stopped when the validation error is at a minimum. The output of the neural network for the classification of isolated photon candidates is shown in figure 5.6 b).

### Range Search Algorithm

In the Range Search (RS) algorithm [107, 102] the classification is based on the number of signal and background events in the vicinity of an event to be classified. The vicinity is defined as a hyper-box  $B_{\vec{x}}$  in feature space centred around the input vector  $\vec{x}$ . The box edges are the crucial parameters of the algorithm. The method suffers from insufficient statistics and overtraining occurs for too small box sizes; too large box sizes on the contrary degrade the performance. Adaptive box sizes might therefore better model the probability density by readjusting the size to the local density of the data. In the present analysis the box size is fixed and chosen such that the performance on a validation sample is optimised.

The number of signal events  $N_S(B_{\vec{x}})$  and background events  $N_{BG}(B_{\vec{x}})$  in the hyper-box immediately define the range search output

$$output(\vec{x}) = \frac{N_S(B_{\vec{x}})}{N_S(B_{\vec{x}}) + N_{BG}(B_{\vec{x}})}. \quad (\text{B.8})$$

The efficient counting of events inside the hyper-box among several million signal and background events is a nontrivial task. In the present analysis the events are stored in a binary tree [108], which needs to be traversed only partially for one range search evaluation. The range search classification of isolated photon candidates is shown in figure 5.6 c).





## APPENDIX C

### DVCS AND BH EVENT SAMPLES

---

For the determination of systematic errors and in-situ energy calibration of the final state photons two additional event samples are used. The first sample denoted BH contains Bethe-Heitler events with an electron reconstructed in the LAr calorimeter, a photon in the SpaCal and nothing else in the detector. The final state photon is emitted from the initial or final state electron, while the proton leaves undetected through the beam pipe. The second (complementary) sample denoted DVCS provides an electron in the SpaCal and a photon in the LAr and no further detected particle in the event. Such events originate to a large part from deeply virtual Compton scattering, which is the diffractive scattering of a virtual photon off a proton. The processes, illustrated in figure C.1, are discussed in [109]. The samples are independent of the main selection for isolated photons and provide a clean sample of electromagnetic clusters in the LAr calorimeter.

The measured photons and electrons in these samples can be compared to simulated SP photons and SP electrons, which are reweighted in order to provide the same phasespace distribution. Figure C.2 and figure C.3 show the transverse energy and polar angle distribution of the photons and electrons, respectively, together with the corresponding reweighted SP events.

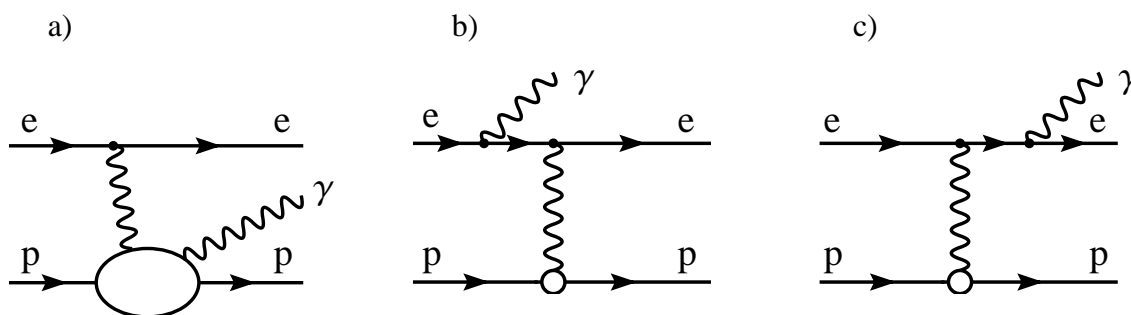


FIGURE C.1: Feynman diagrams illustrating the deeply virtual Compton scattering (a) and the Bethe-Heitler (b and c) processes.

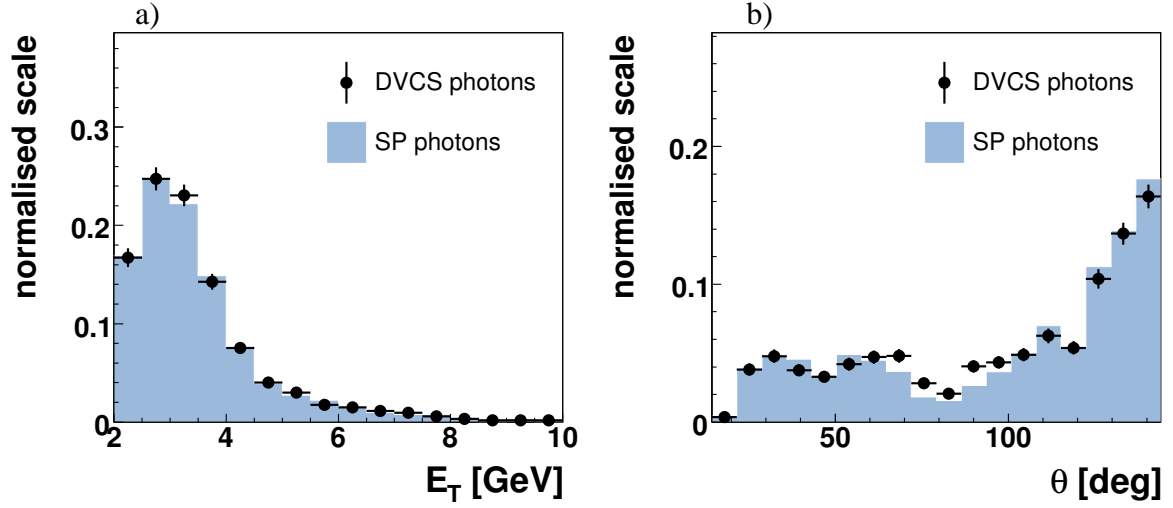


FIGURE C.2: Transverse energy (a) and polar angle (b) of the selected photons in the DVCS event sample compared with reweighted SP photons.

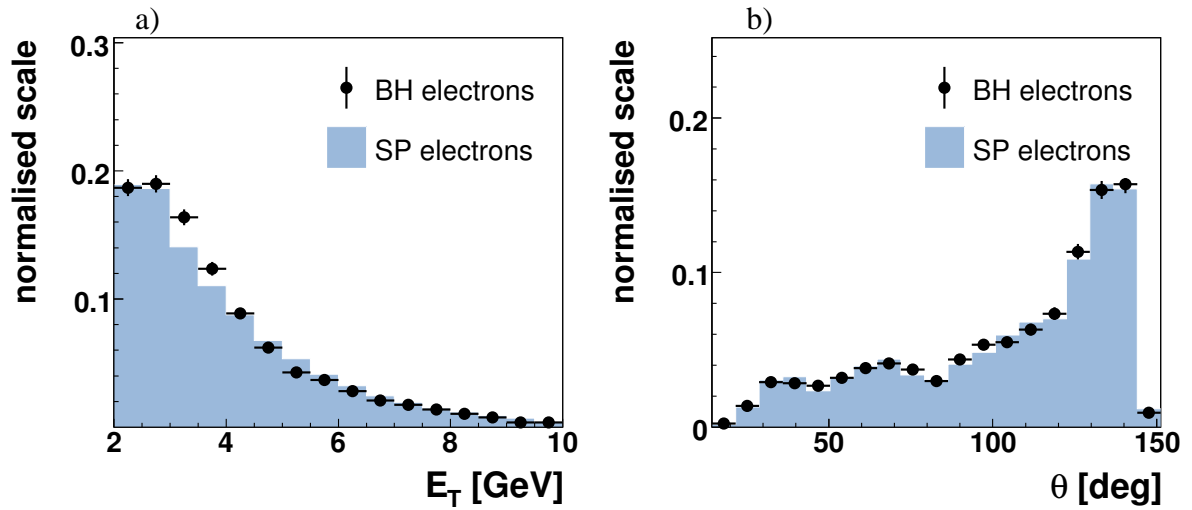


FIGURE C.3: Transverse energy (a) and polar angle (b) of the selected electrons in the BH event sample compared with reweighted SP electrons.

# APPENDIX D

## TRACK QUALITY CRITERIA

---

TABLE D.1: *Good* track quality criteria (Definition of variables in [81]).

central tracks	combined (fwd./cent.) tracks
$p_T > 120 \text{ MeV}$	$p_T > 120 \text{ MeV}$
$20^\circ < \theta < 160^\circ$	$0^\circ < \theta < 40^\circ$
$ \text{dca}'  \leq 2 \text{ cm}$	$ \text{dca}'  \leq 5 \text{ cm}$
$R_{\text{start}} \leq 50 \text{ cm}$	$R_{\text{start}} \leq 50 \text{ cm}$
$R_{\text{length}} \geq 10 \text{ cm} \forall \theta \leq 150^\circ$	$R_{\text{length}} \geq 0 \text{ cm}$
$R_{\text{length}} \geq 5 \text{ cm} \forall \theta > 150^\circ$	$\Delta p/p \leq 99999.9$
$n_{\text{CJC-hits}} \geq 0$	$n_{\text{CJC-hits}} \geq 0$
	$\chi_{\text{dtra}}^2 \leq 50$
	$\chi_{\text{cent.-forw.}}^2 \leq 50$



# APPENDIX E

## ANALYSIS BINS

---

TABLE E.1: Analysis bins in  $(E_T^\gamma, \eta^\gamma)$  and  $Q^2$ . They are employed in the photon signal extraction (chapter 5) and cross section measurement (chapters 6 and 7).

Bins in $(E_T^\gamma, \eta^\gamma)$					Bins in $Q^2$			
Bin	Wheel	$\eta^\gamma$ range		$E_T^\gamma$ range [GeV]		Bin	$Q^2$ range [GeV <sup>2</sup> ]	
1	1 (CB1)	-1.2	-0.6	3.0	4.0	1	4.0	10.0
2	1 (CB1)	-1.2	-0.6	4.0	6.0	2	10.0	20.0
3	1 (CB1)	-1.2	-0.6	6.0	10.0	3	20.0	40.0
4	2 (CB2)	-0.6	0.2	3.0	4.0	4	40.0	80.0
5	2 (CB2)	-0.6	0.2	4.0	6.0	5	80.0	150.0
6	2 (CB2)	-0.6	0.2	6.0	10.0			
7	3 (CB3)	0.2	0.9	3.0	4.0			
8	3 (CB3)	0.2	0.9	4.0	6.0			
9	3 (CB3)	0.2	0.9	6.0	10.0			
10	4 (FB1)	0.9	1.4	3.0	4.0			
11	4 (FB1)	0.9	1.4	4.0	6.0			
12	4 (FB1)	0.9	1.4	6.0	10.0			
13	5 (FB2)	1.4	1.8	3.0	4.0			
14	5 (FB2)	1.4	1.8	4.0	6.0			
15	5 (FB2)	1.4	1.8	6.0	10.0			



# APPENDIX F

## CROSS SECTION TABLES

---

TABLE F.1: Differential cross sections for inclusive isolated photon production in the kinematic range specified in table 7.2.  $f^{had}$  denotes the hadronisation correction factor applied to the LO calculation.

### H1 Inclusive Isolated Photon Cross Sections

$E_T^\gamma$ [GeV]	$d\sigma/dE_T^\gamma$ [pb/GeV]	stat.	syst.	$f^{had}$
3.0 4.0	16.98	$\pm 1.20$	$+2.79$ $-2.61$	0.78
4.0 6.0	10.51	$\pm 0.47$	$+1.50$ $-1.86$	0.89
6.0 10.0	3.08	$\pm 0.20$	$+0.46$ $-0.60$	0.98

$\eta^\gamma$	$d\sigma/d\eta^\gamma$ [pb]	stat.	syst.	$f^{had}$
-1.2 -0.6	26.15	$\pm 1.67$	$+3.60$ $-4.16$	0.92
-0.6 0.2	20.69	$\pm 1.34$	$+3.53$ $-3.73$	0.85
0.2 0.9	15.83	$\pm 0.93$	$+1.97$ $-3.25$	0.81
0.9 1.4	9.57	$\pm 0.87$	$+1.99$ $-2.00$	0.80
1.4 1.8	5.50	$\pm 1.15$	$+1.04$ $-1.75$	0.80

$Q^2$ [GeV <sup>2</sup> ]	$d\sigma/dQ^2$ [pb/GeV <sup>2</sup> ]	stat.	syst.	$f^{had}$
4.0 10.0	2.48	$\pm 0.21$	$+0.34$ $-0.41$	0.87
10.0 20.0	1.17	$\pm 0.07$	$+0.19$ $-0.21$	0.83
20.0 40.0	0.52	$\pm 0.03$	$+0.07$ $-0.10$	0.81
40.0 80.0	0.235	$\pm 0.013$	$+0.033$ $-0.048$	0.83
80.0 150.0	0.063	$\pm 0.006$	$+0.009$ $-0.012$	0.87

TABLE F.2: Differential cross sections for inclusive isolated photon production  $d\sigma/dE_T^\gamma$  in different  $\eta^\gamma$  bins, corresponding to the wheel structure of the LAr calorimeter (see text). The kinematic region is defined in table 7.2.  $f^{had}$  denotes the hadronisation correction factor applied to the LO calculation.

### H1 Inclusive Isolated Photon Cross Sections

$E_T^\gamma$ [GeV]	$d\sigma/dE_T^\gamma$ [pb/GeV]	stat.	syst.	$f^{had}$	
$-1.2 < \eta^\gamma < -0.6$					
3.0	4.0	4.86	$\pm 0.67$	$^{+0.88}_{-0.63}$	0.86
4.0	6.0	3.46	$\pm 0.28$	$^{+0.48}_{-0.66}$	0.96
6.0	10.0	0.98	$\pm 0.12$	$^{+0.13}_{-0.23}$	1.00
$-0.6 < \eta^\gamma < 0.2$					
3.0	4.0	5.81	$\pm 0.75$	$^{+1.27}_{-1.20}$	0.76
4.0	6.0	3.20	$\pm 0.28$	$^{+0.56}_{-0.65}$	0.88
6.0	10.0	1.09	$\pm 0.13$	$^{+0.15}_{-0.17}$	0.99
$0.2 < \eta^\gamma < 0.9$					
3.0	4.0	3.94	$\pm 0.51$	$^{+0.59}_{-0.72}$	0.72
4.0	6.0	2.39	$\pm 0.16$	$^{+0.28}_{-0.51}$	0.84
6.0	10.0	0.59	$\pm 0.06$	$^{+0.09}_{-0.14}$	0.96
$0.9 < \eta^\gamma < 1.4$					
3.0	4.0	1.66	$\pm 0.31$	$^{+0.22}_{-0.31}$	0.69
4.0	6.0	0.82	$\pm 0.12$	$^{+0.21}_{-0.16}$	0.82
6.0	10.0	0.37	$\pm 0.05$	$^{+0.10}_{-0.09}$	0.96
$1.4 < \eta^\gamma < 1.8$					
3.0	4.0	0.72	$\pm 0.28$	$^{+0.23}_{-0.21}$	0.70
4.0	6.0	0.64	$\pm 0.16$	$^{+0.09}_{-0.22}$	0.81
6.0	10.0	0.049	$\pm 0.045$	$^{+0.009}_{-0.016}$	0.94



TABLE F.3: Differential cross sections for inclusive isolated photon production in the kinematic range specified in table 7.2 and  $40 < Q^2 < 150 \text{ GeV}^2$ .  $f^{had}$  denotes the hadronisation correction factor applied to the LO calculation.

### H1 Inclusive Isolated Photon Cross Sections for $Q^2 > 40 \text{ GeV}^2$

$E_T^\gamma$ [GeV]	$d\sigma/dE_T^\gamma$ [pb/GeV]	stat.	syst.	$f^{had}$
3.0 4.0	3.70	$\pm 0.39$	$+0.63$ $-0.59$	0.80
4.0 6.0	2.53	$\pm 0.23$	$+0.43$ $-0.43$	0.87
6.0 10.0	1.30	$\pm 0.15$	$+0.19$ $-0.27$	0.96
$\eta^\gamma$	$d\sigma/d\eta^\gamma$ [pb]	stat.	syst.	$f^{had}$
-1.2 -0.6	9.61	$\pm 1.00$	$+1.48$ $-2.02$	0.97
-0.6 0.2	5.13	$\pm 0.59$	$+0.92$ $-0.97$	0.86
0.2 0.9	3.49	$\pm 0.32$	$+0.45$ $-0.72$	0.78
0.9 1.4	2.37	$\pm 0.33$	$+0.49$ $-0.47$	0.76
1.4 1.8	1.12	$\pm 0.51$	$+0.21$ $-0.34$	0.73

TABLE F.4: Differential cross sections for the production of isolated photons accompanied by no or at least one hadronic jet in the kinematic range specified in table 7.2.  $f^{had}$  denotes the hadronisation correction factor applied to the LO and the NLO calculation.

H1 Photon plus no-Jets					H1 Photon plus Jet				
$E_T^\gamma$ [GeV]	$d\sigma/dE_T^\gamma$ [pb/GeV]	stat.	syst.	$f^{had}$	$d\sigma/dE_T^\gamma$ [pb/GeV]	stat.	syst.	$f^{had}$	
3.0 4.0	8.10	$\pm 0.93$	+1.82 -1.48	0.75	8.85	$\pm 0.70$	+1.37 -1.38	0.82	
4.0 6.0	3.79	$\pm 0.29$	+0.69 -0.77	0.91	6.65	$\pm 0.35$	+0.92 -1.15	0.89	
6.0 10.0	0.77	$\pm 0.10$	+0.14 -0.18	1.10	2.35	$\pm 0.17$	+0.35 -0.46	0.97	
$\eta^\gamma$	$d\sigma/d\eta^\gamma$ [pb]	stat.	syst.	$f^{had}$	$d\sigma/d\eta^\gamma$ [pb]	stat.	syst.	$f^{had}$	
-1.2 -0.6	9.30	$\pm 1.07$	+1.53 -1.72	0.88	16.61	$\pm 1.20$	+2.67 -2.64	0.97	
-0.6 0.2	8.46	$\pm 0.95$	+1.73 -1.84	0.81	12.32	$\pm 0.90$	+2.15 -2.19	0.88	
0.2 0.9	5.98	$\pm 0.71$	+1.16 -1.34	0.82	9.94	$\pm 0.59$	+1.16 -2.03	0.81	
0.9 1.4	2.57	$\pm 0.47$	+0.64 -0.61	0.85	6.99	$\pm 0.73$	+1.38 -1.40	0.79	
1.4 1.8	2.40	$\pm 0.73$	+0.78 -0.74	0.91	3.22	$\pm 0.85$	+0.61 -1.01	0.77	
$Q^2$ [GeV <sup>2</sup> ]	$d\sigma/dQ^2$ [pb/GeV <sup>2</sup> ]	stat.	syst.	$f^{had}$	$d\sigma/dQ^2$ [pb/GeV <sup>2</sup> ]	stat.	syst.	$f^{had}$	
4.0 10.0	1.09	$\pm 0.16$	+0.21 -0.22	0.88	1.39	$\pm 0.13$	+0.20 -0.22	0.87	
10.0 20.0	0.44	$\pm 0.05$	+0.09 -0.09	0.81	0.76	$\pm 0.05$	+0.11 -0.14	0.86	
20.0 40.0	0.21	$\pm 0.02$	+0.04 -0.05	0.80	0.31	$\pm 0.02$	+0.04 -0.06	0.83	
40.0 80.0	0.071	$\pm 0.008$	+0.012 -0.017	0.81	0.162	$\pm 0.010$	+0.024 -0.033	0.84	
80.0 150.0	0.021	$\pm 0.004$	+0.005 -0.007	0.88	0.040	$\pm 0.005$	+0.005 -0.007	0.89	

TABLE F.5: Differential cross sections  $d\sigma/dz$  (left) and total cross section  $\sigma_{tot}$  in dependence of  $R_0$  (right) for inclusive photon production as well as for the photon plus no-jets and photon plus jet production in the kinematic range specified in table 7.2 (constraint on  $z$  and parameter  $R_0$  corresponding to the table entries).

Photon Cross Sections					Photon Cross Sections				
$z$		$d\sigma/dz$	stat.	syst.	$R_0$		$\sigma_{tot}$	stat.	syst.
		[pb]					[pb]		
Inclusive					Inclusive				
0.5	0.6	167.5	$\pm 13.2$	+40.5 -42.4	0.1	90.4	$\pm 4.1$	+15.3 -16.7	
0.6	0.7	147.5	$\pm 12.9$	+29.9 -31.8	0.2	86.2	$\pm 3.8$	+14.8 -16.1	
0.7	0.8	115.7	$\pm 11.8$	+19.5 -21.3	0.4	73.8	$\pm 2.9$	+13.5 -11.4	
0.8	0.9	96.6	$\pm 10.8$	+14.0 -15.7	0.6	64.0	$\pm 2.2$	+9.8 -9.9	
0.9	1.0	503.1	$\pm 17.2$	+68.4 -78.0	0.8	56.7	$\pm 1.7$	+8.9 -8.8	
Photon plus no-Jets					Photon plus no-Jets				
0.5	0.6	102.9	$\pm 9.7$	+27.3 -27.9	1.0	50.3	$\pm 1.7$	+6.8 -7.8	
0.6	0.7	83.7	$\pm 9.9$	+19.3 -19.8	1.2	43.6	$\pm 1.6$	+5.9 -6.8	
0.7	0.8	68.5	$\pm 9.5$	+13.8 -14.3	1.5	36.2	$\pm 1.4$	+4.9 -5.6	
0.8	0.9	47.5	$\pm 8.6$	+8.6 -9.0	2.0	25.8	$\pm 1.2$	+3.5 -4.0	
0.9	1.0	187.8	$\pm 11.8$	+32.9 -34.4	Photon plus no-Jets				
Photon plus Jets					0.1	65.1	$\pm 3.5$	+13.1 -13.6	
0.5	0.6	57.0	$\pm 7.6$	+13.7 -14.4	0.2	60.5	$\pm 3.2$	+12.4 -12.8	
0.6	0.7	60.6	$\pm 7.5$	+12.1 -13.0	0.4	44.9	$\pm 2.3$	+10.2 -8.2	
0.7	0.8	46.9	$\pm 6.6$	+7.8 -8.6	0.6	33.7	$\pm 1.7$	+6.7 -6.2	
0.8	0.9	47.3	$\pm 6.1$	+6.7 -7.6	0.8	25.5	$\pm 1.4$	+5.5 -4.7	
0.9	1.0	315.6	$\pm 12.0$	+42.0 -48.3	1.0	18.8	$\pm 1.2$	+3.3 -3.4	
					1.2	14.1	$\pm 1.0$	+2.5 -2.6	
					1.5	8.7	$\pm 0.8$	+1.5 -1.6	
					2.0	4.8	$\pm 0.6$	+0.8 -0.9	
					Photon plus Jets				
					0.1	26.0	$\pm 1.5$	+4.3 -4.8	
					0.2	27.4	$\pm 1.6$	+4.5 -4.9	
					0.4	29.6	$\pm 1.4$	+4.7 -4.5	
					0.6	30.4	$\pm 1.3$	+4.2 -4.7	
					0.8	30.8	$\pm 1.2$	+4.3 -4.7	
					1.0	31.6	$\pm 1.2$	+4.2 -4.8	
					1.2	29.4	$\pm 1.2$	+3.9 -4.5	
					1.5	27.1	$\pm 1.1$	+3.6 -4.1	
					2.0	20.4	$\pm 0.9$	+2.7 -3.1	



# LIST OF FIGURES

---

1.1	Lowest order Feynman graphs for the $ep$ scattering process. . . . .	6
1.2	$Q^2$ dependence of the neutral and charged current cross sections. . . . .	8
1.3	Deep-inelastic scattering at lowest order in the quark parton model. . . . .	10
1.4	Higher order corrections in Quantum Chromodynamics. . . . .	11
1.5	The four splitting functions in the DGLAP evolution equations. . . . .	13
1.6	The proton structure function $F_2$ . . . . .	14
1.7	Leading order Feynman graphs for isolated photon production in DIS. . . . .	15
1.8	Feynman graph for the quark fragmentation into a highly energetic photon. . . . .	17
1.9	Inclusive prompt photon cross sections in $\gamma p$ of H1 and ZEUS. . . . .	20
1.10	Isolated photon plus jet cross sections in $\gamma p$ as measured by ZEUS. . . . .	21
1.11	Inclusive isolated photon cross sections in DIS measured by ZEUS. . . . .	22
1.12	Ratios data/theory for collider and fixed target $pp$ and $p\bar{p}$ data. . . . .	23
1.13	Photon production cross sections measured in $pp$ and $p\bar{p}$ collisions . . . . .	24
2.1	Higher order processes in the isolated photon production in DIS. . . . .	29
2.2	Schematic view of the event generation and detector simulation. . . . .	30
2.3	Comparison of the data with the RAPGAP (non-rad.) MC. . . . .	34
2.4	Illustration of the neutral hadron composition. . . . .	35
3.1	Schematic view of the HERA collider . . . . .	40
3.2	Integrated H1 luminosity over the time of running . . . . .	41
3.3	Isometric view of the H1 detector . . . . .	43
3.4	Simple model of an electromagnetic shower. . . . .	44
3.5	Longitudinal cross section of the Liquid Argon calorimeter . . . . .	47
3.6	Transversal cross section of the Liquid Argon calorimeter . . . . .	47
3.7	Illustration of the readout granularity of the LAr . . . . .	48
3.8	Longitudinal cross section of the H1 tracking system . . . . .	51
3.9	Transverse view of the central tracking detectors . . . . .	52
3.10	The H1 luminosity system . . . . .	54
3.11	Data flow in the designed H1 trigger system layout . . . . .	55

4.1	Event yield for the DIS event selection. . . . .	59
4.2	Trigger efficiency as function of $R_{\text{SpaCal}}$ . . . . .	62
4.3	Trigger efficiency as function of further observables. . . . .	63
4.4	Distributions of $Q^2$ and $y$ for isolated photon candidates. . . . .	65
4.5	The mass of the hadronic system $W_X$ . . . . .	66
4.6	Mass of the generated hadronic system versus the number of good tracks. . .	67
4.7	Energy fraction of photon and pion clusters in the first two LAr layers. . . .	69
4.8	Distributions of the transverse cluster radius $R_T$ . . . . .	70
4.9	Invariant mass $M_{\gamma\gamma}$ of the photon candidate with neighbouring cluster. . . .	70
4.10	Schematic representation of the $k_T$ algorithm. . . . .	73
4.11	Distributions of transverse momentum and polar angle of the hadronic jet. . .	74
4.12	Distribution of the fraction $z$ . . . . .	74
4.13	Correlations of the hadronic jets transverse momentum. . . . .	76
4.14	Distributions of variables relevant to the DIS selection. . . . .	77
4.15	Photon candidate related distributions. . . . .	78
4.16	Relative deviation of the DA energy from the generated electron energy. . . .	80
4.17	Relative deviation of the DA energy from the scattered electron energy. . . .	80
4.18	Cluster energy compared to track measurement and DA energy. . . . .	82
4.19	Resolution of the transverse energy and pseudorapidity of isolated photons. .	82
5.1	Schematic representation of different shower profiles. . . . .	85
5.2	Illustration of the transverse plane in the context of shower shape variables. .	86
5.3	Distributions of the six shower shape variables. . . . .	89
5.4	Shower shape comparison between the SPs and full event MCs. . . . .	90
5.5	Two dimensional correlation plots between the six shower shape variables. . .	91
5.6	Output of the multivariate classification methods. . . . .	94
5.7	Signal efficiency versus background rejection graph. . . . .	95
5.8	The discriminator $D$ versus the decay symmetry for SP neutral pions. . . . .	95
5.9	Signal efficiency versus background rejection for different kinematic bins. . .	96
5.10	Normalised distributions of the discriminator $D$ for the 15 analysis bins. . . .	98
5.11	Discriminator $D$ with SP predictions scaled according to the fit results. . . . .	101
5.12	Number of photons extracted for the three multivariate methods. . . . .	103
5.13	Photon candidate energy over the energy of the incident neutral particle. . . .	104
5.14	Discriminator distribution for SP background with modelled cluster overlap. .	105
5.15	Deviation in the extracted signal photons using SPs and full event MCs. . . .	106
6.1	Acceptance factor $\mathcal{A}$ , purity $\mathcal{P}$ and stability $\mathcal{S}$ in $(E_T^\gamma, \eta^\gamma)$ . . . . .	108
6.2	Acceptance factor $\mathcal{A}$ , purity $\mathcal{P}$ and stability $\mathcal{S}$ in $Q^2$ . . . . .	109
6.3	Hottest cell fraction of DVCS photons compared to distorted simulation. . . .	111
6.4	$\chi^2/\text{NDF}$ distribution in dependence of the stretching factor $k$ . . . . .	112

---

7.1	Differential inclusive cross sections $d\sigma/dE_T^\gamma$ , $d\sigma/d\eta^\gamma$ , and $d\sigma/dQ^2$ . . . . .	120
7.2	Differential inclusive cross sections $d\sigma/dE_T^\gamma$ in $\eta^\gamma$ bins. . . . .	121
7.3	Differential inclusive cross sections $d\sigma/dE_T^\gamma$ , $d\sigma/d\eta^\gamma$ for $40 < Q^2 < 150 \text{ GeV}^2$ . . . . .	122
7.4	Differential cross sections $d\sigma/d\eta^\gamma$ compared to ZEUS. . . . .	123
7.5	Differential cross sections for photon plus no-jets and photon plus jet. . . . .	125
7.6	Transverse radius and discriminator for less isolated photon candidates. . . . .	127
7.7	Acceptance factor $\mathcal{A}$ , purity $\mathcal{P}$ and stability $\mathcal{S}$ in $(E_T^\gamma, \eta^\gamma)$ for $0.8 < z < 0.9$ . . . . .	129
7.8	Differential inclusive cross sections $d\sigma/dz$ . . . . .	130
7.9	Differential cross sections $d\sigma/dz_\gamma$ for photon plus no-jets(jet). . . . .	131
7.10	Differential cross sections $d\sigma/dz_\gamma$ of 2-jet and 3-jet events by ALEPH. . . . .	132
7.11	Differential cross sections $d\sigma/dz_\gamma$ of 2-jet events measured by ALEPH. . . . .	132
7.12	Total inclusive cross section as function of the jet resolution parameter $R_0$ . . . . .	134
7.13	Total cross section for photon plus no-jets(jet) as function of $R_0$ . . . . .	134
A.1	Properties of the $\pi^0 \rightarrow \gamma\gamma$ decay in dependence of the opening angle. . . . .	143
A.2	Non-separable background from neutral pion decays. . . . .	144
B.1	Artificial neuron and activation function. . . . .	149
B.2	Topology of a neural network with one hidden layer. . . . .	150
C.1	Feynman diagrams illustrating the DVCS and the Bethe-Heitler processes. . . . .	153
C.2	Transverse energy and polar angle of selected photons in DVCS events. . . . .	154
C.3	Transverse energy and polar angle of selected electrons in BH events. . . . .	154





# LIST OF TABLES

---

2.1	Relative contribution of the neutral hadrons to the background composition. . .	35
2.2	Summary of used Monte Carlo event samples. . . . .	37
3.1	Longitudinal shower parameters derived with Rossi's Approximation B . . .	45
4.1	Summary of analysed data samples. . . . .	58
4.2	The used subtriggers listed for different years of data taking. . . . .	60
4.3	Total trigger efficiencies. . . . .	63
4.4	Summary of selection requirements. . . . .	75
5.1	Correlation coefficients between the six shower shape variables. . . . .	93
5.2	Maximum separation power and the minimum fraction of misclassification. . .	97
5.3	Total number of signal events for the considered event samples. . . . .	99
5.4	Fit results for any considered analysis bin. . . . .	100
5.5	Effect of the redefined discriminator made up from five shower variables. . .	102
5.6	Total number of photons extracted for different multivariate methods. . . . .	102
6.1	Derived uncertainties of the shower shape variables. . . . .	113
7.1	Predictions used for comparison to the cross sections. . . . .	118
7.2	Phase space region for isolated photon cross sections. . . . .	119
7.3	Number of photon candidates and the signal fraction for several $z$ bins. . . . .	129
A.1	Parameters of the neutral pion $\pi^0$ . . . . .	141
A.2	Extreme configurations in the $\pi^0 \rightarrow \gamma\gamma$ decay. . . . .	146
D.1	<i>Good</i> track quality criteria. . . . .	155
E.1	Analysis bins in $(E_T^\gamma, \eta^\gamma)$ and $Q^2$ . . . . .	157
F.1	Cross sections for inclusive isolated photon production. . . . .	159
F.2	Cross sections for inclusive isolated photon production in $\eta^\gamma$ bins. . . . .	160
F.3	Cross sections for the isolated photon production at $40 < Q^2 < 150 \text{ GeV}^2$ . . .	161

F.4	Cross sections for the photon plus no-jets(jet) production. . . . .	162
F.5	Cross sections $d\sigma/dz$ and total cross section $\sigma_{tot}$ in dependence of $R_0$ . . . . .	163

## BIBLIOGRAPHY

---

- [1] **ZEUS** Collaboration, S. Chekanov *et al.*, “Observation of isolated high-E(T) photons in deep inelastic scattering,” *Phys. Lett.* **B595** (2004) 86–100, [hep-ex/0402019](#).
- [2] A. Gehrman-De Ridder, T. Gehrman, and E. Poulsen, “Measuring the photon fragmentation function at HERA,” *Eur. Phys. J.* **C47** (2006) 395–411, [hep-ph/0604030](#).
- [3] **H1** Collaboration, F. D. Aaron *et al.*, “Measurement of Isolated Photon Production in Deep-Inelastic Scattering at HERA,” *submitted to Eur. Phys. J. C* (2007) [arXiv:0711.4578 \[hep-ex\]](#).
- [4] **H1** Collaboration, C. Adloff *et al.*, “Measurement and QCD analysis of neutral and charged current cross sections at HERA,” *Eur. Phys. J.* **C30** (2003) 1–32, [hep-ex/0304003](#).
- [5] E. D. Bloom *et al.*, “High-energy inelastic e p scattering at 6-degrees and 10- degrees,” *Phys. Rev. Lett.* **23** (1969) 930–934.
- [6] M. Breidenbach *et al.*, “Observed behavior of highly inelastic electron-proton scattering,” *Phys. Rev. Lett.* **23** (1969) 935–939.
- [7] J. Callan, Curtis G. and D. J. Gross, “High-energy electroproduction and the constitution of the electric current,” *Phys. Rev. Lett.* **22** (1969) 156–159.
- [8] G. Altarelli and G. Parisi, “Asymptotic Freedom in Parton Language,” *Nucl. Phys.* **B126** (1977) 298.
- [9] Y. L. Dokshitzer, “Calculation of the Structure Functions for Deep Inelastic Scattering and e+ e- Annihilation by Perturbation Theory in Quantum Chromodynamics,” *Sov. Phys. JETP* **46** (1977) 641–653.
- [10] V. N. Gribov and L. N. Lipatov, “Deep inelastic e p scattering in perturbation theory,” *Sov. J. Nucl. Phys.* **15** (1972) 438–450.

- [11] J. Pumplin *et al.*, “New generation of parton distributions with uncertainties from global QCD analysis,” *JHEP* **07** (2002) 012, [hep-ph/0201195](#).
- [12] M. Glück, E. Reya, and A. Vogt, “Dynamical parton distributions revisited,” *Eur. Phys. J. C* **5** (1998) 461–470, [hep-ph/9806404](#).
- [13] A. D. Martin, R. G. Roberts, W. J. Stirling, and R. S. Thorne, “MRST2001: Partons and alpha(s) from precise deep inelastic scattering and Tevatron jet data,” *Eur. Phys. J. C* **23** (2002) 73–87, [hep-ph/0110215](#).
- [14] A. D. Martin, R. G. Roberts, W. J. Stirling, and R. S. Thorne, “Uncertainties of predictions from parton distributions. I: Experimental errors. ((T)),” *Eur. Phys. J. C* **28** (2003) 455–473, [hep-ph/0211080](#).
- [15] E. W. N. Glover and A. G. Morgan, “Measuring the photon fragmentation function at LEP,” *Z. Phys. C* **62** (1994) 311–322.
- [16] **ALEPH** Collaboration, D. Buskulic *et al.*, “First measurement of the quark to photon fragmentation function,” *Z. Phys. C* **69** (1996) 365–378.
- [17] **ZEUS** Collaboration, S. Chekanov *et al.*, “Study of the effective transverse momentum of partons in the proton using prompt photons in photoproduction at HERA,” *Phys. Lett. B* **511** (2001) 19–32, [hep-ex/0104001](#).
- [18] **H1** Collaboration, A. Aktas *et al.*, “Measurement of prompt photon cross sections in photoproduction at HERA,” *Eur. Phys. J. C* **38** (2005) 437–445, [hep-ex/0407018](#).
- [19] A. Gehrmann-De Ridder and E. W. N. Glover, “Final state photon production at LEP,” *Eur. Phys. J. C* **7** (1999) 29–48, [hep-ph/9806316](#).
- [20] W. T. Giele and E. W. N. Glover, “Higher order corrections to jet cross-sections in  $e^+e^-$  annihilation,” *Phys. Rev. D* **46** (1992) 1980–2010.
- [21] A. Gehrmann-De Ridder, T. Gehrmann, and E. W. N. Glover, “Radiative corrections to the photon + 1jet rate at LEP,” *Phys. Lett. B* **414** (1997) 354–361, [hep-ph/9705305](#).
- [22] L. Bourhis, M. Fontannaz, and J. P. Guillet, “Quark and gluon fragmentation functions into photons,” *Eur. Phys. J. C* **2** (1998) 529–537, [hep-ph/9704447](#).
- [23] **ZEUS** Collaboration, J. Breitweg *et al.*, “Measurement of inclusive prompt photon photoproduction at HERA,” *Phys. Lett. B* **472** (2000) 175–188, [hep-ex/9910045](#).
- [24] **ZEUS** Collaboration, S. Chekanov *et al.*, “Measurement of prompt photons with associated jets in photoproduction at HERA,” *Eur. Phys. J. C* **49** (2007) 511–522, [hep-ex/0608028](#).

- [25] P. Aurenche, M. Fontannaz, J.-P. Guillet, E. Pilon, and M. Werlen, “A new critical study of photon production in hadronic collisions,” *Phys. Rev.* **D73** (2006) 094007, [hep-ph/0602133](#).
- [26] **Fermilab E706** Collaboration, L. Apanasevich *et al.*, “Measurement of direct photon production at Tevatron fixed target energies,” *Phys. Rev.* **D70** (2004) 092009, [hep-ex/0407011](#).
- [27] **CDF** Collaboration, D. Acosta *et al.*, “Comparison of the isolated direct photon cross sections in  $p\bar{p}$  collisions at  $\sqrt{s} = 1.8\text{-TeV}$  and  $\sqrt{s} = 0.63\text{-TeV}$ ,” *Phys. Rev.* **D65** (2002) 112003, [hep-ex/0201004](#).
- [28] **CDF** Collaboration, D. Acosta *et al.*, “Direct photon cross section with conversions at CDF,” *Phys. Rev.* **D70** (2004) 074008, [hep-ex/0404022](#).
- [29] **D0** Collaboration, V. M. Abazov *et al.*, “Measurement of the isolated photon cross section in  $p\bar{p}$  collisions at  $\sqrt{s} = 1.96\text{-TeV}$ ,” *Phys. Lett.* **B639** (2006) 151–158, [hep-ex/0511054](#).
- [30] **OPAL** Collaboration, K. Ackerstaff *et al.*, “Measurement of the quark to photon fragmentation function through the inclusive production of prompt photons in hadronic  $Z^0$  decays,” *Eur. Phys. J.* **C2** (1998) 39–48, [hep-ex/9708020](#).
- [31] A. Gehrmann-De Ridder, T. Gehrmann, and E. Poulsen, “Isolated photons in deep inelastic scattering,” *Phys. Rev. Lett.* **96** (2006) 132002, [hep-ph/0601073](#).
- [32] A. Gehrmann-De Ridder, G. Kramer, and H. Spiesberger, “Photon plus jet cross sections in deep inelastic ep collisions at order  $O(\alpha^2 \alpha(s))$ ,” *Nucl. Phys.* **B578** (2000) 326–350, [hep-ph/0003082](#).
- [33] S. Caron, *Jets in Photoproduction at HERA*. PhD thesis, RWTH Aachen, 2002.
- [34] M. Bengtsson and T. Sjostrand, “Parton Showers in Leptoproduction Events,” *Z. Phys.* **C37** (1988) 465.
- [35] T. Sjostrand and M. Bengtsson, “The Lund Monte Carlo for Jet Fragmentation and e+e- Physics. Jetset Version 6.3: An Update,” *Comput. Phys. Commun.* **43** (1987) 367.
- [36] B. Andersson, G. Gustafson, G. Ingelman, and T. Sjostrand, “Parton Fragmentation and String Dynamics,” *Phys. Rept.* **97** (1983) 31.
- [37] G. C. Fox and S. Wolfram, “A Model for Parton Showers in QCD,” *Nucl. Phys.* **B168** (1980) 285.

- [38] T. Sjostrand, L. Lonnblad, and S. Mrenna, “PYTHIA 6.2: Physics and manual,” [hep-ph/0108264](#).
- [39] T. Sjostrand, “High-energy physics event generation with PYTHIA 5.7 and JETSET 7.4,” *Comput. Phys. Commun.* **82** (1994) 74–90.
- [40] C. Friberg and T. Sjostrand, “Total cross sections and event properties from real to virtual photons,” *JHEP* **09** (2000) 010, [hep-ph/0007314](#).
- [41] C. Friberg and T. Sjostrand, “Jet production by virtual photons,” *Eur. Phys. J.* **C13** (2000) 151–174, [hep-ph/9907245](#).
- [42] C. Friberg and T. Sjostrand, “Effects of longitudinal photons,” *Phys. Lett.* **B492** (2000) 123–134, [hep-ph/0009003](#).
- [43] G. Corcella *et al.*, “HERWIG 6.5 release note,” [hep-ph/0210213](#).
- [44] H. Jung, “Hard diffractive scattering in high-energy e p collisions and the Monte Carlo generation RAPGAP,” *Comp. Phys. Commun.* **86** (1995) 147–161.
- [45] H1-Collaboration, “ep Physics Beyond 1999,” *H1 internal report H1-10/97-531* (1997).
- [46] U. Schneekloth, “Recent HERA results and future prospects,” [hep-ex/9806010](#).
- [47] G. H. Hoffstaetter, “The luminosity upgrade of HERA,” *ICFA Beam Dyn. Newslett.* **24** (2001) 8–18.
- [48] J. Becker *et al.*, “A vertex trigger based on cylindrical multiwire proportional chambers,” *physics/0701002* (2007).
- [49] **H1** Collaboration, I. Abt *et al.*, “The H1 detector at HERA,” *Nucl. Instrum. Meth.* **A386** (1997) 310–347.
- [50] **H1** Collaboration, I. Abt *et al.*, “The Tracking, calorimeter and muon detectors of the H1 experiment at HERA,” *Nucl. Instrum. Meth.* **A386** (1997) 348–396.
- [51] W.-M. Yao *et al.*, “Review of Particle Physics,” *Journal of Physics G* **33** (2006) 1+.
- [52] Y.-S. Tsai, “Pair production and bremsstrahlung of charged leptons,” *Rev. Mod. Phys.* **46** (1974) 815.
- [53] U. Amaldi, “Fluctuations in Calorimetry Measurements,” *Phys. Scripta* **23** (1981) 409.
- [54] E. Longo and I. Sestili, “Monte carlo calculation of photon initiated electromagnetic showers in lead glass,” *Nucl. Instrum. Meth.* **128** (1975) 283.

- [55] B. Rossi, *High Energy Particles*. Prentice Hall, NY, 1952.
- [56] C. W. Fabjan, “Calorimetry in high-energy physics,” *NATO Adv. Study Inst. Ser. B Phys.* **128** (1985) 281.
- [57] G. Bathow, E. Freytag, M. Koeberling, K. Tesch, and R. Kajikawa, “Measurements of the longitudinal and lateral development of electromagnetic cascades in lead, copper and aluminum at 6 gev,” *Nucl. Phys.* **B20** (1970) 592–602.
- [58] W. R. Nelson, T. M. Jenkins, R. C. McCall, and J. K. Cobb, “Electron induced cascade showers in copper and lead at 1- gev,” *Phys. Rev.* **149** (1966) 201–208.
- [59] C. Grupen, *Particle Detectors*. Cambridge University Press, 1996.
- [60] **H1 Calorimeter Group** Collaboration, B. Andrieu *et al.*, “The H1 liquid argon calorimeter system,” *Nucl. Instrum. Meth.* **A336** (1993) 460–498.
- [61] **H1 Calorimeter Group** Collaboration, B. Andrieu *et al.*, “Beam tests and calibration of the H1 liquid argon calorimeter with electrons,” *Nucl. Instrum. Meth.* **A350** (1994) 57–72.
- [62] **H1 Calorimeter Group** Collaboration, B. Andrieu *et al.*, “Results from pion calibration runs for the H1 liquid argon calorimeter and comparisons with simulations,” *Nucl. Instrum. Meth.* **A336** (1993) 499–509.
- [63] **H1 SPACAL Group** Collaboration, R. D. Appuhn *et al.*, “The H1 lead/scintillating-fibre calorimeter,” *Nucl. Instrum. Meth.* **A386** (1997) 397–408.
- [64] R. Pöschl, *Measurement of the Double Differential Dijet Rate in Deep Inelastic Scattering at HERA and Comparison to NLO QCD Calculations*. PhD thesis, Universität Dortmund, 2000.
- [65] **H1 SPACAL Group** Collaboration, T. Nicholls *et al.*, “Performance of an electromagnetic lead / scintillating fiber calorimeter for the h1 detector,” *Nucl. Instrum. Meth.* **A374** (1996) 149–156.
- [66] D. Reyna, “Modifications to SpaCal for H1 High Luminosity Operation and the Effect on Acceptance,” *H1 internal report H1-11/98-555* (1998).
- [67] J. Burger *et al.*, “The Central jet chamber of the H1 experiment,” *Nucl. Instrum. Meth.* **A279** (1989) 217–222.
- [68] B. Schwab, *Das Rückwärtsdriftkammersystem des H1 Experiments: Simulationen, Rekonstruktion, Kalibration und erste Datenanalyse*. PhD thesis, Universität Heidelberg, 1996.

- [69] A. Makankin *et al.*, “Backward Proportional Chamber at the H1 Experiment (website).” <http://www-h1.desy.de/h1det/tracker/bpc/BPCpage.htm>.
- [70] V. Shekelyan, “Simulation and Reconstruction in H1 Liquid Argon Calorimetry,” *H1 internal report H1-04/93-288* (1993).
- [71] R. Brun *et al.*, “GEANT3 user’s guide,” *CERN-DD/EE-84-1* (1987).
- [72] S. Peters, *Die parametrisierte Simulation elektromagnetischer Schauer*. PhD thesis, MPI Munich, 1992.
- [73] R. Lemrani-Alaoui, *Prompt Photon Production at HERA*. PhD thesis, Universität Hamburg, 2003.
- [74] M. Ellerbrock *et al.*, “Improved Description of Electromagnetic Showers in H1FAST,” *H1 internal report H1-01/05-617* (2005).
- [75] V. Boudry *et al.*, “The inclusive electron trigger for the SpaCal: Design and CERN-test results,” *H1 internal report H1-03/95-430* (1995).
- [76] T. Wolff *et al.*, “A Drift chamber track finder for the first level trigger of the H1 experiment,” *Nucl. Instrum. Meth.* **A323** (1992) 537–541.
- [77] A. Baird *et al.*, “A fast high resolution track trigger for the H1 experiment,” *IEEE Trans. Nucl. Sci.* **48** (2001) 1276–1285, [hep-ex/0104010](https://arxiv.org/abs/hep-ex/0104010).
- [78] S. Egli *et al.*, “Calculating Event Weights in Case of Downscaling on Trigger Levels 1-4,” *H1 internal report H1-04/97-517* (1997).
- [79] L. Finke, *Measurement of Charm and Beauty Dijet Cross Sections in Photoproduction*. PhD thesis, Universität Hamburg, 2006.
- [80] H. Abramowicz and A. Caldwell, “HERA collider physics,” *Rev. Mod. Phys.* **71** (1999) 1275–1410, [hep-ex/9903037](https://arxiv.org/abs/hep-ex/9903037).
- [81] T. H. O. group, “The H1 OO physics analysis project (website).” <https://www-h1.desy.de/icas/oo/current/oo.ps.gz>.
- [82] M. Peez *et al.*, “An energy flow algorithm for Hadronic Reconstruction in OO: Hadroo2,” *H1 internal report H1-01/05-616* (2005).
- [83] S. D. Ellis and D. E. Soper, “Successive combination jet algorithm for hadron collisions,” *Phys. Rev.* **D48** (1993) 3160–3166, [hep-ph/9305266](https://arxiv.org/abs/hep-ph/9305266).
- [84] G. C. Blazey *et al.*, “Run II jet physics,” [hep-ex/0005012](https://arxiv.org/abs/hep-ex/0005012).



- [85] M. H. Seymour, “Jets in QCD,” *AIP Conf. Proc.* **357** (1996) 568–587, [hep-ph/9506421](#).
- [86] S. Bentvelsen *et al.*, “Proceedings of the Workshop ‘Physics at HERA’, vol. 1, eds. W. Buchmüller and G. Ingemann,” *DESY* **23** (1992).
- [87] A. A. Glazov, *Measurement of the Proton Structure Functions  $F_2$  and  $F_L$  with the H1 Detector at HERA*. PhD thesis, Humboldt-Universität Berlin, 1998.
- [88] U. Bassler and G. Bernardi, “On the kinematic reconstruction of deep inelastic scattering at HERA: The Sigma method,” *Nucl. Instrum. Meth.* **A361** (1995) 197–208, [hep-ex/9412004](#).
- [89] B. Heinemann, *Measurement of charged current and neutral current cross sections in positron-proton collisions at  $\sqrt{s}=300$  GeV*. PhD thesis, Universität Hamburg, 1999.
- [90] M. Abramowitz and Stegun, *Handbook of Mathematical Functions with Formulas, Graphs, and Mathematical Tables*. New York: Dover, 1972.
- [91] J. F. Kenney and E. S. Keeping, *Mathematics of Statistics*. NJ: Van Nostrand, 1962.
- [92] **H1** Collaboration, A. Aktas *et al.*, “Measurement and QCD analysis of the diffractive deep- inelastic scattering cross section at HERA,” *Eur. Phys. J.* **C48** (2006) 715–748, [hep-ex/0606004](#).
- [93] **H1** Collaboration, C. Adloff *et al.*, “Measurement of neutral and charged current cross-sections in positron proton collisions at large momentum transfer,” *Eur. Phys. J.* **C13** (2000) 609–639, [hep-ex/9908059](#).
- [94] K. Nowak, “private communication.”
- [95] D. Pitzl, “private communication.”
- [96] K. Müller, “private communication.”
- [97] A. D. Martin, R. G. Roberts, W. J. Stirling, and R. S. Thorne, “Parton distributions incorporating QED contributions,” *Eur. Phys. J.* **C39** (2005) 155–161, [hep-ph/0411040](#).
- [98] P. Domingos and M. Pazzani, “On the Optimality of the Simple Bayesian Classifier under Zero-One Loss,” *Machine Learning* **29** (1997) 103–130.
- [99] M. Pazzani, “Searching for dependencies in Bayesian classifiers,” in *Learning from Data: AI and Statistics*. Springer-Verlag, 1996.

- 
- [100] H. Zhang, “Exploring conditions for the optimality of naïve bayes,” *International Journal of Pattern Recognition and Artificial Intelligence* **19** (2005), no. 2, 183–198.
- [101] C. Bishop, *Neural Networks for Pattern Recognition*. Oxford: Clarendon Press, 1995.
- [102] R. Duda, P. Hart, and D. Stork, *Pattern classification*. Chichester: John Wiley and Sons, 2001.
- [103] H. Abdi, “Neural networks,” in *Encyclopedia for research methods for the social sciences*, M. Lewis-Beck, A. Bryman, and T. Futing, eds., pp. 725–728. Thousand Oaks (CA), 2003.
- [104] Hecht-Nielsen, R., “Kolmogorov’s mapping neural network existence theorem,” in *IEEE International Conference on Neural Networks*. SOS Printing, San Diego, 1987.
- [105] P. Werbos, *The Roots of Backpropagation*. New York: Wiley, 1994.
- [106] D. E. Rumelhart, G. E. Hinton, and R. J. Williams, “Learning representations by back-propagating errors,” *Nature* **323** (1986) 533–536.
- [107] T. Carli and B. Koblitz, “A multi-variate discrimination technique based on range-searching,” *Nucl. Instrum. Meth.* **A501** (2003) 576–588, [hep-ex/0211019](#).
- [108] R. Sedgewick, *Algorithms in C++*, ch. 26. Addison Wesley (Boston), 1992.
- [109] **H1** Collaboration, A. Aktas *et al.*, “Measurement of deeply virtual Compton scattering at HERA,” *Eur. Phys. J.* **C44** (2005) 1–11, [hep-ex/0505061](#).

## ACKNOWLEDGEMENTS

---

Firstly, I would like to thank my supervisor Prof. Dr. Ulrich Straumann for giving me the opportunity to work on this non-isolated photon project. I am grateful for his support and confidence in my work throughout my PhD. On his initiative the collaboration with the Institute of Theoretical Physics at the University of Zurich was established, which motivated the topic of this thesis and triggered the related theoretical calculation at the same time.

In this respect I wish to thank Prof. Dr. Thomas Gehrmann, Dr. Aude Gehrmann-De Ridder and Eva Poulsen for their calculation and many fruitful discussions which had a major influence on this analysis. It was a rewarding experience to work on an experimental analysis in such close contact to the relevant theorists. Many thanks also go to Prof. Dr. Gustav Kramer and Dr. Hubert Spiesberger for providing the NLO calculation.

I am deeply indebted to Dr. Katharina Müller, not just for the simulation of so many Monte Carlo events. Much of this work would not have been possible without her invaluable and experienced advice at all times. I thank her for the unwearrying support, the best team-work and for the certainly tastiest *Swiss Röstis*.

Special thanks go to the H1 group at the University of Zurich: Prof. Dr. Ulrich Straumann, Dr. Katharina Müller, Dr. Stefania Xella-Hansen, Dr. Linus Lindfeld, Dr. Stefan Schmitt, Dr. Max Urban and Krzysztof Nowak for the pleasant environment in Hamburg, Zurich and at the weekly video conferences. The work in the experimental hall on the group's CIP2k project was as well an exciting and unique experience.

Many thanks also go to my referees in the publication procedure for the H1 paper related to this work, Dr. Jörg Gayler and Prof. Dr. Jacek Turnau, for the many helpful discussions and also to Dr. Cristinel Diaconu for his support in the publication process and for his external expert's report. I wish to thank the H1 Collaboration for the professional and friendly atmosphere I enjoyed and for allowing me to work at the frontier of modern particle physics research.

Sincere thanks also go to those who participated in the proofreading of the manuscript, especially to my friend Martin Schäfer who fortunately did not suspect what was in store for him. I thank Dres. Lars Finke and Linus Lindfeld for the many years of best friendship. It was brilliant to have you around all the time!

The sweetest thanks go to my lovely Trias for being in my life and meaning so much to me. Meiner Familie und insbesondere meinen Eltern möchte ich danken, dass sie immer für mich da sind und mir stets ein liebevolles Zuhause geben.

This work has been supported by the Swiss National Science Foundation.



# LEBENS LAUF

---

## PERSÖNLICHE DATEN

Name	Carsten Schmitz
Geburtsdatum	3. März 1976
Geburtsort	Dortmund, Deutschland
Nationalität	deutsch

## AKADEMISCHE LAUFBAHN

Okt 03 – Okt 07	Promotion, Universität Zürich / DESY Hamburg Prof. Dr. U. Straumann, Physik Institut Universität Zürich <i>Isolated Photon Production in Deep-Inelastic Scattering at HERA</i>
Aug 02	Studienabschluss Diplom Physik, RWTH Aachen
Jul 01 – Jul 02	Diplomarbeit, DESY Hamburg Prof. Dr. Ch. Berger, I. Physikalisches Institut RWTH Aachen <i>Elektroproduktion von Myon-Paaren im Massenbereich der <math>\Upsilon</math>-Resonanz</i>
Okt 99 – Jul 01	Hauptstudium Diplom Physik, RWTH Aachen
Jul 99 – Sep 99	Forschungspraktikum, Infineon Technologies AG, München <i>Computer-Modellierung des CMP Prozesses in der Herstellung von Silikon-Wafern</i>
Sep 98 – Jul 99	Auslandsstudium Physik, University of Edinburgh, UK
Okt 96 – Aug 98	Grundstudium Diplom Physik, RWTH Aachen
Aug 95 – Sep 96	Zivildienst, Dortmund
Aug 86 – Jun 95	Stadtgymnasium Dortmund, Abschluss: Abitur